Perylene Bisimide Foldamers: Synthesis and In-Depth Studies of the Ground- and Excited States Properties

Dissertation zur Erlangung
des naturwissenschaftlichen Doktorgrades
der Julius-Maximilians-Universität Würzburg

vorgelegt von
Benjamin Fimmel
aus Neuruppin

Würzburg 2015

Eingereicht bei der Fakultät für Chemie und Pharmazie am
03.08.2015

Gutachter der schriftlichen Arbeit:
1. Gutachter: Prof. Dr. Frank Würthner
2. Gutachter: Prof. Dr. Bernd Engels

Prüfer des öffentlichen Promotionskolloquiums
1. Prüfer: Prof. Dr. Frank Würthner
2. Prüfer: Prof. Dr. Bernd Engels
3. Prüfer: Prof. Dr. Christoph Lambert

Datum des öffentlichen Promotionskolloquiums
21.10.2015

Doktorurkunde ausgehändigt am _____

Meinen Liebsten

List of Abbreviations

AFM	atomic force microscopy
AMBER	assisted model building and energy refinement (a force field)
ATR	attenuated total reflection
B3LYP(-D3)	Becke-3-parameter-Lee-Yang-Parr (with dispersion correction) (an exchange-correlation functional)
B97D	Grimme's functional including dispersion (pure stand alone functional)
CD	circular dichroism
CR	charge recombination
CS	charge separation
CT	charge transfer
CV	cyclic voltammetry
DCTB	2-[(2*E*)-3-(4-*tert*-butylphenyl)-2-methylprop-2-enylidene]malononitrile
DFT	density functional theory
DSA	dynamic self-assembly
ESA	excited state absorption
ESI	electrospray ionization
fwhm	full width at half maximum
GPC	gel permeation chromatography
GSB	ground state bleaching
HOMO	highest occupied molecular orbital
IC	internal conversion
IR	infrared
ISC	intersystem crossing
LUMO	lowest unoccupied molecular orbital
MALDI	matrix-assisted laser desorption/ionization
MCH	methylcyclohexane
MD	molecular dynamics
MM3*	a force field used for molecular mechanics
m.p.	melting point
MS	mass spectrometry
NEt_3	triethylamine
NIR	near-infrared
NMR	nuclear magnetic resonance
OPE	*oligo*-phenylene ethynylene
OPLS-AA	optimized potentials for liquid simulations-all atoms (a force field)
PBI	perylene-3,4:9,10-bis(dicarboximide) (often mentioned as perylene-3,4:9,10-tetracarboxylic acid bisimide or perylene bisimide)
PET	photoinduced electron transfer
PM6(-DH2)	PM6 Hamiltonian (with corrections for dispersion and hydrogen-bonding) (a semi-empirical method used for calculations)

RT	room temperature
S_n	singlet state (n = 0,1,2,...)
SE	stimulated emission
SVP	single valence potential (a basis set for calculations)
SWV	squarewave voltammetry
T_n	triplet state (n = 0,1,2,...)
TA	transient absorption
TBAF	tetra-*n*-butylammonium fluoride
TBAHFP	tetra-*n*-butylammonium hexafluorophosphate
TCSPC	time-correlated single photon counting
THF	tetrahydrofuran
TIPS	triisopropylsilyl
UV	ultraviolet
Vis	visible

Table of Contents

Chapter 1

–

Introduction and Aim of the Thesis

Over millions of years plants and algae have developed highly efficient strategies to provide enough resources crucial for the surviving of living beings. In contrast, the current enormous need of energy in form of electricity and heat requested by mankind can barely be achieved exclusively by limited natural products, *i.e.* black or brown coal, oil, biomass, or natural gas. Therefore, the direct use of renewable resources (*e.g.*, sunlight) has emerged as a promising source for the growing demand. In Germany the generation of power using renewable energy sources is already achieved with market shares of 25.4% (for the gross electricity consumption in 2013).[1] For solar cells funneling solar energy the silicon-based approaches already have come up in the mid 1950's and have made until today already considerable contributions as energy sources (approximately 20% of the renewable energy sources).[1] To reduce costs and the consumption of materials, and to improve different factors like weight and biocompatibility, aromatic organic dye molecules have established to act as viable alternatives to its Si-antagonists. Early in 1986, the first organic solar cell was reported by Ching W. Tang consisting of copper phthalocyanine and a perylene tetracarboxylic derivative.[2] Although the conversion efficiency and few other important parameters appeared to be rather poor in comparison to solar cells nowadays, this preliminary step played an important role for developing functional materials with better performances using light as energy source. Recently, on December 23rd, 2013,[3] the United Nations Educational, Scientific and Cultural Organization (UNESCO) announced this year 2015 for the international year of light and light-based technologies (IYL2015).[4] Such highlighting expresses the tremendous importance of light as energy source – it might be better to see it as elixir of life – in ancient, present, and also future times. However, the further enhancement of those technologies may play the most crucial part as this issue is in

the hands of mankind by reinventing chemistry and applying new chemical strategies for a rapidly changing world.[5] Primarily, the present processes have to be understood in terms of their photophysical basics, *i.e.* how dye molecules or functional materials interact with light and what happens after their excitation by light. Also the precise interplay between adjacent chromophores has to be elucidated, which indeed influences the overall performance of the bulk material. Thus, rather complex investigations are needed for a growing number of potential candidates in order to achieve knowledge about the structure-property-relationships and the behavior of such functional materials.

In light of the versatility in naturally and artificially constructed, photofunctional systems, organic dye molecules play an essential role for funneling, converting, and distributing energy or producing and redirecting charged species.[6] In other words, in those colorants, carbon-based, light-absorbing materials are used to harvest and transform light into other forms of energy or to ensure the transport of electrons or protons. In natural and artificial photofunctional systems many dye molecules are often embedded in an array or layer-like structure to form ensembles responsible for the functional properties of such bulk materials. Nevertheless, fundamental processes occurring in the ensemble are usually the result of events taking place in small subunits. In order to understand the pivotal, photophysical processes it may be sufficient to investigate the smaller representative entities. Thus, for developing new functional materials, profound studies of oligomeric and small dye systems also mimicking the properties of their larger homologues are often adequate to fathom the bulk performance. Most importantly, for such evaluation a highly defined structure of the oligomers is required. As a result of the inherent efforts to conglomerate into self-assembled structures seen for several dyes especially in the solid state, direct linking of a set number of chromophores seems to be most promising to exclusively investigate the properties of the systems of interest. Covalent tethers can be employed to easily predefine and control the amount of participating subunits in solution.

Besides others, perylene bisimide (PBI) chromophores[7-9] have gained very much attention because of their structural, optical, and functional properties.[10-12] These beneficial properties of the parent, flat PBI molecule are the chemical and thermal robustness, the high tinctorial strength, their intrinsic desire to self-assemble into ordered architectures and also their electron-deficient character. As a result of the latter point, PBI dyes have big potential as n-conducting semiconductors.[13,14] Furthermore, by ingenious variation of the PBI chromophore at the various positions the optical, structural, and electrochemical properties can easily be adjusted in a preferred manner. As could be shown in various examples, PBI

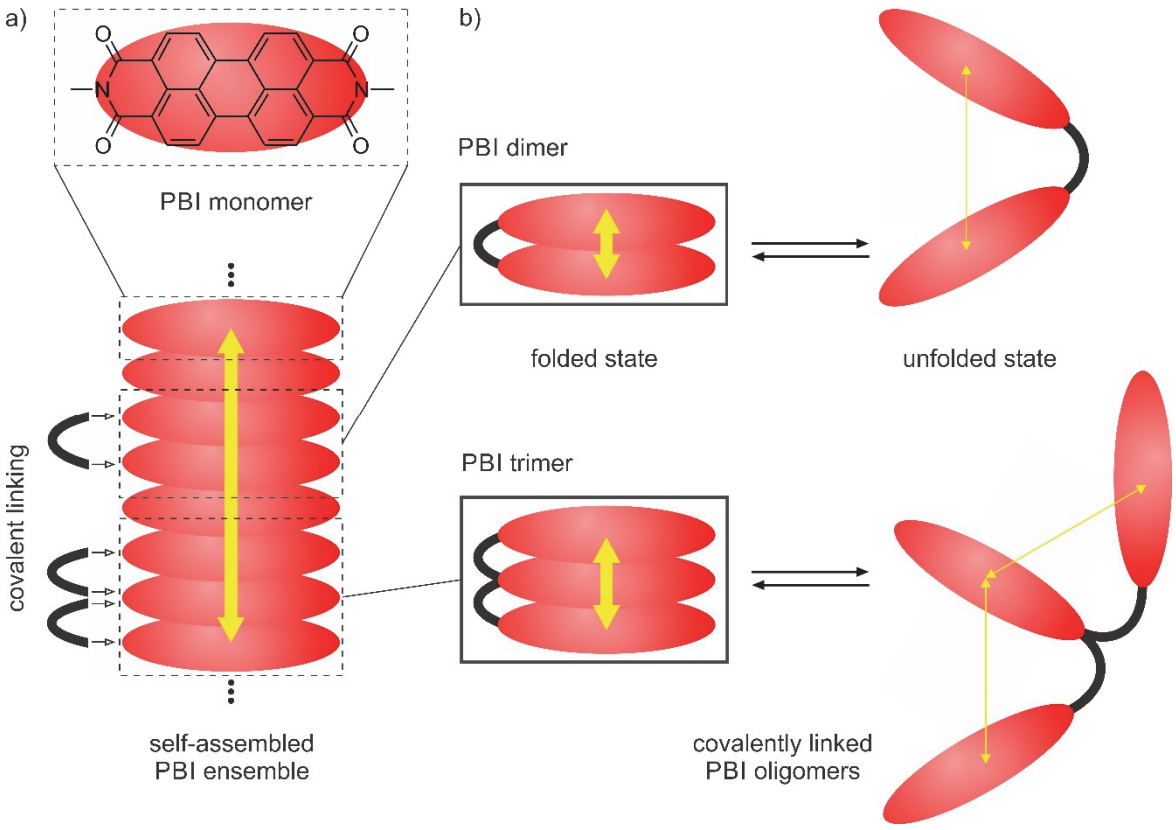

Figure 1. a) Schematic representation of aggregated PBI ensemble (bottom) achieved by self-assembly of monomeric PBI units (top), which exhibits a strong interplay between chromophores (depicted as yellow bold double arrow). b) Concept of foldable PBI oligomers: PBI dimer (top) and PBI trimer (bottom) as covalently tethered (black linkages) PBI systems enabling an externally controlled folding/unfolding in their folded states (left) with pronounced interactions (bold yellow double arrows) or in the respective unfolded states (right) with less interchromophoric interactions (thin yellow double arrows).

aggregate systems often form large stacks (see Figure 1a, bottom) driven by the favorable π–π-interactions. Efforts to overcome the self-assembly of monomeric PBI dyes into large size inhomogeneous structures could be gained by utilizing bulky substituents.[15-20] Nevertheless, self-assembly into larger aggregates is hard to avoid for these dyes. By using molecular tethers or covalent linkages on both sides of the PBI chromophores small PBI stacks could be achieved, in which undesired rearrangement processes are almost completely suppressed.[21-24] As the aforementioned ability to self-assemble often asserts and complicates the study of individual dye molecules and the forcing of coupled PBI system by tethers from two sides shuts down any dynamic behavior, the covalent linking strategy was used in this thesis to form the singly linked PBI-dimer and PBI-trimer depicted schematically in Figure 1b. To reduce the degrees of freedom phenylene ethynylene fragments were used, which connect the PBI chromophores. For a related octameric PBI system, which was synthesized by co-polymerization, this π-conjugated, alternating scaffold was already utilized in a previous work.[25,26] As a consequence of the controllable and tunable self-assembly behavior of PBI dyes in solution, these systems exhibit solvent-

triggered equilibria between folded and unfolded state each. Whereas the former states exhibit only a very small number of PBI arrangements with almost congruent structures, the latter are composed of a set of different conformations with partially large center-to-center distances between PBI moieties. Due to this dependence on the surrounding solvation sphere either folded or unfolded states can be adopted, respectively, leading to pronounced or almost no chromophoric interactions – mimicking small, self-assembled aggregates or PBI dyes in their monomeric state, respectively.

In **Chapter 2** a detailed literature survey of covalently linked PBI architectures ranging from rigid to more flexible examples with some dynamic character with pronounced intramolecular dye–dye interactions is given. These literature-known examples are especially mentioned in the context of exciton theory, dealing with the excitation of such small-sized ensembles, and with the following deactivation of the excited PBI systems.

The syntheses and in-depth investigations of two foldable PBI systems exhibiting a solvent-dependent folding/unfolding-behavior will be presented in **Chapter 3**. In these studies the ground and excited states properties of both ensembles are extensively analyzed by means of steady-state and time-resolved spectroscopic and theoretical experiments to shed light on the structural and photophysical preferences.

Furthermore, **Chapter 4** and **Chapter 5** give the summary in English and German language, respectively.

The Experimental Section follows in **Chapter 6** including all applied methods and materials, new synthetic routes, or improved strategies to obtain the respective molecules.

Chapter 2
–
Literature Survey

By assembling perylene bisimide (PBI) units in close contact, their intrinsic desire to communicate can be vividly observed by spectral changes. These are a consequence of the modified photophysical properties accomplished upon self-assembly. However, due to structural inhomogeneities and variations in size the precise identification of photophysical processes is challenging for self-assembled systems and thus the direct evaluation of structure-property-relationships remains difficult. In contrast to these noncovalent approaches, the covalent linking of PBI chromophores to yield small and well-defined architectures appears to be more suited to examine the correlation between structure, geometrical aspects, and resulting properties. Therefore, understanding of the fundamental processes between individual PBI moieties in such small-sized systems has a pivotal role also for gaining insights into the photophysical processes in self-assembled structures.

Indeed, in the past years numerous covalently linked PBI oligomers have been elaborated and valuable insights into the dye–dye interactions have been acquired. Thus, in the following chapter (2.1) first the possible aggregate structures will be discussed and explained in terms of Kasha's exciton coupling theory. Upon absorption of light, different energy levels of the excited dye system can be populated depending on geometrical parameters of the involved chromophore units. The subsequent deactivation from the electronically excited to the ground state can involve various relaxation processes, which will be mentioned at that point. In relation to this introductory part, prominent examples of rather rigid and thus well-defined dye–dye arrangements of PBI systems exhibiting electronic interactions between chromophore units will be discussed (2.2). Furthermore, flexible PBI oligomers revealing some dynamic character (2.3) as well as also small- and

large-sized macrocyclic PBI systems (2.4) exhibiting interchromophoric properties will be presented. Whereas the main focus is on small and thus simple dimeric systems, only some representative PBI ensembles with larger numbers of chromophores will be mentioned.

2.1. Excitonic Coupling and Deactivation Processes of Photoexcited PBIs

Most PBI dyes show strong absorption in the visible spectral region with absorption maxima roughly between 500 and 600 nm depending on core substituents (X,Y,Z shown in the general structure of a monomeric PBI molecule (**PBI**) in Figure 2) and fluorescence quantum yields typically higher than 90%.[7-9,27] Exceptions are PBI dyes bearing amino substituents at the bay positions, which possess absorption maxima at larger wavelengths from 650 nm up to 710 nm and only modest fluorescence quantum yields.[28-30]

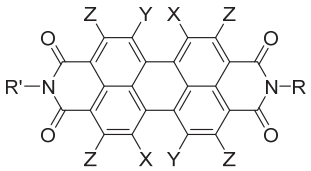

PBI

Figure 2. General structure of a monomeric PBI dye (**PBI**) with different imide (R,R'), bay substituents (X,Y), and so-called headland- or *ortho*-positions (Z). As the variation at the latter positions introduced in 2009 for the first time requires transition metal catalyzed reaction conditions[31-37] and thus only a small number of variations are reported, in the following this substituent Z is always related to hydrogen.

Upon self-assembly of PBI building blocks, *i.e.*, of **PBI** (Figure 2), their absorption and fluorescence properties, and thus the spectral features, are drastically changed. Absorption bands of PBI assemblies are shifted either hypsochromically (to shorter wavelengths) with concomitant band broadening and decrease in intensity or bathochromically (to longer wavelengths) with significant band sharpening and increase of absorption coefficients with regard to the band shape of the respective monomers as shown in Figure 3 for two PBI dyes, **1**[38] and **2**,[39] as illustrative examples. Self-assemblies with bathochromic shifts of absorption bands, as seen for **2**, are commonly termed as J-aggregates (J denotes Jelley, one of the discoverer of such dye aggregates)[40,41] and those with hypsochromic shifts (*e.g.*, like **1**) as H-aggregates (H denotes hypsochromic).[42,43] Both types of PBI assemblies exhibit in general lower fluorescence quantum yields as compared to those of their respective monomers. While such fluorescence quenching due to aggregation is well-explained for H-aggregates by exciton coupling theory (see below), the situation for J-aggregates is more

subtle (here exciton coupling theory predicts a strongly emissive aggregate) and probably involves quenching by trap sites[44,45] or processes such as singlet fission.[46]

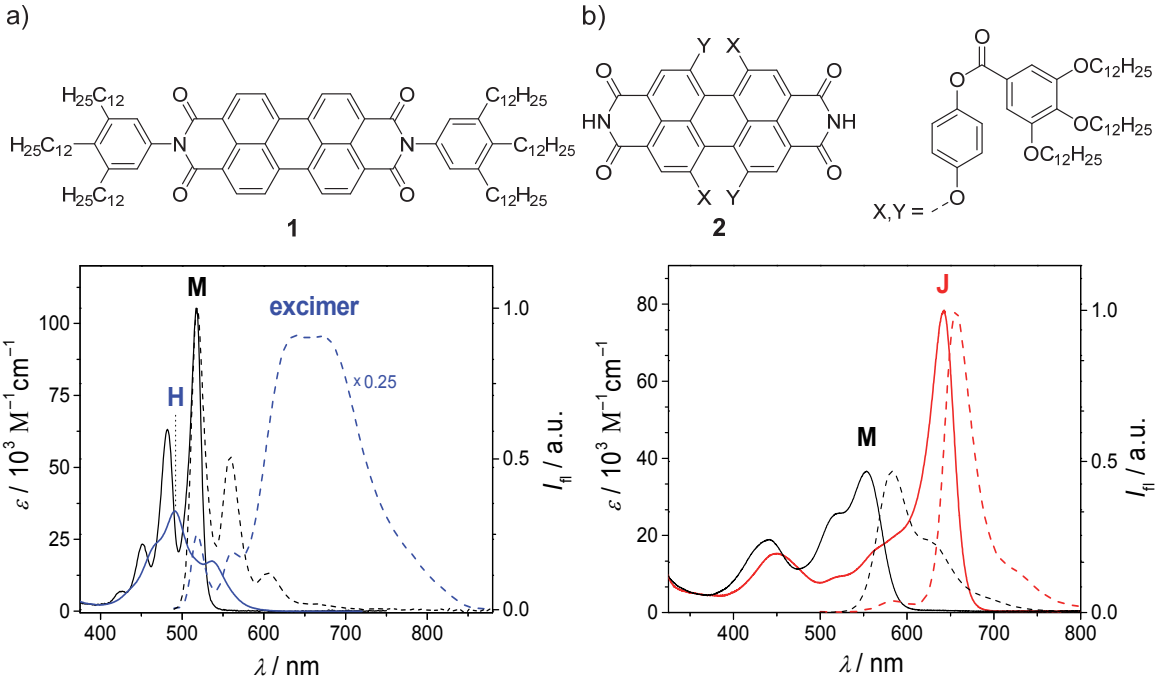

Figure 3. UV/Vis absorption (solid lines) and fluorescence spectra (dashed lines) of a) H-aggregating PBI **1** and b) J-aggregating PBI **2** in methylcyclohexane. a) Monomer absorption (black, solid line; denoted with **M**) and emission spectra (black, dashed line) of PBI **1** at low concentration of 2×10^{-7} M and hypsochromically shifted absorption (blue, solid line; denoted with **H**) and bathochromically shifted, broad excimer emission spectra (blue, dashed line, intensity divided by a factor of 4) upon aggregation at higher concentration of 1×10^{-3} M at 25 °C. b) Monomer absorption (black, solid line; at 90 °C; denoted with **M**) and emission spectra (black, dashed line; at 50 °C) of PBI **2**, and bathochromically shifted J-aggregate absorption (red, solid line; denoted as **J**) and emission spectra (red, dashed line) at 15 °C. For b) the concentrations of the absorption measurements are 6×10^{-7} M and of the fluorescence experiments 2×10^{-7} M. Adapted with permissions from refs [38] and [39]. Copyrights 2007 Wiley-VCH Verlag GmbH & Co. KGaA, Weinheim.

The above-mentioned optical properties of PBI self-assemblies can be explained on the basis of Kasha's exciton coupling theory,[47-49] which deals with the interaction of transition dipole moments of chromophores upon photoexcitation with respect to their geometrical arrangements. In the following, Kasha's model will be discussed in a qualitative manner based on a dimeric system (Figure 4) to explain the spectral changes observed for H- and J-type PBI assemblies.

According to Kasha's model, the vertical excitation from S_0 to S_1 can lead to different higher electronic states depending on the spatial arrangement of the dye units in a composite molecule. The prerequisites for the simplest situation depicted in Figure 4 are the coplanar, parallel, and equidistant orientation of the participating transition dipole moments (μ_{eg}; depicted as black, solid double arrows in the schematic illustration in Figure 4). In a dimeric dye aggregate, the energies of the ground state as well as the excited state are reduced

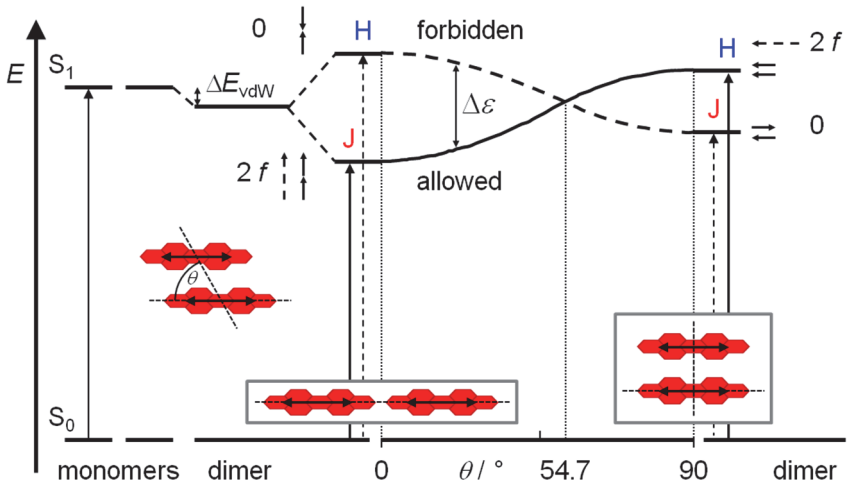

Figure 4. Schematic energy level diagram for the excitonic coupling of PBI dimers with coplanar transition dipole moments (μ_{eg}, depicted as double arrows) tilted toward the interconnecting axis by the slip angle θ. The two borderline cases, *i.e.*, in-line (θ = 0°) and sandwich-like arrangement (θ = 90°), are shown in the gray boxes on the left and right sides of the diagram, respectively. Additionally, for these two alignments, the resulting overall oscillator strengths (small dashed arrows) as well as the oscillator strengths (f, small solid arrows) of the two individual PBI units are indicated. For further explanation on this model, see the text below.

relative to those of the respective monomer units due to the energy gain achieved by van der Waals forces. Equalizing the ground state energy levels of the monomers and the formed dimer results in an energetically more stable excited dimer situation because the more polarizable excited molecule shows an increased van der Waals interaction (ΔE_{vdW}). As a consequence of excitonic coupling, however, the excited singlet state of such dimers splits into two energetic states, the so-called Frenkel excitons. The extent of this splitting ($\Delta\varepsilon$) depends on the magnitude of the dyes' transition dipole moments, the distance between the chromophores, and their mutual arrangement (Figure 4). While both excitonic states for the general case of not coplanar and/or not parallel dye units are at least partially allowed, the more simple and highly illustrative situation depicted in Figure 4 arises for coplanar, parallel chromophores. Here two borderline cases in which the transition dipole moments are either in-line (with a slip angle of θ = 0°, J-aggregate) or stacked on top of each other (θ = 90°, H-aggregate) are shown on the left and right sides, respectively, while the alignment with no energy level splitting of both states is indicated by the middle dashed line at the so-called magic angle (θ = 54.7°). At this value, both sigmoidal curves have an intersection point, and the two states are equal in energy. It is noteworthy to point out the fact that the spectra of such kind of aggregates can not be distinguished from those of their monomers. The transitions from the S_0 state to the different S_1 energy levels on the solid sigmoidal curve are strongly allowed (high oscillator strengths), whereas the ones to the energy levels on the dashed line are strictly forbidden (no oscillator strength, f = 0). Thus, for PBI–PBI

arrangements with θ values smaller than 54.7°, the transition is energetically decreased with respect to the monomers' transition, whereas larger θ values result in an energy increase. Consequently, the aggregates' absorption maxima are shifted bathochromically to lower energies or hypsochromically to higher energies, respectively. In this simplistic picture, only longitudinal shifts along the dyes' transition dipole moments are considered. However, other geometrical arrangements, that is, the transversal displacement as well as a rotational offset to each other, also influence the excitonic coupling and the resulting spectral behavior.[50] For rotationally displaced PBI dimers and also larger oligomers, the excitonic coupling has been elucidated by quantum dynamical calculations by Engel and co-workers.[51-53] These calculations have also taken into account the pronounced vibronic progressions of the PBI chromophores, which make the analysis of the excitonic coupling more cumbersome than for dyes with less strong vibronic coupling, *e.g.*, cyanine dyes.[54-56]

Upon photoexcitation of a chromophore from the electronic ground state (S_0) to higher energy levels (S_n, $n \geq 2$), a very fast relaxation to the first excited state (S_1) occurs, which according to Kasha's rule[57] serves as a starting point for further relaxation processes from $S_1 \rightarrow S_0$. The main deactivation channel for excited PBI monomers is the radiative process to the ground state (fluorescence), while the intersystem crossing (ISC) to the triplet state (T_1) is a spin-forbidden and thus relatively slow process. Furthermore, PBIs are very rigid; therefore, also the radiationless internal conversion (IC) to the ground state is slow. As a result, the fluorescence quantum yields of PBIs are in general very high. However, for an ensemble of coupled chromophores, several additional relaxation processes become feasible, which may lead to either radiative or nonradiative decays. For instance, structural rearrangements among aggregated PBIs may lead to excimer states, ^{1}(PBI–PBI)*, with enhanced lifetimes (up to 30 ns as compared to approximately 4 ns[58-61] for PBI monomers), markedly displaced fluorescence, and modest to high quantum yields as observed for the H-type aggregate shown in Figure 3.[38] Furthermore, other relaxation pathways, which direct the system to its ground state, may become more prominent upon PBI aggregation. For a hypothetical PBI dimer (PBI–PBI), the possible radiationless and radiative decays are schematically illustrated in Figure 5. Another relaxation channel than the $S_1 \rightarrow S_0$ pathway or excimer fluorescence is the ISC to triplet states, resulting in a single triplet state (^{3}PBI–PBI). While the $S_1 \rightarrow T_1$ process is very slow for the PBI monomers due to the large energy gap,[62] this process may be accelerated in PBI aggregates, for example *via* an intermediate PBI^+-PBI^- charge transfer[63] or excimer state. Spin-allowed singlet (exciton) fission is also a possible deactivation pathway, which has, however, only been observed in

solid materials so far.[46] In this process, one excited state (^{1}PBI–PBI) converts to two excited triplet states (^{3}PBI-^{3}PBI). According to these studies, this pathway is slightly endergonic and might therefore only occur in the solid state where it becomes favored by entropy. Finally, a nonradiative process (neither fluorescence nor phosphorescence) results from a photoinduced electron transfer (PET), so that after charge separation (CS, PBI^+–PBI^-) the subsequent charge recombination (CR) takes place.[30,63]

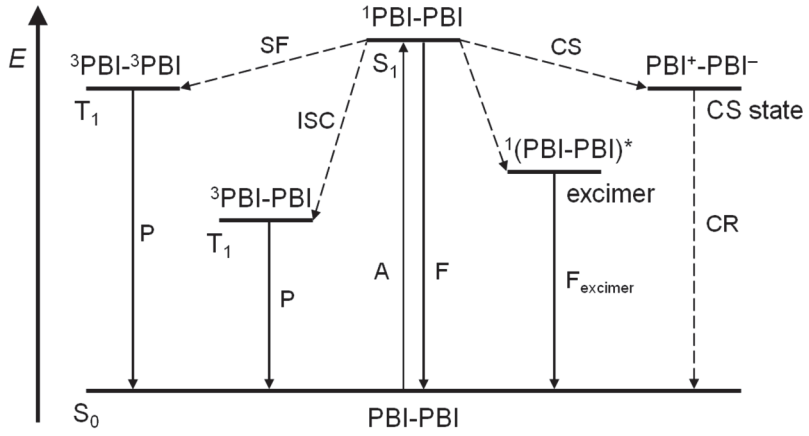

Figure 5. Simplified schematic energy level diagram for different excited states of a hypothetical PBI dimer (PBI–PBI) with possible radiative (solid arrows) or radiationless (dashed arrows) relaxation and excitation processes (A, absorption; F, fluorescence; SF, singlet fission; ISC, intersystem crossing; P, phosphorescence; CS, charge separation; CR, charge recombination). The respective higher vibrational levels of each state are not shown for clarity.

2.2. Rigid PBI Dimers

Covalently tethered PBI dimers are well suited to derive structure-property-relationships with regard to electronic communication between the constituent chromophores depending on their center-to-center distance and spatial alignment. Thus, through-space electronic coupling can be studied with such PBI dimers if appropriate linkers are used that bring the monomer units into a predictable contact to each other. Indeed, in the past years, quite a few PBI dimers that are tethered by rigid linkers have been reported. These PBI dimer systems can be grouped into two classes. The first class contains molecules in which the two PBI dyes are connected by rigid π-conjugated spacer units (Chart 1), while the second class exhibits spacer units that preorganize the two PBI chromophores into different kinds of π–π-contacts (Chart 2). Furthermore, few PBI systems with three chromophores exhibiting pronounced π–π-stacking capabilities will also be mentioned (Chart 3).

One of the first examples of such PBI dimers, in which the monomeric units are directly linked by a N–N single bond between the imide nitrogen atoms (**3a**), was reported by

Chart 1. Covalent PBI dimers with in-plane arrangements.

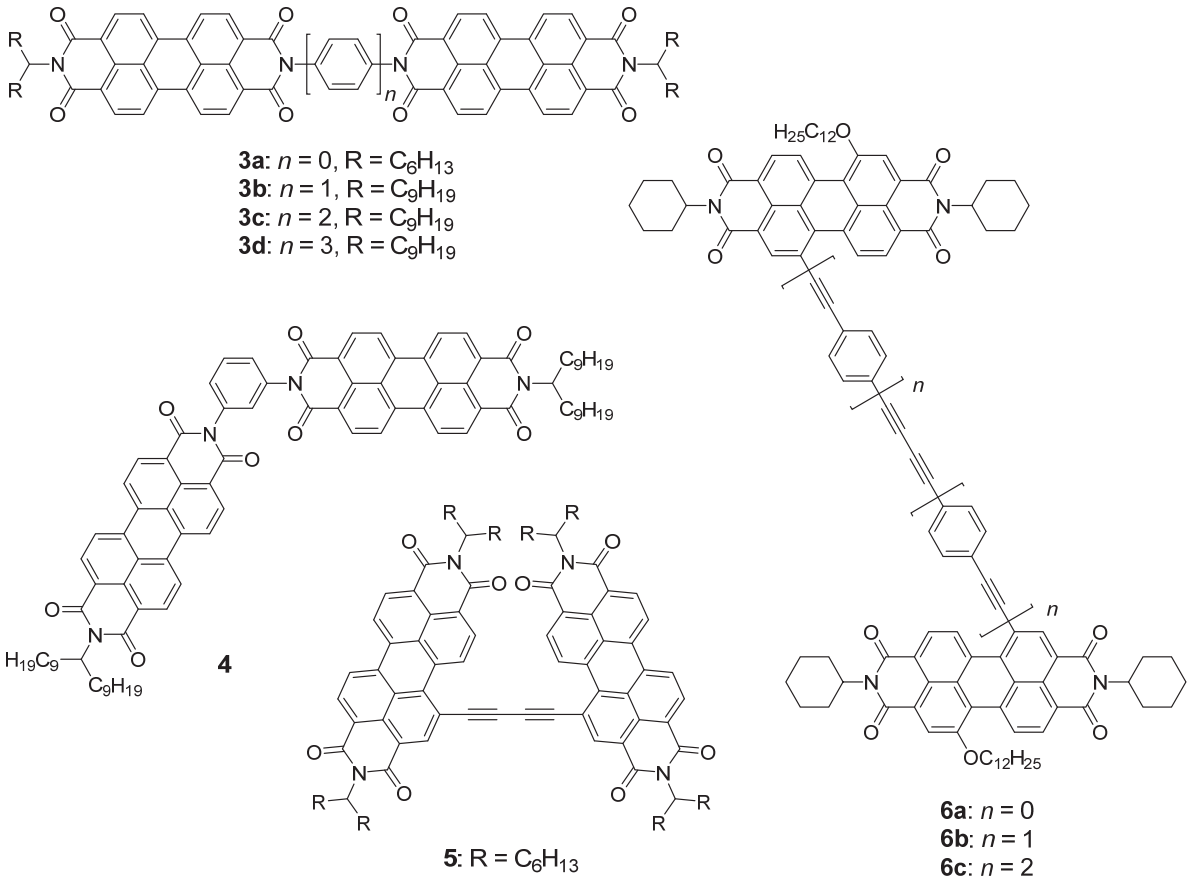

Langhals and Jona.[64] This dimer showed a bathochromically shifted (*ca.* 10 nm) lowest energy absorption maximum at 535 nm in chloroform with significant band narrowing and increase in absorption coefficient ($\varepsilon = 241800\ M^{-1}cm^{-1}$)[64] as compared to a related monomeric PBI ($\varepsilon = 85700\ M^{-1}cm^{-1}$).[65] These spectral properties are reminiscent of J-aggregates pointing at intramolecular exciton coupling conferred by linear arrangement of the chromophore units. Linear PBI dimers with larger distances between the monomeric units were achieved by connecting the monomers with mono-, di-, and tri-*para*-phenylene bridges (PBIs **3b-d**).[59,66,67] Adams and co-workers have studied this homologous series of PBI dimers **3a-d** in a comparative manner to explore their photoinduced intramolecular electron transfer properties by steady-state and time-resolved fluorescence spectroscopy as well as femtosecond transient absorption (TA) spectroscopy and single-molecule spectroscopy.[59,67,68] These studies have shown that the rate constants for photoinduced electron transfer in these dimers are strongly dependent on the length of the oligomeric spacer, the chromophore geometry, and the solvent polarity (dielectric constant). Single-molecule spectroscopic studies have shown that fluorescence blinking behavior of these PBI dimers is dependent on their bridge length and chromophore geometry, which affect the

electronic coupling and thus the through-bridge electron transfer. Very recently, this series of PBI dimers has also been investigated by single-molecule spectroscopy in condensed state on thin films by Basché and co-workers.[69] These authors have shown that electronic coupling and static disorder control the quantum-mechanical coherence between the electronically excited PBI units in these dimers. The coherences were clearly found to influence fluorescence lifetimes as well as the emission spectra.[69] Further interesting photophysical studies of in-line arranged PBI ensembles, in particular with trimer analogues similar to **3a**, were performed by Matile,[70] Hulst, Hoogenboom, and García-Parajó,[71-74] Müllen, De Schryver, and Hofkens,[75] Debije and Schenning,[76,77] Herz,[78] and their co-workers.

The wedge-shaped PBI dimer **4** with a *meta*-phenylene bridge, a regioisomer of linear dimer **3b**, was reported to exhibit a slightly more bathochromically shifted absorption maximum as compared to that of its linear *para*-phenylene bridged isomer.[66] A similar PBI dimer and its trimer homologue were subjected to photophysical investigations at their ensemble and on single-molecule levels by Osuka and Kim.[79] These PBI ensembles were shown to be weakly coupled systems and to exhibit incoherent Förster-type energy hopping.

More conformational dynamics are present in PBI dimers **5**[80] and **6a-c**[81] in which the monomeric chromophores are tethered at a bay position either with a diethynylene bridge (**5** and **6a**) or with phenylene ethynylene linkers of different lengths (**6b**,**c**). The dimers **5** and **6a** with shorter intramolecular distances showed markedly blue-shifted absorption bands in the excitation spectra as compared to that of a monomeric reference PBI bearing the respective bay substituent, revealing an H-type excitonic coupling between the constituent monomers.[80,81] The prominent hypsochromism observed for **6a** (λ_{max} = 534 nm) was attributed to intramolecular interactions through the conjugated linker, which completely disappeared for **6b** and **6c** with larger distances between the chromophore units. Thus, for the latter examples, no communication between PBI moieties occurred which resulted in absorption spectra similar to those of the respective monomeric PBIs.[81] In addition to the pronounced blue-shift of the absorption spectra, the fluorescence quantum yields were drastically reduced for the H-coupled PBI dimers **5** and **6a**, whereas dimers **6b**,**c** showed higher values.[80,81]

In contrast to the PBI dimers discussed in the previous section, the covalent PBI ensembles shown in Chart 2 enforce considerable π–π-interactions as the constituent chromophores are in close vicinity to each other with predefined alignments imposed by the respective rigid backbones. In the atropo-enantiomeric PBI dimers **7a** and **7b** (one enantiomer of each is

Chart 2. Covalent PBI dimers with close PBI–PBI distances.

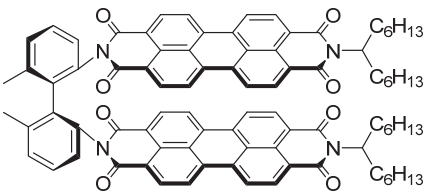

7a

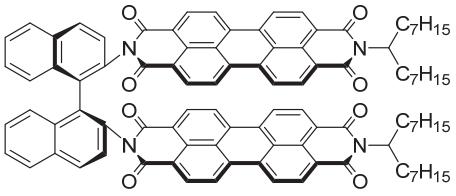

7b

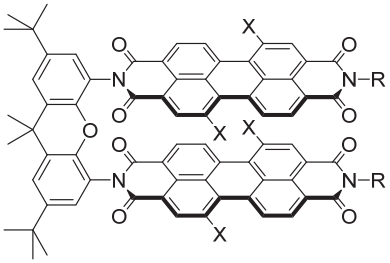

8a: X = H, R = C_8H_{17}

8b: X = H, R = $CH(C_{11}H_{23})_2$

8c: X =  , R = C_6H_{11}

8d: X = 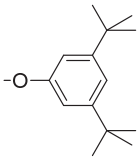 , R = C_8H_{17}

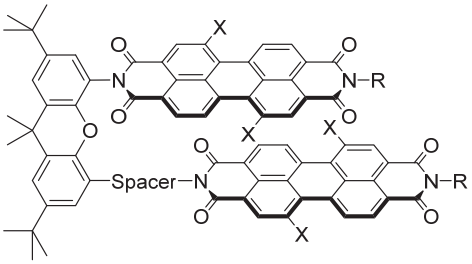

9a,b: X = H, R = C_8H_{17},

Spacer: 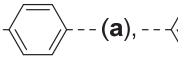 (**a**), 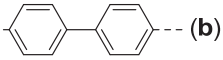 (**b**)

9c,d: X = 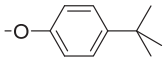 , R = C_6H_{13}

Spacer: 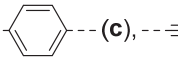 (**c**), 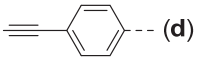 (**d**)

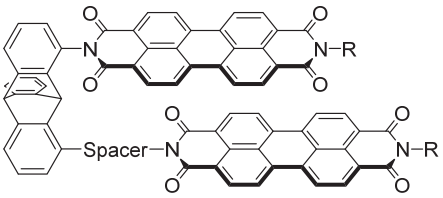

10a: Spacer = none, R = C_8H_{17}

10b: Spacer = 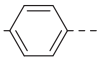 , R = C_8H_{17}

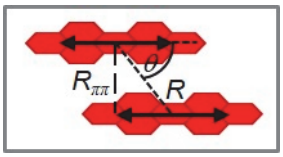

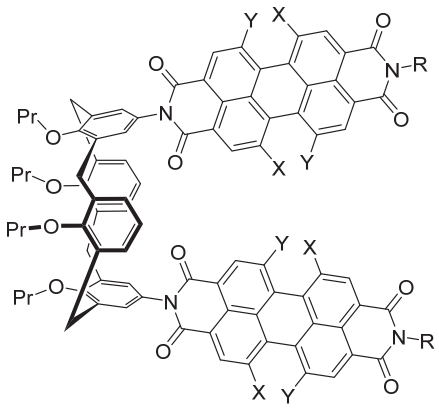

11a: X,Y = H, R = $CH(C_6H_{13})_2$

11b: X = H, Y = , R = 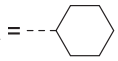

11c: X,Y =  , R = C_4H_9

shown) with axially chiral biphenylene (**7a**)[82] or binaphthylene (**7b**)[83] tether, the chromophore units are aligned in an almost perpendicular fashion as revealed by quantum chemical calculations.[82,83] The center-to-center distances of PBI units in these dimers are much shorter as compared to those of the dimers with in-line arrangement (Chart 1), which

results in more pronounced changes of the absorption spectra of these chiral dimers, in particular, a decreased 0-0 absorption band with an additional shoulder at the higher-energy flank (H-coupling). In recent years, another axially chiral binaphthylene-linked PBI dimer with slightly shorter branched alkyl chains, $CH(C_6H_{13})_2$, than in **7b**, $CH(C_7H_{15})_2$, at the imide positions has been investigated very elaborately with regard to their circularly polarized luminescence properties by the groups of Kawai[84-87] and Cohen.[88]

Further PBI dimers with close distances between PBI scaffolds were achieved by employing xanthene derivatives as rigid backbones (**8a-d**) by Wasielewski and co-workers.[30,61] In dimer **8a** containing core-unsubstituted PBIs and linear alkyl imide substituents, both chromophore units are stacked cofacially mimicking an almost perfect H-dimer.[61] Only a small deviation occurred when more bulky branched alkyl imide substituents were used as in **8b**, whereas sterically constrained bay-substituents, as in **8c-d**, led to contortion of the PBI scaffold. The ratio of the 1-0 *vs*. 0-0 transition bands ($A_{1\text{-}0}/A_{0\text{-}0}$) of **8a** is greater than that for **8b**,[61] corroborating a more pronounced H-type coupling for **8a** (see Figure 6a). As a consequence, a 10-fold lower fluorescence quantum yield (2%) for **8a**, as compared with that for **8b** (19%), was observed with each excimer-like, broad emission bands shifted to lower energies (Figure 6b).

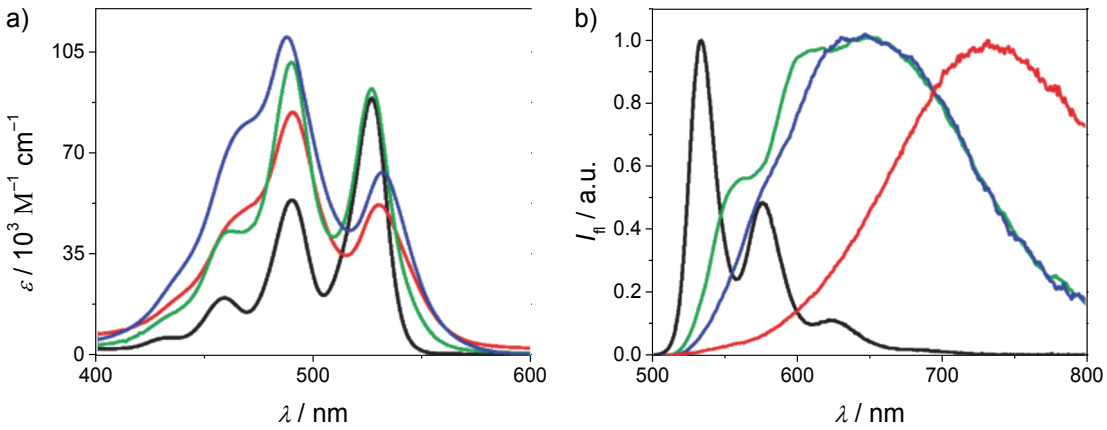

Figure 6. a) UV/Vis absorption spectra and b) fluorescence spectra of **8a** (red), **8b** (green), and a related PBI trimer **13** (blue; for a structure, see Chart 3) and, for comparison, of a respective PBI monomer (black; **PBI** with R^1,R^2 = $CH(C_{11}H_{23})_2$, X,Y = H; for a structure, see Figure 2) in a) $CHCl_3$ and b) toluene (λ_{exc} = 490 nm). The emission intensities are normalized at their maxima. Reproduced with permission from ref. [61]. Copyright 2008 American Chemical Society.

Intramolecular electron transfer properties of such xanthene-tethered PBI dimers have also been studied by femtosecond transient absorption spectroscopy. Interestingly, Janssen and co-workers discussed the pronounced decrease of the fluorescence quantum yield in a molecule similar to **8b** (differing only in the alkyl imide substituents) as a consequence of triplet state formation.[63] For **8c** bearing two pyrrolidinyl substituents on each PBI moiety,

the electron transfer kinetics showed subpicosecond charge separation into PBI^{+}-PBI^{-} with subsequent recombination.[30] Notably, such a charge transfer process is not observed for the related linear, dipyrrolidinyl-substituted PBI dimer (structurally similar to **3a**) as the distance between PBI centers in the linear dimer is more than 3 times larger than that in cofacially arranged dimer **8c**.[30]

More insight into the slip angle dependency for the energy splitting of excitonic states (*cf*. Figure 4) was gained by shifting one of the two chromophores in the longitudinal direction that could be achieved by introducing linear fragments with varied lengths to the xanthene tether. As accomplished by the groups of Wasielewski[89] and Li,[90] phenylene, phenylene ethynylene, or *para*-diphenylene spacer allowed the adjustment of the interchromophoric distances and their angular relationship in dimers **9a-d**. For the parent systems **8a-d** (without an additional spacer), the cofacial alignment ($\theta \approx 90°$) revealed center-to-center distances (R, see the inset in the bottom left corner of Chart 2) of approximately 3.5 to 4.0 Å, which could be extended up to 9 Å with concomitant decrease of the angles to 23° (**9b**). With decreasing θ values from 44° (**9a**)[89] to 41° (**9c**),[90] 32° (**9d**),[90] and 23° (**9b**),[89] the energy splitting and the population of both excitonic states became more distinctive. However, the biggest impact on the photophysical properties comes from the center-to-center distance, even if the distances between π-surfaces ($R_{\pi\pi}$, compare the schematic graph in Chart 2) for all systems discussed here are close to the optimal values for π–π-stacking. For **9b** having the largest longitudinal shift of 7.9 Å (with $\theta = 23°$), the most favored deactivation pathway is not anymore the evolution of an excimer, but the formation of the triplet state.[89] This deactivation mode could be reached either by rapid singlet exciton fission ($S_1 \rightarrow 2\ T_1$), by conventional spin-orbit induced ISC, or by spin-orbit charge transfer ISC. For the latter process, proper energetics for the charge-separated state are required. In PBI dimers **9a**,**b**, the xanthene spacer can indeed serve as electron donor to yield the xanthene^{+}-PBI^{-} intermediate, which enables subsequent deactivation to the triplet state.[89] Hence, for larger distances the excimer formation becomes less important and other relaxation pathways arise. A similar series for PBI dimers bearing triptycene linkers with (**10a**) or without (**10b**) an additional phenylene fragment was introduced by the Wasielewski group as well. Photophysical studies of these dimers provided further insight into the distance dependency.[91]

For the PBI dimers with calix[4]arene backbone **11a-c**, Würthner and co-workers could demonstrate the solvent-driven equilibria between nonstacked and π-stacked conformations.[92] As mentioned before, the extent of stacking is strongly dependent on the

structural features of the chromophores and the surrounding environment. Thus, the more flat PBI units bearing hydrogens at the bay-positions of the perylene core in **11a** exhibited a better stacking ability, which resulted in folded states of closely stacked PBIs for low polarity media or unfolded conformations in solvents with higher polarity. This example nicely demonstrates that stacking-unstacking processes can be controlled by external conditions. However, gradual distortion of the perylene core by introducing more bulky substituents (**11b**, two pyrrolidinyl groups in 1,7-positions; **11c**, four 4-*tert*-butylphenoxy substituents in the bay area) led to a less or even completely vanished stacking ability. It is important to note, however, that the electron donor character as well as the conformational versatility of the macrocyclic calix[4]arene moiety complicate the control and precise evaluation of PBI–PBI interactions by ensemble measurements in these dimers. Therefore, for the PBI dimer **11c**, single-molecule spectroscopic studies have been performed recently. The results of these studies suggest that the photoblinking of **11c** mainly occurs due to the presence of three different levels of intensity, attributable to dimer, monomer, and one intermediate level.[93,94] Moreover, photophysical properties of multichromophoric PBI-calix[4]arene arrays containing up to five PBI chromophores have been investigated with the result that these arrays exhibit sequential fluorescence-resonance energy transfer (FRET) processes (Figure 7).[95,96]

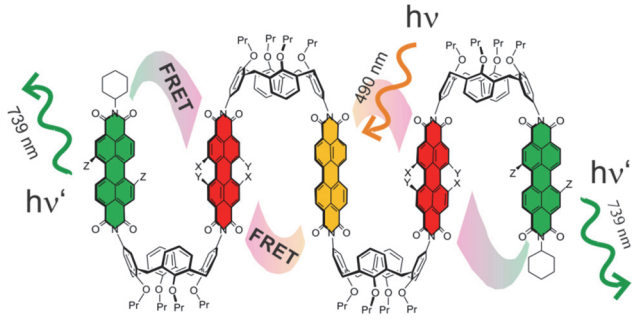

Figure 7. PBI-calix[4]arene array consisting of five PBI moieties (X,Y = 4-*tert*-butylphenoxy; Z = pyrrolidinyl) exhibiting sequential FRET processes by excitation of the middle PBI yielding emission of light with λ_{max} = 739 nm. Reproduced with permission from ref. [95]. Copyright 2006 American Chemical Society.

Other PBI systems consisting of more than two PBI units with fairly rigid and thus predefined dye–dye arrangements were published, for example, by the groups of Li[90] and Wasielewski.[61] The structures of these selected PBI trimers are depicted in Chart 3.

Whereas Li and co-workers presented their results of PBI trimers **12a**,**b** in view of the distance and angle dependencies,[90] Wasielewski and his group utilized xanthene tethers to build up trimeric systems bearing cofacially stacked, bay-unsubstituted PBI chromophores (**13**) or 1,7-bis-(3,5-di-*tert*-butyl)phenoxy-substituted PBI dyes (**14**).[61] As shown for **13** the

Chart 3. Trimeric PBI systems with different tethers.

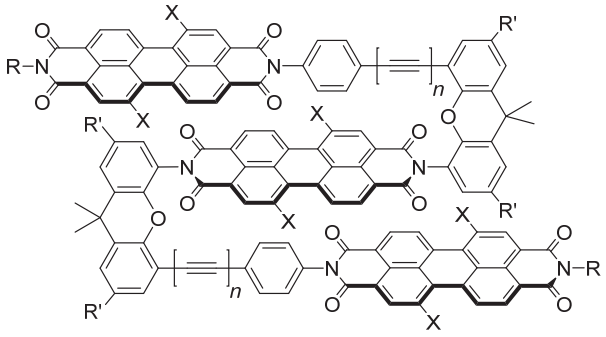

12a,b: X = , R = C_6H_{13}, R' = *t*-C_4H_9, *n* = 0 (**a**), 1 (**b**)

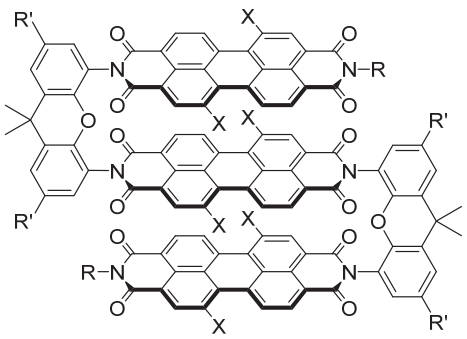

13: X = H, R = C_8H_{17}, R' = *t*-C_4H_9

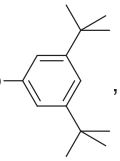

14: X = , R = C_8H_{17}, R' = H

UV/Vis absorption spectrum of this PBI trimer in chloroform (Figure 6a) reveals the reversal of the 0-0 and 1-0 transition bands with a prominent maximum at 488 nm very similar to **8a**, whereas emission properties resemble those of **8b** (*cf*. Figure 6b). Thus, a very tough coupled PBI trimeric stack can be anticipated with fluorescence properties strikingly influenced by the bulky imide substituents as also for PBI dimer **8b**. Hence, the addition of a third PBI fragment to the existing dimer stack (as in **8b**) results in an increase of the tinctorial strength and a further reduction of the emissive power (13%).[61]

2.3. Flexible PBI Ensembles

Covalent PBI systems highlighted in Chapter 2.2 possess stiff tethers which in most cases enforce one of the possible PBI–PBI arrangements controlled by the linker unit. In this section, PBI ensembles that are tethered by flexible bridges allowing for different arrangements of the constituent chromophores by folding and unfolding processes will be presented. It is worth a note that so far much less examples of flexible, covalently linked PBI systems were reported as compared to the rigid ensembles discussed in the previous section. This might be due to the possibility that for allowing flexibility the complete loss of conformational control could result. However, by prudent design allowing the system to fold into a predictable and thus defined way, the conformational diversity can be reduced to a minimum set of possible structures as masterly exemplified by proteins. In favorable cases, these structures are almost congruent, *i.e*. exhibit very similar alignments of the monomeric

PBI units. To achieve some dynamic character for these systems, however, external stimuli are needed, which drive the systems to different states. Consequently, in one of the resultant states, the chromophores are prone to interact with each other due to their close vicinity, and in other states no electronic communication can occur due to larger distances between the chromophores. Thus, the excitonic coupling can be switched on or off by the surrounding environment.

Li and co-workers have synthesized a broad series of homologous PBI oligomers containing up to 10 core-unsubstituted PBI chromophores that are tethered by flexible tetra(ethylene glycol) linkers (**15a-i** in Chart 4) and investigated their folding *vs.* self-assembling properties.[97-101]

^{1}H NMR and UV/Vis spectroscopic studies, for example in chloroform, revealed that the folding and self-assembly of these flexible PBI oligomers are strongly dependent on the concentration. Thus, at low concentrations (< ~1 mM) folding prevails, while at higher concentrations (~1–100 mM) self-assembly occurs.[98-100] Upon folding, the perylene core protons are significantly up field shifted due to aromatic shielding effects, which indicates the formation of cofacial π-stacks. As pointed out by the authors, the degree of folding, that is, the aggregation of PBI units within the chain, was vividly displayed in the UV/Vis absorption spectra. Whereas the excitation spectrum of the respective monomer PBI reveals the characteristic vibronic signal pattern with increasing intensity from the 2-0 to 1-0 and 0-0 transitions, higher oligomers show the characteristic, inverse intensity distribution of the 0-0 and 1-0 vibronic bands that can be rationalized according to Engel *et al*. and Spano *et al*. by vibronic-excitonic coupling within the intermediate coupling regime.[51,53,102,103] Thus, with increasing number of PBI units, the intensity of hypsochromically shifted absorption maximum at about 495 nm increases with concomitant diminishing of the 0-0 band at about 530 nm. The ratios of these bands increase significantly upon embedding more chromophores; that is, $A_{1\text{-}0}/A_{0\text{-}0}$ is 0.61 for the monomer, 1.07 for **15a** (dimer), 1.22 for **15b** (trimer), or 1.36 for **15e** (hexamer).[100] Furthermore, Li and co-workers have shown by single-molecule spectroscopy of oligomers **15a-i** that the emission properties have a saturation effect for the tetramer **15c**, so that the implementation of more chromophores does not shift the emission maximum more bathochromically.[99] In a further work, the same group has shown that large oligomers consisting of alternating DNA and PBI sequences exhibit hyperthermophilic properties as they undergo folding at higher temperatures.[104]

By embedding PBI chromophores to the outer periphery of a polyisocyanide strand, the groups of Hernando, Nolte, and Rowan were able to synthesize large PBI fibers (Chart 4)

Chart 4. Flexible PBI oligomers with PBI as main and side chain fragments.

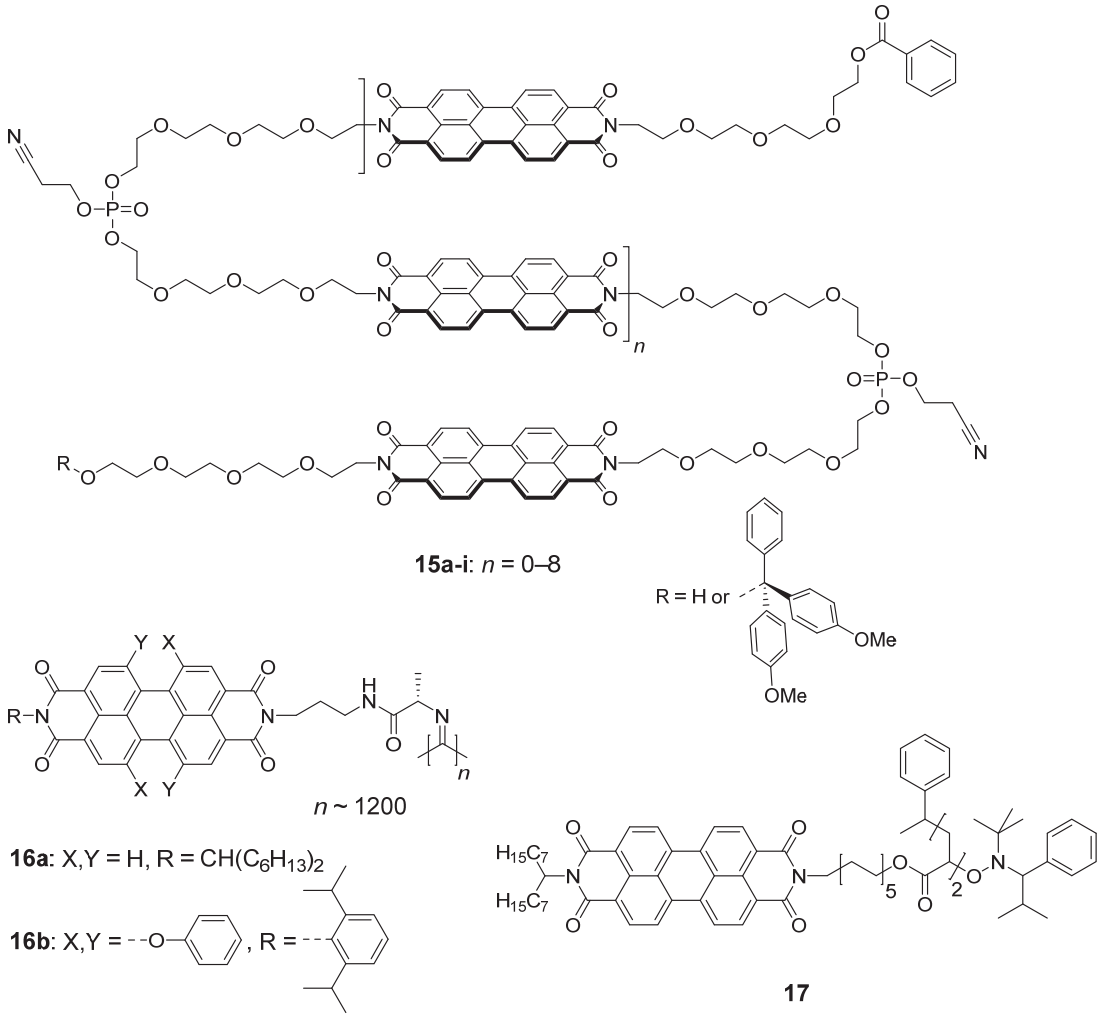

with lengths in the micrometer regime.[105] For the highly defined polymers **16a**, close contacts between the *x* th and *x*+4 th PBI units are ensured by the helical scaffold (see Figure 8). As chirality is introduced to the monomeric units by the scaffold, a preferred handedness of the helices is present, revealing exceptionally strong Cotton effects in the respective circular dichroism (CD) spectrum. The prominent PBI–PBI interactions for the polymers become apparent by the strong excimer emission with a maximum at 620 nm and hypsochromic shift of the absorption maximum as compared to that of a related monomeric isocyanide-functionalized PBI. Further structural features of **16a** and **16b** were elucidated by atomic force microscopy (AFM), molecular dynamics (MD) simulations, and theoretical calculations.[105-107] The applicability of **16a** polymers for photovoltaic cells could be confirmed later, revealing much better performance than for the constituent PBI dyes.[108]

More recently, Thelakkat and Köhler reported on the synthesis and spectral properties of a PBI dimer **17** (Chart 4) obtained by nitroxide-mediated polymerization reaction of the

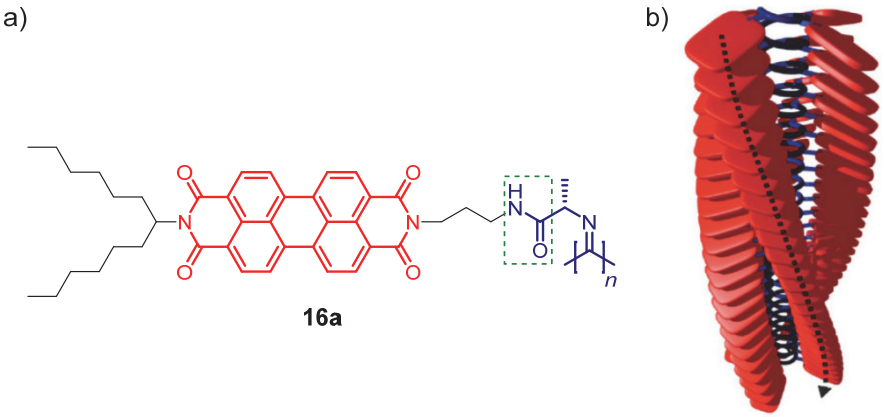

Figure 8. a) Molecular structure of **16a** with colored fragments used in b) the schematic illustration representing the helical arrangement of the polyisocyanide strand (blue helix) with attached PBI dyes (red plates). The green dashed rectangle in the molecular structure depicts the amide group enabling H-bonding within the strand. In b) the dashed arrow indicates one of the four electronic transport pathways between adjacent PBI chromophores. Reproduced with permission from ref. [106]. Copyright 2008 Wiley-VCH Verlag GmbH & Co. KGaA, Weinheim.

respective acrylate bearing PBI monomer and subsequent isolation by gel permeation chromatography.[109,110] As discussed by the authors, this dimer can adopt a highly preferable state in which both PBI moieties exhibit a parallel stacking to each other besides a less stable antiparallel stacked form or the open (nonstacked) state. The ambiguous spectral behavior observed for this dimer was explained in terms of the various orientations of PBI chromophores to each other.[109,110]

While the conformations and concomitant properties of the so far discussed examples showed response to the solvent, an even better switching of PBI aggregation should be possible by the incorporation of photochromic dyes in a suitable spacer unit. Such an approach has been demonstrated by Browne and Feringa with PBI dimer **18** (Figure 9).[111] Due to the overcrowded character of the photoisomerizable alkene fragment, the prevalent *trans*-configuration can be converted to the respective *cis*-isomer by irradiation with light of 312 nm. In the *trans*-state, both PBI units are far away from each other, and thus no excitonic coupling occurs. Upon excitation with appropriate light, the *cis*-isomer is formed, in which the PBI chromophores interact with each other. The reversal of the absorption maxima, the significant decrease of the monomer emission as well as the enhanced emission in the range between 600 and 675 nm, further corroborates the folding in *cis*-conformer. Notably, in the photostationary state, only about 80% of the molecules prevail in the *cis*-form, which upon exposition to light of 365 nm return to the *trans*-state.[111] The spectral features of this photoswitchable system indeed resemble those of **17**[109,110] discussed before.

In the approach toward semi-flexible PBI foldamers by Würthner and co-workers, an alternating *ortho-meta* phenylene ethynylene scaffold (often also termed as *oligo*-phenylene

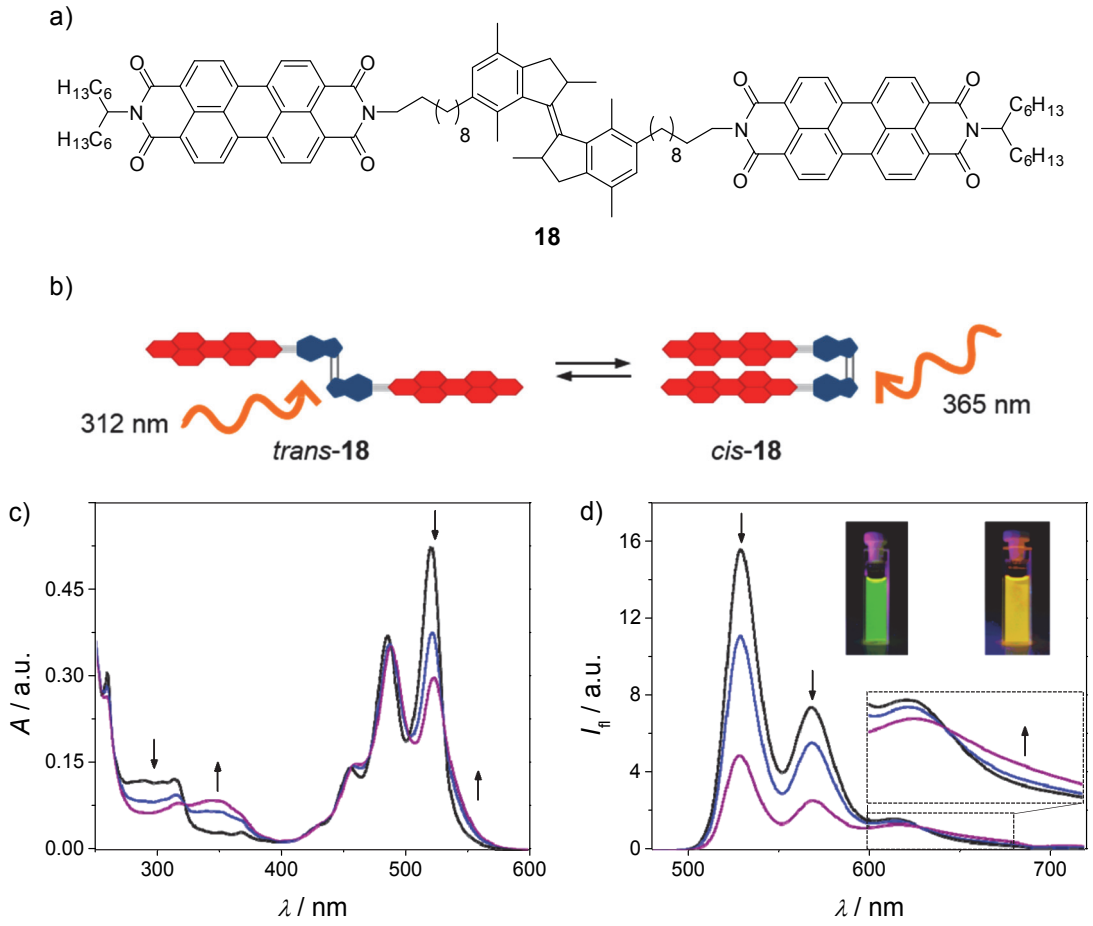

Figure 9. a) Chemical structure of photoisomerizable PBI dimer **18**. b) Schematic illustration of reversible *cis-trans* switching controlled by photoirradiation with wavelengths indicated in the sketch. c) UV/Vis absorption and d) fluorescence spectra of **18** in THF. Arrows indicate the spectral changes upon photoirradiation with light of 312 nm for 50 s. Insets in d) show the solution of **18** in THF under UV irradiation with light of 365 nm (left image) and 312 nm (right image) and an expansion of the fluorescence spectra between 600 and 680 nm (bottom). Reproduced with permission from ref. [111]. Copyright 2010 American Chemical Society.

ethynylene (OPE) backbone; *cf.* structure **19**) was used to allow solvent-triggered coiling from an unfolded state to the folded state (Figure 10).[25] The PBI system depicted in Figure 10a exhibits a solvent-dependent folding and unfolding process, leading to distinctive spectroscopic features of the folded and unfolded states.[25] With the nonpolar solvent MCH the folding by intramolecular aggregation of **19** could be achieved. In Figure 10b the UV/Vis absorption spectra of **19** in $CHCl_3$, MCH, and mixtures thereof are shown.[25] The major differences in the spectra of foldamer **19** in the good solvent ($CHCl_3$), yielding the opened or unfolded state, and in the bad solvent (MCH), enforcing stacking events to folded species, were observed for the most red-shifted band representing the 0-0 vibronic transition between S_0 and S_1.[25] Notably, the absorption band representing the 1-0 vibronic transition (located with the maximum between 490 and 495 nm), showed less hypochromic effects upon folding. In this regard, it is worth to mention, that similar spectral

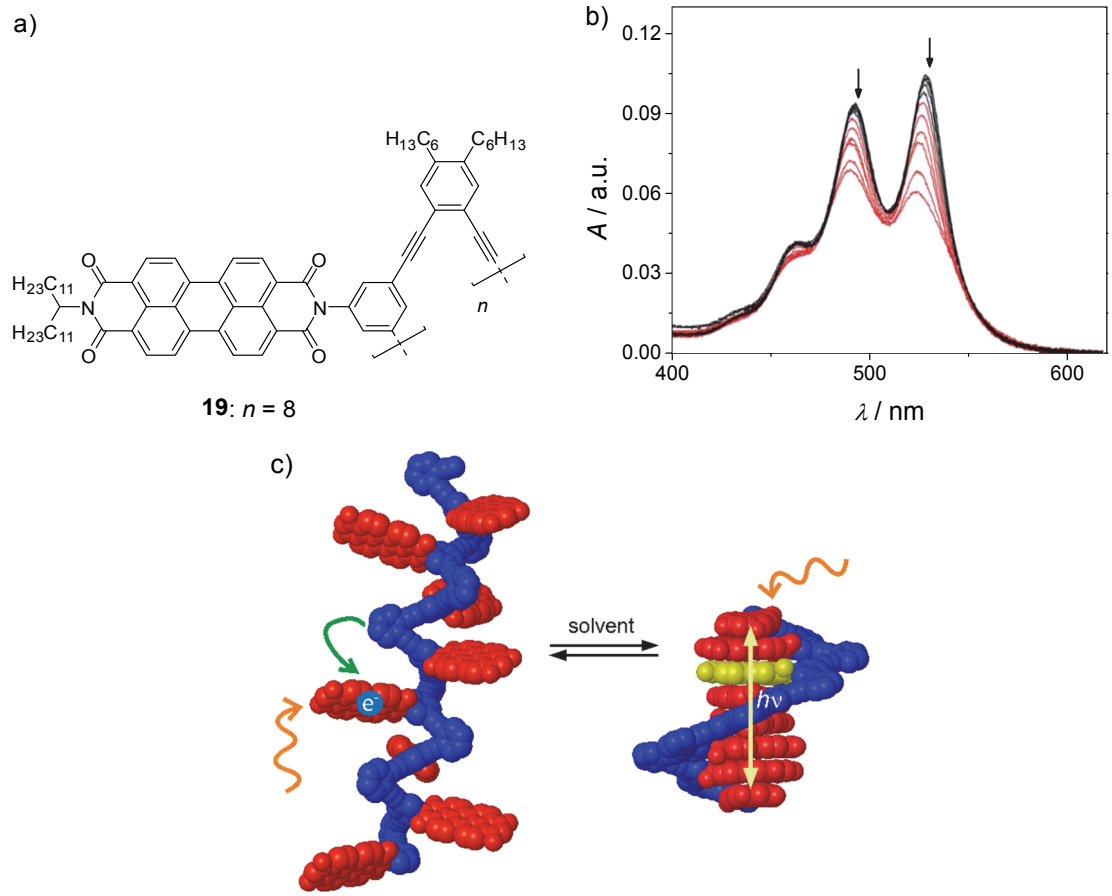

Figure 10. a) Chemical structure of PBI foldamer based on an *oligo*-phenylene ethynylene (OPE) scaffold. b) Solvent-dependent UV/Vis absorption spectra of foldamer **19** (4.08 mg L^{-1}) in $CHCl_3$/MCH mixtures at 20 °C starting with pure MCH (lower red line; folded state) changed to pure $CHCl_3$ (upper black line; unfolded state) by increasing $CHCl_3$ content in steps of 10 vol%. Reproduced with permission from ref. [25]. Copyright 2011 The Royal Society of Chemistry. c) Schematic illustration of solvent-triggered folding of PBI foldamer **19** (red, PBI moieties; blue, *oligo*-phenylene ethynylene backbone; hydrogens and long alkyl chains are omitted for clarity) that exhibits competitive PET (green arrow) and excimer formation followed by exciton migration (yellow double arrow) depending on its overall conformation.

features were observed for the rigid xanthene-containing PBI dimer **8b**[61] and the biphenylene-bridged dimer **7a**,[82] indicating that similar excitonic interactions take place in the present folded ensembles and aforementioned rigid dimers.

Recent photophysical investigations of **19** by Kim and co-workers have shown that the folding to a compact π-stack architecture (for an illustration of the equilibrium between unfolded and folded octamer, see Figure 10c) almost completely suppressed the competing photoinduced electron transfer (PET) from the electron-donating OPE scaffold to the electron-deficient PBI cores.[112] Thus, while photoinduced charge transfer from electron-rich *oligo*-phenylene ethynylene backbone to PBIs constitutes the exclusive deactivation channel for the unfolded, excited systems, the formation of excimeric state by π–π-stacking seems to disfavor charge separation and to switch the excited molecule into another deactivation pathway.[112]

2.4. Cyclic PBI Systems

In this section, prominent examples of cyclic PBI dimers that contain two PBI chromophores bridged with either rigid linkers or flexible tethers (like in cyclophanes), and PBI macrocycles consisting of 3 or more chromophore units will be highlighted. It is noteworthy to point out here that macrocycles are, in contrast to linear oligomers, often considerably well preorganized molecules. For this reason, macrocycles constituted the preferred class of supramolecular hosts as demonstrated by crown ethers, cryptands, and carcerands from the early beginning.[113-115] The structures of a selection of PBI cyclophanes with dodecylene tethers (**20**), rigid *ortho*-phenylene bridges (**21**) or *s*-triazinylene (**22a-c**), phenylene ethynylene (**23**), or *para*-xylylene linkages (**24**) are displayed in Chart 5.

Cyclic dimer **20** is one of the earliest examples of PBI cyclophanes reported by Langhals and Ismael.[21] Spectroscopic studies of this cyclic scaffold revealed excitonic coupling between the PBI chromophores with a hypsochromically shifted absorption maximum and a strongly bathochromically shifted broad emission band, which should be attributable to an excimer state. These spectroscopic properties are indicative of cofacial arrangement of the PBI units. Interestingly, this PBI dimer exhibited a comparatively high fluorescence quantum yield of 40% despite H-type excitonic coupling. Because this cyclophane is inherently chiral but racemic, solvent-induced CD effects were observed in enantiomerically pure (*S*)- or (*R*)-1-phenylethylamine.[21]

In the cyclophanes bearing very rigid *ortho*-phenylene (**21**)[24] or *s*-triazinylene (**22a-c**)[22] spacers (see Chart 5), the PBI chromophores remain in close π–π-contact to each other with a cofacial arrangement. The PBI cyclophane **21** was synthesized mainly for the evaluation of excited state dynamics, including those of energetically higher lying charge transfer states.[24] Whereas the excitation spectrum (Figure 11a) of **21** suggests similar H-coupling character as for previously discussed xanthene-bridged rigid noncyclic PBI dimers **8a** and **8b** (see Chart 2),[61] this cyclic dimer shows an even more pronounced red shift (more than 250 nm; compare Figure 11b) of the fluorescence emission maximum close to the near-infrared (NIR) region with respect to its monomer. Although monomer emission apparently remained, the fluorescence of the excimer state was determined to be about 0.1%. The authors suggested that the lowering in energy of the excited state was largely related to Frenkel–charge transfer exciton mixing.[24] According to theoretical investigations by Liang and co-workers, this mixing is highly distance-dependent.[116] As **21** remained in its predefined PBI–PBI stacked arrangement due to the short and rigid tethers, this kind of exciton mixing became fairly pronounced for this rigid cyclophane.

Chart 5. PBI cyclophanes (TIPS = triisopropylsilyl).

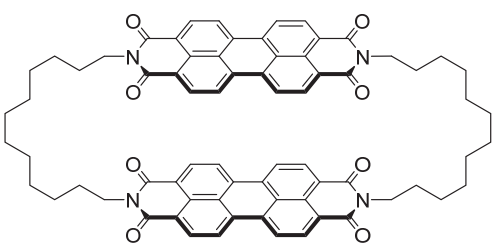

20

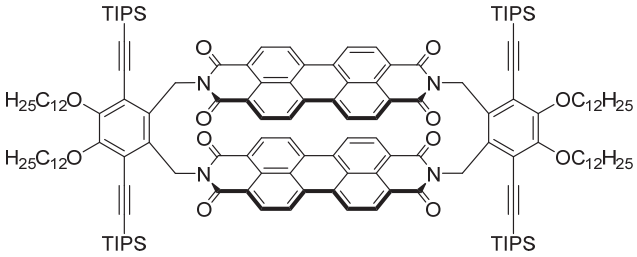

21

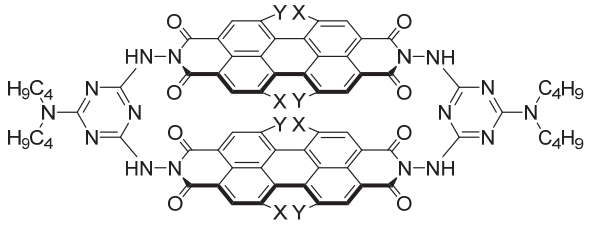

22a-c

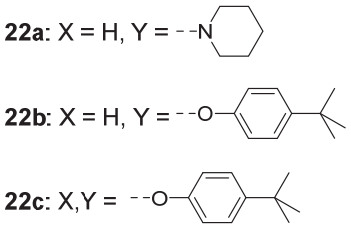

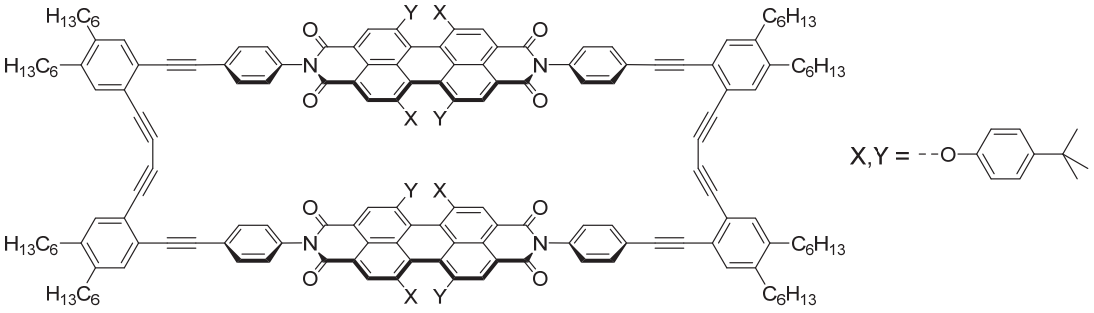

23

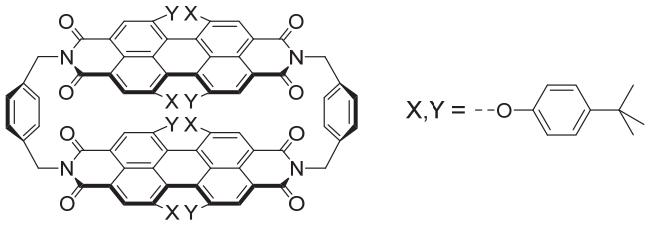

24

The excitation spectra of **22a-c** showed hypsochromically shifted absorption maxima, and the emission spectra of **22b** and **22c** exhibited significant or slight red shifts, respectively, as compared to that of monomeric references, while for **22a** no fluorescence was observed. No further insights into the possible deactivation channels for **22a-c** were provided.[22]

PBI cyclophane **23** containing more rigid phenylene ethynylene bridging units also exhibits strong excitonic coupling of the two chromophores as evidenced by the reversal of the absorption band intensities for the 1-0 and 0-0 transitions as compared to those of the related PBI monomer.[23] However, the fluorescence quantum yield of this cyclophane is markedly

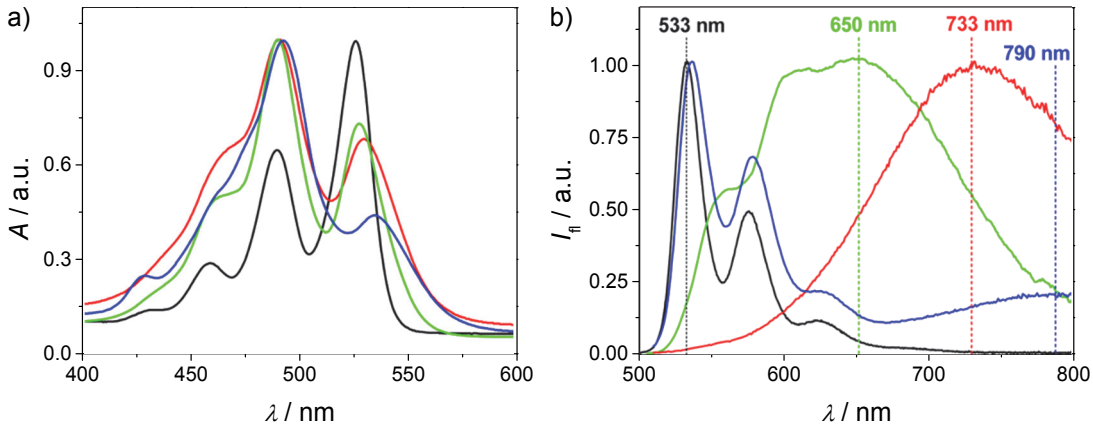

Figure 11. Normalized a) steady-state absorption and b) fluorescence data of **21** (blue) and, for comparison, of noncyclic PBI dimers **8a** (red, *cf.* Chart 2), **8b** (green; *cf.* Chart 2), and PBI monomer **PBI** (black; R^1,R^2 = $CH(C_{11}H_{23})_2$, X,Y = H; for a structure, *cf.* Figure 2) in toluene. Emission data are generated with 490 nm excitation. Dashed lines indicate emission peak maxima (λ_{max}) as indicated above those. Reproduced with permission from ref. [24]. Copyright 2014 American Chemical Society.

decreased to 6% as compared to that of the monomeric reference (nearly 100%). The stronger fluorescence quenching for **23**, as compared to that of the more flexible cyclophane **20**, may be related to photoinduced electron transfer processes from the electron-donating spacer unit to the PBIs. Cyclophane **23** exhibits interesting conformational dynamics as evidenced particularly by cyclic voltammetry (CV) and also temperature-dependent ^{1}H NMR spectroscopy. The electrochemical studies of **23**, in combination with simulations, revealed dynamic behavior with increasing scan rate and stepwise reduction up to its tetra-anion. As schematically shown in Figure 12, the third reduction leading to $\mathbf{23}^{3-}$ is accompanied by the aforementioned ring expansion due to the increased electrostatic repulsions. Thus, the subsequent fourth reduction to the tetra-anion $\mathbf{23}^{4-}$ could be achieved at less negative potential as the Coulomb repulsions in the ring widened cyclophane are significantly reduced.[23]

Most recently, Spenst and Würthner reported on the first example of a *para*-xylylene bridged PBI cyclophane (**24**) that encapsulates a large variety of aromatic guest molecules in its cavity leading to the respective 1:1 host-guest complexes.[117] A unique functional feature of this novel PBI cyclophane is the variation of its emission depending on the electronic nature of the encapsulated aromatic guest. Thus, the complexation with rather electron-poor guest molecules like, *e.g.*, 9-fluorenone, biphenyl, and phenylnaphthalene results in a dramatic increase of fluorescence quantum yield up to 100% as compared to 21% in chloroform of the free PBI cyclophane, whereas more electron-rich guests such as anthracene, perylene, and pyrene quench the fluorescence by charge transfer (CT) interactions. Accordingly, this PBI cyclophane can be used as a dual ("turn-on" and

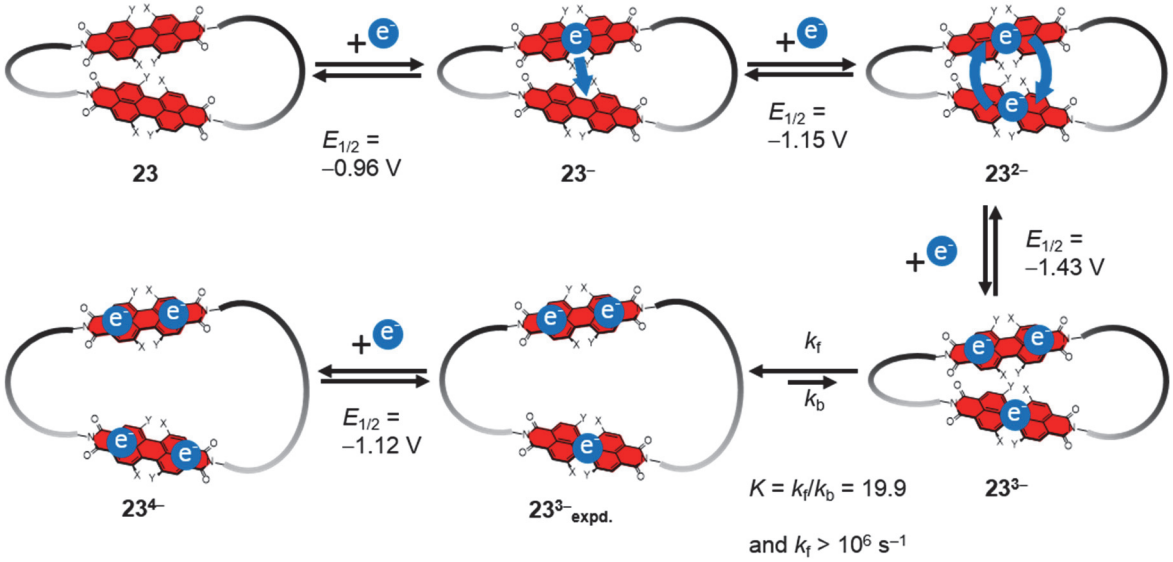

Figure 12. Reduction processes and reversible contraction/expansion of cyclophane **23** (X,Y = 4-*tert*-butylphenoxy). The redox potentials and equilibrium constant were obtained by digital fit to the cyclic voltammograms (CV) at different scan rates. Adapted with permission from ref. [23]. Copyright 2013 Wiley-VCH Verlag GmbH & Co. KGaA, Weinheim.

"turn-off") fluorescence probe for the sensing of electron-poor and electron-rich guest molecules.[117]

Conformationally, highly flexible cyclic PBI dimers consisting of hydrophilic ethylene glycol chains connected by disulfide or phosphoramidite moieties (Chart 6) were reported by Li and co-workers.[118-120] The cyclic PBI dimers **25**,[118] **27**,[119] and **28**[120] were obtained by self-assembly directed cyclization of the respective PBI monomer building blocks bearing terminal thioacetyl groups through reversible disulfide coupling reaction, while the cyclic dimers **26a-e**[120] were achieved by phosphoramidite coupling. Detailed studies by these authors revealed that the cyclization as well as the catenation (*e.g.*, leading to catenane (**25**)$_2$) of the corresponding PBI building blocks are governed by dynamic self-assembly (DSA) process through π–π-stacking of PBI chromophores.[118] UV/Vis absorption and fluorescence spectroscopic studies of dimer **25** and catenane (**25**)$_2$ revealed similar spectral features as observed for the respective linear dimer **15a** or tetramer **15c** discussed before, as significantly hypsochromically shifted absorption maxima and reddish emission for these flexible cyclic systems were observed.[118] In a further study, it was convincingly demonstrated that molecular codes, imparted by size, shape, and geometry of molecules, effectively control the reaction pathway and product formation in self-assembly directed cyclization of PBI building blocks.[120] Thus, for the reaction of different core-substituted PBI monomers, having varied twist angles (θ) with one flat bay-unsubstituted PBI moiety, the product with the largest core twist difference of both PBI units (heterodimer **26e**,

Chart 6. Flexible cyclic PBI dimers and catenane.

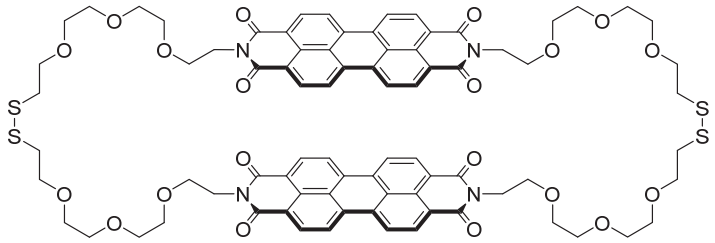

25

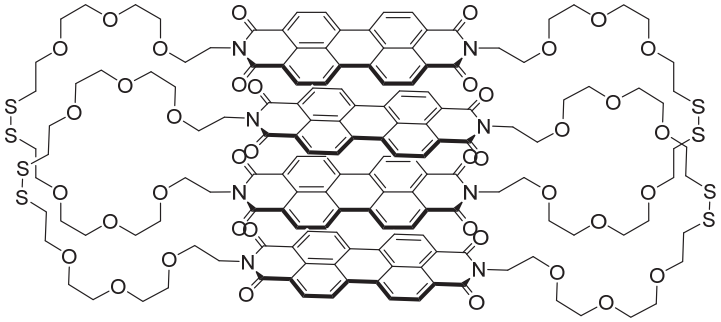

$(\mathbf{25})_2$

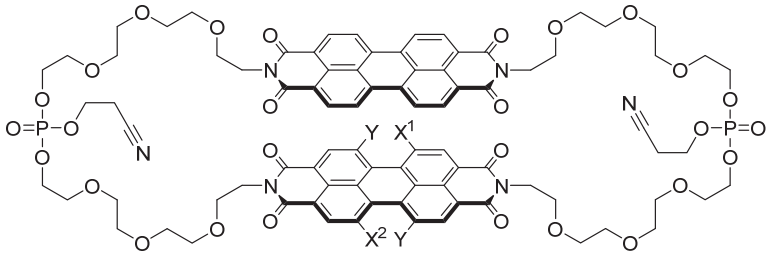

26a: X^1,X^2,Y = H
26b: X^1 = Br, X^2,Y = H
26c: X^1,X^2 = Br, Y = H
26d: X^1,X^2,Y = 
26e: X^1,X^2,Y = Cl

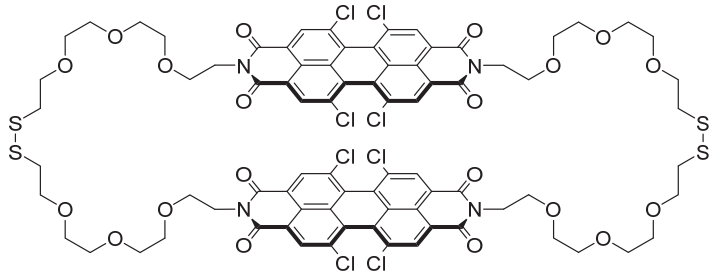

27

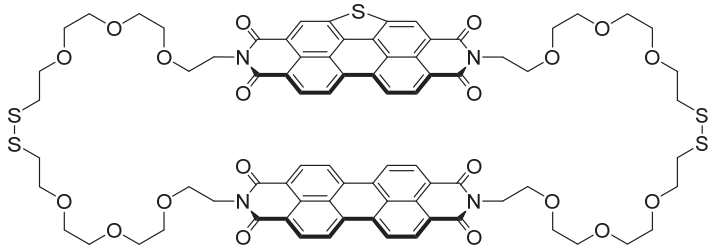

28

$\Delta\theta = 37°$) was obtained in lowest yield (4%). The respective homodimer **26a** ($\Delta\theta = 0°$) and the heterodimer **26b** ($\Delta\theta = 14°$), which possesses one PBI moiety bearing a bromo-

substituent at 1-position (leading to only slightly distorted perylene core), were formed in 27% each as the major products. Core twisting in the intermediate range as in heterodimers **26c** ($\Delta\theta = 23°$) and **26d** ($\Delta\theta = 25°$) resulted in 6% yield of each of these cyclic dimers. Consequently, mixing of flat PBI monomers and their core-tetrachlorinated analogues led to the formation of the corresponding homodimers **25** and **27**, respectively, and heterodimer (with structural resemblance to **26e**) was not formed at all. However, for similarly coded planar PBIs cyclization afforded heterodimer as shown in **28**.[120] Notably, PBI dimer **27** with strongly core twisted chromophore units was only formed if the homochiral isomer (*P*- or *M*-enantiomer) of the respective monomer building blocks prevailed, whereas for heterochiral monomers the open-chained, linear dimer was formed exclusively.[119]

A synthetic strategy toward larger PBI macrocycles consisting of 3 and more chromophore units (**29a-d**; see, Chart 7) was developed by Würthner and co-workers.[121,122] In-depth photophysical investigations of such PBI macrocycles with varying ring sizes from trimer (**29a**) to hexamer (**29d**) by steady-state and time-resolved spectroscopy provided profound insights into their optical properties and excitation energy migration processes.[122-124]

Chart 7. PBI macrocycles with more than two PBI chromophores.

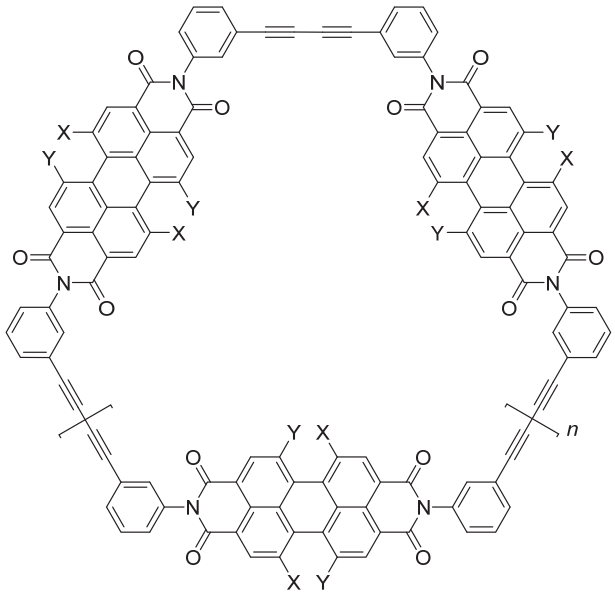

29a: *n* = 1
29b: *n* = 2
29c: *n* = 3
29d: *n* = 4

These studies revealed that the excitation energy migration process was strongly dependent on the size of the macrocycles. Thus, for the smaller cycle (**29a**), an excitation energy hopping time of $\tau_{hop} = 3.6$ ps suggests a far better energy transfer than for the bigger cycle

(**29d**) with τ_{hop} = 10.3 ps.[122] Atomic force microscopy (AFM) and single-molecule fluorescence spectroscopy of these multichromophoric cycles in condensed phase showed ordered layers of triangular and quadratic molecules on the surface, accompanied by high fluorescence lifetimes for the rigid smaller rings (**29a** and **29b**). In contrast, for the larger cycles **29c** and **29d**, no structured assemblies on the surface were observed, which came along with much broader fluorescence lifetime distributions.[123] More recently, single-molecule defocused wide-field imaging was applied by Kim and co-workers to these macrocyclic PBI systems (see Figure 13).[124] With this technique, a reliable reconstruction of the orientation of the transition dipole moments of each PBI chromophore in macrocycles could be achieved and additional information on the angular relationships between the PBI fragments could be gained (Figure 13a). By means of these achievements, the previously obtained results of theoretical MD simulations could be verified in terms of structural inhomogeneities of the large, and thus flexible macrocycles.[124]

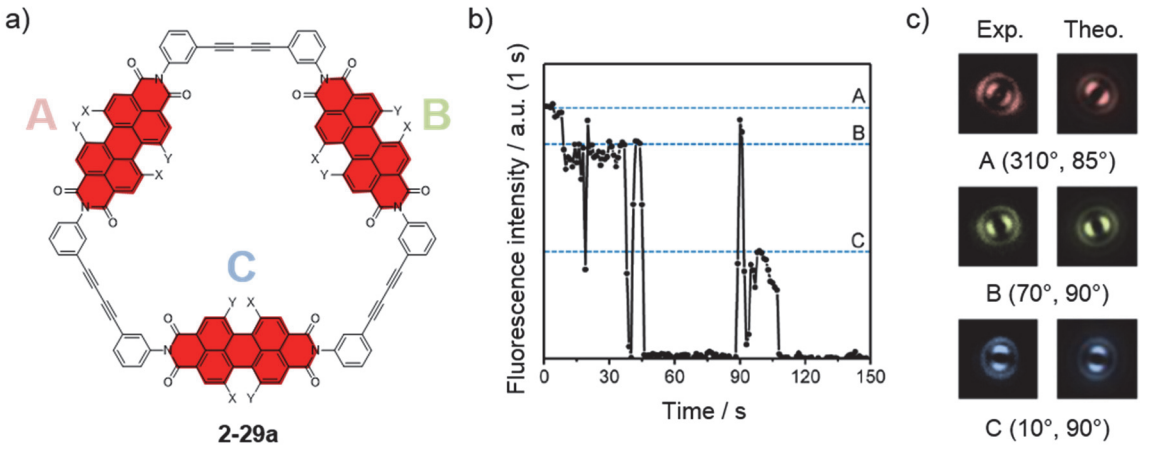

Figure 13. a) Simplified molecular structure of PBI macrocycle **29a** (X,Y = 4-*tert*-butylphenoxy) with single PBI chromophores denoted with A, B, and C. b) Representative fluorescence intensity trajectories (FITs) with corresponding defocused images of **29a**. exhibiting the three distinct levels indicative for A, B, or C. FITs are plotted as the integrated intensity of each defocused image measured at a bin time with 1 s. (c) Left images are experimental and right images are the corresponding simulated ones revealing specific orientations for individual chromophores A, B, and C in **29a**. Adapted with permission from ref. [124]. Copyright 2014 American Chemical Society.

As shown in Figure 13b the individual fluorescence intensity levels can be used to identify three distinct levels for trimeric PBI macrocycle **29a** which corresponds to the three individual PBI chromophores. The experimental orientations evaluated by single-molecule defocused wide-field imaging as well as the theoretical orientations of the three PBI units in **29a** are shown in Figure 13c.

Chapter 3

–

Results and Discussion*

3.1. Introduction

In this chapter, the synthesis as well as the ground and excited state properties of two foldable systems **32** and **33** (see Chart 8) bearing perylene bisimide (PBI) moieties connected to an alternating *ortho*-*meta*-(phenylene ethynylene) scaffold are described. As the next subchapters will show, the folding from a set of different open (unfolded) dye–dye arrangements to a small set of folded structures of almost unique PBI–PBI arrangements can be triggered externally by the solvent. Thus, the evaluation of suitable solvents will be of importance. Next, the ground state properties resulting from the folded or unfolded states will be demonstrated in terms of UV/Vis absorption and detailed ^{1}H NMR spectroscopic studies and, for comparison, together with reference compounds **30** and **31** (Chart 8). At that point, molecular dynamics simulations applying semi-empirical methods also help to mimic the folding process in detail and also to interpret results obtained by ^{1}H NMR experiments. Further fluorescence and transient absorption spectroscopic studies reveal insights into the excited state features, which are greatly influenced by the internal photoinduced electron transfer from the electron-donating phenylene ethynylene backbone to the electron-deficient PBI chromophores.

By recapitulating the examples discussed in the literature survey, the present PBI folda-dimer **32** and PBI folda-trimer **33** captivate due to their intrinsic folding behavior, which can be gently controlled at ambient conditions by an external stimuli, namely by the solvent. Whereas most of systems in Chapter 2 either exhibit structural rigidity with or without close

* This chapter was communicated in B. Fimmel, M. Son, Y. M. Sung, M. Grüne, B. Engels, D. Kim, F. Würthner, *Chem. Eur. J.* **2015**, *21*, 615–630. Reproduced in parts with permission. Copyright 2015 Wiley-VCH Verlag GmbH & Co. KGaA, Weinheim.

π–π-contacts, are constructed by co-polymerization and thus lacking in a precise structure, or are formed instantaneously to its permanent state, even if flexible linker fragments would allow some dynamic rearrangements, **32** and **33** can fold and unfold depending only on the surrounding environment. Nevertheless, for a comprehensive understanding some examples of important PBI oligomers and their spectral features introduced in subchapters 2.2 and 2.3 will be mentioned at certain points, while interpreting results obtained for **32** or **33**.

Chart 8. Chemical structures of investigated PBI molecules.

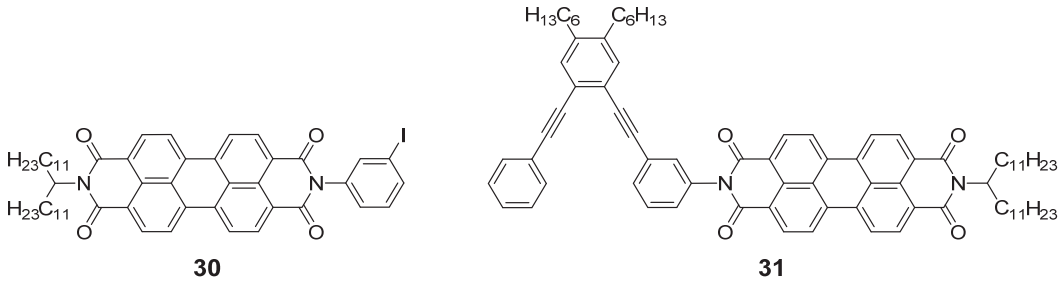

30 **31**

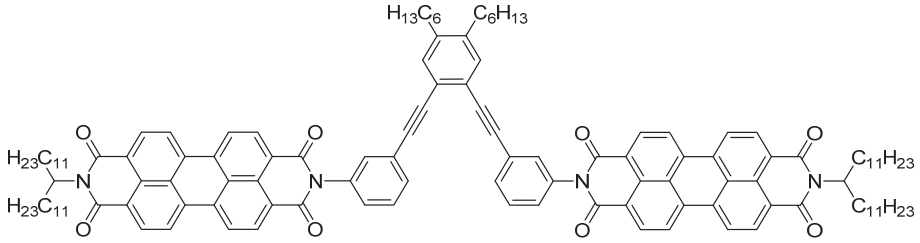

32

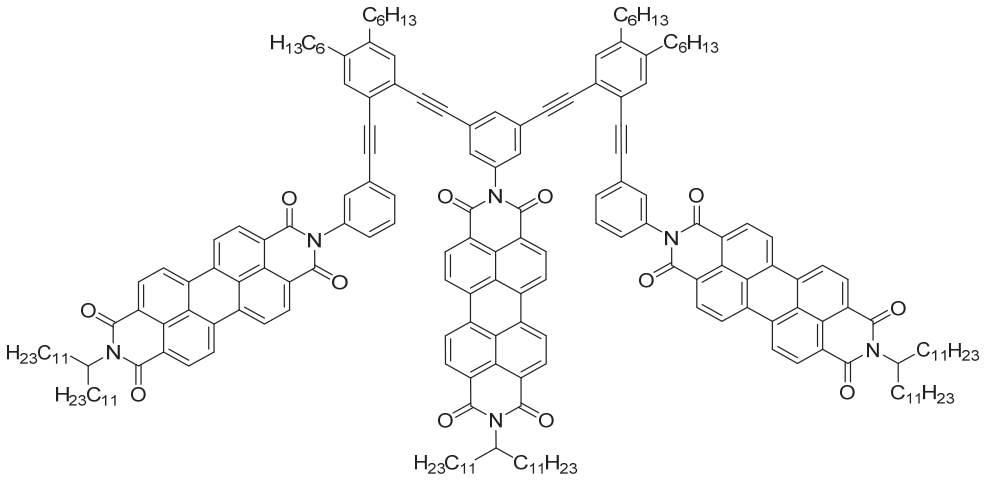

33

3.2. Syntheses of PBI Folda-Systems and Reference Compounds

The target phenylene ethynylene tethered folda-dimer **32** and folda-trimer **33** were synthesized according to the routes depicted in Scheme 1. Starting with literature-known 4,5-di-*n*-hexyl-1,2-diiodobenzene **34**,[125] the monosilyl-protected 1,2-diethynylbenzene

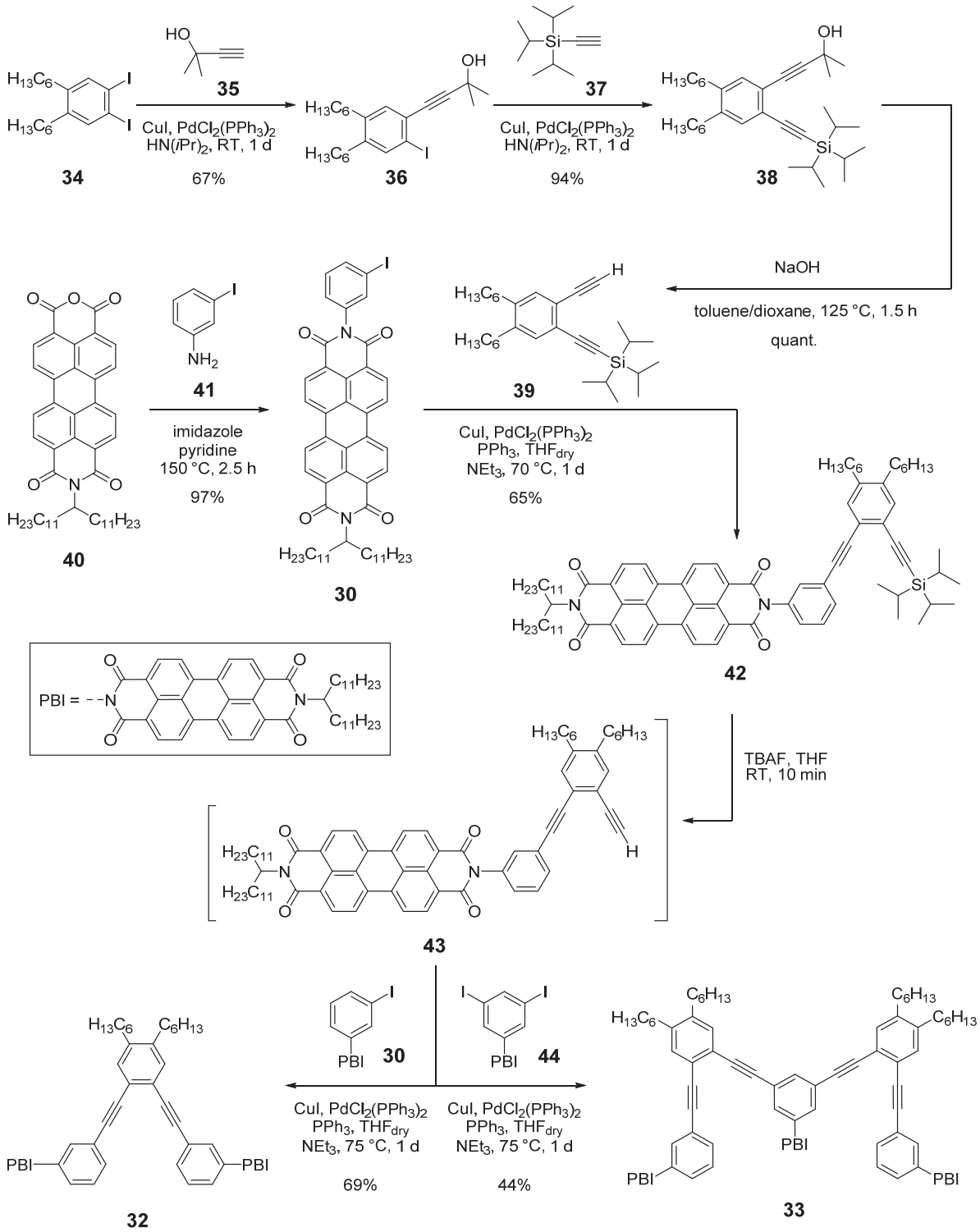

Scheme 1. Synthetic routes to folda-dimer **32** and folda-trimer **33**.

derivative **39** was synthesized by two sequential Pd/Cu-catalyzed *Sonogashira–Hagihara* reactions with 2-methylbut-3-yne-2-ol (**35**) and triisopropylsilylacetylene (**37**) in diisopropylamine under inert conditions, followed by quantitative cleavage of the tertiary alcohol protective group in precursor **38** with sodium hydroxide in a boiling toluene/dioxane mixture in an overall yield of 63%. Compound **39** was previously synthesized by a different

route;[23] however, the present pathway using a polar tagging strategy[126] resulted in significantly higher yield. In the next step, 12-tricosanyl-substituted[65,127] (first mentioned as "swallow-tailed"[128] alkyl substituents for smaller chains attached to steroids by Louw *et al*.) perylene-3,4:9,10-tetracarboxylic acid-3,4-anhydride-9,10-imide **40**[129] was reacted with 3-iodoaniline (**41**) to obtain PBI **30** in a yield of 97% in analogy to the literature-known reaction of symmetric 3,5-diiodoaniline with **40** affording PBI **44**,[25] which was used to build up the inner PBI moiety in folda-trimer **33**. The unsymmetrical PBI dye **30** was subjected to *Sonogashira-Hagihara* coupling reaction with **39** in degassed triethylamine (NEt_3) and dry tetrahydrofuran (THF) in the presence of triphenylphosphine to obtain the key intermediate **42** (65% yield) for the target compounds **32** and **33**. The *Sonogashira-Hagihara* reaction of *in situ* generated terminal alkyne **43**, which could also be isolated for characterization purposes from **42** by using tetra-*n*-butylammonium fluoride (TBAF), with either **30** or **44** under similar reaction conditions as applied for the synthesis of **42** afforded the desired folda-dimer **32** and folda-trimer **33** in 69% and 44% yield, respectively. The compounds **32** and **33** were separated from byproducts and purified by recycling gel permeation chromatography (GPC). The synthetic pathway of the reference compound **31** is depicted in Scheme 2 and the detailed synthesis is given in the Experimental Section (*cf*. subchapter 6.2). In addition the PBI-free reference molecule **49** was synthesized (Scheme 3), which was built up using 1,2-diethynyl-4,5-di-*n*-hexylbenzene (**48**) and iodobenzene (**45**) as also described in 6.2. All new compounds, including the target compounds **32** and **33**, were characterized by NMR spectroscopy, high resolution mass spectrometry, and elemental analysis.

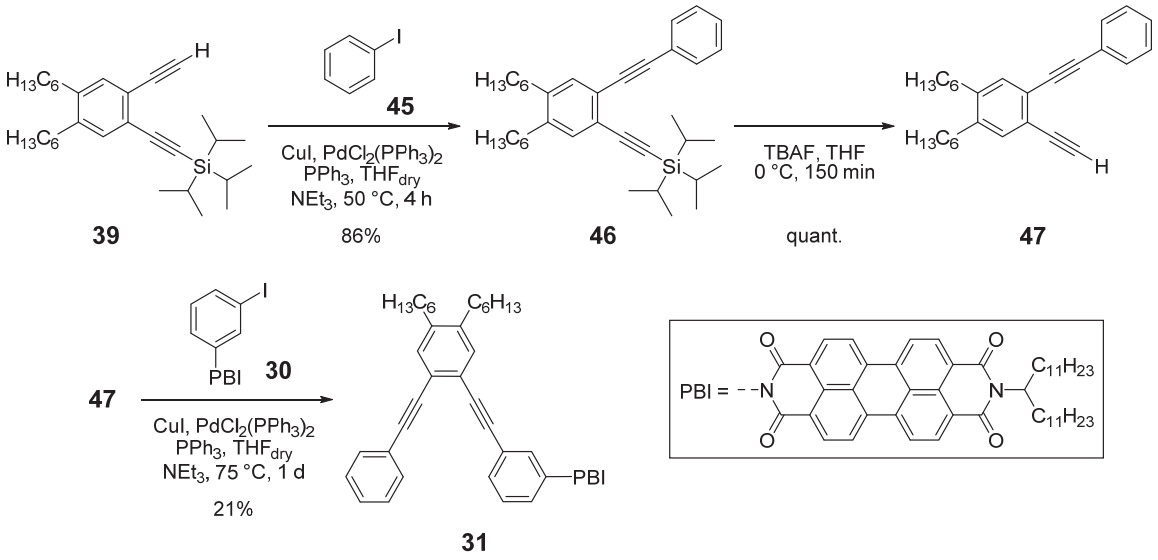

Scheme 2. Synthetic route to reference molecule **31**.

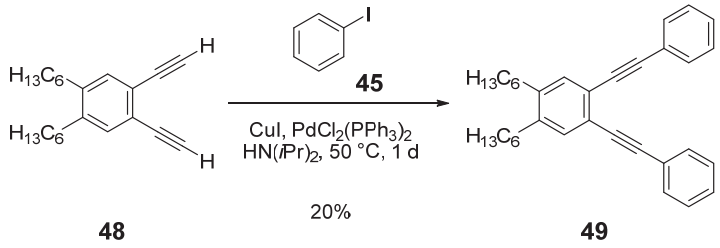

Scheme 3. Synthetic pathway to reference molecule **49**.

3.3. Solvent-Dependent Folding Properties in the Ground State

3.3.1 Choice of Proper Solvents

The folding properties of the newly synthesized folda-dimer **32** and folda-trimer **33** in the ground state were investigated by UV/Vis absorption and ^{1}H NMR spectroscopy. To ascertain the suitable solvents or solvent combinations for these studies, first the UV/Vis absorption spectra of PBI dimer **32** in a broad variety of solvents ranging from nonpolar methylcyclohexane to considerably polar, chlorinated solvents and to highly polar benzonitrile were measured (Figure 14). Since only minor spectral changes are observed at higher and shorter wavelengths depending on the solvent, the spectral changes in the region between 400 and 600 nm will be discussed.

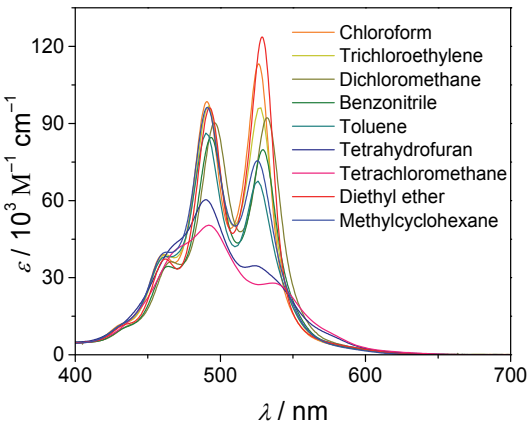

Figure 14. UV/Vis absorption spectra of PBI dimer **32** in nine different solvents (c = 6 × 10^{-6} M) at 25 °C.

As PBI dyes are known to have a distinctive vibronic fine structure representing the transitions between the different vibrational energy levels of the electronic ground state (S_0) and the first excited state (S_1) for monomeric dyes as well as for small oligomeric PBI ensembles[18,25,61,83,92,97,111,130-132] and a more broadened spectrum for large aggregates,[38,133] the analysis of these bands can serve as an important tool to understand the 'excitonic communication' of PBI chromophores.

Whereas two distinct bands are present at approximately 490 and 525 nm with different ratios of band intensities to each other for most of the solvents applied, the spectra in MCH and Et_2O are completely broadened and exhibit lower intensities. The two spectra showing the most striking changes are in $CHCl_3$ and MCH, which have also been used earlier to investigate a similar folda-system[25] and the self-assembly of monomeric PBI dyes.[18]

UV/Vis experiments of folda-dimer **32** in different $CHCl_3$/MCH mixtures were then carried out. The spectra recorded in pure $CHCl_3$ and solvent mixtures with increasing content of MCH are shown in Figure 15. From these spectra it becomes obvious that only for MCH contents < 80% a simple folding process prevails, while the loss of isosbestic points and a notable hypsochromism at higher MCH contents suggest additional structural changes that may be attributed to further intermolecular aggregation steps induced by solvophobicity.

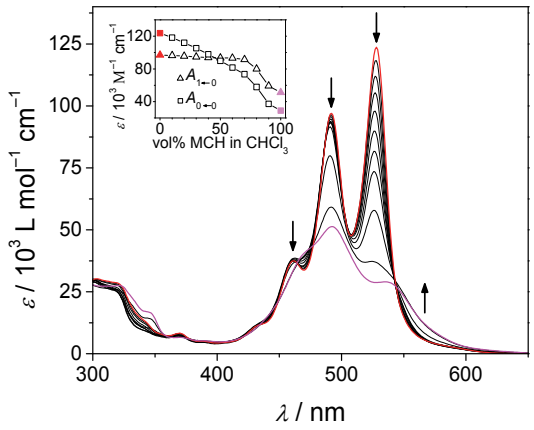

Figure 15. Solvent-dependent UV/Vis experiments of **32** ($c = 6 \times 10^{-6}$ M) in $CHCl_3$/MCH mixtures at 25 °C starting in pure $CHCl_3$ (red line) to pure MCH (pink line) by increasing MCH content in steps of 10 vol%. The arrows indicate the spectral changes with increasing content of MCH in $CHCl_3$. The inset shows the plot of the absorption maxima $A_{1\leftarrow0}$ (triangles) and $A_{0\leftarrow0}$ (rectangles) against the content of MCH (0 to 100 vol%) in $CHCl_3$.

This assumption was further substantiated by ^{1}H NMR spectroscopic studies, which revealed only one broad signal for aromatic protons of PBI **32** in [D_{14}]MCH. This merging into one band covering the range of several ppm suggests that a couple of different species are formed, whose aromatic protons are then overlapping.

Because of the complexity arising from competing intra- and intermolecular aggregation processes in MCH, this solvent was not considered as a suitable one for the elucidation of folding properties of dimer **32** and trimer **33**. As shown in this work, tetrahydrofuran (THF) is appropriate to investigate exclusive intramolecular folding events in oligomeric PBI systems like **32** and **33** and thus chloroform, tetrahydrofuran, and mixtures of these two solvents were chosen for the elucidation of folding properties of **32** and **33**.

3.3.2 UV/Vis Spectroscopic Studies

The UV/Vis absorption spectra of folda-dimer **32** and folda-trimer **33** in pure $CHCl_3$ and THF and in different mixtures of these solvents are shown in Figure 16 and important optical properties are summarized in Table 1 together with those of monomeric PBI reference compounds **30** and **31**. The spectrum of folda-dimer **32** in pure $CHCl_3$ exhibits two sharp absorption bands at 529 and 493 nm with extinction coefficients of 123600 and 96100 M^{-1} cm^{-1}, respectively, along with a shoulder at 462 nm and a broad slope in the region of 300 to 370 nm. Upon increasing the content of THF in $CHCl_3$/THF mixtures from 0 to 100% the lowest-energy band (at 529 nm) shows significant changes with large hypochromic shifts ($\Delta\varepsilon$ down to 49800 M^{-1} cm^{-1}, which corresponds to a loss in intensity of about 40%) and a small hypsochromic shift of 3 nm, while the band at 493 nm remains nearly unchanged ($\Delta\varepsilon$ up to 4700 M^{-1} cm^{-1}, loss in intensity < 5%). The plot of extinction coefficients ε of PBI **32** against the contents of THF in $CHCl_3$ (Figure 16a, inset) reveals a gradual decrease of ε value for the band at 529 nm with increasing the THF content from 0 to 60%. For solvent mixtures consisting of > 60% THF, the intensities of both bands (at 529 and 493 nm) remain virtually unchanged. Accordingly, the ratio of absorption maxima of both prominent bands $A_{529\,nm}/A_{493\,nm}$ of folda-dimer **32** is 1.29 in $CHCl_3$ which gradually decreases down to 0.80 upon increasing the THF content from 0 to 100%. It is noteworthy that for the reference PBI dyes **30** and **31**, which contain only one PBI unit and thus cannot fold, this ratio is close to 1.65 in both solvents (Figure 17 and Figure S1). In this regard, it should also be mentioned that for the rigid cofacially stacked PBI dimer **8a** (*cf.* Chart 2) of Wasielewski, a $A_{0\text{-}0}/A_{1\text{-}0}$ ratio of around 0.9 in $CHCl_3$ was reported,[61] whereas for the rigid

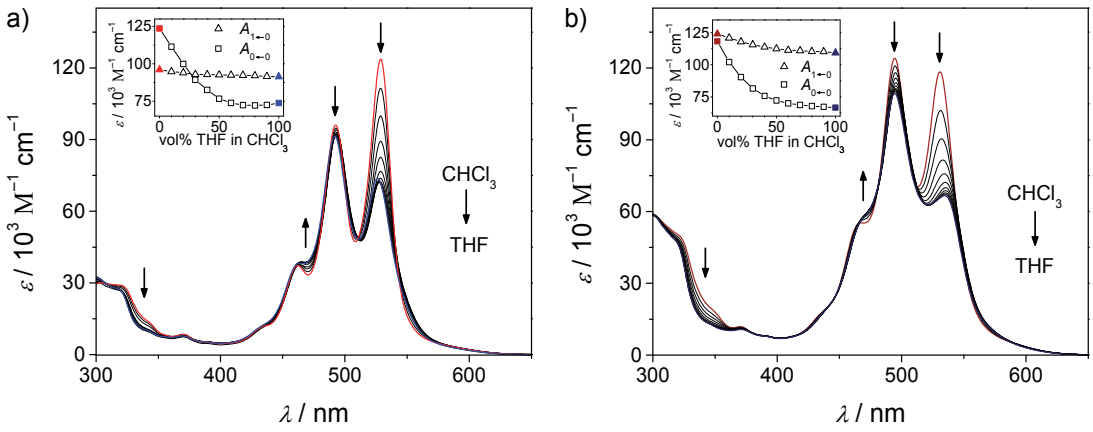

Figure 16. Solvent-dependent UV/Vis absorption spectra of a) **32** ($c = 5 \times 10^{-6}$ M) and b) **33** ($c = 6 \times 10^{-6}$ M) in $CHCl_3$/THF mixtures at 25 °C starting in pure $CHCl_3$ (reddish lines) changed to pure THF (bluish lines) by increasing THF content in steps of 10 vol%. Inset: Plot of the absorption maxima $A_{1\leftarrow0}$ (triangles) and $A_{0\leftarrow0}$ (rectangles) against the content of THF (0 to 100 vol%) in $CHCl_3$.

Table 1. Optical properties of PBI systems **30**, **31**, **32**, and **33** investigated in $CHCl_3$ and THF.

PBI	Solvent	λ_{abs} [nm] (λ_{max} [M^{-1} cm^{-1}])[a]	$A_{0\text{-}0}/A_{1\text{-}0}$ ratio[b]
30	$CHCl_3$	528 (83100), 491 (50000), 460 (18100)	1.66
	THF	522 (81900), 486 (49700), 456 (18100)	1.65
31	$CHCl_3$	528 (84200), 491 (50800), 460 (18800)	1.66
	THF	523 (80400), 487 (49200), 457 (18200)	1.63
32	$CHCl_3$	529 (123600), 493 (96100), 462 (37300)	1.29
	THF	526 (73800), 493 (91400)	0.80
33	$CHCl_3$	531 (118300), 495 (124100)	0.95
	THF	534 (66700), 495 (109300)	0.61

[a] Absorption measurements at 25 °C, concentrations were in the range between 5×10^{-6} M to 2×10^{-5} M. [b] The respective absorption band intensities (A) of the two bands representing the 0-0 and 1-0 vibrational energy levels were taken.

biphenylene-bridged PBI dimer **7a** (Chart 2) of Langhals,[82] in which both chromophores are arranged away from each other, this value was reported to be 1.3 in $CHCl_3$. For the photoswitchable PBI dimer **18** (see Figure 9) of Feringa and co-workers, this ratio was changed upon irradiation from 1.4 to 0.8 in THF.[111] The fact that PBI folda-dimer **32** shows $A_{0\text{-}0}/A_{1\text{-}0}$ values of 1.29 in $CHCl_3$ and 0.80 in THF implies that this dimeric PBI exists in folded state in THF, while in the halogenated solvent it is unfolded as the data are in good accordance with the literature-reported values mentioned above.

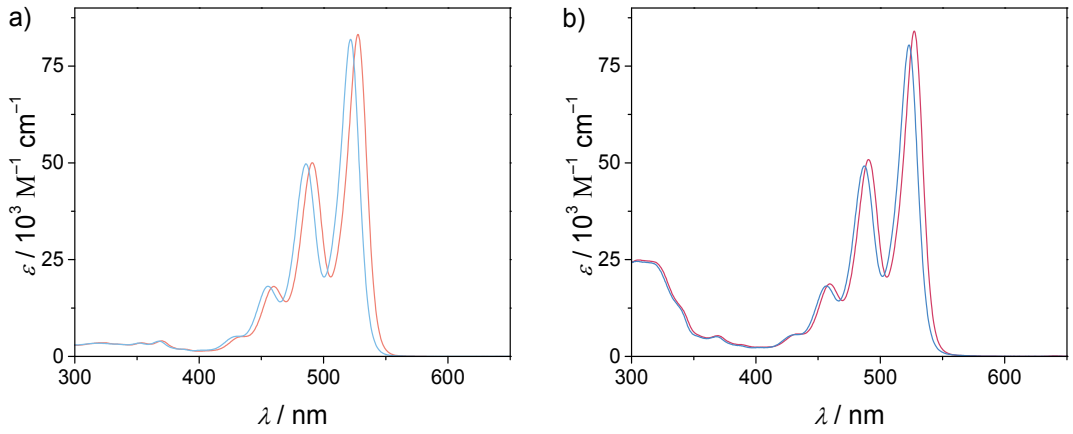

Figure 17. UV/Vis absorption spectra of reference PBIs a) **30** ($c = 1 \times 10^{-5}$ M in $CHCl_3$; $c = 2 \times 10^{-5}$ M in THF) and b) **31** ($c = 1 \times 10^{-5}$ M in $CHCl_3$ and in THF) in $CHCl_3$ (reddish colors) and THF (bluish colors) at 25 °C.

Folda-trimer **33** exhibits similar solvent-dependent changes of absorption spectra (Figure 16b) as observed for **32**. In $CHCl_3$, again two dominant absorption bands can be

seen at 531 and 495 nm with ε values of 118300 and 124100 $M^{-1}cm^{-1}$, respectively, along with a shoulder at 468 nm (Figure 16b). However, the intensities of bands at 531 and 495 nm are already reversed as compared to that of the corresponding bands of folda-dimer **32** and the ratio of the two bands, $A_{531\ nm}/A_{495\ nm}$, for **33** is 0.95. These observations can be taken as an indication for a stronger coupling between the PBI units in partially folded conformations of **33** in $CHCl_3$. Upon increasing the content of THF both bands are hypochromically shifted ($\Delta\varepsilon$ down to 51600 and 14800 M^{-1} cm^{-1}, which corresponds to an intensity loss of 44% and 12% for the bands at 531 and 495 nm, respectively). The ratio of $A_{534\ nm}/A_{495\ nm}$ in pure THF is reduced to 0.61, which is markedly smaller than that observed for folda-dimer **32**. For the cofacial PBI trimer **13** with a rigid xanthene unit (Chart 3) an $A_{0\text{-}0}/A_{1\text{-}0}$ ratio of 0.6 (*cf.* Figure 6) was reported by Wasielewski and co-workers.[61] Thus, a folded conformation of **33** in THF can be implied, whereas in $CHCl_3$ this molecule is apparently in a more unfolded state with already remarkable dye–dye interactions. To assess whether any further self-assembly by intermolecular interactions between individual molecules occurs, temperature- and concentration-dependent UV/Vis studies were carried out for folda-dimer **32** (Figure 18a,b

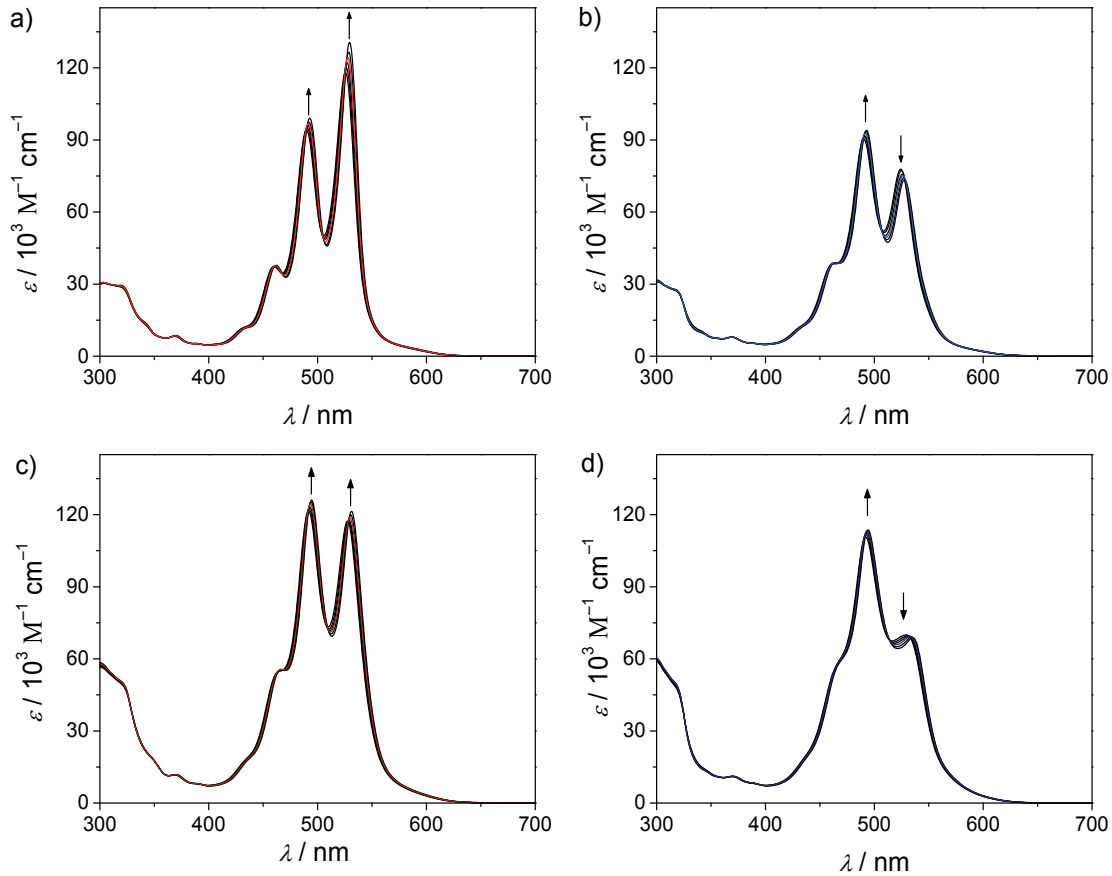

Figure 18. Temperature-dependent UV/Vis absorption spectra of a), b) folda-dimer **32** ($c = 5 \times 10^{-6}$ M) and c), d) folda-trimer **33** ($c = 6 \times 10^{-6}$ M) in $CHCl_3$ (left graphs) and THF (right graphs), starting at 55 °C down to 5 °C in 10 °C intervals. The respective spectra of **32** (top graphs) and **33** (bottom graphs) at 25 °C are colored in each graph. The arrows indicate the spectral changes with decreasing temperature.

as well as Figures S2 and S3 in subchapter 6.3) and folda-trimer **33** (Figure 18c,d and Figure S4 in subchapter 6.3) in $CHCl_3$ and THF. In both solvents the temperature- and concentration-dependent spectral changes for **32** and **33** are almost negligible. These observations suggest that, on the one hand, the PBI molecules are appropriately solvated and do not build larger supramolecular ensembles and, on the other hand, the intramolecularly folded dimer **32** and trimer **33** are held together by rather strong π–π-interactions in THF as no spectral changes were observed at higher temperatures (see Figure 18b,d as well as Figures S3 and S4 in subchapter 6.3).

3.3.3 ^{1}H NMR Spectroscopy

To get more insight into the solvent-dependent conformations of folda-dimer **32** and folda-trimer **33**, and to explore whether additional dynamic processes are involved, temperature-dependent ^{1}H NMR studies in [D_8]THF and $CDCl_3$ have been conducted. In contrast to the research on biomolecules, application of NMR methods is much rare for the elucidation of conformational preferences of synthetic oligomer backbones. However, in the field of PBI dyes a few studies have been reported, *e.g.* by Li,[100] Castellano,[134] and Wasielewski.[135] In $CDCl_3$, which is known as a good solvent for the solvation of π-extended aromatic systems, in particular PBI dyes,[136] a surprisingly complex signal pattern was observed in the aromatic region (8.8 to 7.2 ppm) for folda-dimer **32** at 293 K (Figure 19, top). Such signal pattern suggests the coexistence of different conformations of **32** in $CDCl_3$ whose interconversion is not fast enough on the NMR time scale for signal averaging. While the signals for PBI core protons (between 8.8 and 8.2 ppm) are not reliably assignable due to overlapping of signals, the major signals between 7.7 and 7.2 ppm) of phenylene ethynylene scaffold could be assigned (Figure 19, top spectrum). Variation of temperature in the range from 274 to 323 K did not simplify the spectra of **32** in $CDCl_3$ (Figure 21). On the other hand, variable temperature (from 274 to 333 K) ^{1}H NMR spectra of **32** in [D_8]THF (Figure 19) showed comparatively simple signal pattern with perylene core protons located in a narrow range (8.4 to 8.2 ppm). At lower temperature (274 to 298 K) some dynamic broadening of the signals of perylene core protons at 8.4 to 8.2 ppm was observed. Upon increasing the temperature to 313 K and higher, the broadened perylene proton signals got increasingly sharper and nicely resolved in four doublets. The signals of the perylene protons of folda-dimer **32** in [D_8]THF are significantly up field shifted as compared with the spectra in $CDCl_3$, which is in stark contrast to monomeric PBI reference compound **31** since for the latter an opposite trend is evident in these solvents (see Figure 21). The

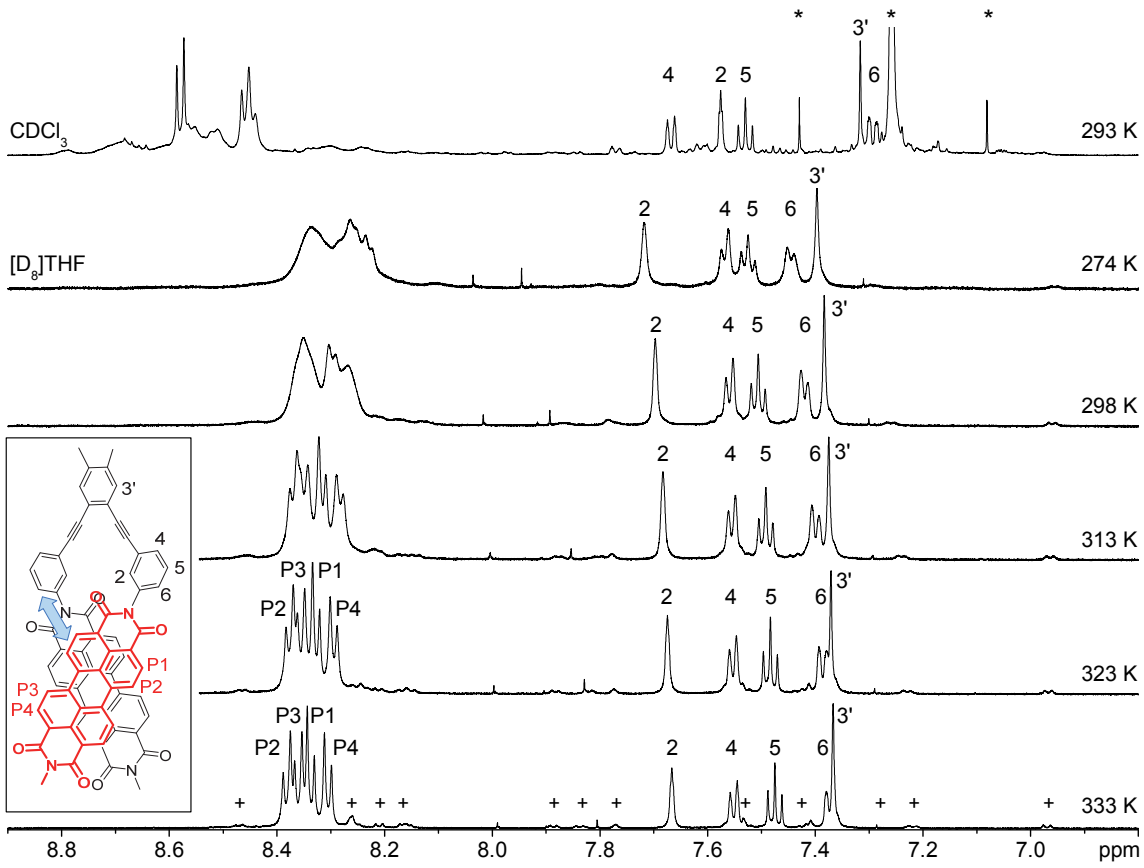

Figure 19. Aromatic regions of temperature-dependent ^{1}H NMR spectra (600 MHz) of folda-dimer **32** ($c = 5 \times 10^{-4}$ M) in [D$_8$]THF at 274 to 333 K and, for comparison, in $CDCl_3$ at 293 K (top). Solvent signals are marked with asterisks (*). In the ^{1}H NMR spectrum of **32** in [D$_8$]THF at 333 K (bottom) signals of the low-populated conformer (see discussion below) are marked with plus symbols (+). Inset: Chemical structure (methyl instead of long alkyl chains are shown) of folded **32** with the assignment of aromatic protons of PBI core (P1, P2, P3, and P4) and phenylene ethynylene scaffold (2, 4, 5, 6, and 3'). Strong interactions between adjacent protons observed in the 2D ROESY NMR spectrum (see Figure 20) are indicated as a blue arrow.

observed up field shift for the perylene protons of PBI **32** in [D$_8$]THF can be taken as an indication for the formation of a π–π-stacked PBI dimer, *i.e.* folding of **32**. Since increase (from 274 to 333 K) of temperature resulted in sharpening of the aromatic proton signals without any considerable shift or change of coupling pattern (Figure 19), an intramolecular dynamic process that preserves the π–π-stacking should be responsible for the observed temperature-dependent changes of the NMR spectra of **32** in [D$_8$]THF.

To shed light on this dynamic process, the variable temperature NMR study of reference PBI **31** (Figure 22a), which is a simpler monomeric analogue of **32**, in [D$_8$]THF is very instructive. A selection of temperature-dependent ^{1}H NMR spectra of **31** in [D$_8$]THF is shown in Figure 23c (for the complete set of spectra measured at temperature range 274 to 333 K see Figure S7 in subchapter 6.4). In the spectrum at lower temperature (274 K) four nicely separated doublets were observed at 8.94, 8.71, 8.68, and 8.64 ppm with a signal integral ratio of 4:2:1:1, respectively. These doublets could be assigned to the perylene

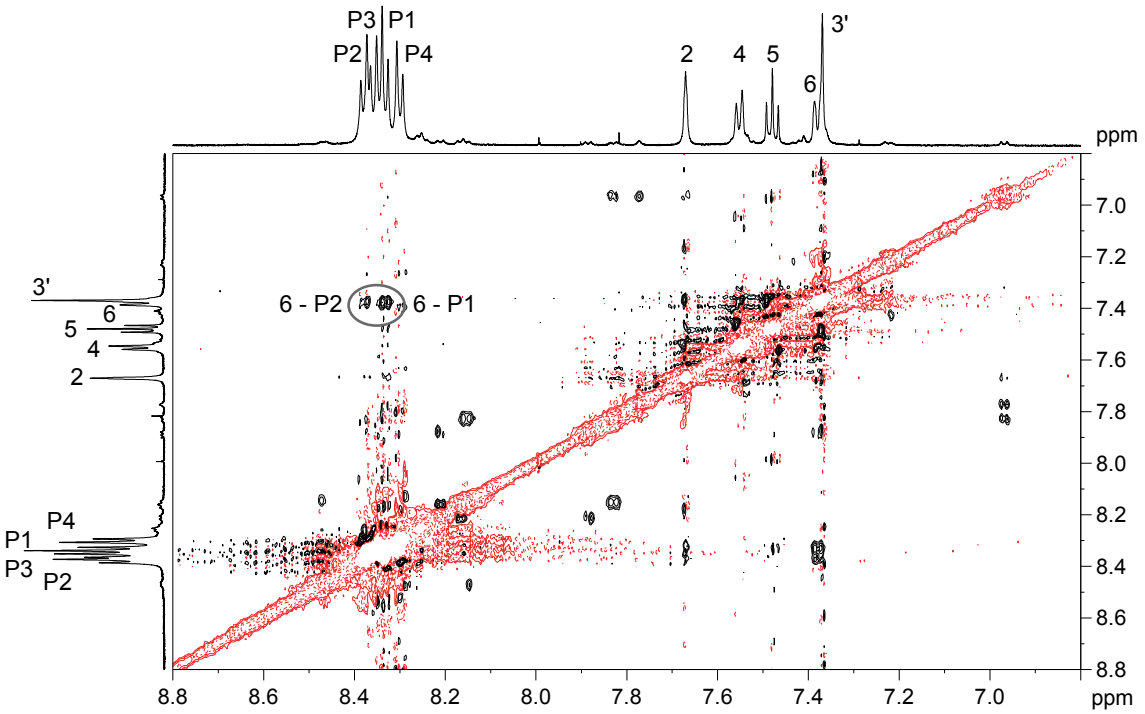

Figure 20. ^{1}H,^{1}H-2D-ROESY NMR spectrum (aromatic region, 600 MHz, black: positive, red: negative cross couplings) of folda-dimer **32** in [D$_8$]THF ($c = 5 \times 10^{-4}$ M) at 328 K. Signals marked with a circle are cross couplings, that are not present in the ^{1}H,^{1}H-2D-COSY NMR spectrum.

protons as shown in Figure 22a. Upon increasing the temperature, the two doublets at 8.68 and 8.64 ppm (for protons P4/P4') become gradually broader and merge into a broad signal at around 303 K (see also Figure S7 in subchapter 6.4). Upon further increasing the

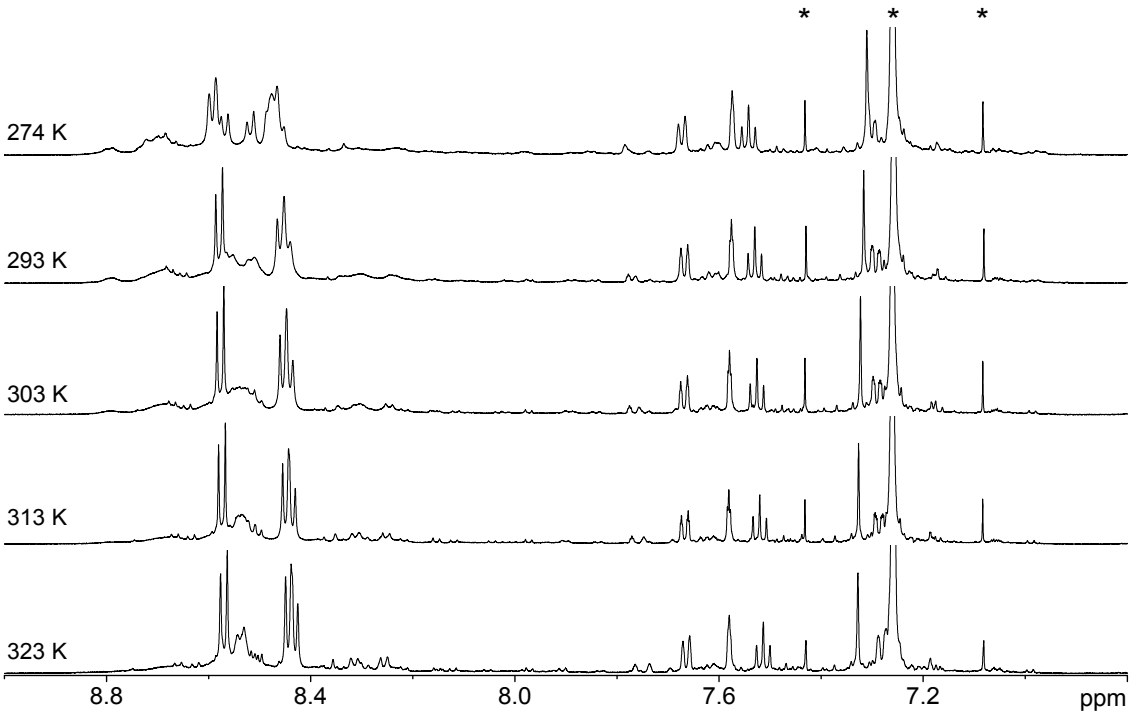

Figure 21. Temperature-dependent (from 274 to 323 K) ^{1}H NMR spectra (aromatic region, 600 MHz) of folda-dimer **32** in $CDCl_3$ ($c = 8 \times 10^{-4}$ M). The temperature is indicated above the respective spectrum. Solvent signals are marked in the top spectrum with asterisks (*).

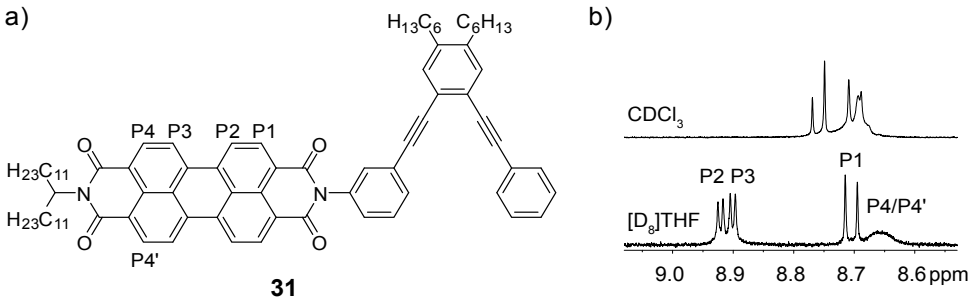

Figure 22. a) Chemical structure of reference compound **31** with the assignment of perylene protons P1 to P4/P4'. b) ^{1}H NMR spectra (region of perylene protons P1–P4/P4', 400 MHz) of **31** ($c \sim 10^{-4}$ M) in $CDCl_3$ (top spectrum) and in [D_8]THF (bottom spectrum) at 300 K.

temperature, this broad signal gets again narrower and above 323 K a doublet arises, which becomes very sharp at 333 K. With the concomitant separation of the signals for protons P2 and P3 the expected four doublets with intensity ratio of 2:2:2:2 are now realized. The observed temperature-dependent spectral changes for **31** in [D_8]THF can be attributed to a hindered rotation around the C–N bond with swallow tail (12-tricosanyl) imide substituent.

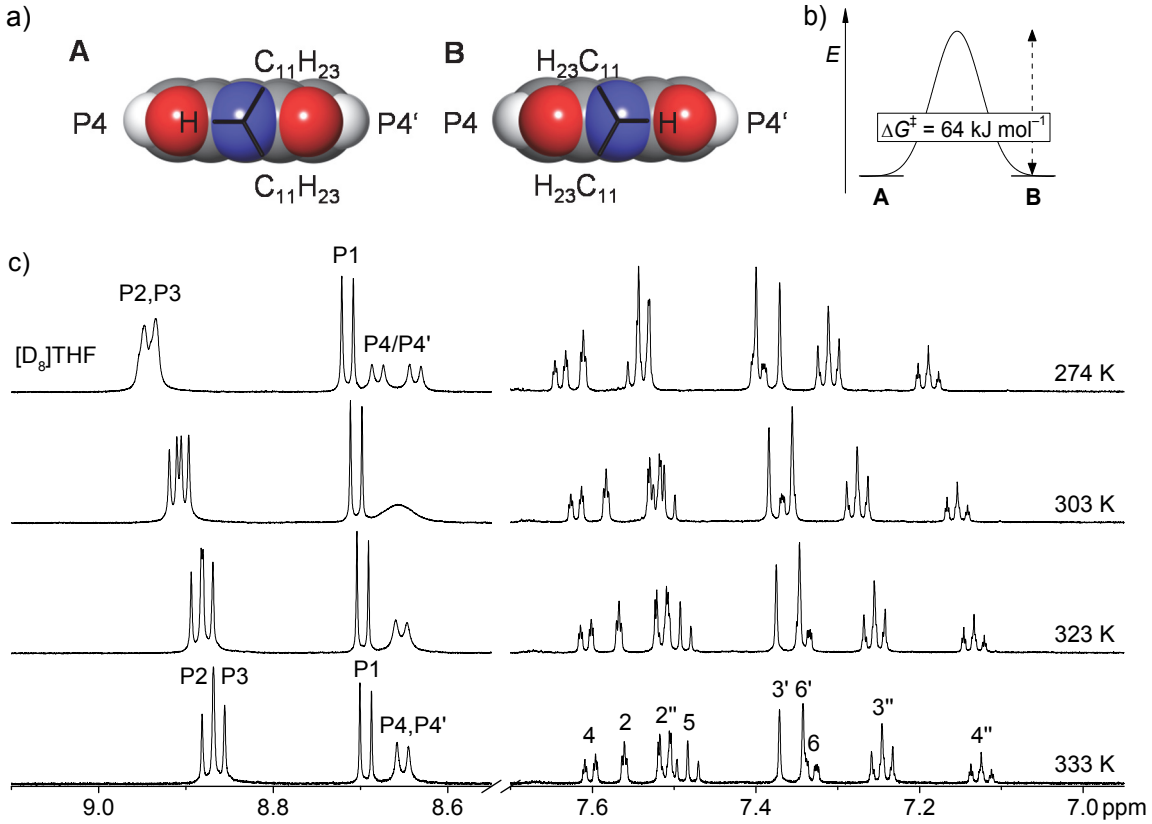

Figure 23. a) Representative CPK models of the two rotational conformations (**A** and **B**) arising from the hindered rotation of swallow tail around the C–N bond in PBI **31** schematically shown for *N*-(12-tricosanyl)-1,8-naphthalene imide (view along the C–N bond). The two different perylene core protons P4 and P4', distinguishable at low temperature, are labelled in both sketches. b) Schematic representation of the energy profile for the dynamic interconversion of the two rotamers. c) Aromatic regions of selected temperature-dependent ^{1}H NMR spectra (600 MHz) of **31** ($c = 5 \times 10^{-4}$ M) in [D_8]THF from 274 to 333 K (below). Temperature is indicated above the respective spectrum. Signals are assigned as depicted in Figure 22a.

Indeed, perylene bisimides and similar imide compounds that exhibit restricted rotation around C–N imide bond with considerably high rotational barriers have been reported previously.[134,137-142] Such rotational isomers can be frozen at low temperature. For PBI **31** two doublets at 8.68 and 8.64 ppm were observed for the two perylene *ortho*-protons P4/P4' at low temperature (274 K) in [D$_8$]THF, while for the other two *ortho*-protons (P1) only one doublet at 8.71 ppm was observed. This spectral feature can be attributed to a slower rotation of the swallow tail substituent around the respective C–N bond on the NMR time scale, and thus freezing of the two rotamers **A** and **B** shown in Figure 23a. Upon increasing the temperature, these doublets get gradually broadened and at around 303 K show coalescence, revealing a dynamic equilibrium of these rotamers on the NMR time scale. At temperatures above 303 K, the rotation gets faster than the NMR time scale and thus the two perylene protons P4/P4' become chemically equivalent, giving rise to a sharp doublet. An energy barrier ($\Delta G^{\ddagger}$) of about 64 kJ mol^{-1} (see Figure 23b) could be estimated for this intramolecular rotation process by using the coalescence method (*cf.* Equation 1).[143]

$$\Delta G^{\ddagger} = T_c R \ln\left(\frac{T_c R\sqrt{2}}{\pi N_A h \Delta\nu}\right) \qquad \textbf{(Eq. 1)}$$

where T_c is the coalescence temperature, R the gas constant, N_A the Avogadro constant, h the Planck constant and $\Delta\nu$ the difference between both separated proton signals, which exhibit the coalescence phenomenon. Similar $\Delta G^{\ddagger}$ values have been reported for the rotational barrier of PBIs bearing branched alkyl substituents at the imide positions.[137] By employing a smaller reference system, namely *N*-(*iso*-propyl)-1,8-naphthalene imide, the energy barrier of about 61 kJ mol^{-1} was estimated by DFT calculations (B3LYP/6-311G**, *cf.* Table S1 in subchapter 6.5).[144-148] For comparison, an energy barrier of only 25 kJ mol^{-1} was calculated for a related 1,8-naphthalene imide compound bearing a *meta*-ethynyl phenylene imide substituent[123] instead of *iso*-propyl. Accordingly, also DFT calculations support the conclusion that the hindered rotation around the C–N bond with swallow tail imide substituent, and not that of ethynylene phenylene substituent is responsible for the observed temperature-dependent ^{1}H NMR spectral changes in the 274–333 K temperature regime in [D$_8$]THF (see also the subchapter 3.4).

In light of the above discussion on variable-temperature ^{1}H NMR study of monomeric reference PBI **31**, the temperature-dependent spectral changes observed for the folda-dimer **32** in [D$_8$]THF (Figure 19) can be ascribed to a similar hindered rotation around the C–N bonds of two PBI units bearing swallow tail substituents. The broad signal observed at 8.4 to 8.2 ppm for the perylene protons of PBI **32** at low temperature (274 K) can be attributed

to a slow rotation of the swallow tail substituents around C–N bonds on the NMR time scale. At higher temperature (> 313 K) the rotation around the C–N bond gets much faster than the NMR time scale, and thus the perylene protons (P1, P2, P3, and P4) of the two PBI units are nicely resolved in four sharp doublets, which could be clearly assigned (as shown in Figure 19) based on 2D ROESY NMR spectrum (Figure 20). The observation of only four doublets at higher temperatures (323 K) for 16 perylene protons of folda-dimer **32**, implies that the respective proton pairs (P1, P2, P3, and P4) in both PBI units of **32** are chemically equivalent. This can be taken as an indication for a tightly packed and symmetric folding of PBI **32** in [D_8]THF.

A closer look at the high temperature ^{1}H NMR spectrum of **32** in [D_8]THF at 333 K reveals the appearance of an additional set of weaker signals (Figure 19, bottom). These signals presumably arise from a second folded conformation of **32** with quite differing ^{1}H NMR shifts, which are difficult to assign reliably as they are low in intensity and, moreover, overlap partially with the prominent signals. From signal integration of C–H-proton resonances of imide substituents at 5.25 to 5.10 ppm (for an enlarged spectrum see inset in Figure 24) a 1:10 ratio of the conformers can be estimated. For this population distribution, an energy difference of approximately 6 kJ mol^{-1} between the two conformers can be estimated by applying a Boltzmann analysis. Backbone flapping in folded PBI **32** may indeed result in two different conformations as revealed below by theoretical calculations

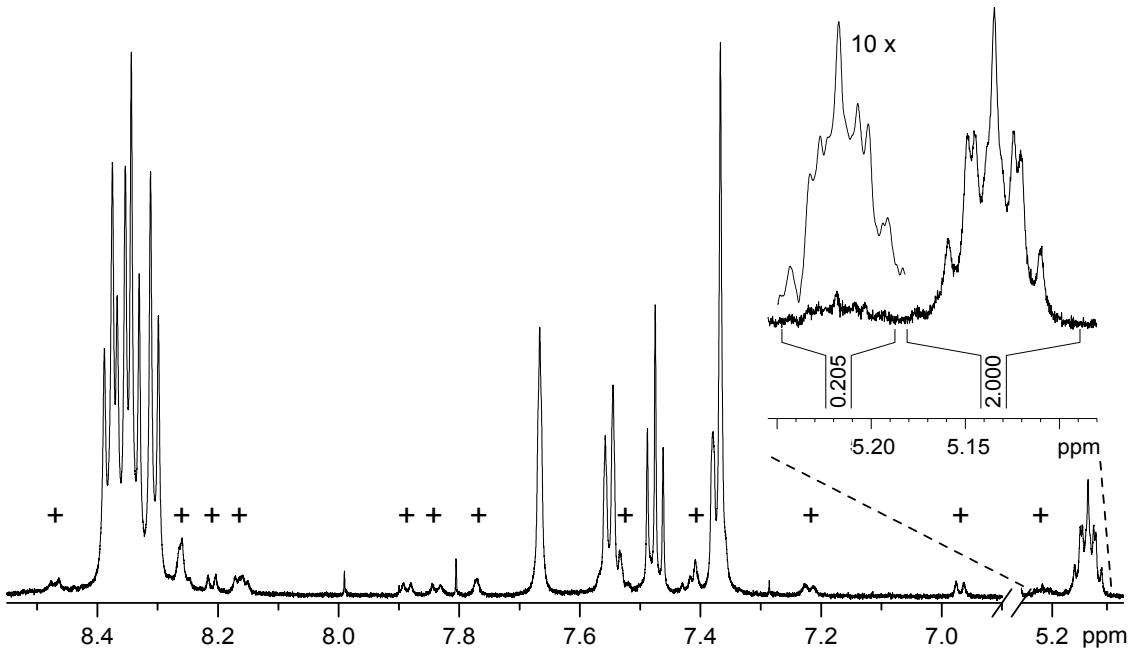

Figure 24. Region of all aromatic protons (8.55 to 6.9 ppm) and the protons attached to the branching C–H unit of the swallow tail imide substituents in the ^{1}H NMR spectrum (600 MHz, line broadening 0.1 Hz) of folda-dimer **32** ($c = 5 \times 10^{-4}$ M) in [D_8]THF at 333 K. Inset: Magnified signals of C–H protons with integration of signal areas (line broadening 1 Hz).

local optimization of one gradually distorted phenylene unit in folded **32** with PM6-DH2), which provide an energy barrier of approximately 50 kJ mol^{-1} for the backbone flapping, which might be significantly underestimated by a factor of 2 (for details see subchapter 3.4). Temperature-dependent ^{1}H NMR spectroscopic studies of folda-trimer **33** in $CDCl_3$ and [D_8]THF were performed as well (Figure 25 and Figure 26). In $CDCl_3$ a broad signal pattern spreading over the whole aromatic range from 8.9 to 6.9 ppm is observed, which is, as expected, more complex than that observed for **32** in this solvent. Although the assignment of signals to the protons of **33** appears rather elusive, the large number of peaks provides an indication for the co-existence of different conformations with varying spatial arrangements of the PBI subunits. The variation of temperature from 274 to 333 K did not appreciably affect the spectral shape in $CDCl_3$ (Figure 25). However, the temperature-dependent ^{1}H NMR spectra of **33** in [D_8]THF exhibit, as in the case of **32**, a simpler signal pattern (Figure 26). Thus, the signals of all aromatic protons between 8.4 and 7.2 ppm become

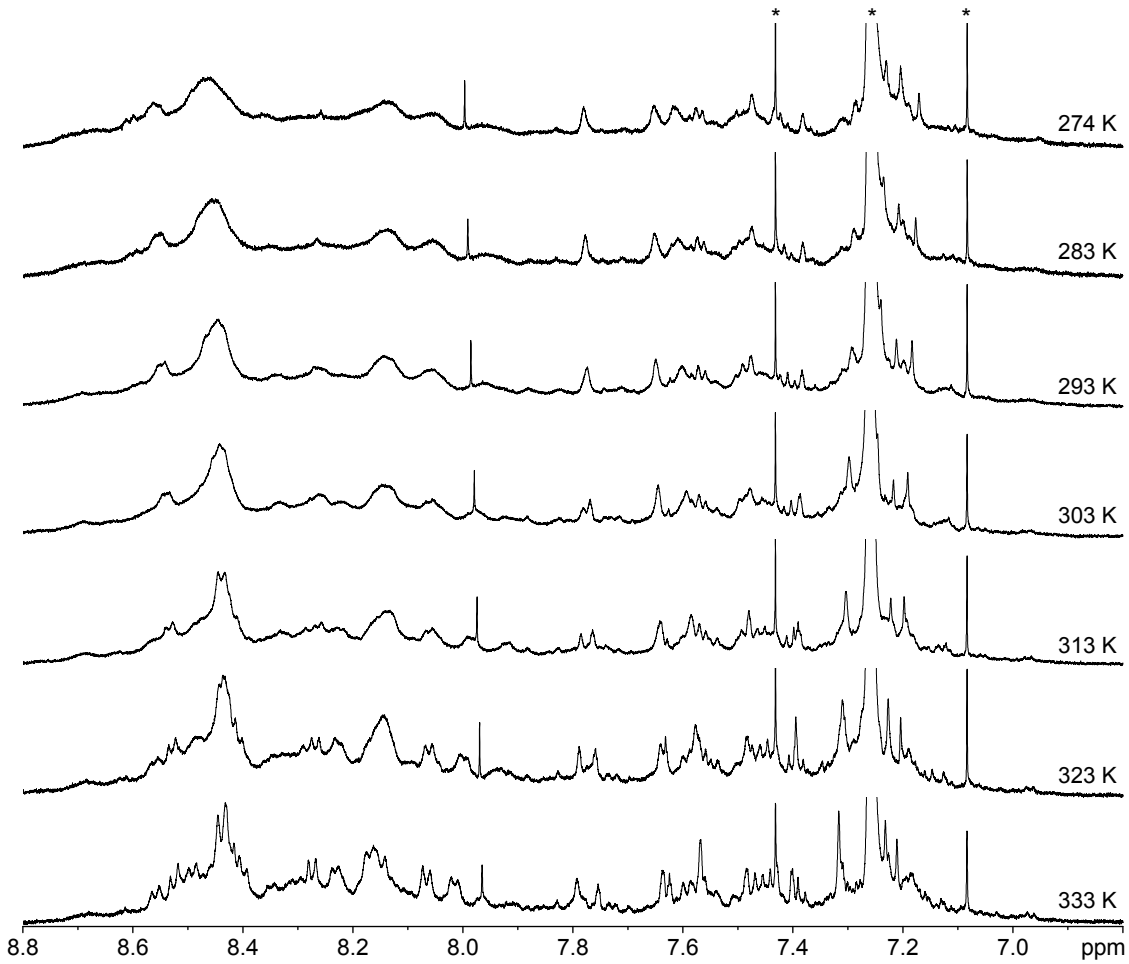

Figure 25. Temperature-dependent ^{1}H NMR spectra (aromatic region, 600 MHz) of folda-trimer **33** in $CDCl_3$ ($c = 4 \times 10^{-4}$ M). The temperature is indicated above the respective spectrum. Solvent signals are marked in the top spectrum with asterisks (*).

significantly narrower with increasing temperatures from 274 to 333 K. Most impressive temperature-dependent changes are observed for the two doublets at 8.41 and 8.37 ppm, and for the broad signals at 8.2 ppm that appear in the spectrum at 274 K. Upon increasing the temperature these two doublets (at 8.41 and 8.37 ppm) are gradually broadened and merged into a broad signal at around 313 K, and at higher temperatures (333 K) again become a doublet.

Likewise, with increasing temperature the broad signals at 8.2 ppm first change into a broad singlet and become finally resolved to a sharp doublet at higher temperature (333 K). This dynamic spectral behavior of folda-trimer **33** may account for hindered rotation around the C–N bonds bearing branched alkyl substituents (swallow tail) as discussed before for folda-dimer **32**. As in the case of dimeric analogue **32**, for folda-trimer **33** the existence of a second, low-populated conformer can be anticipated from the additional signal set (labelled with symbol +) observed at 333 K (Figure 26, bottom spectrum). A ratio of 1:4 between the two conformers was determined by signal integration in the higher field (C–H protons of alkyl substituents, *cf.* the expanded spectrum in the inset in Figure 27). By applying a Boltzmann analysis an energy difference of approximately 4 kJ mol^{-1} could be

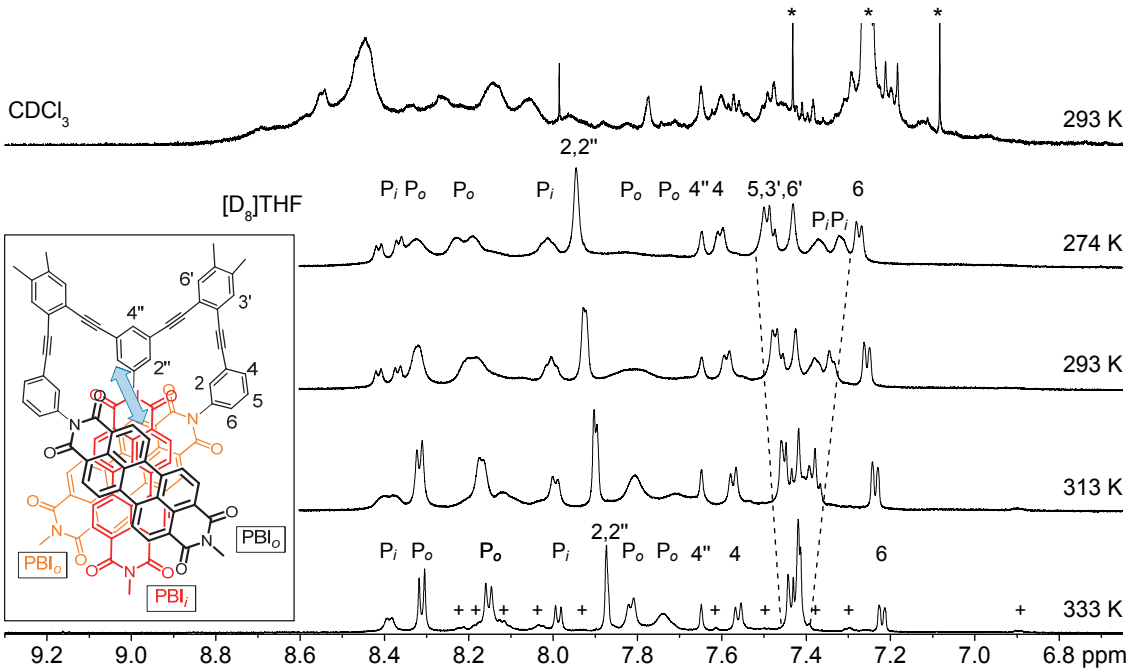

Figure 26. Temperature-dependent ^{1}H NMR spectra of folda-trimer **33** in [D$_8$]THF at 274 to 333 K and, for comparison, in $CDCl_3$ at 293 K (top) ($c = 4 \times 10^{-4}$ M, 600 MHz). Solvent signals are marked with asterisks (*). In the proton spectrum in [D$_8$]THF at 333 K (bottom) smaller signals are marked with plus symbols (+). Inset: Chemical structure of folded **33** with the assignment of aromatic phenylene protons. Alkyl chains are represented by methyl substituents for simplicity. Perylene protons of outer PBI units (PBI$_o$, bold black and orange in the sketch) are marked with P$_o$, and those of the inner PBI (PBI$_i$, bold red in the sketch) with P$_i$. The blue arrow indicates a strong interaction between adjacent protons in the ROESY spectrum. The changes in chemical shifts of the signals in the region of 7.5 to 7.3 ppm upon increasing temperature are illustrated by dashed lines.

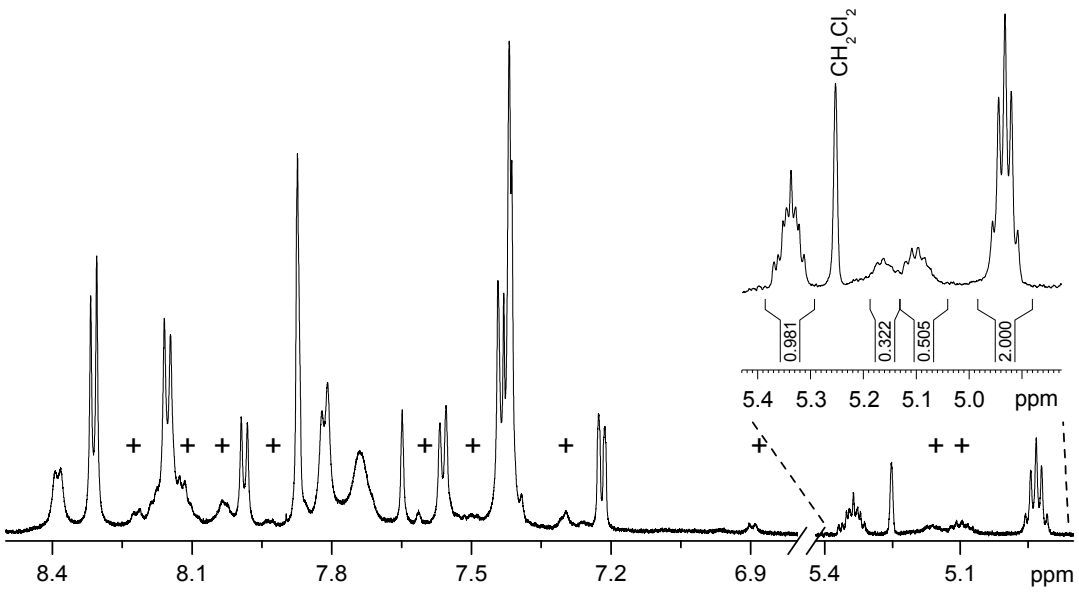

Figure 27. Region of all aromatic protons (8.5 to 6.8 ppm) and the two protons attached to the branching C–H unit of the swallow tail imide substituents in the ^{1}H NMR spectrum (600 MHz, line broadening 0.1 Hz) of folda-trimer **33** ($c = 4 \times 10^{-4}$ M) in [D$_8$]THF at 333 K. Inset: Magnified signals of C–H protons with integration of signal areas (line broadening 1 Hz).

estimated for this distribution. This value is slightly smaller than that determined for **32**. The reason for this might be that in **33** the two PBI bridging scaffold subunits are influencing and preorganizing each other.

Moreover, 2D-NMR spectroscopic studies were performed to gain more insight into the structural features of folded conformations of folda-dimer **32** and trimer **33**. Since the neighboring PBI units are arranged close to each other in the folded state, prominent cross couplings would provide information on spatial arrangement of PBI dye units in conformers. However, due to potentially high C_2 symmetry of the folded structures, NOE effects visualized by 2D-ROESY NMR spectroscopy can only partially be used to reveal the PBI interactions upon folding. The most expressive through-space proton-proton cross couplings in the folded states are given between the two H2 protons in **32** (see the inserted structure in Figure 19) and the protons at the H2 and H2" positions in **33** of the phenylene imide substituents in [D$_8$]THF (see the inserted structure in Figure 26). Unfortunately, these cross couplings cannot be identified because of the overlapping with the diagonal in the ROESY spectra. In particular, couplings between perylene core protons P1 and P2 or H6 of the phenylene ethynylene scaffold can be observed for **32** in [D$_8$]THF (*cf.* Figure 20), which supports the proposed folded structure for dimer **32** (the evaluated distances between these protons, P1–H6 and P2–H6, respectively, by the calculations are 2.4 and 3.3 Å). On the other hand, the dominant signals of **32** in CDCl$_3$ do not show any cross couplings (Figure S8 in subchapter 6.4). This corroborates the suggestion that unfolded states of **32** prevail in

chlorinated solvent. As mentioned, PBI **32** adopts different conformations in $CDCl_3$, while few of them bring both chromophores in sufficient contact to each other to communicate. This PBI–PBI distance narrowing, although not completely folded, results in particularly strong ROESY cross couplings (see Figure S8 in subchapter 6.4). Likewise, the 2D ROESY spectrum of folda-trimer **33** in $CDCl_3$ (Figure S9 in subchapter 6.4) does not exhibit any significant cross coupling as the PBI dye units are apparently not arranged in spatial proximity. However, in the [D_8]THF spectra of **33** prominent through-space interactions are present (Figure 28). These include signals that arise from couplings between protons of the two outer PBI moieties (P_o) with those of the inner PBI (P_i) as well as those between the outer PBI moieties (P_o) and the backbone H2" protons. These through-space couplings can take place only in folded state (depicted as blue arrow in the structure shown in Figure 26). A comparison of the 2D-COSY NMR spectrum of **33** in [D_8]THF (Figure S10 in subchapter 6.4) with the 2D-ROESY spectrum (Figure 28) reveals such through-space couplings. Additionally, the number of carbon atoms and the amount of C–H units comply with the signals present in the ^{13}C NMR spectra (besides overlapping of signals with similar shifts) as well as in the 2D-HSQC NMR spectra both for PBI **32** (Figure S11; compare also the

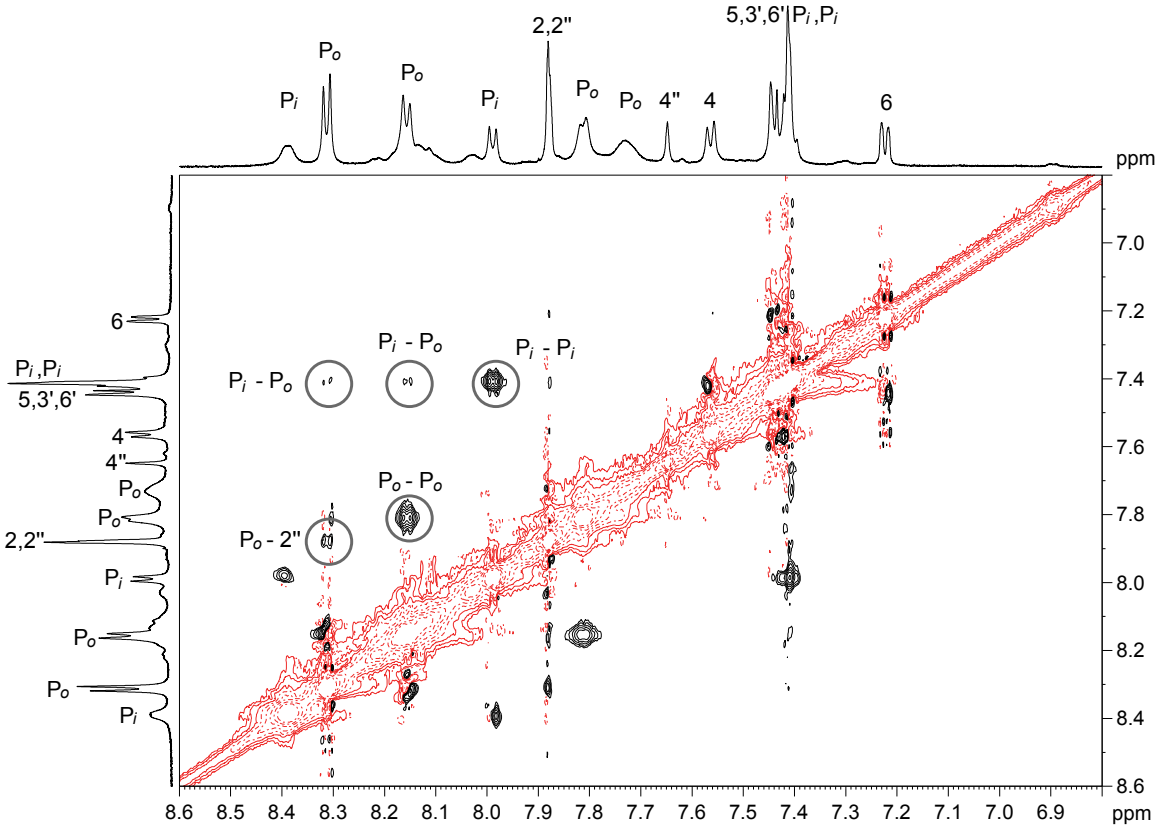

Figure 28. $^1H,^1H$-2D-ROESY NMR spectrum of **33** in [D_8]THF at 328 K ($c = 4 \times 10^{-4}$ M, 600 MHz). Signals which are marked by circles correspond to cross couplings that are not present in the $^1H,^1H$-2D-COSY NMR spectrum (Figure S10).

2D-HMBC NMR spectrum in Figure S12) and PBI **33** (Figure S13; for the 2D-HMBC NMR spectrum, see Figure S14) in [D8]THF.

DOSY NMR spectroscopic studies were performed to assess the molecular dimensions of both foldamers (Figures 29 and 30). For folda-dimer **32** in [D8]THF at 298 K (Figure 29), a

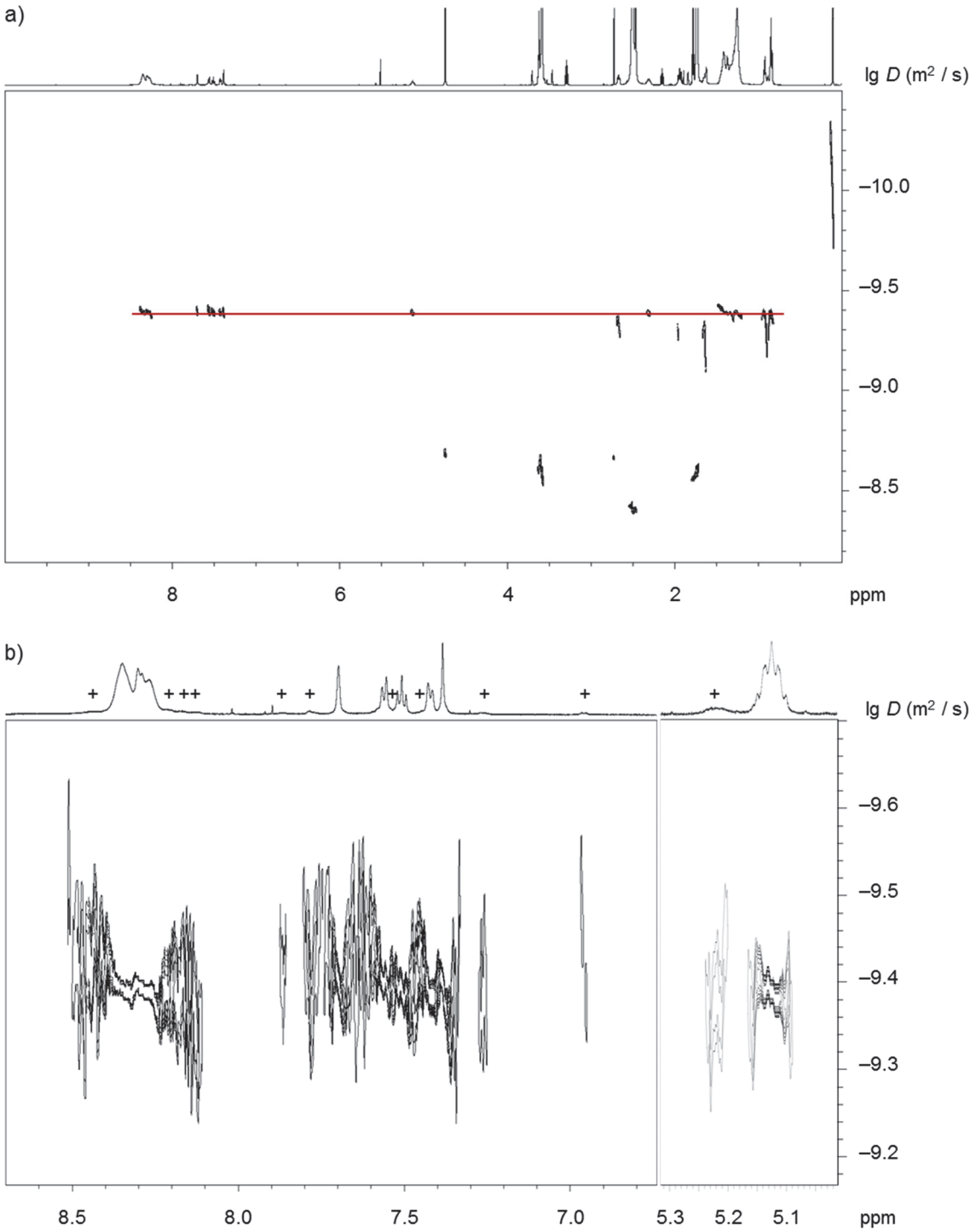

Figure 29. a) DOSY NMR spectrum (600 MHz) of folda-dimer **32** in [D8]THF ($c = 10^{-4}$ M) at 298 K. The red line indicates the signals arising from folda-dimer. b) Magnified regions of aromatic (8.7–6.75 ppm) and aliphatic protons (5.32–5.01 ppm). Signals arising from the minor species are labelled with plus symbol (+).

diffusion coefficient (D) of 6.3×10^{-10} m^2 s^{-1} was estimated, which can be used according to the Stokes-Einstein equation (*cf.* Equation 2)[149] to estimate the molecular dimension.

$$D = \frac{k_B T}{6\pi\eta r} \qquad \textbf{(Eq. 2)}$$

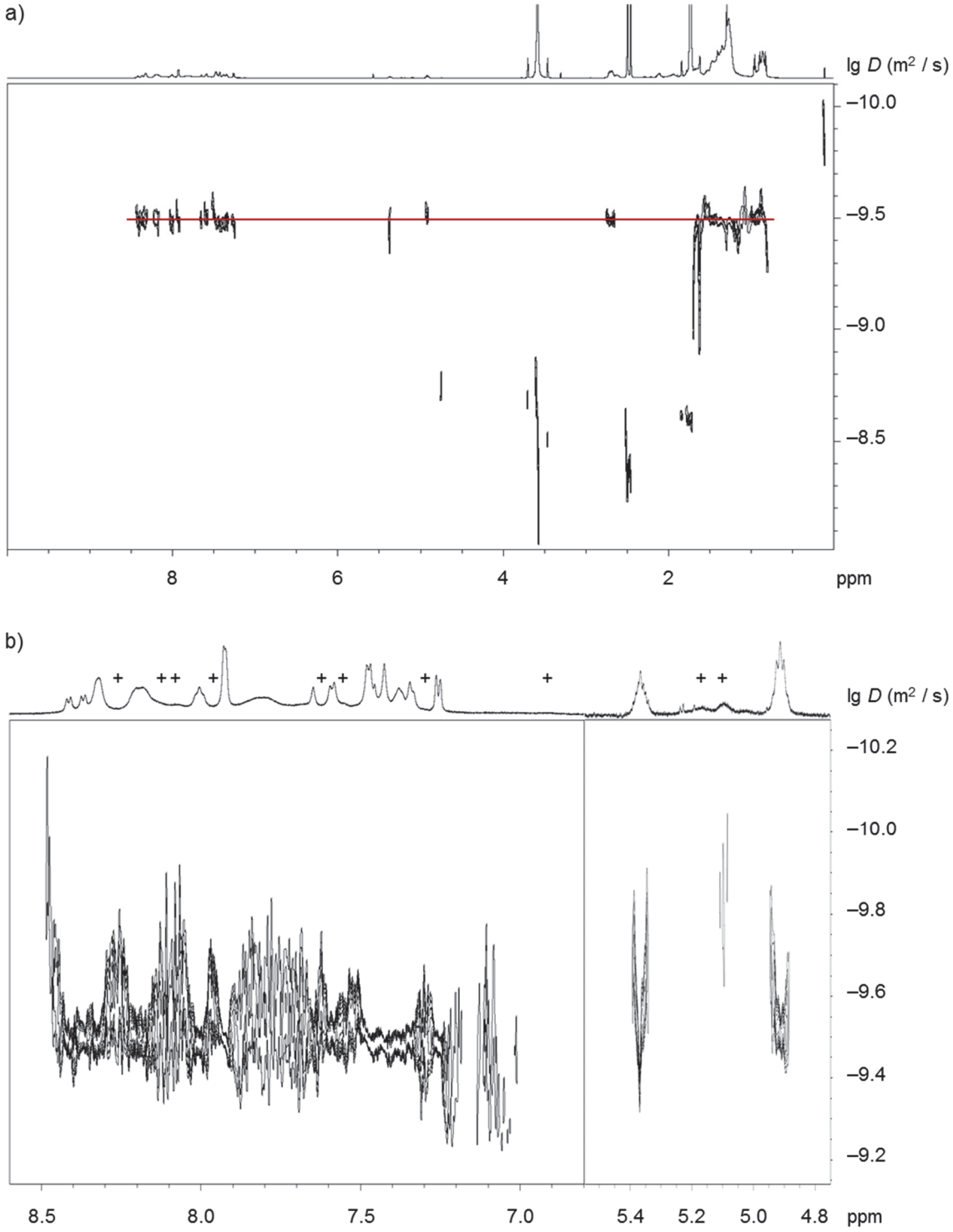

Figure 30. a) DOSY NMR spectrum (600 MHz) of folda-trimer **33** in [D$_8$]THF ($c = 10^{-4}$ M) at 293 K. The red line indicates the signals arising from folda-trimer b) Magnified regions of aromatic (8.6–6.8 ppm) and aliphatic protons (5.5–4.75 ppm). Signals arising from the minor species are labelled with plus symbol (+).

In Equation 2 k_B is the Boltzmann constant, η the solvent viscosity, and r the radius of the hypothetically spherical molecule. The evaluated diffusion coefficient corresponds to a diameter of 22.6 Å for **32** in [D8]THF. For the folded state of dimer **32**, the geometry optimized structure revealed a distance of 22.4 Å between the first carbon atom of the imide substituent and the alkyl chain on the middle phenylene spacer unit, which is in good accordance with the experimentally obtained value of 22.6 Å. Notably, the other set arising from the weaker NMR signals shows almost the same diffusion behavior, which is further in accordance with a second folded conformer of PBI **32**. For folda-trimer **33** a diffusion coefficient of 3.3×10^{-10} m^2 s^{-1} was determined by DOSY NMR spectroscopy in [D8]THF at 293 K (Figure 30). Based on this data, a diameter of 27.8 Å is calculated for the folded trimer **33**, which is, as expected, slightly higher than the value determined for **32** in [D8]THF. As in the case of PBI **32**, similar diffusion constants are obtained for the NMR signal set with low intensity for PBI **33**. Therefore, both signal sets of **33** appear to correspond to the same state, *i.e.* the folded state.

3.4. Theoretical Studies on the Conformational Preferences

3.4.1 Determination of Starting Structures and Evaluation of a Reliable Method for Molecular Dynamics Simulations

The NMR spectroscopic studies revealed that in $CHCl_3$ the PBI units of folda-dimer **32** and folda-trimer **33** adopt a larger conformational space due to good solvation of the aromatic scaffolds, while in THF the conformational diversity is appreciably reduced due to intramolecular folding into helically arranged π-stacks. To obtain more detailed information on the energetically most favorable structures for the PBI systems **32** and **33** and thus to corroborate the results of NMR studies, calculations were performed by applying various methods. First the force fields OPLS-AA, AMBER, and MM3* were used to determine the equilibrium structures of **32** and **33**. The resulting structures, which are summarized in Figure 31, indicate strong variations depending on the force fields. The force fields MM3* and AMBER predicted folded structures, while the OPLS-AA force field computed open structures as the most favorable conformers.

In the next step, the structural moieties responsible for flexibility in dimer **32** and trimer **33** were identified and analyzed in terms of their impact on the overall energy. The most flexible linkages, which are capable of driving the molecules to folded or unfolded states, are the single and triple bonds between the inner imide moieties and the phenylene imide

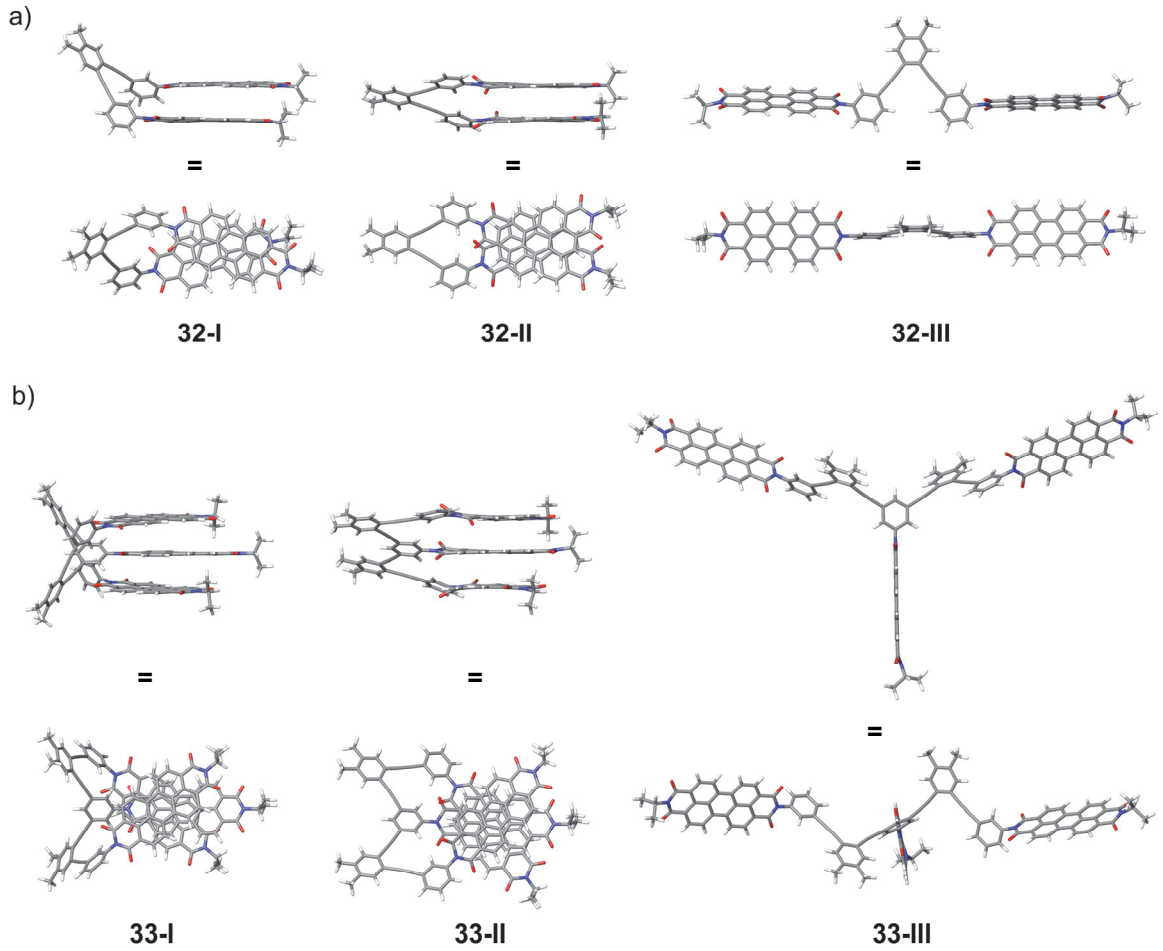

Figure 31. Geometry optimized structures (upper rows, side views; lower rows, top views) of a) folda-dimer **32** and b) folda-trimer **33** obtained by different force field optimizations (**I**, MM3*; **II**, AMBER; **III**, OPLS-AA).

substituents as well as in the tolan subunits as schematically depicted for the reference PBI **31** (Figure 32a). To test the accuracy of various approaches, the relative energies of gradual distortion (0° to 180°) of dihedrals for the related, simple model compounds tolan and *N*-phenyl-1,8-naphthalimide of different force fields, semi-empirical, and DFT approaches were compared (Figure 32b–d). On the basis of these theoretical studies, the use of the semi-empirical PM6-DH2[150,151] approach to perform molecular dynamics (MD) simulations for **32** and **33** to elucidate structural preferences and the flexibility of the systems seems to be most promising.

PM6-DH2 includes dispersion forces and should be sufficiently flexible for the description of unusual conformations, which might be energetically overestimated by force field approaches. In addition, the PM6-DH2 approach is an ideal compromise between accuracy and efforts. As starting structures for the MD simulations the minimum structures predicted by the force fields (Figure 31) were used.

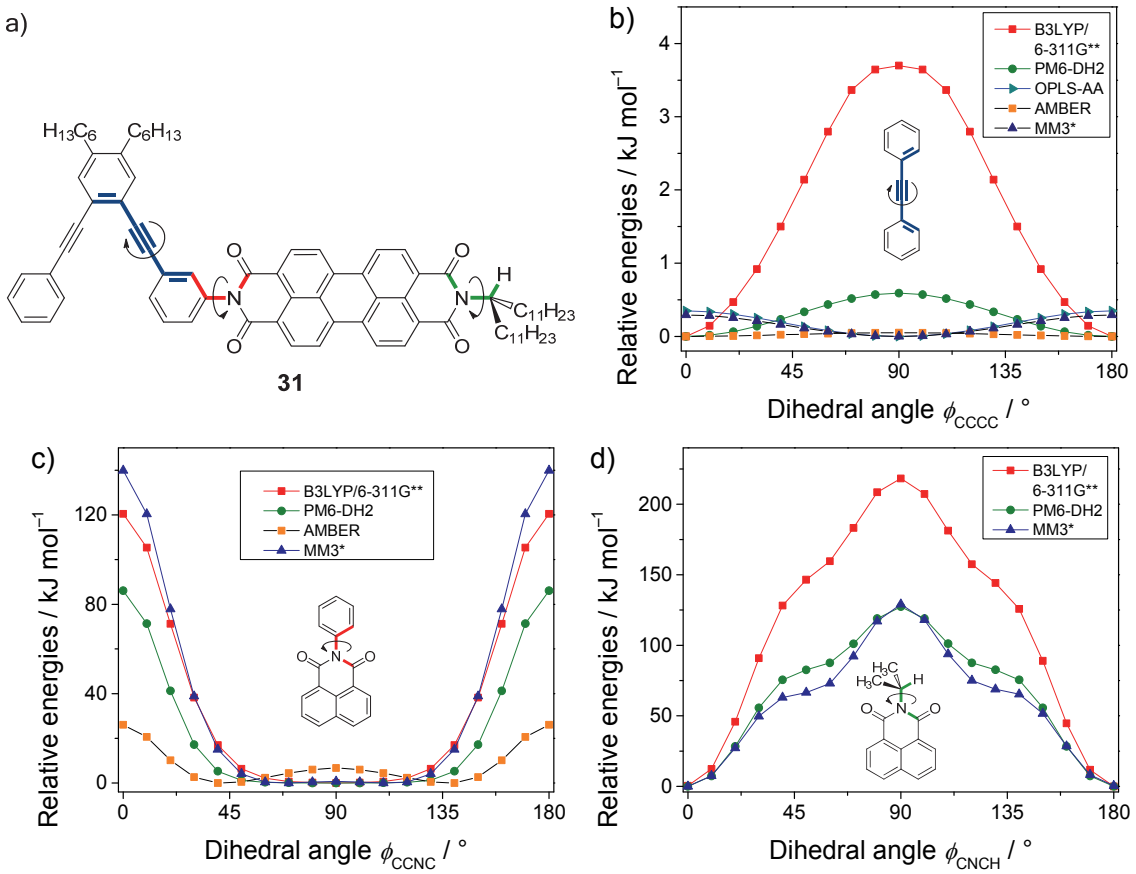

Figure 32. a) Schematic illustration of potential flexible dihedral angles ϕ_{CCCC} (blue), ϕ_{CCNC} (red), and in addition ϕ_{CNCH} (green) in reference compound PBI **31**. Relative energies of simple model compounds b) tolan, c) *N*-phenyl-1,8-naphthalimide, and, for comparison, d) *N*-(*iso*-propyl)-1,8-naphthalimide in respect to the internal dihedral motion around the indicated bonds investigated with different force-field, semi-empirical, and DFT methods.

3.4.2 Molecular Dynamics Simulations

The energy distributions given in Figure 33 reflect the relative energies of the minima, which are obtained when the MD frames of the last 50 ps of the MD simulations are optimized. The abbreviation **i-iii** denotes that the MD run started from the structures **I-III**, respectively. The energies summarized in Figure 33 are relative to the lowest energy structures of folda-dimer **32** and folda-trimer **33**, respectively. All MD runs were performed for the gas phase.

The MD simulations revealed the following important results: First, both unfolded conformations **III** of PBI **32** and **33** already form completely folded structures after a time period of 8 ps (PBI dimer **32**) and 25 ps (PBI trimer **33**) (see conformations **iii** in Figure 34), implying that the intramolecular folded arrangements are much more favored than the unfolded conformations. For dimer **32** and trimer **33** these folding processes from **III** to **iii** can nicely be visualized by the distance narrowing from 26 and 23 Å (in unfolded conformations **III**) to around 3.7 and 3.6 Å (in folded conformations **iii**) of adjacent PBI

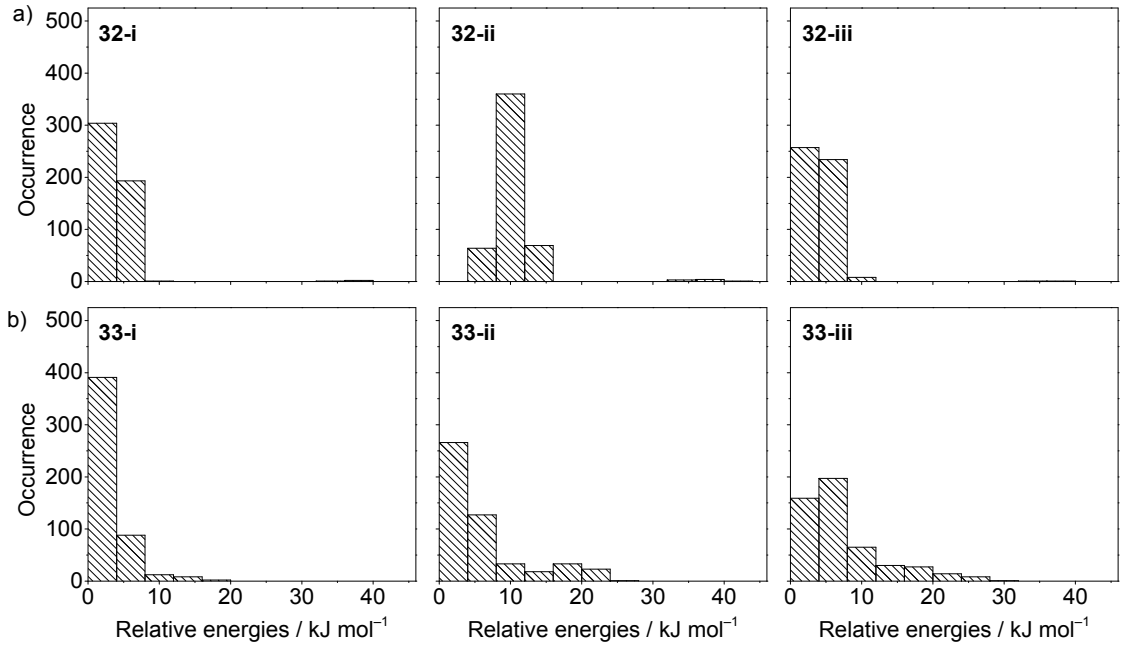

Figure 33. Relative energies in kJ mol^{-1} of a) folda-dimer **32** and b) folda-trimer **33** obtained from molecular dynamics simulations (PM6-DH2, 300 K, 50 ps) and subsequent local optimization with PM6-DH2.

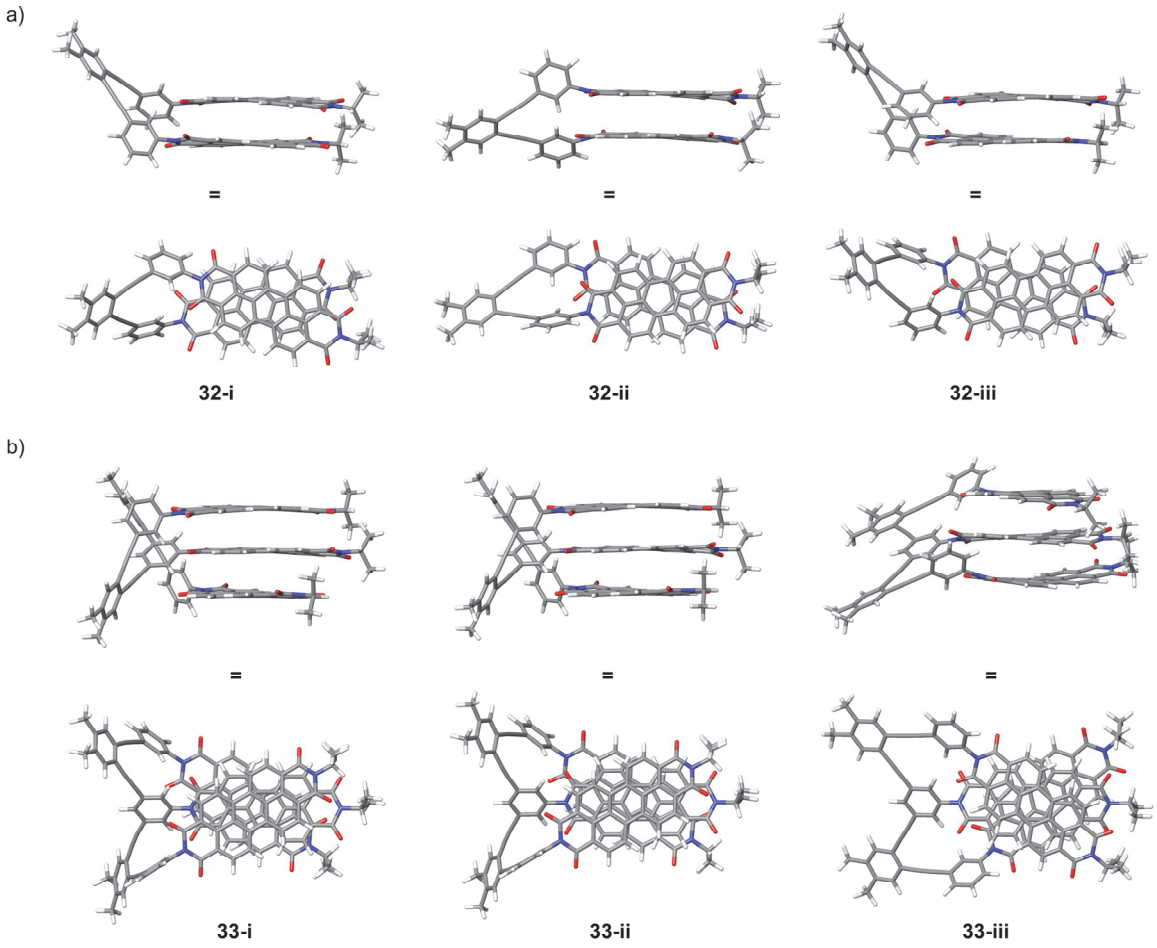

Figure 34. Lowest energy structures (upper rows, side view; lower rows, top views) of a) PBI dimer **32-i** to **32-iii** and b) PBI trimer **33-i** to **33-iii** obtained after MD simulations and local optimization with PM6-DH2.

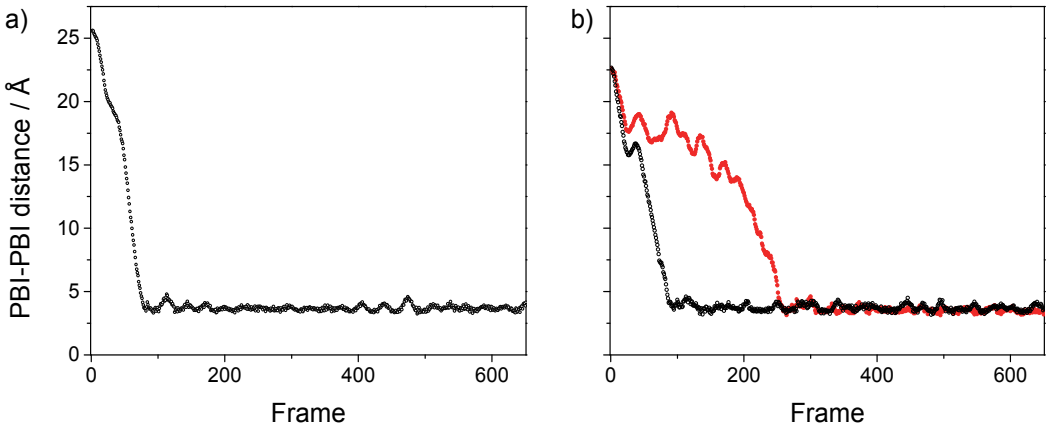

Figure 35. Center-to-center distances (PBI centers) of initially unfolded conformations a) **32-III** (black circles) and b) **33-III** (black and red circles) obtained by MD simulations with PM6-DH2 over a time range of 65 ps (= 650 frames) at 300 K.

centers in **32** and averaged for **33** as shown in Figure 35. Although gas phase calculations cannot take into account explicit solute–solvent interactions, *i.e.* the difference between $CHCl_3$ and THF for the folding process, the outcome of the MD indicates the presence of very flexible bridging units in PBI **32** and **33**. For the DFT-D geometry optimized structure of the unfolded conformation **32-III-c** (Figure 36), an energy difference to **32-I-a** of 165 kJ mol^{-1} was computed on the B97D/STO-3G[152-154] level of sophistication. Notably, this value is very similar to the binding energy of two PBI monomers forming the energetically most favorable π–π-stacked dimer (125 kJ mol^{-1}, BLYP-D/TZV(P)).[103] The higher energy difference obtained in the present computations can be reduced to basis set superposition errors of the smaller STO-3G basis. The small variation in the calculated values strongly underlines that the phenylene ethynylene backbone is sufficiently flexible that both PBI units are not hindered in the formation of favorable π-stacked structures. In the case of PBI dimer **32-III**, the folding leads to the conformation **32-iii**. The latter one is very similar to the conformation **32-i** obtained from **32-I**, *i.e.* their energy difference is 0 kJ mol^{-1}, with **32-i** being almost identical with the MM3* geometry optimized structure **32-I** (ΔE (**32-I** – **32-i**) = 4 kJ mol^{-1}). Notably, the relative energies of all structures adopted

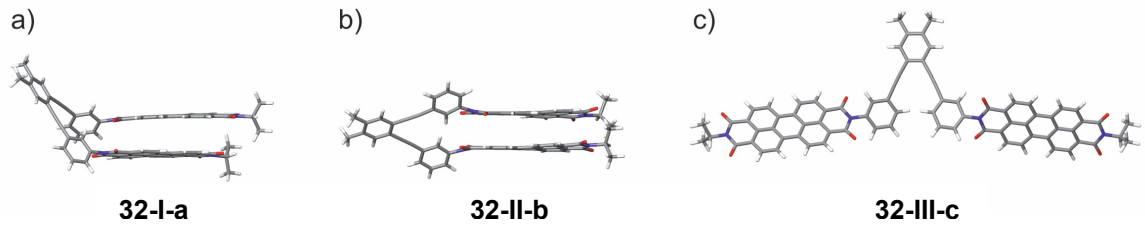

Figure 36. Geometry optimized structures of folda-dimer **32**: both folded conformations a) **32-I-a** and b) **32-II-b** as well as c) the unfolded state **32-III-c** obtained by the B97D/STO-3G approach. Cartesian coordinates of all 3 structures are listed in Tables S2, S3, and S4 (subchapter 6.5).

during MD simulations (after local optimizations with PM6-DH2 of the last 50 ps structures) of **32-i** and **32-iii** are in narrow distribution (0–8 kJ mol^{-1}) as the structures are nearly congruent. In contrast, the MD simulation starting from **32-II** leads to structure **32-ii**. It differs from **32-i** and **32-iii** by the orientation of the bridge relative to the PBI planes. The average energies of the minima obtained by optimizing the corresponding MD frames are shifted to somewhat higher values (Figure 33a, 8 kJ mol^{-1}). This indicates that the minima **32-II** and **32-ii** are separated from the other minima (**32-I**, **32-i**, and **32-iii**), by barriers which are not crossed during the MD simulations.

For the folda-trimer **33**, the MD simulations gave similar results as for folda-dimer **32**. Also for the conformation **33-i** the relative energies are within 0 and 4 kJ mol^{-1}, which suggests that the ideal conformation has already been adopted. Although conformations **33-i** and **33-ii** possess virtually the same spatial arrangement after approximately 8 ps MD simulation and local optimization, the relative energies of structures from conformation **33-ii** show a wider distribution spreading over 0 to 24 kJ mol^{-1}. However, the main portion (~80%) of the structures is again within 0 and 4 kJ mol^{-1} (see Figure 33b). For the conformation **33-iii**, which is obtained from the MD simulation starting with the unfolded conformation **33-III**, the primarily populated structures are higher in energy (energy difference about 4 kJ mol^{-1}) and the lowest energy conformation **33-iii** resembles more the nonoptimal structure of **33-II**.

These results explain the appearance of a second low-populated signal set observed in ^{1}H NMR spectra of folda-dimer **32** and folda-trimer **33** in [D$_8$]THF most expressive at higher temperatures (see Figures 19 and 26, bottom spectra). Because **32-i** and **32-ii** are nearly identical to **32-I** and **32-II**, further considerations focus on these two structures. The schematic energy profile as well as the suggested dynamic process caused by backbone flapping between conformation **32-I** and **32-II** are shown in Figure 37. Notably, the conformations **32-I** and **32-I'** with the backbone directed upwards and downwards, respectively, are chemically and energetically equivalent and thus are not distinguishable by NMR spectroscopy.

The energy difference between **32-I** and **32-II** is computed to approximately 4 kJ mol^{-1} (by PM6-DH2), which enables a detectable population of **II** by NMR. Using geometry optimizations on the B97D/STO-3G level of sophistication an energy difference between **32-I-a** and **32-II-b** (see Figure 36) of about 8 kJ mol^{-1} is obtained. Accordingly, the calculated values are in reasonable agreement with the NMR data (*ca*. 6 kJ mol^{-1}).

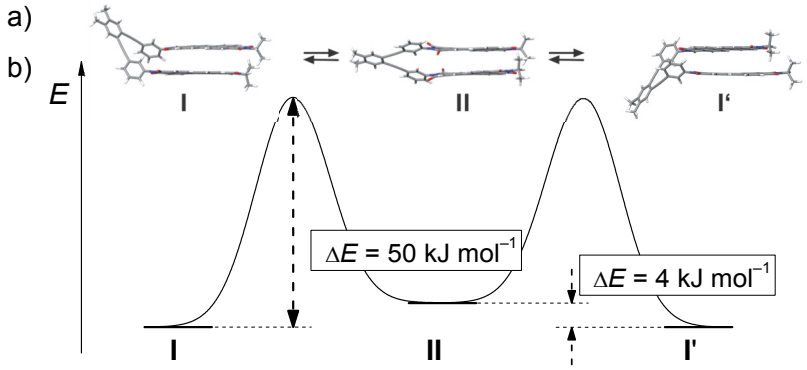

Figure 37. a) Schematic representation of the dynamic interconversion between conformations **I**, **II**, and **I'** of folded PBI dimer **32** caused by flapping of the phenylene ethynylene scaffold. b) Schematic illustration of the energy profile for the dynamic interconversion of the flapping with relative energies calculated by local optimization (PM6-DH2) of gradually distorted phenylene spacer unit in the scaffold (*cf.* Table S5 and S6).

For folda-dimer **32**, a subsequent distortion of one phenylene spacer in conformation **II** was used to estimate the energy barrier of the flapping process. For this approach, gradually distorted structures were locally optimized using PM6-DH2 (Table S5). Small distortions did not significantly change the relative energies of the system since the conformation **II**, especially the mutual orientation of both PBI moieties did not show a large impact. The barrier of the flapping process was calculated to be about 50 kJ mol^{-1} (Figure 37b). This value might be significantly underestimated as compared to the related energy barrier of a swallow tail imide substituent. For the latter one, the energy barrier was computed to be approximately 33 kJ mol^{-1} (Table S6) using local optimization on PM6-DH2 level, which is almost the half of the experimental value of 64 kJ mol^{-1} based on temperature-dependent NMR analysis (Figure 23). Accordingly, the barrier for the flapping process is expected to be about 100 kJ mol^{-1}, which explains why no coalescence of NMR signals of the major and the minor conformations of backbone-flapped folded species of PBI **32** could be observed in the accessible temperature regime (Figure 19). The same situation holds true for PBI **33** where the two conformations **33-i** and **33-iii** (Figure 33d) exhibit similar energies and the NMR experiment (Figure 26) also revealed the coexistence of two conformations that show no coalescence in the accessible temperature range in [D$_8$]THF.

3.4.3 Estimation of PBI–Solvent Interactions

Calculations in which the solvent is approximated by a continuum approach (COSMO) predict that folda-dimer **32** and folda-trimer **33** fold in $CHCl_3$ and THF. Hence, the difference in the folding behavior (folding in THF but not in $CHCl_3$) must stem from molecular effects. For a definitive answer the folded systems **32** and **33** have to be simulated in sufficiently large solvent boxes. However, because the corresponding simulations are

very costly and time-consuming only rough estimates were performed to get some more insights into the underlying reasons.

Entropic effects will favor the folded conformations of folda-dimer **32** and folda-trimer **33** in $CHCl_3$ and THF because solvent molecules are set free by the folding processes. Hence, the enthalpy of dissolution should be one important factor for the different behavior. Assuming that the enthalpy of dissolution is mainly determined by the first solvation shell, it can be roughly estimated by the scheme depicted for **32** in Figure 38. For the unfolded structure both PBI chromophores can be completely solvated (PBI–solvent full), while for the folded conformer only one side is solvent-accessible (PBI–solvent half). Hence, to estimate enthalpy differences between the folded and the unfolded situation the nonsolvated conformer was used and the binding energy of the respective first solvation shells of the chromophore was added. The solvation energies are approximated as the differences between the binding energy of the optimized solvated chromophore-solvent cluster (first solvation shell) and the binding energy of the corresponding optimized pure solvent-molecule cluster. The binding energy is always determined as the energy difference between the full cluster and the summation of the energies of its parts.

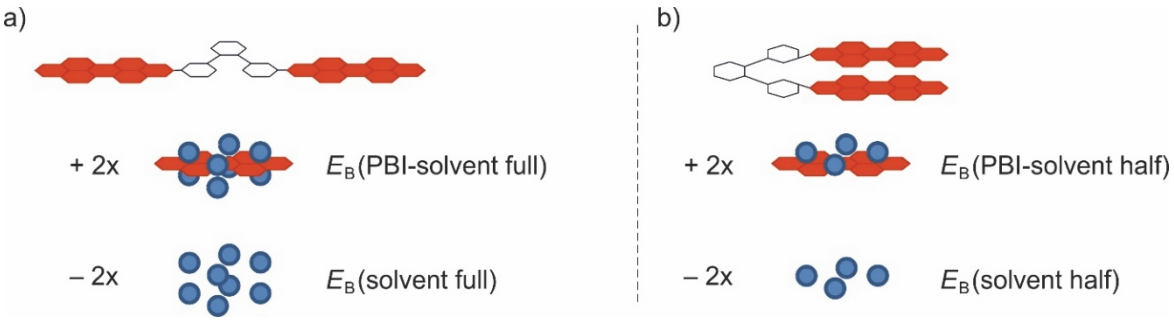

Figure 38. Scheme used to estimate the enthalpic contributions to the solvation of folda-dimer **32** in the a) unfolded and b) folded state.

To achieve knowledge about the geometrical structure of the first solvation shells, clusters in which the PBI is surrounded by one solvent molecule were employed. First the 4 different $CHCl_3$ and 5 various THF arrangements depicted in Figure 39 were investigated. The values predicted by B3LYP-D3/SVP[155,156] level of sophistication are given in Table 2. While the orientation of $CHCl_3$ seems to be less important for the PBI–solvent systems, the orientation **THF-5** binds considerably stronger than the other orientations (**THF-1** to **THF-4**). In the second step, possible mutual orientations of PBI and solvent molecules by varying the position of one solvent molecule on the PBI surface were evaluated. For this

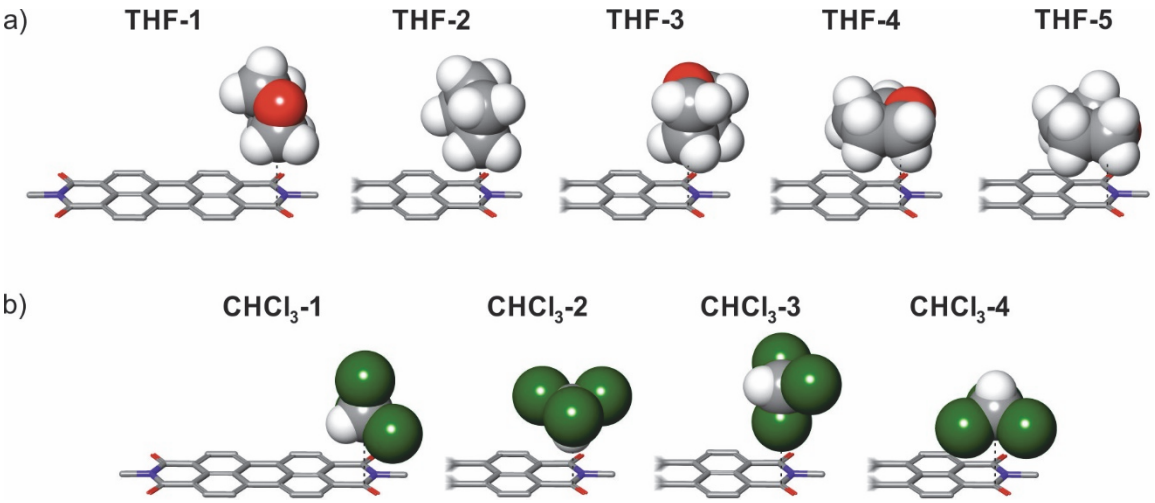

Figure 39. Initial solvent alignments for a) THF (**THF-1** to **THF-5**, upper row) and for b) $CHCl_3$ (**$CHCl_3$-1** to **$CHCl_3$-4**, lower row) on the PBI plane investigated by B3LYP-D3/SVP geometry optimizations. The thin, dashed lines connect the two atoms (of the solvent molecule and the perylene C-3 atom) vertically positioned on top of each other.

approach, $CHCl_3$ in the alignment **$CHCl_3$-1** and THF in alignment **THF-5** were deposited on one quarter of the PBI molecule (including the 9 different starting positions, which are labelled in Figure 40a) and optimized. The used orientations represent all possible positions due to symmetry operations. For $CHCl_3$, four positions which are almost equally in energy (–45 to –47 kJ mol^{-1}) forming a line on the PBI plane as indicated in Figure 40b were discovered. For THF, one predominant location on the center of the imide ring (–55 kJ mol^{-1}) and two further positions (–44 and–49 kJ mol^{-1}) were found (Figure 40c). Based on these findings the first solvation shell of a PBI chromophore with both solvents was imitated. In total 16 $CHCl_3$ molecules but only 8 THF molecules could be surrounded around both sides of one PBI chromophore (Figure 41). If more solvent molecules were added the second solvent shell began to form. The various binding energy contributions

Table 2. Relative energies of geometry optimized (B3LYP-D3/SVP) PBI–solvent systems; starting structures are shown in Figure 39.

Alignments PBI–THF	E[a]	Alignments PBI–$CHCl_3$	E[a]
THF-1	–26	**$CHCl_3$-1**	–46
THF-2	–44	**$CHCl_3$-2**	–46[b]
THF-3	–29	**$CHCl_3$-3**	–46[c]
THF-4	–34	**$CHCl_3$-4**	–46
THF-5	–55	–	–

[a] In kJ mol^{-1}. [b] Final alignment of $CHCl_3$ similar as in **$CHCl_3$-1**. [c] Final alignment of $CHCl_3$ similar as in **$CHCl_3$-4**.

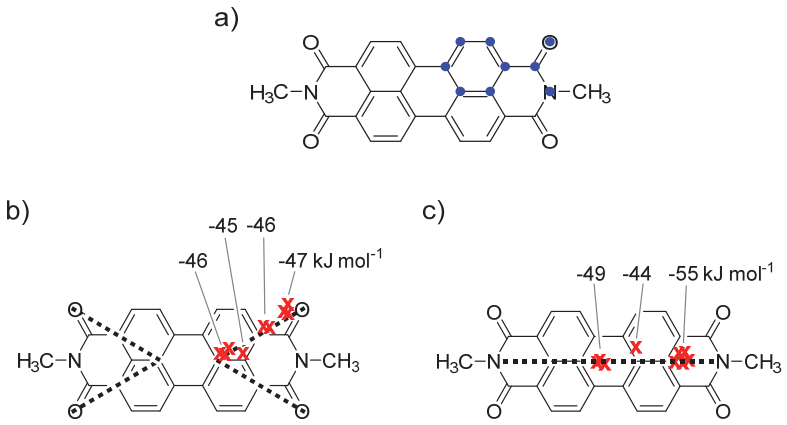

Figure 40. a) Starting points of geometry optimizations of the PBI–solvent systems (blue points indicate the position of the carbon atom of $CHCl_3$ or the center of the heterocycle on top of the PBI plane). b), c) Geometry optimized (B3LYP-D3/SVP) PBI–solvent alignments with b) $CHCl_3$ and c) THF (red crosses indicate the final position of the b) carbon atom and c) the center of the heterocycle on top of the PBI plane). For individual or merged places marked by red crosses the relative energy is listed. The dashed lines represent the extrapolated best positions for PBI–solvent ensembles on the entire PBI plane.

discussed in Figure 38 are summarized in Table 3. For folda-dimer **32** solvated by THF, the energy of the unfolded conformer can be set to zero because only differences between the folded and the unfolded states are of interest. The binding energy of the first THF solvation shell around two isolated PBI moieties as in the unfolded state is –268 kJ mol^{-1}. This value is the sum of a binding energy for the completely solvated PBI–THF clusters of –418 kJ mol^{-1} (2 PBI moieties with 8 THF molecules, respectively) and the binding energy of the respective optimized solvent molecule clusters consisting each of 8 THF molecules (+284 kJ mol^{-1}). Hence, in total a binding energy of –268 kJ mol^{-1} is estimated for the unfolded state of **32** in THF.

For the folded conformation, the inner parts of the chromophores cannot be solvated so that smaller chromophore-solvent clusters result. The corresponding chromophore-solvent

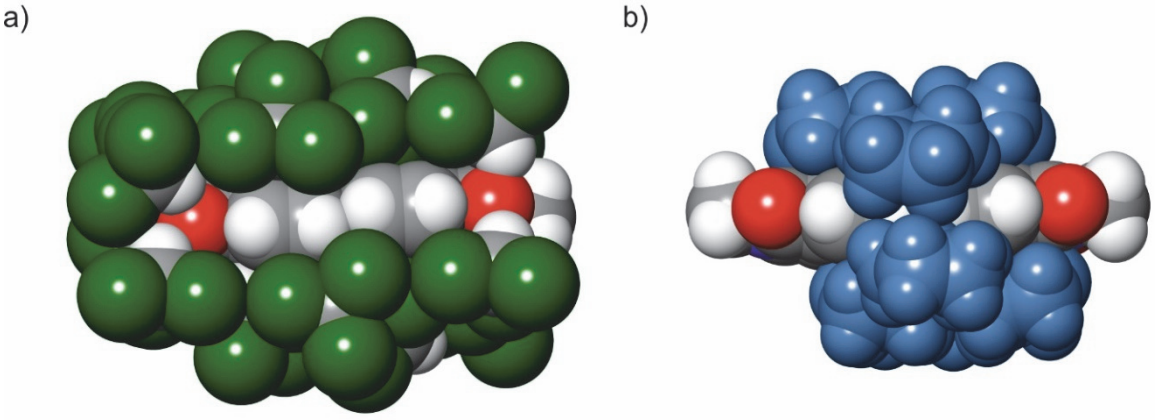

Figure 41. Geometry optimized structures of a *N*,*N*'-dimethyl PBI monomer with a) 16 $CHCl_3$ molecules and b) 8 THF molecules mimicking the first solvation shell.

Table 3. Individual binding energy contributions (E_B) and energies[a] of folded and unfolded states of folda-dimer **32** in the respective solvent as schematically depicted in Figure 38.

	$CHCl_3$	THF
E_B (PBI–solvent full)	–935	–418
E_B (PBI–solvent half)	–454	–221
E_B (solvent full)	+714	+284
E_B (solvent half)	+307	+111
E_{Solv}[b] (**32** unfolded)	–440	–268
E_{Solv}[b] (**32**, folded)	–434	–358

[a] In kJ mol^{-1}. [b] For calculating E_{Solv} the relative energy difference (138 kJ mol^{-1}) between the folded and unfolded state of folda-dimer **32** in the gas phase determined by geometry optimization (B3LYP-D3/SVP) was considered.

cluster (2 PBIs with 4 THF molecules on one side, respectively) possesses a binding energy of –221 kJ mol^{-1} from which the binding energy of the corresponding two solvent clusters (each with a total number of 4 THF molecules) has to be subtracted (+111 kJ mol^{-1}). Hence, for the folded conformer the first solvation shell has a binding energy of only –220 kJ mol^{-1}. However, to get the difference between the folded and the unfolded state, the binding energy between both chromophores has to be added. To estimate this contribution the energy difference between the folded and the unfolded conformer as computed in the gas phase (–138 kJ mol^{-1}) was used. Adding everything together the folded conformer has a binding energy of about –358 kJ mol^{-1}, *i.e.* it is lower in energy than the unfolded one by 90 kJ mol^{-1}. This value is, of course, grossly overestimated because the dynamic effects are neglected. In this static picture, each solvent molecule adopts a position which is optimal in respect of enthalpy of solvation. Due to the dynamic of the solvent shell, the various solvent molecules will take less optimal positions most of the time. Nevertheless, the folding process is also favored by entropic effects. Along the same line of arguments the unfolded state (–440 kJ mol^{-1}) becomes more favorable than the folded one (–434 kJ mol^{-1}) for $CHCl_3$ (Table 3). Obviously, the difference to THF results because PBI can be surrounded by 8 $CHCl_3$ molecules but only 4 THF molecules per one side.

3.5. Folding Properties in the Excited State

Optical excitation of folda-dimer **32** and folda-trimer **33** afford excited molecules, whose initial conformational distribution equals the one given in the ground state (Franck-Condon

principle). Subsequently, however, the molecules may relax into energetically more favorable excited state conformations such as excimers[38,157,158] (where two PBI units are stacked in a more coplanar arrangement) or interact with the electron-donating phenylene ethynylene backbone.[89,159] To elucidate these processes steady-state and time-resolved fluorescence as well as transient absorption (TA) spectroscopy experiments were performed.

3.5.1 Steady-State and Time-Resolved Fluorescence Spectroscopy†

The fluorescence emission and excitation spectra as well as the absorption spectra of folda-dimer **32** and folda-trimer **33** in $CHCl_3$ and THF are shown in Figure 42. The emission spectrum of folda-dimer **32** in $CHCl_3$ consists of two sharp bands located at 537 and 580 nm, which are hypsochromically shifted to 533 and 575 nm in THF, respectively (Figure 42a,b).

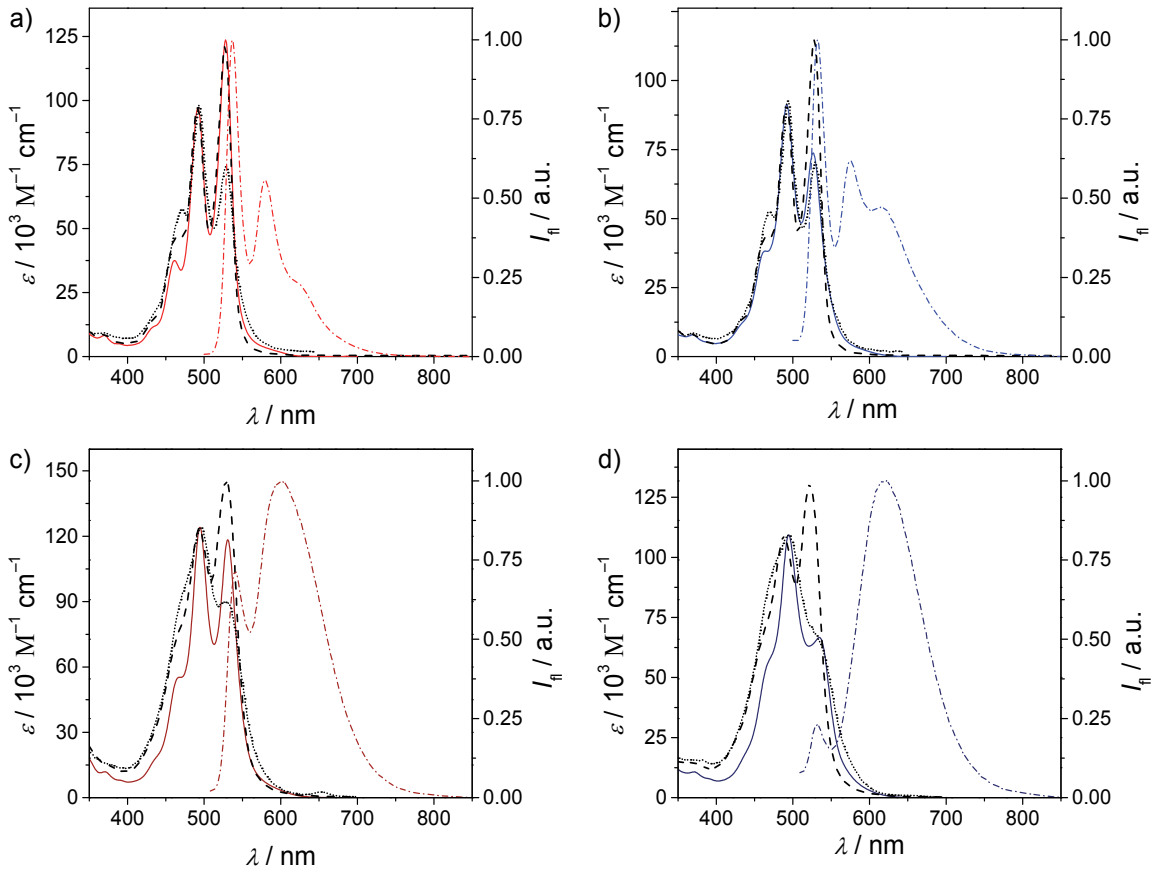

Figure 42. Absorption (solid line), fluorescence emission (λ_{exc} = 480 nm; dash-dotted line), and fluorescence excitation spectra (λ_{det} = 530 nm, dashed line; λ_{det} = 650 nm, dotted line) of **32** in a) $CHCl_3$ and b) THF, and **33** in c) $CHCl_3$ and d) THF at room temperature. The fluorescence excitation spectra are normalized to the absorption spectra at approximately 490 nm.

† Time-resolved fluorescence experiments and analyses were performed by M. Sc. Minjung Son at the Spectroscopy Laboratory for Functional π-Electronic Systems (FPIES) at Yonsei University, Seoul, South Korea.

Moreover, a strong third band was observed at 615 nm in THF, while a small, barely recognizable shoulder appears in $CHCl_3$ at 630 nm. For each solution, fluorescence excitation spectra were recorded at the detection wavelengths (λ_{det}) of 530 and 650 nm. In both solvents, the excitation spectra of folda-dimer **32** for λ_{ex} = 530 nm perfectly resemble the absorption spectrum of **32** in $CHCl_3$, whereas the ones for λ_{det} = 650 nm match with the absorption spectrum of folda-dimer **32** in THF. This result suggests that the observed emission can be related to the ground state conformational populations of unfolded and folded molecules, *i.e*. similar conformations prevail for ground state and excited molecules. The fluorescence spectra of folda-trimer **33** in $CHCl_3$ and THF (Figure 42c,d) show strong changes as compared to those of folda-dimer **32** or reference compounds **30** and **31** (Figure S5). The emission spectrum of PBI **33** in $CHCl_3$ is composed of a broad band with a maximum at 600 nm and a smaller signal at 540 nm, in which the former band could be ascribed to the emission of excited folded molecules. Upon change of solvent from $CHCl_3$ to THF both bands are slightly shifted (532 and 617 nm, respectively) and the intensity of the smaller band significantly decreased, which indicates the prevalence of folded molecules. The fluorescence excitation spectra of **33** for λ_{det} = 530 nm in $CHCl_3$ and THF again resemble the absorption spectra of unfolded molecules in $CHCl_3$, while those at λ_{det} = 650 nm resemble the absorption spectrum of **33** in THF. Moreover, the fluorescence quantum yields (Φ_{fl})[160] were determined and were collected together with other significant optical properties of folda-dimer **31**, folda-trimer **33**, and reference compounds **30** and **31** in Table 4.

As shown in Table 4, the fluorescence quantum yields of monomeric PBI dye **30** are close to unity (around 97%), which is in accordance with the generally observed outstanding fluorescence of monomeric PBI dyes. For the reference compound **31** that bears a phenylene ethynylene substituent, the quantum yields are significantly reduced to 21% in $CHCl_3$ and 36% in THF, indicating another deactivation process than fluorescence. This nonradiative relaxation might be related to an intramolecular electron transfer process[89,92,135,161,162] between the electron-rich phenylene ethynylene backbone and the electron-deficient PBI chromophore which becomes more efficient in $CHCl_3$ than in THF (see subchapter 3.5.2).

For folda-dimer **32** and folda-trimer **33**, a contrasting behavior is observed, *i.e*. the Φ_{fl} values are always lower in THF as compared with those in $CHCl_3$, which suggests the prevalence of a second radiationless deactivation pathway in THF induced by folding into less emissive excimers.[163-165] In THF this process is obviously more prominent as the individual dye molecules are already in a π-stacked, folded conformation in the ground state. Likewise, the

Table 4. Excited states properties of folda-dimer **32** and folda-trimer **33** as well as those of the reference compounds PBI **30** and PBI **31** in $CHCl_3$ or THF.

PBI	Solvent	λ_{em} [nm][a,b]	Φ_{fl} [%][a,c]
30	$CHCl_3$	532, 574, 622	97 ± 3 (89)
	THF	531, 571, 618	97 ± 6 (94)
31	$CHCl_3$	537, 579, 627	21 ± 1 (17)
	THF	531, 571, 617	36 ± 5 (38)
32	$CHCl_3$	537, 580, 630 (sh)[d]	28 ± 2 (31)
	THF	533, 575, 615	16 ± 2 (16)
33	$CHCl_3$	540, 600	22 ± 2 (24)
	THF	532, 617	12 ± 1 (13)

[a] High dilution method ($OD_{max} < 0.05$) at room temperature. [b] $\lambda_{exc} = 480$ nm. [c] Under magic angle conditions ($\theta = 54.7°$), $\lambda_{exc} = 470–490$ nm; values in brackets are the results obtained from measurements without using polarizers. [d] sh = shoulder.

lower fluorescence quantum yields and more pronounced excimer emission of **33** as compared to **32** suggest that only a very minor portion of unfolded molecules are present in the excited state.

The time-resolved fluorescence decay profiles of folda-dimer **32** and folda-trimer **33** along with those of **30** and **31** as reference compounds were measured by using the time-correlated single photon counting (TCSPC) technique and their fitted fluorescence lifetimes are collected in Figure 43 and Table 5. In the case of monomeric PBI dye **31**, the observed transfer (PET) process from the electron-donating backbone to the electron-deficient PBI

Table 5. Time-resolved fluorescence decay profiles of investigated PBIs **30**, **31**, **32**, and **33** in $CHCl_3$ and THF.

PBI	Solvent	τ_1 [ns]	τ_2 [ns]	τ_3 [ns]
30	$CHCl_3$	–	3.9	–
	THF	–	4.0	–
31	$CHCl_3$	0.08	2.7	–
	THF	0.16	2.3	–
32	$CHCl_3$	0.12	2.7	20.0
	THF	0.16	2.0	20.0
33	$CHCl_3$	0.11	3.1	20.0
	THF	0.10	2.7	26.0

fluorescence lifetimes (2.7 ns in $CHCl_3$ and 2.3 ns in THF) were relatively short in both solvents as compared to those of **30** (3.9 ns in $CHCl_3$ and 4.0 ns in THF) and other PBI monomers.[58-61] In addition to the long decay components, shorter components with the time constants of 80 ps (81%) in $CHCl_3$ and 160 ps (36%) in THF were observed for PBI **31**, which are completely absent in the backbone-free monomer **30**. This can be attributed to the existence of a nonradiative pathway originating from the photoinduced electron core. Here the much higher amplitude value (81%) of the short time constant corroborates the

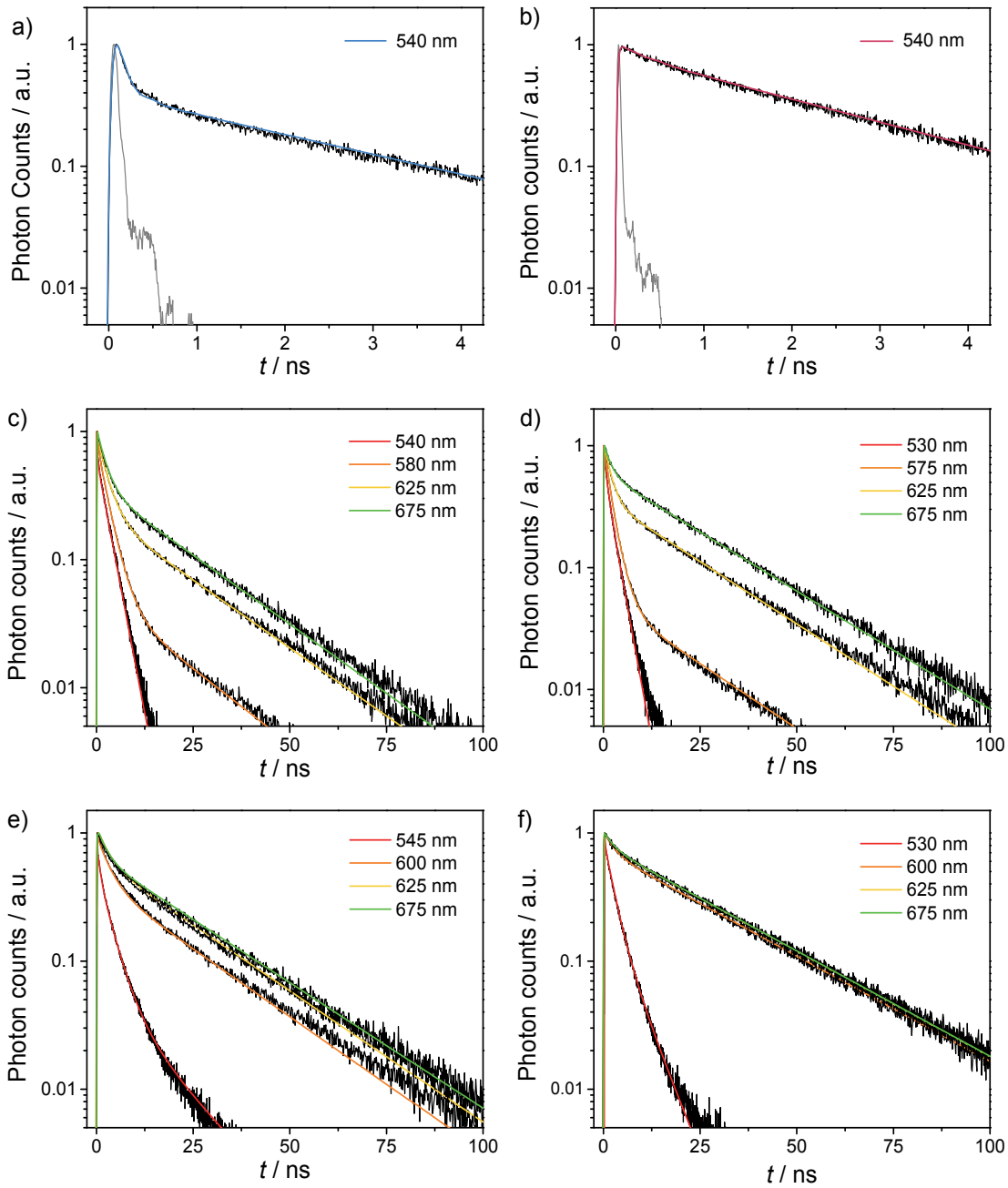

Figure 43. Time-resolved decay profiles of a), b) reference compound **31**, c), d) folda-dimer **32**, and e), f) folda-trimer **33** in chloroform (left graphs) and THF (right graphs) (λ_{ex} = 450 nm). Respective emission wavelengths (λ_{em}) are indicated in each graph. The instrumental response functions are shown in gray traces.

previous interpretation of the trends in fluorescence quantum yields that this process is more efficient in $CHCl_3$, *i.e.* in the extended form.

For folda-dimer **32** and folda-trimer **33**, fluorescent species with *ca*. 10-fold longer lifetimes (20–26 ns) grew dominant, which can be assigned as the enhanced lifetimes of molecules in relaxed excited states, *i.e.* excimer states.[163-165] In particular for the folded structure of **33** in THF, the relative amplitude of the long-lived species was found to be as high as 77% when the excimer emission band was directly probed. Meanwhile, when the 0-0 fluorescence peaks (530–540 nm) were monitored in **32** and **33**, short components with the time constants of approximately 100 ps were observed in all cases in addition to the singlet excited-state lifetimes of the PBI units (2.0–3.1 ns). The shorter components here can be related to the fast fluorescence quenching by the PET process as mentioned above.

3.5.2 Femtosecond Transient Absorption Spectroscopic Studies‡

In order to acquire an in-depth understanding of the fast dynamics responsible for the reduced fluorescence of the PBI foldamers, *i.e.* photoinduced charge separation (CS) and charge recombination (CR), femtosecond transient absorption (TA) spectroscopy was performed for **31**, **32**, and **33** in $CHCl_3$ and THF. As it is already known that formation of PBI radical anions ($PBI^{\bullet-}$) through chemical reduction is easily recognized by the decrease of PBI absorption in the range of 400–550 nm and the concomitant increase of new absorption bands at 713, 800, and 960 nm,[159,166-169] the attention was focused on the detection of this spectral feature in the transient excited-state absorption (ESA) signals. The TA spectra (see Figure 44) of all compounds probed at visible region showed negative ground-state bleaching (GSB) signals at 450–530 nm and stimulated emission (SE) up to ~600 nm. Strong positive signals which come from the excited-state absorption from S_1 state to higher (S_n) states were revealed in the 600–850 nm spectral range.[159,166-169] Interestingly, the characteristic sharp structures with peaks at ~705 nm, attributed to the most intense absorption band of the PBI radical anion,[24,25,46,119,121] turn progressively broader and lose their structures as the molecules go from the extended forms to the compact folded forms in THF, suggesting a decreased efficiency of the CS process from the monomer to the trimer (Figure 44b,d,f). In $CHCl_3$ this trend is also visible but is not as pronounced (*cf.* Figure 44a,c,e).

‡ Transient absorption measurements were performed together with M. Sc. Minjung Son and partially Dr. Young Mo Sung at the Spectroscopy Laboratory for Functional π-Electronic Systems (FPIES) at Yonsei University, Seoul, South Korea. The data were analyzed by M. Sc. Minjung Son.

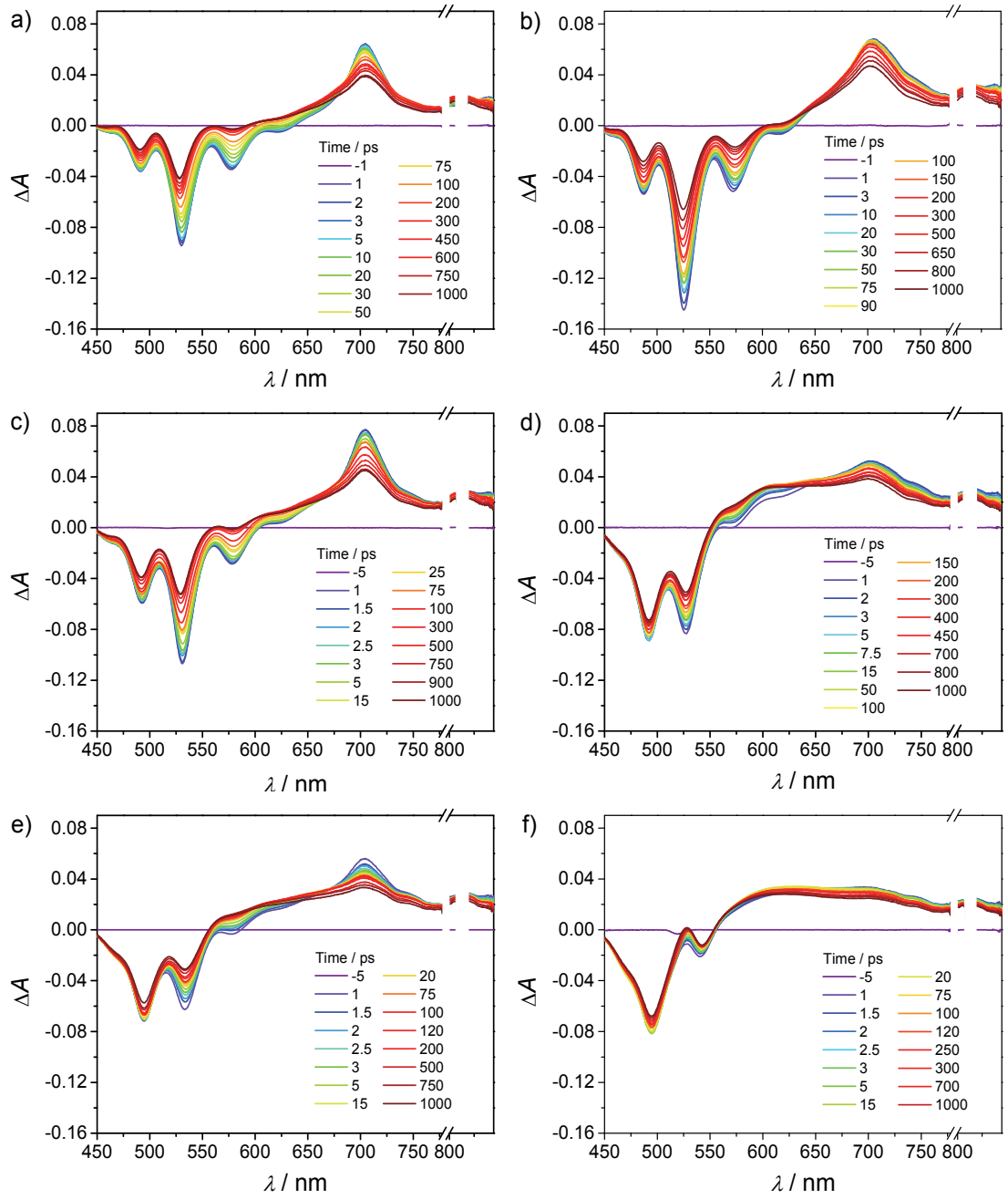

Figure 44. Femtosecond transient absorption spectra in the visible region of a), b) reference PBI compound **31**, c), d) folda-dimer **32**, and e), f) folda-trimer **33** (for all measurements λ_{ex} = 520 nm; $c = 1 \times 10^{-5}$ M) in $CHCl_3$ (left graphs) and THF (right graphs).

Further analysis of the PET dynamics was performed by assessing the TA spectra at near-infrared (NIR) wavelengths of 860–1100 nm, which are shown in Figure 45. The spectra of **31** and **32** show characteristic features in which the broad (~850–1100 nm) ESA of the neutral PBI decays in time and a sharper band peaking at ~960 nm (characteristic for the PBI radical anion) emerges at the same time, which is another evidence of the photoinduced formation of $PBI^{\bullet-}$ by the PET process. Interestingly, while this prominent signature for the PBI radical anion of the monomer **31** is already decreased for folda-dimer **32**, it is almost

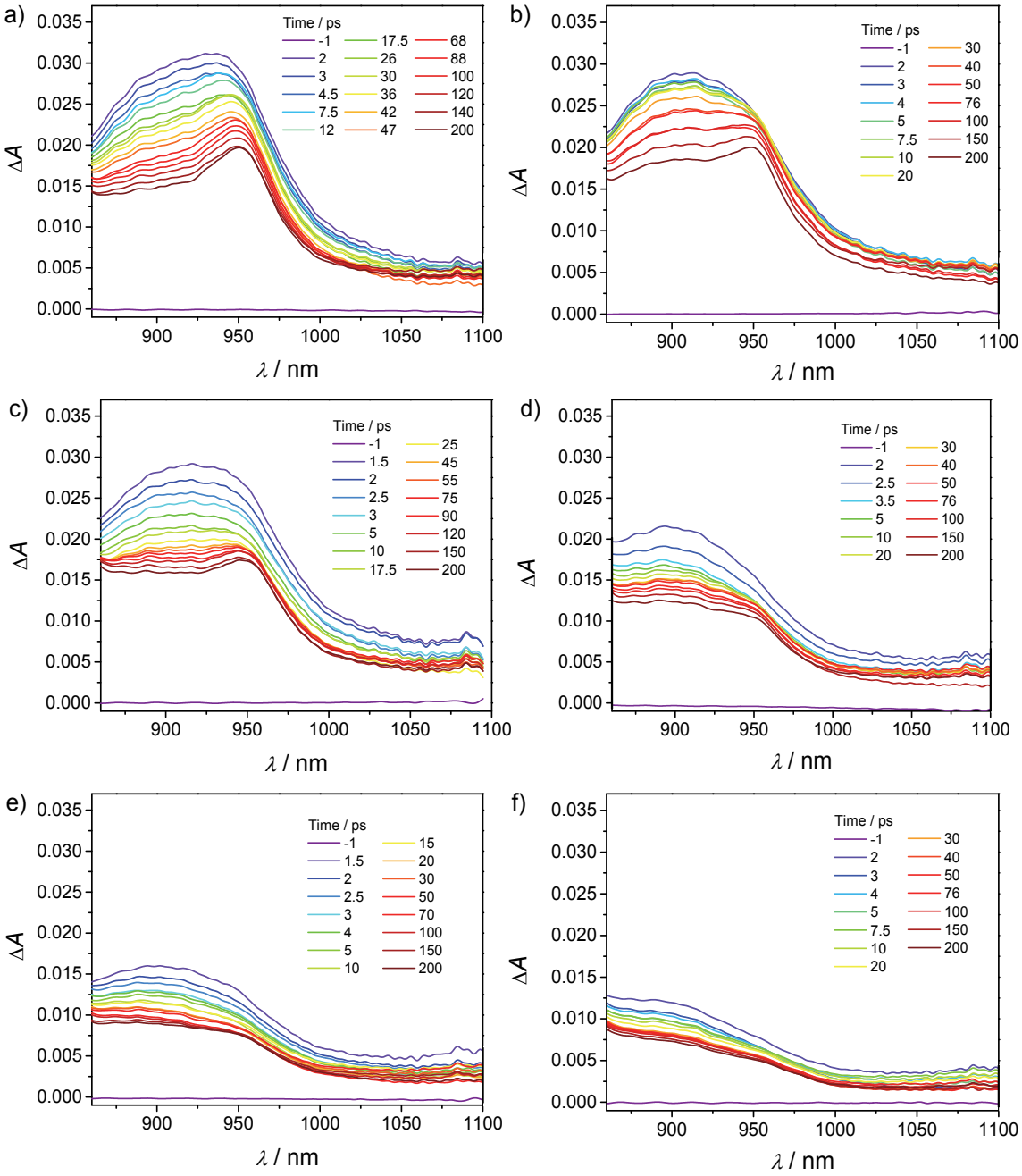

Figure 45. Femtosecond transient absorption spectra in the near-infrared region of a), b) reference PBI compound **31**, c), d) folda-dimer **32**, and e), f) folda-trimer **33** (for all measurements $\lambda_{ex} = 520$ nm; $c = 1 \times 10^{-5}$ M) in $CHCl_3$ (left graphs) and THF (right graphs).

entirely vanished for folda-trimer **33**. A similar tendency is given in $CHCl_3$, where the radical anion signatures are even more prominent than in THF. From these results it can be concluded that the efficiency of the PET process is closely related to the spatial configuration of the chromophores within the systems. In other words, the more the molecules are folded, the less efficient the PET process is.

To further substantiate these findings, the time constants (see Table 6) extracted from the kinetic traces were analyzed, which gave rise to double exponential decay profiles for folda-

dimer **32** and folda-trimer **33** in both solvents. Here the two time components are ascribable to CS and CR times, respectively. Since it was impossible to directly probe the rising $PBI^{\bullet-}$ band which is largely immersed in the strong ESA signal, instead the decay rate of the ESA of neutral PBI was monitored (~920 nm), which was gradually converted into the PBI radical anion absorption band (~960 nm) with time (see Figure 46). In dimer **32**, the CS time was *ca*. 3 times faster in the extended form in $CHCl_3$ (1.5 ps) than in its folded counterpart in THF (4.3 ps). Similar trend was observed in folda-trimer **33** despite much less clear

Table 6. Charge separation (CS) and recombination (CR) time constants of folda-dimer **32** and folda-trimer **33** from TA measurements in $CHCl_3$ and THF.

PBI	$CHCl_3$		THF	
	τ_{CS} [ps][a]	τ_{CR} [ps][a]	τ_{CS} [ps][a]	τ_{CR} [ps][a]
32	1.5	50	4.3	60
33	3.9	57	4.5	96

[a] Probe wavelength of λ = 920 nm was applied.

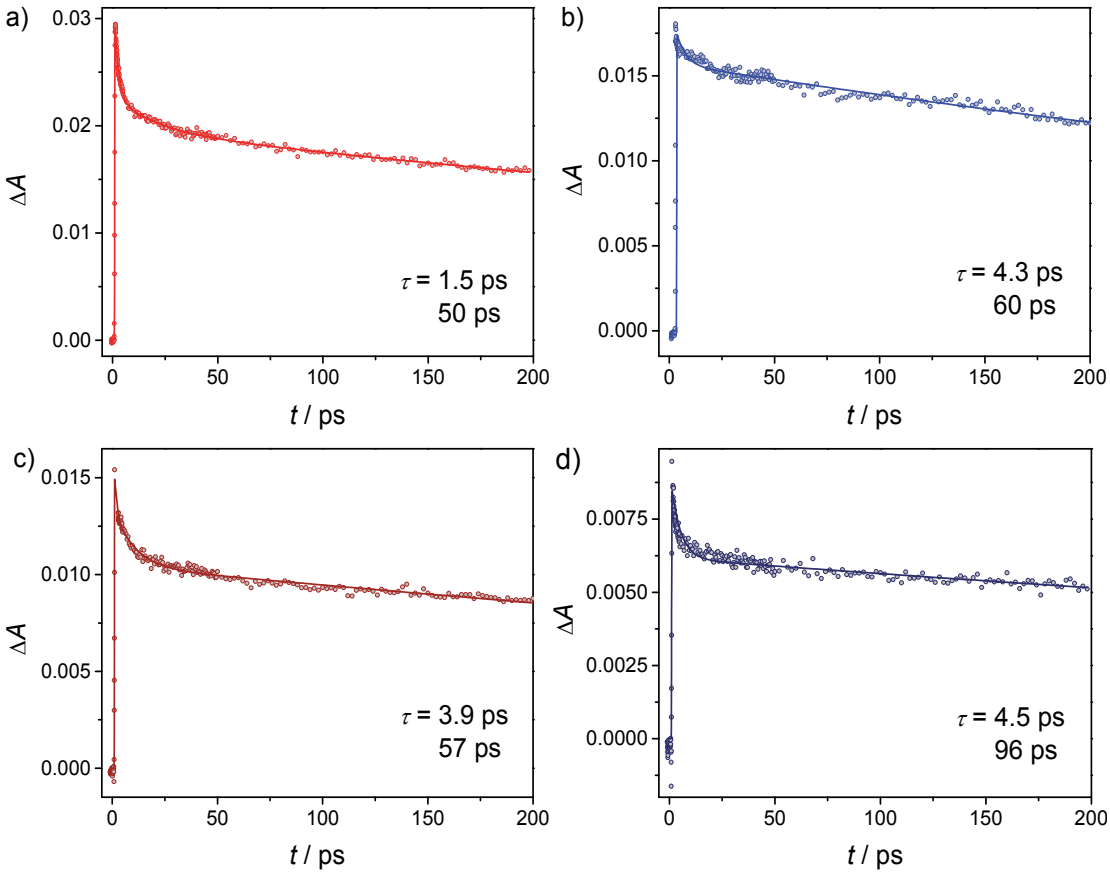

Figure 46. Decay profiles obtained from the NIR femtosecond transient absorption spectroscopy of a), b) folda-dimer **32** and c), d) folda-trimer **33** in chloroform (left graphs) and THF (right graphs) (for all measurements λ_{ex} = 520 nm, λ_{probe} = 920 nm). The fitted decay times are indicated in each spectrum.

difference in the CS rates (3.9 and 4.5 ps in $CHCl_3$ and THF, respectively). This is in compliance with the previous findings that **33** already resides in a more folded structure even in $CHCl_3$.

3.5.3 Interpretation of Excited State Processes

To determine the thermodynamic driving force ($\Delta G°$) of the photoinduced electron transfer (PET) in PBI-OPE systems like folda-dimer **32** and folda-trimer **33**, the Rehm-Weller equation (see Equation 3) was used.[170-172] For this analysis optical and electrochemical parameters of the donor and the acceptor units are needed to qualitatively estimate whether the charge transfer is an endergonic or exergonic process.

$$\Delta G° = e[E_{ox}(D) - E_{red}(A)] - E_{00} - \frac{e^2}{4\pi\varepsilon_0\varepsilon_S r} - \frac{e^2}{8\pi\varepsilon_0}\left(\frac{1}{r^+} + \frac{1}{r^-}\right)\left(\frac{1}{\varepsilon_{ref}} - \frac{1}{\varepsilon_S}\right) \qquad \textbf{(Eq. 3)}$$

In Equation 3 the prior two values to be inserted are the first oxidation potential, E_{ox} (D), of the donor (abbreviated with D) and the first reduction potential, E_{red} (A), of the acceptor (A) moiety obtained by electrochemical measurements. E_{00} equals the energy of the intersection point between the excitation and emission spectrum of the excited unit as also e is the elementary charge, ε_0 the vacuum permittivity, ε_S the permittivity of the solvent used in the spectroscopic studies, and r the center-to-center distance between the donor and acceptor central points. By employing the same solvent for electrochemical and spectroscopic measurements ($\varepsilon_{ref} = \varepsilon_S$), the last, solvent-related term of the Rehm-Weller equation becomes zero and thus information about the ionic radii of the resulting cationic (r^+) and anionic counterparts (r^-) is not required.

It is important to note, that the ongoing charge transfer processes, which can be vividly observed by the spectral signatures in the transient absorption spectra of reference PBI molecule **31** and the unfolded state of folda-dimer **32** in $CHCl_3$, originate from the electron-rich phenylene ethynylene unit to the initially photoexcited PBI chromophores. As explained above (see 3.5.2) the electron transfer is almost completely disabled by folding into more compact structures in THF for both **32** and **33**. For folda-trimer **33** also in $CHCl_3$ the excimer formation predominates, suggesting that for **33** already considerable π–π-interactions are present.

In this analysis, only the reference PBI compound **31** was examined. For this system contributions arising from the dye–dye interplay are completely absent at all. Thus, a reliable evaluation of the PET thermodynamics can be given, which may also hold true for

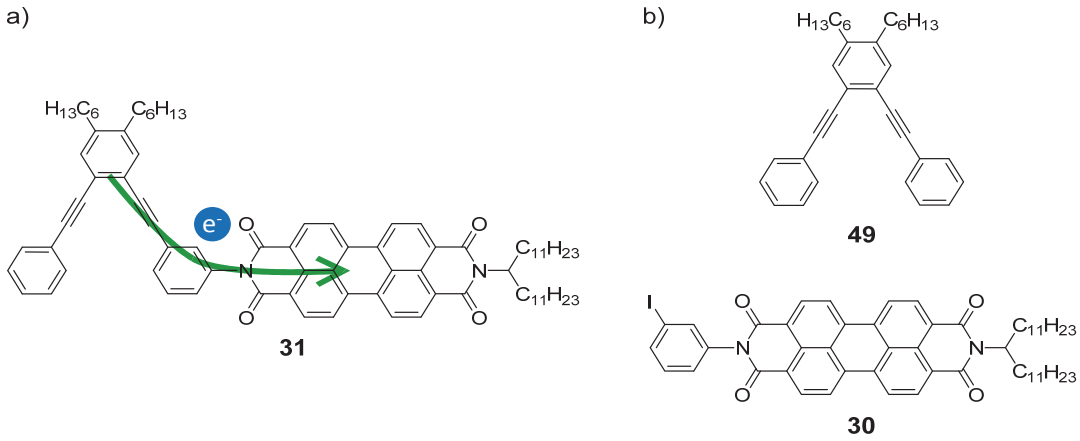

Figure 47. a) Chemical structures of a) **31** with the proposed electron transfer pathway (indicated by the green arrow) from the donor to the initially photoexcited PBI acceptor and b) both compounds **49** and **30** used for calculation of the driving force of the PET process.

larger PBI-OPE ensembles. To calculate the $\Delta G°$ value of the electron transfer process for **31** (Figure 47a), the system was splitted into the two counterparts (*cf.* Figure 47b), *i.e.* the phenylene ethynylene-containing donor unit **49** and the PBI acceptor moiety (equal to monomeric PBI **30**). As nodes are present in the highest occupied molecular orbital (HOMO) and in the lowest unoccupied molecular orbital (LUMO) at the imide nitrogen atoms and also the entire long molecular axis in PBI chromophores,[173] the imide substituents may not change the electrochemical properties significantly. Therefore, **30** is a good candidate to obtain the first reduction potential for the analysis. Although similar compounds to **30** and **49** have been studied extensively in the past with respect to their electrochemical behavior,[174-176] a comprehensive investigation dealing with PBI chromophores in combination with phenylene ethynylene units is absent. Additionally, the energy of the intersection point from the absorption and fluorescence emission spectra of **30** was taken for calculating the driving force. To avoid the estimation of ionic radii for $\mathbf{30}^-$ and $\mathbf{49}^+$ and to take the modest solubility of **30** into account, the same chlorinated solvent was used for both the optical and electrochemical measurements. Therefore, dichloromethane (CH_2Cl_2) was employed for solubility and feasibility reasons. This choice may appear to be ill-suited, as all other spectroscopic studies presented here were performed either in $CHCl_3$ or THF exclusively. Nevertheless, as the three solvents, *i.e.* CH_2Cl_2, THF, and $CHCl_3$, have similar values in the middle range of the solvent permittivity (8.93, 7.58, and 4.81) and in addition conformational rearrangement processes are not of relevance for **31**, CH_2Cl_2 is indeed appropriate for the determination of the PET thermodynamics.

For **30** the first reduction potential was determined by the cyclic voltammetry (CV) setup using ferrocene/ferrocenium (Fc/Fc^+) as internal reference and tetra-*n*-butylammonium

hexafluorophosphate (TBAHFP) as supporting electrolyte in CH_2Cl_2. Two reversible reduction steps were identified for **30** in the cyclic voltammogram (*cf.* Figure 48a) at –1.04 V (**30**/**30**$^-$) and –1.24 V (**30**$^-$/**30**$^{2-}$), which are in a similar range as other monomeric PBI dyes.[60,175,176] However, the precise assignment of the first oxidation potential of **49** was not possible examinating the cyclic voltammogram. Apparently, the oxidation from **49** to **49**$^+$ seems to be at rather high voltage (and presumably is irreversible) and thus is completely obscured by the electrochemical signature of the beginning decomposition of the solvent. Nevertheless, a value of +1.18 V could be determined by interpreting the results obtained by squarewave voltammetry (SWV) of **49** in CH_2Cl_2 (Figure 48b) with ferrocene/ferrocenium and TBAHFP.

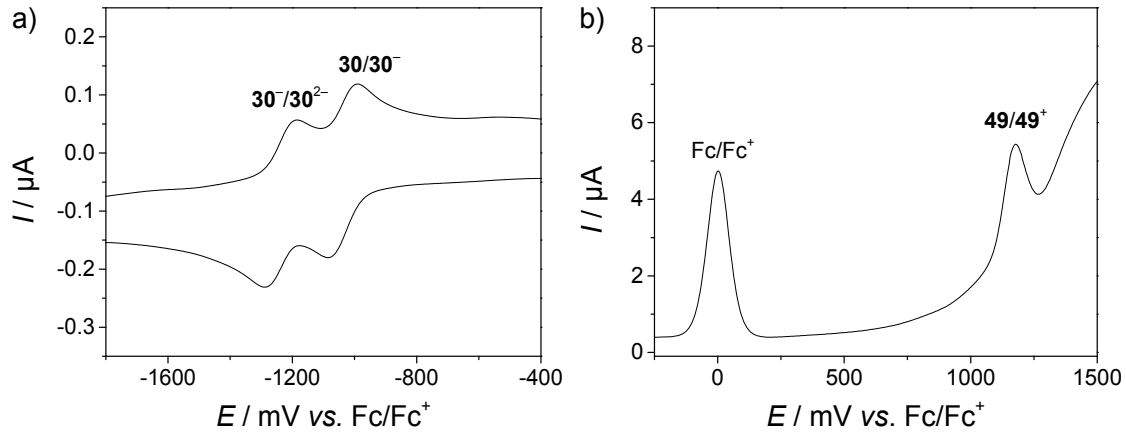

Figure 48. a) Cyclic voltammogram (scan rate 250 mV s^{-1}) of **30** (2.5×10^{-4} M) and b) squarewave voltammogram of **49** (3×10^{-4} M) in CH_2Cl_2 *vs.* Fc/Fc^+ with TBAHFP (0.1 M) at RT.

Furthermore, the normalized UV/Vis and fluorescence spectra of **30** in CH_2Cl_2 revealed an energy of E_{00} = 2.34 eV (equal to an intersection point at 529 nm, *cf.* Figure S6). The center-to-center distance (r) between the donor and acceptor moieties in **31** was calculated by geometry optimization with PM6 to be approximately 10.1 Å (omitting long alkyl chains). With these values a driving force of $\Delta G° = -0.28$ eV was estimated for the PET in **31** originating from the phenylene ethynylene donor to the PBI acceptor unit. Accordingly, the photoinduced electron transfer is a rather exergonic and thus thermodynamically favored process.

By attaching more PBI dyes to a more expanded scaffold the situation might be changed, although, as the aforementioned spectroscopic studies revealed, the PET is actually taking place also for the smaller folda-systems **32** and **33**. For the folda-dimer **32** this switching between PET and excimer formation was indeed nicely controlled by the surrounding environment, *i.e.* by the solvent. Because the permittivity differences of the utililzed

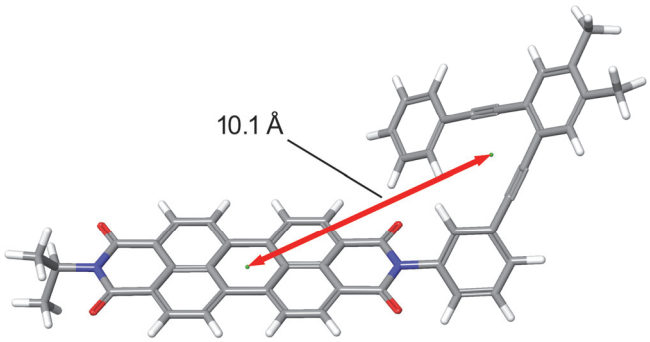

Figure 49. Molecular structure of **31** obtained by geometry optimization with PM6 for calculating the center-to-center distance (red double arrow connecting the green centroids) between donor and acceptor units yielding a value of 10.1 Å.

solvents $CHCl_3$, THF, and CH_2Cl_2 are not very different and the center-to-center distances between donor and acceptor moieties are also not very different for folded and unfolded states, it may indeed be concluded that the energetics for PET is always favorable (the *r*-related term does only further decrease the already negative $\Delta G°$ value (–0.12 eV) originating from the first part of the Rehm-Weller equation, $e\,[E_{ox}\,(D) - E_{red}\,(A)] - E_{00}$, and that the selectivity between PET pathway and excimer formation is indeed due to changes in the kinetics: For folded conformations the faster pathway is the formation of the excimer and for open conformations it is the PET. Because the excimer constitutes an energetically relaxed state, no PET from this conformation is feasible anymore because the driving force is too much decreased. This is most evident for folda-trimer **33**, for which already in $CHCl_3$, owing to considerable PBI–PBI-interactions, excimer formation prevails and PET becomes a disfavored process.

It is quite interesting to relate these conformation-dependent processes to those taking place in an organic solar cell based on p-type semiconducting polymers[50,177-181] (also such as *poly*-phenylene ethynylene) and aggregated PBI molecules, the latter constituting the n-type species (Figure 50). In such bulk materials excited PBI molecules have to transport the exciton to the p/n interface of the conducting polymer where a sufficient driving force (about 0.3 eV are usually considered to be appropriate)[182-185] is required to form the charge separated (CS) state. Subsequently, the hole (h^+) and electron (e^-) have to migrate to the respective electrodes (Figure 50). As our study for folda-dimer **32** and folda-trimer **33** revealed, conformational heterogeneity may account for the failure of such devices as commonly observed for PBI based bulk heterojunction solar cells.[186,187] Thus, aggregated PBIs favor relaxation into excimer states that constitute traps for the exciton transport and are energetically too low to support the required electron transfer at the p/n heterojunction interface (*cf.* Figure 50). Only if this process is prohibited by proper molecular design,

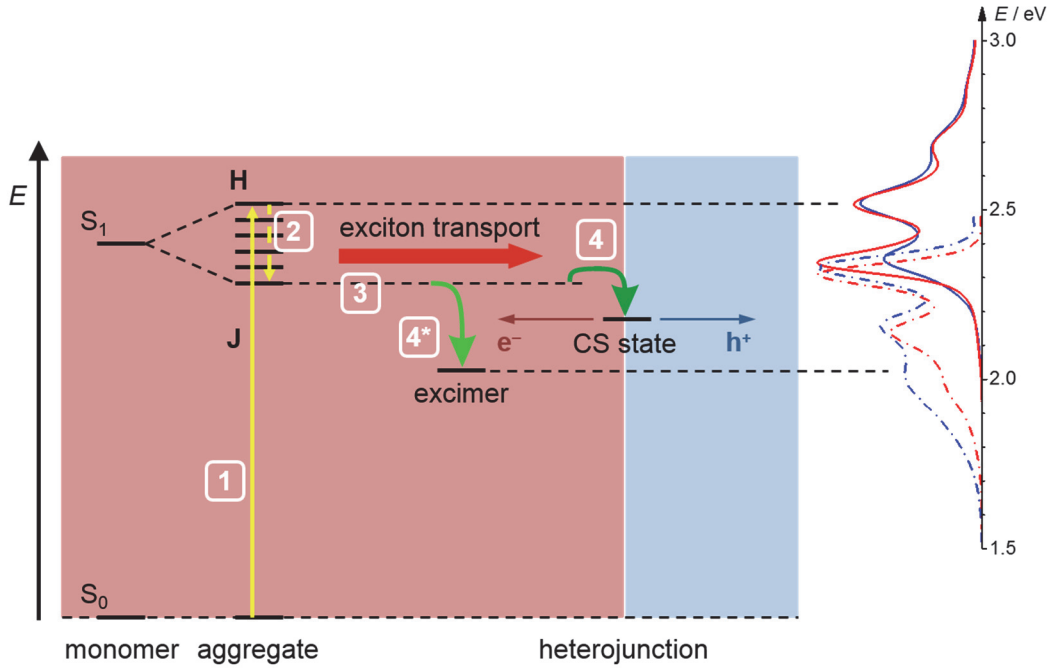

Figure 50. Schematic energy state diagram describing light absorption by a PBI H-aggregate (1, solid yellow arrow), exciton relaxation (2, dashed yellow arrow) to the lowest energy Frenkel exciton state (J-state), exciton migration to the heterojunction interface (3, red arrow), and formation of a charge separated (CS) state (4, dark green arrow) with subsequent migration of electrons and holes through the donor (red shaded) and acceptor (blue shaded) phases towards the electrodes. The absorption and emission spectra of folda-dimer **32** in THF (blue) and chloroform (red) are shown on the right side and related by dashed lines to the energy levels of the upper excitonic H-state and the excimer state in the schematic diagram on the left. Relaxation into the latter (4*, light green arrow) as a competitive pathway to exciton transport is illustrated as well.

highly efficient organic solar cell devices become available based on this class of dyes.[180,181,188-190]

Chapter 4

–

Summary

In this work, the syntheses and fundamental studies on the folding behavior of two perylene bisimide (PBI) systems containing two (**32**) or three chromophores (**33**) are presented. Based on the parent octameric PBI foldamer synthesized by co-polymerization revealing an alternating *ortho*-*meta*-phenylene ethynylene connected framework the PBI dimer and trimer were obtained by copper- and palladium-catalyzed *Sonogashira-Hagihara* cross coupling reactions. The synthetic pathways to **32** and **33** as well as their monomeric reference compounds **30** and **31** are depicted in Scheme 4.

Starting with the 1,2-diiodobenzene derivative **34**, the moiety, which covalently connected two adjacent PBI fragments in **32** and **33**, could be received by using orthogonal protecting groups and polar tagging strategy. In **38** the hydroxy-containing protective group could be cleaved under basic conditions exclusively to afford singly protected intermediate **39**. The subsequent cross coupling with **30**, deprotection of the triisopropylsilyl-bearing ethynylene fragment and second reaction with **30** yielded in folda-dimer **32**. To obtain the related folda-trimer **33**, in the last step the 3,5-diiodophenyl analogue **44** was employed instead of **30**. To separate the two folda-systems from by-products the use of recycling gel permeation chromatography (GPC) was necessary. First spectroscopic studies were employed to identify proper solvents, which induced solely the intramolecular stacking (folding) of adjacent PBI chromophores in **32** and **33** and, furthermore, avoided any self-assembly caused by intermolecular interactions. Whereas in earlier studies of the octameric PBI system and also in self-assembly studies of PBI monomers nonpolar solvents proved to be an excellent choice to achieve π–π-stacked structures, it was shown that for **32** in highly nonpolar solvents the intermolecular interplay dominated. Thus, the two solvents showing

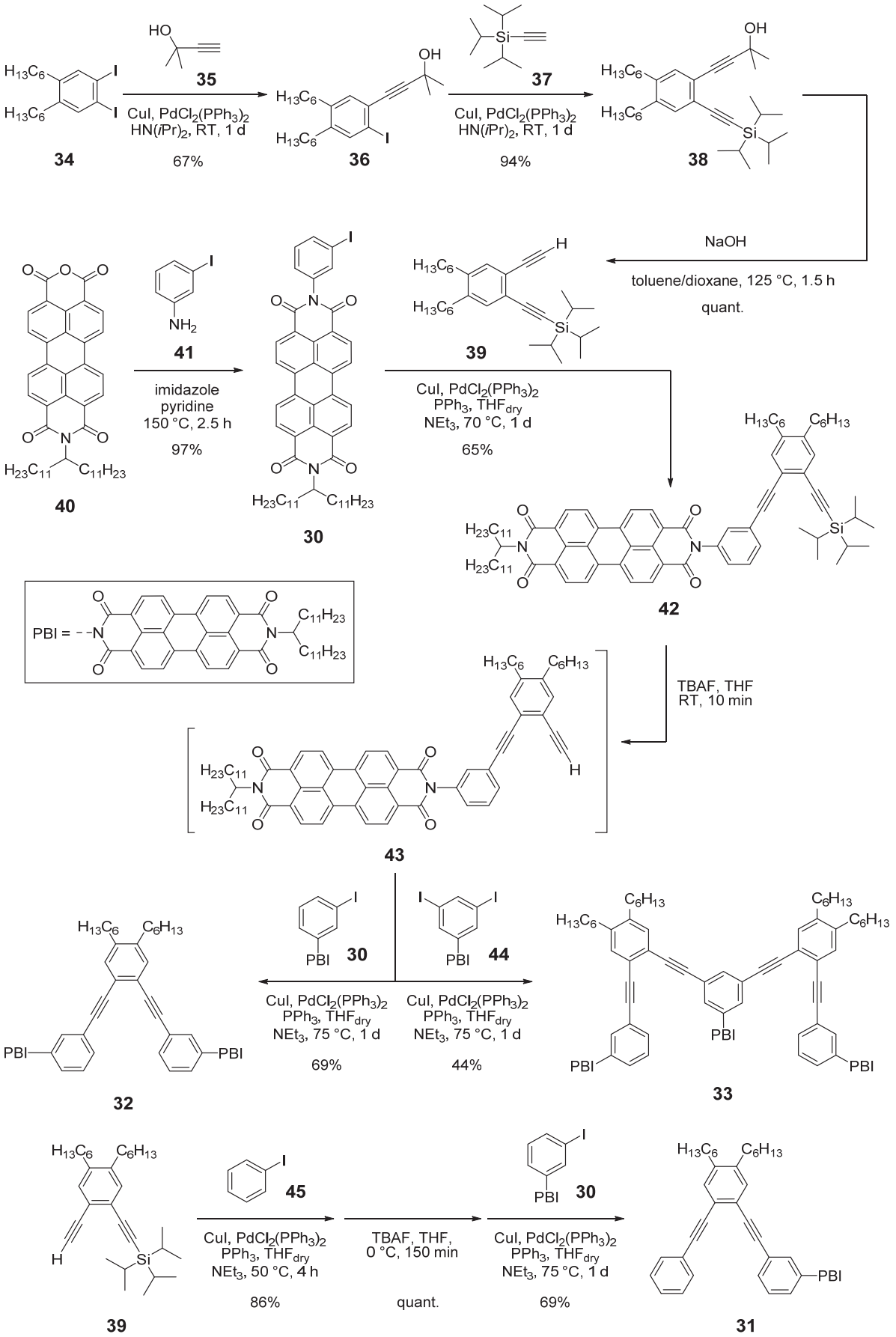

Scheme 4. Syntheses of PBI folda-dimer **32**, folda-trimer **33**, and their reference compounds **30** and **31**.

the largest spectral changes without collapse into self-assembled structures were chloroform ($CHCl_3$) and tetrahydrofuran (THF). Originating from its pronounced solubilizing properties like, in general, for large π-conjugated aromatics, in $CHCl_3$ the individual PBI moieties of **32** and **33** remain mainly covered by the solvent with only small interchromophoric communication (Figure 51). Thus, the chromophores can be seen as monomers, *i.e.* having properties revealing more monomer-like character. Triggered by solvophobic forces the respective folded, H-type structures with π-stacked PBI units were achieved in THF as solvent. Upon folding the chromophores are in much closer distances revealing blue-shifted absorption maxima. In addition, nuclear magnetic resonance (NMR) spectroscopy was used to analyze the folding of **32** and **33**. Whereas the perylene core protons of monomeric reference PBI **31** in THF are significantly down field shifted in comparison to **31** in $CDCl_3$, for **33** and in particular **32** (owing to the less complex structure consisting of only two perylene moieties instead of three) the ^{1}H NMR spectra exhibit pronounced up field shifts of the folded ensembles indicative of stacked aromatic compounds. Although spectra of **32** and **33** in THF were less complicated than the ones in $CDCl_3$, the hindered rotation around the C–N imide bond yielded different isomers. Indeed, as also found experimentally for monomeric reference PBI **31** and theoretically for a much smaller model compound, the barrier to overcome is rather high, but can already be reached by gentle heating. Variation of the temperature showed this simplification of the ^{1}H NMR spectra. By increasing temperature a second minor populated set of aromatic protons raised for **32** and **33** in [D_8]THF, which was explained in terms of the orientation of the phenylene ethynylene scaffold (compare Figure 51b). Based on earlier theoretical investigations by force field calculations the backbone in the parent PBI octamer might be arranged regularly as spiral staircase, what was refined for **32** with semi-empirical and density functional theory (DFT) approaches with dispersion-corrections. As a result it was shown that the orientation of the backbone had some influence on the overall energy of the system yielding two conformers with particularly different proton shifts. The presence of two conformers with one major and one minor component could be explained in terms of a Boltzmann distribution. Furthermore, molecular dynamics with the semi-empirical PM6-DH2 method was employed to visualize the folding of **32** and **33** starting with quite differing structures ranging from unfolded to already folded states. Indeed, both folded states varying only in the orientation of the phenylene ethynylene linker were adopted during a simulation time of 65 ps for both **32** and **33**, which suggested that both were also accessible in solution and were separated by relatively high energy barriers (Figure 51c). Thus, also for the minor

conformers detectable portions were identified in the ^{1}H NMR spectra. For the simpler folda-dimer **32** a detailed theoretical investigation with regard to the solvents applied for spectroscopic studies was presented neglecting the tether. For the halogenated solvent it was shown that the unfolded state was enthalpically more favored than the π-stacked arrangement. The situation was completely changed for THF as solvent, what fully reflected the situation evaluated by different spectroscopic methods. Remarkably, this distinct differentation was mainly a consequence of the number of solvent molecules, which was greater for chloroform. However, it is also important to note that the folded species is always favored for entropic reasons. Once the two systems adopt the folded or unfolded states, their photophysical properties are completely changed. Whereas the charge transfers from the electron-donating phenylene ethynylene moieties to the electron-poor chromophores dominates as deactivation pathways in the open forms (Figure 51a), the reversible folding into compact states favors excimer formation between already closely π-stacked chromophores (*cf.* Figure 51b). Thus, a switching between both relaxation pathways is possible by adjusting the surrounding environment (solvent). Accompanied with the bathochromically shifted emissions of the excimer states the fluorescence quantum yields are markedly decreased as the deactivation is not anymore the return from the first excited state (S_1) to the ground state (S_0) like typically for monomeric PBI dyes, *e.g.* **30**. However,

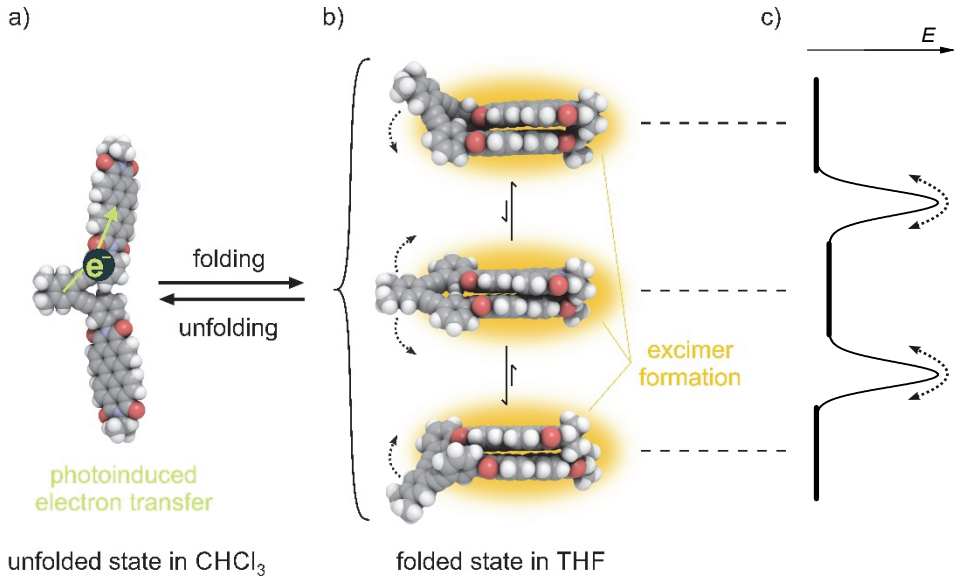

Figure 51. Simplified illustration of the reversible folding/unfolding-behavior of PBI dimer **32**, exhibiting solvent-dependent switching between the a) unfolded and b) folded state. Whereas in the unfolded state the intrinsic photoinduced electron transfer prevails, the folded arrangement yields in pronounced interchromophoric interactions (excimer formation). In b) the inherent up and down flapping of the phenylene ethynylene scaffold is indicated by the dashed arrows. For clarity linear alkyl chains are depicted as methyl substituents in a) and b). c) Schematic energy level diagram of the different folded conformers with energy barriers between those.

for both systems **32** and **33** the excimer formation is the more competitive relaxation channel for the $S_1 \rightarrow S_0$ fluorescence than the charge transfer. Thus, in the unfolded states the fluorescence quantum yields are almost twice those of the folded species. Further time-resolved transient absorption spectroscopic studies indicate that the photoinduced electron transfer from the scaffold to the chromophores is highly surpressed in the folded state as the PBI radical anion signature is absent. For the respective unfolded species of **32** and **33** pronounced spectral features appear in the visible and near-infrared (NIR) regime at approximately 700 nm and 950 nm.

In conclusion, herein a detailed investigation on two foldable PBI systems **32** and **33** was presented. The reversible, solvent-dependet folding/unfolding-behavior, which was already communicated for a polydisperse PBI octamer **19** obtained by co-polymerization, was used to study the ground and excited states properties of folda-dimer **32** and folda-trimer **33** by means of different spectroscopic methods as well as theoretical studies. The switching between charge transfer or excimer formation pathways of photoexcited molecules influenced by the spatial arrangement of chromophores within defined dye systems illustrates the impact of conformational preferences on functional properties. Properly applied it may pave the way for highly functional materials, as the deactivation channel can be externally controlled.

Chapter 5

–

Zusammenfassung

In dieser Arbeit wurden die Synthese und die profunde Charakterisierung der optischen wie auch strukturrelevanten Eigenschaften von faltbaren Perylenbisimid (PBI)-Systemen mit zwei oder drei Chromophoren beschrieben. Basierend auf früheren Arbeiten über ein copolymerisiertes und daher polydisperses PBI-Oktamer sind die einzelnen Farbstoffeinheiten durch ein alternierendes *ortho-meta*-Phenylen-Ethinylen-Grundgerüst mithilfe von Palladium- und Kupfer-katalysierten *Sonogashira-Hagihara*-Kreuzkupplungsreaktionen kovalent miteinander verknüpft worden. In Schema 4 sind die Synthesen der beiden wohldefinierten Zielmoleküle **32** und **33** sowie der monomeren Referenzverbindung **30** und die Schritte hin zur Referenzverbindung **31** gezeigt.

Ausgehend vom 1,2-Diiodbenzolderivat **34** konnte die Vorstufe **38** synthetisiert werden, welche die verbrückende Einheit zweier benachbarter PBI-Chromophore darstellt (s. Schema 4). Hierbei wurden orthogonale Schutzgruppen verwendet sowie die Strategie der polaren Kennzeichnung angewandt. Durch selektive, basische Abspaltung der Hydroxy-enthaltenden Schutzgruppe konnte das nunmehr einfach geschützte Derivat **39** dargestellt werden. Die anschließende C–C-verknüpfende Reaktion mit **30**, die darauffolgende Entschützung und erneute Umsetzung mit **30** brachte das PBI-Dimer **32** hervor. Zur Darstellung des PBI-Trimers **33** wurde in der letztgenannten Verknüpfung statt **30** das 3,5-Diiodphenyl-Analogon **44** eingesetzt. Nach erfolgreicher Synthese wurden die beiden PBI-Systeme **32** und **33** mithilfe der Recycling-Gelpermeationschromatographie (GPC) isoliert.

Für alle weiteren spektroskopischen Untersuchungen erwies sich die Identifizierung geeigneter Lösungsmittel als Schlüsselpunkt, die lediglich die intramolekulare Annäherung

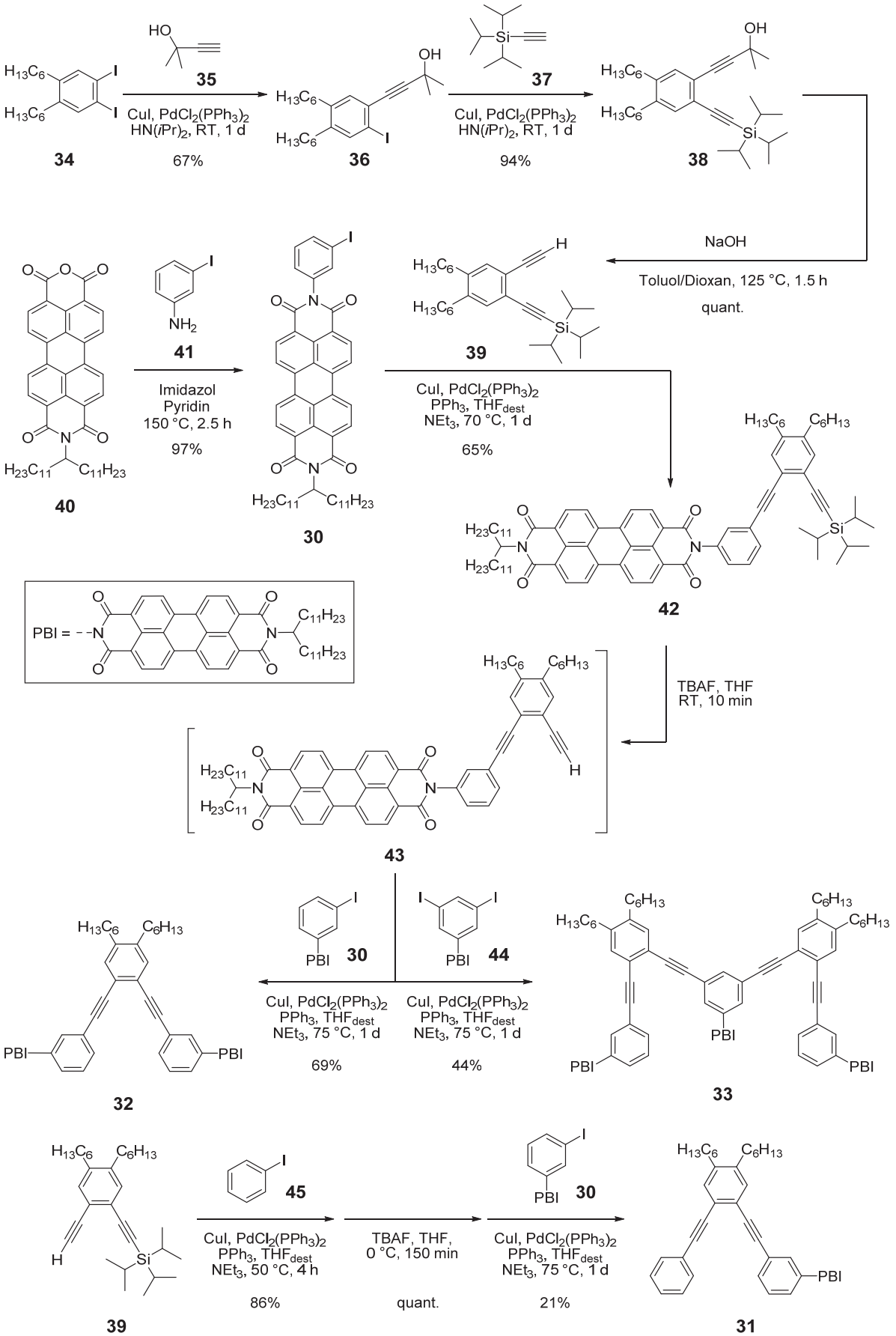

Schema 4. Synthese der faltbaren PBI-Systeme **32** und **33** sowie ihrer monomeren Analoga **30** und **31**.

begünstigen und zwischenmolekulare Interaktionen nicht zu lassen. Intermolekulare Wechselwirkungen sind in stark unpolaren Lösungsmitteln zu finden, was in ersten UV/Vis-spektroskopischen Studien für **32** demonstriert werden konnte. Weiterhin konnte für das PBI-Dimer mittels Absorptionsspektroskopie in verschiedenen Lösungsmitteln von schwacher bis starker Polarität gezeigt werden, dass die deutlichsten spektralen Änderungen auf intramolekularer Ebene in Chloroform ($CHCl_3$) und Tetrahydrofuran (THF) auszumachen sind. Für folgende spektroskopische Untersuchungen wurden daher diese beiden Lösungsmittel verwendet. Während die einzelnen Chromophore bedingt durch das besonders ausgeprägte Solvatationsvermögen von $CHCl_3$ im ungefalteten Zustand voneinander separiert vorliegen und dem Monomer ähnliche Eigenschaften aufweisen, wird für **32** und **33** in THF der gefaltete Zustand eingenommen (vgl. Abbildung 51). In diesem Fall werden kleine PBI-Stapel gebildet, in welchen die zwei bzw. drei Farbstoffmoleküle aufeinander gesetzt sind und eine H-artige Kopplung gemäß der für Aggregate entwickelten Exzitonentheorie zeigen. Aufgrund dieser räumlichen Nähe sind die Absorptionsmaxima deutlich blauverschoben. Weitere kernspinresonanzspektroskopische (NMR) Messungen in $CDCl_3$ und [D_8]THF zeigen, dass die π–π-Stapelung der Chromophore mit Hochfeldverschiebungen einhergeht, wohingegen der Wechsel des Lösungsmittels für das monomere PBI-Referenzmolekül **31** den gegenteiligen Trend zeigt, d.h. Tieffeldverschiebungen auftreten. Durch Hochtemperatur-NMR-Studien von **32**, **33** und **31** in deuteriertem Chloroform und Tetrahydrofuran konnte weiterhin die interne, gehinderte Rotation um die außenständigen C–N-Imidbindungen untersucht werden. Diese Rotation ist bei normalen Temperaturen nahe unter dem Koaleszenzpunkt, sodass mehrere Konformere nebeneinander vorliegen. Hierfür geht man zu leicht höheren Temperaturen, um den Koaleszenzbereich vollständig zu verlassen. Diese eingeschränkte Bewegungsfreiheit konnte mittels theoretischer Berechnungen anhand einer vereinfachten Modellverbindung verifiziert werden. Zusätzlich konnte durch quantenchemische Überlegungen die Präsenz eines zweiten, gefalteten Konformers von **32** und **33** in THF bestätigt werden, bei dem die Ausrichtung des *oligo*-Phenylen-Ethinylen (OPE)-Rückgrats eine entscheidende Rolle einnimmt (s. Abbildung 51b). Frühere Kraftfeldrechnungen für das zugrundeliegende PBI-Oktamer sagten eine helikale Anordnung vorher, in der sich das Grundgerüst spiralförmig um den PBI-Stapel windet. Neuere theoretische Berechnungen auf semiempirischer Basis sowie auf Dichtefunktionaltheorie (DFT)-Niveau mit Dispersions-Korrektur konnten hier angewandt werden und suggerieren, dass sich der Phenylen-Ethinylen-Strang viel stärker an die Chromophore schmiegt und so kompakter erscheint. Da beide möglichen

Anordnungen des Rückgrats nur einen kleinen Energieunterschied aufweisen, kann anhand einer Boltzmann-Verteilung die Präsenz zweier Konformere mit teilweise stark unterschiedlichen Protonen-Verschiebungen erklärt werden. Weiterhin konnte mithilfe von Moleküldynamik (MD)-Simulationen mit dem PM6-DH2-Ansatz der Faltungsprozess verstanden werden. Diese Experimente zeigten ausgehend von verschiedenen Startstrukturen, dass sowohl beide genannten Anordnungen des Grundgerüsts energetisch begünstigt waren, aber nur über derart hohe Barrieren (Abbildung 51c) erreicht werden können, dass der Übergang zur stabileren Konformation (entsprechend des vornehmlich gebildeten Konformers) bei niedrigen Temperaturen nicht bewältigt wird. Unter Vernachlässigung des energetischen Einfluss des Rückgrats wurde später eine Analyse des Faltens im Hinblick auf das Lösungsmittel für das PBI-Dimer **32** unternommen. Es konnte gezeigt werden, dass für Chloroform enthalpisch die entfaltete, offene Form mehr begünstigt ist als der gefaltete Zustand, während die Situation für das Lösungsmittel THF das genau gegenteilige Bild wiederspiegelt. In diesem Ansatz war allerdings der ausschlaggebende Punkt, dass eine größere Anzahl von $CHCl_3$-Molekülen um das Perylenbisimid-Fragment gelegt werden konnte. Mithilfe der reversiblen Faltungseigenschaft konnte die Desaktivierung der angeregten Spezies zwischen einem

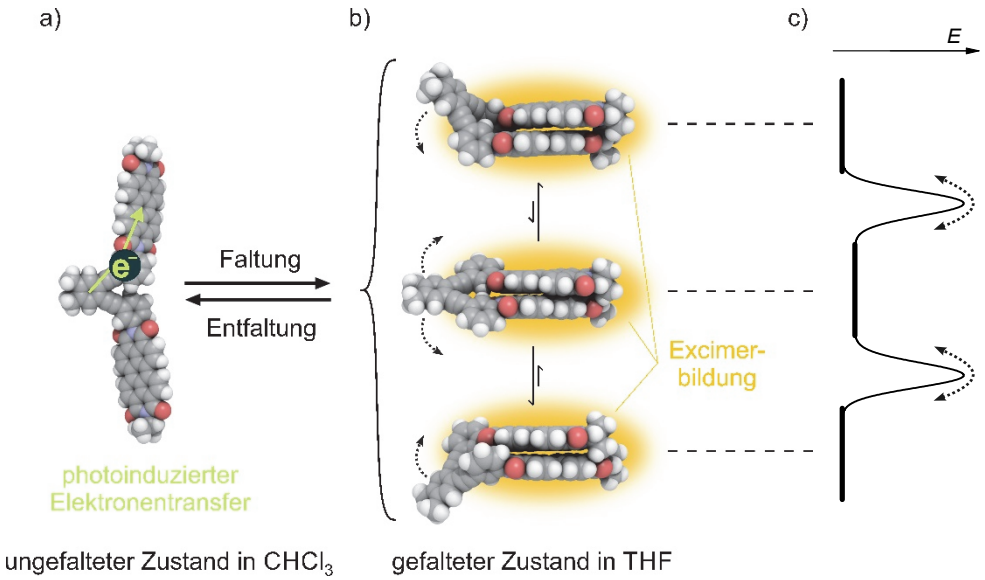

Abbildung 51. Schematische Darstellung des reversible Faltungs-/Entfaltungsprozesses exemplarisch für das PBI-Dimer **32**, welches zwischen einem a) ungefaltetem und b) gefaltetem Zustand geschaltet werden kann. Während in der ungefalteten Form der interne photoinduzierte Elektronentransfer vorherrscht, führt die Faltung hin zur kompakten Anordnung zu starken Wechselwirkungen zwischen den Chromophoren (Excimerbildung). In b) ist die inhärente Auf-und-ab-Bewegung des Grundgerüstes mit gestrichelten Pfeilen symbolisiert. Lineare Alkylketten sind in den Strukturen der besseren Übersichtlichkeit halber als Methyl-Substituenten zu sehen. c) Vereinfachtes Energieprofil, das die Energien der verschiedenen, gefalteten Konformere mit Energiebarrieren zeigt.

Ladungstransfer und einer Excimerbildung innerhalb des Systems geschaltet werden. Während in der offenen Form, in welcher die PBI-Chromophore durch eine Solvatationshülle weiter voneinander entfernt vorliegen, der Elektronentransfer zwischen dem OPE-Rückgrat und dem elektronenarmen PBI-Grundkörper höchst effizient vonstattengeht, weist der mehr kompakte, gefaltete Zustand ein langlebiges Excimer mit der typisch rotverschobenen Emission als Relaxationskanal auf. Da im gefalteten Zustand kleine π–π-Stapel geformt werden und sich somit die Chromophore sehr nahe sind, können diese durch gegenseitige Wechselwirkungen miteinander interagieren. In beiden Fällen ist die für monomere Perylenbisimide wie **30** charakteristisch hohe Fluoreszenz aber deutlich reduziert, was auf die zwei unterschiedlichen photophysikalischen Desaktivierungsprozesse zurückgeführt werden kann. Für die ungefalteten Zustände von **32** und **33** stehen die Elektronentransfers aber weniger stark in Konkurrenz zur Fluoreszenz als für die gefalteten Ensembles, da etwa zweimal so hohe Fluoreszenzquantenausbeuten bestimmt wurden. Anhand zeitaufgelöster transienter Absorptionsspektroskopie konnte aufschlussreich die Unterdrückung des Ladungstransports gegenüber der Excimerbildung im gefalteten Zustand anhand des Fehlens der für Perylenbisimidanion-typischen Absorptionen gezeigt werden. Für die ungefaltete Form sind dagegen im sichtbaren Bereich bei *ca*. 700 nm wie auch im Nahinfrarotbereich bei ungefähr 950 nm deutliche Anzeichen für PBI-Radikalanionen erkennbar.

Zusammenfassend wurde in der vorliegenden Arbeit ein Beitrag zu faltbaren PBI-Systemen mit definierter Struktur geleistet. Das reversible Faltungsvermögen von **32** und **33**, das bereits in früheren Arbeiten für das zugrundeliegende copolymerisierte, polydisperse PBI-Oktamer **19** demonstriert werden konnte, wurde hinsichtlich seiner Eigenschaften im Grundzustand sowie im angeregten Zustand mithilfe unterschiedlicher Methoden eingehend charakterisiert. Das durch die Konstellation der PBI-Chromophore zueinander bedingte Umschalten zwischen Ladungstransfer und Excimerbildung illustriert die große Bedeutung konformativer Präferenzen für die funktionellen Eigenschaften. Richtig angewandt könnten durch solche Prozesse völlig neue, multifunktionale Materialien zugänglich werden, da durch externen Einfluss der vorherrschende Deaktivierungskanal bestimmt werden kann.

Chapter 6

–

Experimental Section

6.1. Materials and Methods

General: All solvents and reagents were purchased from commercial sources and used as received without further purification, unless otherwise stated. Diisopropylamine (99%) was degassed by sparging argon gas for 30 min prior to application. Triethylamine (97%, NEt_3) and tetrahydrofuran (THF) were purified according to literature procedures.[191] 4,5-Di-*n*-hexyl-1,2-diiodobenzene (**34**),[125] *N*-(12-tricosanyl)perylene-3,4:9,10-tetracarboxylic acid-3,4-anhydride-9,10-imide (**40**),[129] *N*-(3,5-diiodophenyl)-*N'*-(12-tricosanyl)perylene-3,4:9,10-tetracarboxylic acid bisimide (**44**),[25,26] and 1,2-diethynyl-4,5-di-*n*-hexylbenzene (**48**)[125] were synthesized according to literature procedures. Although the synthesis of 1-ethynyl-2-(2-triisopropylsilylethynyl)-4,5-di-*n*-hexylbenzene (**39**) is already known (overall yield 47%),[23] in this work, the compound was synthesized using 4,5-di-*n*-hexyl-1,2-diiodobenzene (**34**),[125] 2-methylbut-3-yne-2-ol (**35**), and triisopropylsilylacetylene (**37**). Additionally, the syntheses of the compounds **30**, **38**, **42**, **43**, **33**, and also **39** were already described in an earlier work.[192] However, few individual and the overall yield could be significantly increased. For all known compounds, the spectroscopic data are identical with the published data. Column chromatography was performed using silica gel Si_{60} (0.035–0.070 mm). Recycling gel permeation chromatography (GPC) was performed on a Shimadzu GPC system (LC-20AD prominence pump; SPD-MA20A prominence diode array detector) equipped with two preparative columns (JAIGEL 1H+2H) with $CHCl_3$ as eluent at a flow rate of 3.5 mL min^{-1} and a pressure of 20 MPa. Melting points (m.p.) were determined on a Olympus BX41 polarization microscope and are uncorrected. ^1H and ^{13}C NMR, all 2D-NMR, and DOSY NMR spectra were recorded on Bruker Avance 400 or

Bruker DMX 600 spectrometers at 300 K, unless otherwise stated, and calibrated to the residual solvent signals. Electron ionization-mass spectra were recorded on a MAT90 spectrometer (Finnigan). The matrix-assisted laser desorption/ionization (MALDI) mass spectra were performed with an autoflex II mass spectrometer (Bruker Daltonics, Bremen). High resolution mass spectra (electrospray ionization, ESI) were recorded on an ESI micrOTOF Focus spectrometer from Bruker Daltonics. Elemental analyses were carried out on a vario MICRO cube (Elementar Analysensysteme GmbH) elemental analysis system at the Institute of Inorganic Chemistry, University of Würzburg. The CV and SWV measurements were performed on a standard, commercial electrochemical analyzer (EC epsilon; BASi, West Lafayette, Indiana) in a three electrode single-compartment cell in an argon atmosphere. Dichloromethane (HPLC grade) was dried over calcium hydride in an argon atmosphere and degassed prior to use. The supporting electrolyte TBAHFP was synthesized according to literature,[193] recrystallized from ethanol/water, and dried in high vacuum. The measurements were carried out under exclusion of air and moisture at a concentration of approximately 2.5×10^{-4} M with ferrocene as an internal standard for the calibration of the potential. Working electrode: Pt disc; reference electrode: Ag/AgCl; auxiliary electrode: Pt wire.

Steady-state UV/Vis absorption and fluorescence spectroscopy: All spectroscopic measurements were conducted with spectroscopic grade solvents (Uvasol®) from Merck (Hohenbrunn, Germany) by using conventional quartz cells (light path 1 or 10 mm). UV/Vis spectra were recorded on a Perkin-Elmer UV/Vis spectrometer Lambda 35 or a Lambda 40 and a Perkin Elmer Peltier temperature controller was used. Fluorescence emission and excitation spectra were recorded with a PTI QM-4/2003 spectrometer. Polarizers in the specified set-up applying magic angle conditions (54.7°) were used. The fluorescence quantum yields were determined by optical dilution method ($OD_{max} < 0.05$) and were determined as the average value for at least four different excitation wavelengths using *N*,*N'*-bis-(2,6-diisopropylphenyl)perylene 3,4:9,10-tetracarboxylic acid bisimide as reference compound (Φ_{fl} ($CHCl_3$) = 1.00).[194]

Time-resolved absorption and fluorescence spectroscopy: Time-resolved fluorescence decays were obtained by using a time-correlated single photon counting (TCSPC) technique. A mode-locked Ti:sapphire (MaiTai-BB, SpectraPhysics) oscillator was used as the excitation light source, which provides a *fwhm* (full width at half maximum) of 80 fs

with a high repetition rate of 80 MHz. In order to minimize artifacts such as thermal lensing and accumulation effect, the repetition rate was reduced down to 800 kHz using a home-made acousto-optic pulse selector. The picked fundamental pulses were frequency-doubled by a BBO nonlinear crystal (Eksma) of 1 mm thickness. The fluorescence was collected by a microchannel plate photomultiplier (MCP-PMT, R3809U-51, Hamamatsu) with a thermoelectric cooler (C4878, Hamamatsu). Time-resolved fluorescence signals were calculated by a TCSPC board (SPC-130, Becker & Hickel GmbH). The overall instrumental response function (IRF) was determined to be less than 30 ps (*fwhm*) in all spectral regions. The polarization of the photoexcitation pulses was set to be vertical to the laboratory frame by both a half-wave retarder and a Glan laser polarizer and sheet polarizers were used in the fluorescence collection path at magic angle (54.7°) to obtain polarization-independent population decays. The time-resolved femtosecond transient absorption (fs-TA) spectrometer consisted of optical parametric amplifiers (Palitra, Quantronix) pumped by a Ti:sapphire regenerative amplifier system (Integra-C, Quantronix) operating at 1 kHz repetition rate and an optical detection system. The generated OPA pulses had a pulse width of ~100 fs and an average power of 1 mW in the range of 280–2700 nm, which were used as pump pulses. White light continuum (WLC) probe pulses were generated using a sapphire window (3 mm of thickness) by focusing of small portion of the fundamental 800 nm pulses, which was picked off by a quartz plate before entering to the OPA. The time delay between pump and probe beams was carefully controlled by making the pump beam travel along a variable optical delay (ILS250, Newport). Intensities of the spectrally dispersed WLC probe pulses are monitored by a high speed spectrometer (Ultrafast Systems) for both visible and near-infrared (NIR) measurements. To obtain the time-resolved transient absorption difference signal (ΔA) at a specific time, the pump pulses were chopped at 500 Hz and absorption spectra intensities were saved alternately with or without pump pulse. Typically, 4000 pulses excite samples to obtain the fs-TA spectra at a particular delay time. The polarization angle between pump and probe beam was set at the magic angle (54.7°) using a Glan laser polarizer with a half-wave retarder in order to prevent polarization-dependent signals. Cross-correlation *fwhm* in pump-probe experiments was less than 200 fs and chirp of WLC probe pulses was measured to be 800 fs in the 400–800 nm region. To minimize chirp, all reflection optics in the probe beam path and the 2 mm path length of quartz cell were used. The three-dimensional data sets of ΔA *vs.* time and wavelength were subjected to singular value decomposition and global fitting to obtain the kinetic time constants and their associated spectra using Surface Xplorer software (Ultrafast Systems).

Computational chemistry: Quantum chemical calculations were performed using AMBER in HyperChem 7.0.3,[195] MM3*[196,197] force-field in MacroModel 9.8,[198,199] OPLS-AA force-field in Tinker 6.2,[200] the PM6 Hamiltonian,[201] DFT-(D) calculations (B3LYP-D3,[156] B97D,[154] B3LYP[148]) with basis sets 6-311G**,[144-147] SVP,[155] or STO-3G[152,153] in Gaussian09[202] or TurboMole 6.5,[203] and the dispersion-corrected, semi-empirical PM6-DH2[150,151] method in MOPAC2012[204,205] or the CAST software.[206] For the molecular dynamics (MD) simulations with PM6-DH2 65000 time steps each of 1 fs were taken to achieve a total time period of 65 ps at 300 K using a Nose-Hoover thermostat. Subsequent local optimizations with PM6-DH2 were carried out again with the CAST software.

6.2. Syntheses and Characterization

1-(3-Hydroxy-3-methylbut-1-yn-1-yl)-4,5-di-*n*-hexyl-2-iodobenzene (36)

In a 50 mL two-necked-flask were placed 4,5-di-*n*-hexyl-1,2-diiodobenzene (**34**, 1.43 g, 2.88 mmol), copper(I) iodide (20.9 mg, 110 µmol), and bis(triphenylphosphine)-palladium(II) dichloride (39.2 mg, 54.7 µmol) under an argon atmosphere. The flask was evacuated again and under argon atmosphere degassed diisopropylamine (20 mL) was added. The yellow reaction solution was degassed by three "*freeze-pump-thaw*" cycles with an oil pump to remove residual oxygen. Subsequently, 2-methylbut-3-yne-2-ol (**35**, 246 mg, 2.86 mmol) was added to the slightly turbid reaction mixture *via* a syringe over a period of 15 min. After stirring over night at room temperature the light-brown suspension was poured into a saturated, aqueous ammonium chloride solution and extracted with dichloromethane. The combined organic layers were washed with dilute aqueous HCl solution and water, dried over magnesium sulfate and concentrated under reduced pressure. The resulting brown oil was submitted to column chromatography on silica gel (dichloromethane) to obtain a brownish oil (865 mg, 1.90 mmol, 67%).

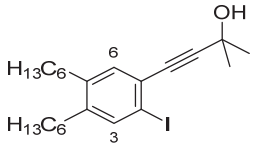

36

^{1}H NMR (400 MHz, CD_2Cl_2): δ = 7.60 (s, 1H, C*H*^{3}), 7.21 (s, 1H, C*H*^{6}), 2.54 (t, J = 6.76 Hz, 2H, CC*H*$_2$), 2.52 (t, J = 6.72 Hz, 2H, CC*H*$_2$), 2.13 (br s, 1H, -O*H*), 1.62 (s, 6H, C(C*H*$_3$)$_2$), 1.58–1.50 (m, 4H, CCH$_2$C*H*$_2$), 1.41–1.28 (m, 12H, C*H*$_2$), 0.90 ppm (2 × t, 6H, 2 × C*H*$_3$); ^{13}C NMR (101 MHz, CD_2Cl_2): δ = 143.9, 141.5, 139.4, 133.4, 126.6, 97.7, 97.0, 84.8, 66.0,

32.6, 32.5, 32.11, 32.09, 31.6, 31.33, 31.28, 29.7, 23.0, 14.3 ppm; IR (ATR): $\tilde{\nu}$ = 3341 cm^{-1} (O–H); MS (EI, 70 eV): *m*/*z* (%): 454.17 (42) [M^+], 439.06 (100) [M^+–CH_3], 327.24 (54) [M^+–I]; MS (MALDI, positive mode, matrix: DCTB, $CHCl_3$): *m*/*z* calcd for $C_{23}H_{35}IO$: 454.173 [M^+], found: 454.147; HRMS (ESI, positive mode, acetonitrile/$CHCl_3$ = 1/1): *m*/*z* calcd for $C_{23}H_{34}I$: 437.17052 [M^+–OH], found: 437.16962; elemental analysis calcd (%) for $C_{23}H_{35}IO$: C 60.79, H 7.76; found: C 61.02, H 7.84.

2-(3-Hydroxy-3-methyl-1-butynyl)-1-(2-triisopropylsilylethynyl)-4,5-di-*n*-hexylbenzene (38)

In a 50 mL two-necked-flask were placed 1-(3-hydroxy-3-methylbut-1-yn-1-yl)-4,5-di-*n*-hexyl-2-iodobenzene (**36**, 816 mg, 1.80 mmol), copper(I) iodide (14.3 mg, 75.1 µmol), and bis(triphenylphosphine)palladium(II) dichloride (30.0 mg, 42.7 µmol) under an argon atmosphere. The reaction flask was evacuated again and degassed diisopropylamine (22 mL) was added. The yellow solution was degassed by three "*freeze-pump-thaw*" cycles with an oil pump to remove residual oxygen and triisopropylsilylacetylene (**37**, 384 mg, 2.10 mmol) was added to the reaction mixture *via* a syringe over a period of 10 min. After stirring over night at room temperature the light-brown suspension was poured into a saturated ammonium chloride solution and extracted with dichloromethane. The organic layer was washed with dilute aqueous HCl solution and water, dried over magnesium sulfate, and concentrated under reduced pressure. The resulting brown oil was submitted to column chromatography on silica gel (dichloromethane/*n*-hexane, 1/1 (v/v)) to obtain an amber-colored oil (862 mg, 1.69 mmol, 94%).

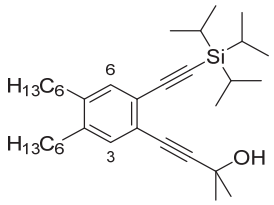

38

^{1}H NMR (400 MHz, CD_2Cl_2): δ = 7.25 (s, 1H, C*H*^{6}), 7.21 (s, 1H, C*H*^{3}), 2.56 (t, ^3J = 7.88 Hz, 4H, CCH_2), 2.00 (s, 1H, O*H*), 1.58 (s, 6H, C(CH_3)$_2$), 1.54 (m_c, 4H, CCH$_2$CH_2), 1.41–1.27 (m, 12H, CH_2CH$_3$), 1.15 (s, 21H, SiC*H*(CH_3)$_2$), 0.90 ppm (t, ^3J = 7.00 Hz, 6H, 2 × CH_3); ^{13}C NMR (101 MHz, $CDCl_3$): δ = 141.4, 141.2, 133.7, 133.2, 123.0, 122.4, 106.0, 96.4, 93.1, 81.5, 65.9, 32.6, 32.5, 31.9, 31.8, 31.6, 31.2, 31.1, 29.48, 29.45, 22.8, 22.7, 18.9, 14.22 (2×), 11.5 ppm; IR (ATR): $\tilde{\nu}$ = 3345 (O–H), 2150 cm^{-1} (C≡C); MS (EI, 70 eV): *m*/*z* (%): 508.29 (4) [M^+], 465.25 (100) [M^+–C_3H_7]; HRMS (ESI, positive mode,

acetonitrile/$CHCl_3$ = 1/1): *m*/*z* calcd for $C_{34}H_{57}OSi$: 509.41787 [M^++H], found: 509.41732; elemental analysis calcd (%) for $C_{34}H_{56}OSi$: C 80.25, H 11.09; found: C 80.48, H 10.81.

1-Ethynyl-2-(2-triisopropylsilylethynyl)-4,5-di-*n*-hexylbenzene (39)

This compound was previously reported to be synthesized with subsequent cross-coupling reactions of 4,5-di-*n*-hexyl-1,2-diiodobenzene with trimethylsilylacetylene and triisopropylsilylacetylene, selective deprotection under basic conditions yielding **39** in an overall yield of 47%.

In a mixture of toluene (7 mL) and 1,4-dioxane (1 mL) was dissolved 2-(3-hydroxy-3-methylbut-1-yn-1-yl)-1-(2-triisopropylsilylethynyl)-4,5-di-*n*-hexylbenzene (**38**, 251 mg, 494 µmol) and heated to 125 °C under argon. To the reaction mixture was added fine powdered sodium hydroxide (33.6 mg, 840 µmol), stirred for 1.5 h at 125 °C, and then allowed to cool down to room temperature, quenched with water and diluted with *n*-hexane. The organic phase was washed with 2 M HCl solution and water, dried over magnesium sulfate, and concentrated under reduced pressure to yield a pale yellow oil (222 mg, 491 µmol, quant.).

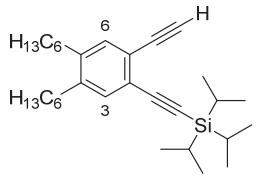

39

^{1}H NMR (400 MHz, CD_2Cl_2): δ = 7.27 (s, 1H, CH^6), 7.26 (s, 1H, CH^3), 3.23 (s, 1H, ≡C*H*), 2.57 (t, ^3J = 7.92 Hz, 4H, CH_2), 1.59–1.51 (m, 4H, CH_2), 1.40–1.30 (m, 12H, CH_2), 1.15 (s, 21H, Si(C*H*(CH_3)$_2$)$_3$), 0.90 (t, ^3J = 7.08 Hz, 3H, CH_3), 0.89 ppm (t, ^3J = 7.02 Hz, 3H, CH_3); ^{13}C NMR (101 MHz, CD_2Cl_2): δ = 142.4, 142.0, 133.6, 133.4, 124.2, 122.5, 105.8, 94.2, 83.1, 80.3, 32.9, 32.8, 32.21, 32.19, 31.5, 31.4, 29.83, 29.76, 23.12, 23.11, 19.0, 14.3, 11.9 ppm; IR (ATR): $\tilde{\nu}$ = 3315 (≡C–H), 2154 cm^{-1} (C≡C); MS (EI, 70 eV): *m*/*z* (%): 450.26 (8) [M^+], 407.23 (100) [M^+–C_3H_7]; MS (EI, exact): *m*/*z* calcd for $C_{31}H_{50}Si$: 450.36818 [M^+], found: 450.36806; elemental analysis calcd (%) for $C_{31}H_{50}Si$: C 82.59, H 11.18; found: C 82.78, H 10.72.

_N_-(3-Iodophenyl)-_N_'-(12-tricosanyl)perylene-3,4:9,10-tetracarboxylic acid bisimide (30)

In a 10 mL flask was placed _N_-(12-tricosanyl)perylene-3,4:9,10-tetracarboxylic acid-3,4-anhydride-9,10-imide (**40**, 269 mg, 377 µmol), 3-iodoaniline (**41**, 118 mg, 540 µmol), and imidazole (1.78 g) under argon. The reaction flask was evacuated once again and purged with argon. Subsequently, pyridine (1.8 mL) was added and the reaction mixture was heated to 150 °C for 2.5 h. The reaction mixture was allowed to cool down to room temperature and then diluted with dichloromethane, washed twice with 2 M HCl solution and water, dried over magnesium sulfate, and concentrated under reduced pressure. The resulting red solid was submitted to column chromatography on silica gel (dichloromethane), recrystallized with dichloromethane/methanol and dried _in vacuo_ (40 °C, 10^{-2} mbar) yielding a deep-red solid (334 mg, 365 µmol, 97%).

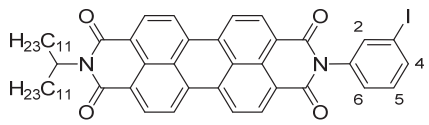

30

M.p. > 300 °C; ^{1}H NMR (400 MHz, $CDCl_3$): δ = 8.75–8.65 (m, 8H, H_{PBI}), 7.85 (dt, ^{3}J(H,H) = 7.5 Hz, ^{4}J(H,H) = 1.6 Hz, 1H, CH^{4}), 7.72 (t, ^{4}J(H,H) = 1.7 Hz, 1H, CH^{2}), 7.35 (dt, ^{3}J(H,H) = 8.1 Hz, ^{4}J(H,H) = 1.6 Hz, 1H, CH^{6}), 7.31 (t, ^{3}J(H,H) = 7.7 Hz, 1H, CH^{5}), 5.22–5.15 (m, 1H, NCH), 2.30–2.20 (m, 2H, CHCH_2), 1.91–1.83 (m, 2H, CHCH_2), 1.38–1.20 (m, 36H, (CH_2)$_9$$CH_3$), 0.84 ppm (t, ^{3}J(H,H) = 6.9 Hz, 6H, CH_2CH_3); ^{13}C NMR (101 MHz, $CDCl_3$): δ = 163.5, 138.1, 137.8, 136.3, 135.5, 134.3, 132.1, 130.9, 130.0, 129.7, 128.4, 126.9, 126.6, 123.5, 123.21, 123.16, 94.1, 55.0, 32.5, 32.0, 29.76, 29.75, 29.72, 29.69, 29.68, 29.5, 27.1, 22.8, 14.2 ppm; IR (ATR): $\tilde{\nu}$ = 1697, 1656 cm^{-1} (C=O); UV/Vis ($CHCl_3$): λ_{max} (ε) = 528 (83100), 491 (50000), 460 (18100), 262 nm (33500 M^{-1} cm^{-1}); fluorescence ($CHCl_3$): λ_{max} = 532, 574, 622 nm (λ_{exc} = 480 nm), Φ_{fl} = 0.97 ± 0.03; MS (EI, 70 eV): _m_/_z_ (%): 914.38 (8) [M^{+}], 83.13 (100); HRMS (ESI, positive mode, acetonitrile/$CHCl_3$ = 1/1): _m_/_z_ calcd for $C_{53}H_{60}IN_2O_4$: 915.3597 [M^{+}+H], found: 915.3591; elemental analysis calcd (%) for $C_{53}H_{59}IN_2O_4$: C 69.57, H 6.50, N 3.06; found: C 69.60, H 6.89, N 2.88; CV (CH_2Cl_2, 0.1 M TBAHFP, _vs_. Fc/Fc^{+}): $E_{1/2}$ (PBI/PBI^{-}) = –1.04 V, $E_{1/2}$ (PBI^{-}/PBI^{2-}) = –1.24 V.

_N_-(3-(2'-(2-Triisopropylsilylethynyl)-4',5'-di-_n_-hexylphenyl)ethynyl)phenyl)-_N_'-(12-tricosanyl)perylene-3,4:9,10-tetracarboxylic acid bisimide (42)

In a 100 mL two-necked-flask was placed *N*-(3-iodophenyl)-*N*'-(12-tricosanyl)perylene-3,4:9,10-tetracarboxylic acid bisimide (**30**, 280 mg, 306 µmol), copper(I) iodide (5.9 mg, 31.0 µmol), triphenylphosphine (7.5 mg, 28.6 µmol), and bis(triphenyl-phosphine)palladium(II) dichloride (10.0 mg, 14.2 µmol) under an argon atmosphere. The flask was evacuated again and dry THF (35 mL) was added. The bright-orange solution was heated at 70 °C for 5 min to dissolve PBI **30**. After being cooled to room temperature, the solution was degassed by three "*freeze-pump-thaw*" cycles with an oil pump to remove residual oxygen. In the meantime, a second solution containing 1-ethynyl-2-(2-triisopropylsilylethynyl)-4,5-di-*n*-hexylbenzene (**39**, 126 mg, 279 µmol) and dry triethylamine (8 mL) was degassed three times by "*freeze-pump-thaw*" cycles. Under light exclusion by covering the flask with aluminium foil, this solution was added dropwise to the reaction mixture within 1.5 h at room temperature. The reaction mixture was refluxed over night at 70 °C. After being cooled to room temperature, the reaction mixture was poured onto 2 M aqueous HCl solution (200 mL), extracted with dichloromethane and washed with water. The organic layer was dried over Na_2SO_4, concentrated under reduced pressure and submitted to column chromatography on silica gel (dichloromethane/*n*-hexane, 2/1 (v/v)). The product was then dried *in vacuo* at 120 °C at 10^{-2} mbar and a red, glassy solid was obtained (225 mg, 181 µmol, 65%).

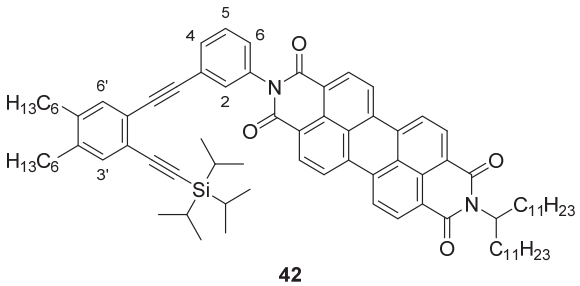

42

M.p. 99–107 °C; ^{1}H NMR (400 MHz, $CDCl_3$): δ = 8.75–8.63 (m, 8H, H_{PBI}), 7.65–7.63 (dt, ^3J(H,H) = 8.00 Hz, ^4J(H,H) = 1.29 Hz, 1H, CH^4), 7.55–7.51 (m, 2H, 2 × C$H^{2,5}$), 7.34–7.31 (dq, ^3J(H,H) = 7.88 Hz, ^4J(H,H) = 1.05 Hz, 1H, C$H^{6'}$), 7.29 (s, 1H, C$H^{6'}$), 7.26 (s, 1H, C$H^{3'}$), 5.22–5.15 (m, 1H, NCH), 2.58–2.53 (dt, J(H,H) = 7.80 Hz, J(H,H) = 1.48 Hz, 4H, CCH_2), 2.30–2.20 (m, 2H, CH(CH_2)$_2$), 1.91–1.83 (m, 2H, CH(CH_2)$_2$), 1.59–1.51 (m, 4H, CH_2(CH$_2$)$_3$CH$_3$), 1.39–1.20 (m, 48H, CH_2), 1.09 (s, 21H, SiCH(CH_3)$_2$)$_3$), 0.92–0.86 (m, 6H, (CH$_2$)$_5$CH_3), 0.84 ppm (t, ^3J(H,H) = 6.90 Hz, 6H, (CH$_2$)$_{10}$CH_3); ^{13}C NMR (101 MHz, $CDCl_3$): δ = 163.6, 142.2, 142.1, 136.0, 135.4, 134.5, 133.8, 133.3, 132.6, 132.1, 131.9, 130.1, 129.8, 129.6, 129.3, 127.0, 126.6, 125.2, 123.7, 123.6, 123.5, 123.4, 123.0, 106.2,

94.1, 91.3, 90.2, 55.1, 32.9, 32.79, 32.78, 32.3, 32.14, 32.11, 31.4, 31.3, 30.06, 30.05, 30.03, 30.00, 29.98, 29.77, 29.76, 29.71, 27.4, 23.09, 23.05, 23.03, 18.9, 14.28, 14.26, 11.8 ppm; IR (ATR): $\tilde{\nu}$ = 2149 (C≡C), 1697, 1656 cm^{-1} (C=O); UV/Vis ($CHCl_3$): λ_{max} (ε) = 527 (83700), 491 (50400), 460 (18300), 324 (18300), 305 (23900), 263 nm (78500 M^{-1} cm^{-1}); fluorescence ($CHCl_3$): λ_{max} = 530, 574, 620 nm (λ_{exc} = 480 nm), Φ_{fl} = 0.55 ± 0.01; MS (MALDI, positive mode, matrix: DCTB; $CHCl_3$): *m*/*z* calcd for $C_{84}H_{109}N_2O_4Si$: 1237.817 [M^++H], found: 1237.825; elemental analysis calcd (%) for $C_{84}H_{108}N_2O_4Si$: C 81.50, H 8.79; N 2.26; found: C 81.27, H 8.95, N 2.40.

_N_-(3-((2'-Ethynyl-4',5'-di-_n_-hexylphenyl)ethynyl)phenyl)-_N'_-(12-tricosanyl)perylene-3,4:9,10-tetracarboxylic acid bisimide (43)

To deprotect the silyl group, *N*-(3-(2'-(2-triisopropylsilylethynyl)-4',5'-di-*n*-hexylphenyl)ethynyl)phenyl)-*N*'-(12-tricosanyl)perylene-3,4:9,10-tetracarboxylic acid bisimide (**42**, 47.3 mg, 38.2 µmol) was dissolved in THF (10 mL) and to the resulting deep-red solution was added tetra-*n*-butylammonium fluoride solution in THF (1 M, 70 µL, 70 µmol). The color of the reaction mixture changed immediately to dark green. After stirring for 10 min at room temperature, a saturated aqueous ammonium chloride solution was added and the reaction mixture was extracted with dichloromethane. The combined organic layers were washed with water, dried over magnesium sulfate, concentrated *in vacuo*, and the residue was submitted to column chromatography on silica gel (dichloromethane/*n*-hexane, 2/1 (v/v)) to obtain a red, glassy solid (39.2 mg, 36.2 µmol, 95%).

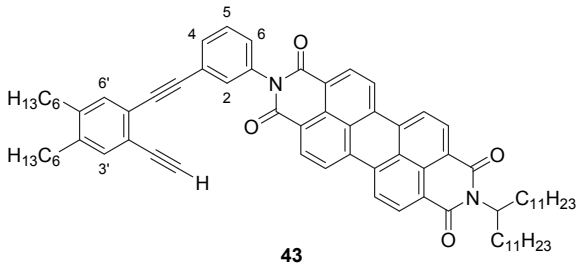

43

M.p. > 300 °C; ^{1}H NMR (400 MHz, CD_2Cl_2): δ = 8.67–8.54 (m, 8H, H_{PBI}), 7.69–7.67 (dt, ^3J(H,H) = 7.9 Hz, ^4J(H,H) = 1.3 Hz, 1H, CH^4), 7.58 (t, ^3J(H,H) = 7.9 Hz, 1H, CH^5), 7.54 (t, ^4J(H,H) = 1.6 Hz, 1H, CH^2), 7.40–7.37 (dq, ^3J(H,H) = 7.9 Hz, ^4J(H,H) = 1.1 Hz, 1H, CH^6), 7.33 (s, 1H, C$H^{6'}$), 7.31 (s, 1H, C$H^{3'}$), 5.20–5.13 (m, 1H, NCH), 3.34 (s, 1H, ≡CH), 2.61–2.57 (m, 4H, 2 × CCH_2), 2.29–2.20 (m, 2H, CH(CH_2)$_2$), 1.92–1.83 (m, 2H, CH(CH_2)$_2$), 1.60–1.53 (m, 4H, 2 × CH_2(CH_2)$_3$$CH_3$), 1.42–1.21 (m, 48H, C$H_2$), 0.92–0.87

(m, 6H, 2 × $(CH_2)_5CH_3$), 0.84 ppm (t, ^3J(H,H) = 6.9 Hz, 6H, 2 × $(CH_2)_{10}CH_3$); ^{13}C NMR (101 MHz, $CDCl_3$): δ = 163.8, 142.6, 142.3, 136.2, 135.6, 134.6, 133.6, 132.9, 132.32, 132.24, 132.0, 129.9, 129.8, 129.4, 127.1, 125.10, 125.06, 123.8, 123.6, 123.5, 123.3, 122.1, 91.5, 89.8, 82.7, 80.5, 55.0, 32.80, 32.77, 32.3, 32.1, 31.2, 30.5, 30.04, 30.01, 29.98, 29.96, 29.75, 29.72, 27.4, 23.1, 23.0, 14.27, 14.26 ppm; IR (ATR): $\tilde{\nu}$ = 3236 (≡CH), 2155 (C≡C), 1696, 1656 cm^{-1} (C=O); UV/Vis ($CHCl_3$): λ_{max} (ε) = 528 (77500), 491 (46800), 460 (17000), 319 (20600), 301 (25300), 257 nm (63400 M^{-1} cm^{-1}) ; fluorescence ($CHCl_3$): λ_{max} = 532, 574, 622 nm (λ_{exc} = 480 nm), Φ_{fl} = 0.86 ± 0.01; HRMS (ESI, positive mode, acetonitrile/$CHCl_3$ = 1/1): *m*/*z* calcd for $C_{75}H_{89}N_2O_4$: 1081.68221 [M^++H], found: 1081.68105.

Folda-dimer 32

To a mixture of *N*-(3-(2'-(2-triisopropylsilylethynyl)-4',5'-di-*n*-hexylphenyl)-ethynyl)phenyl)-*N*'-(12-tricosanyl)perylene-3,4:9,10-tetracarboxylic acid bisimide (**42**, 299 mg, 241 µmol) and dry THF (10 mL) under argon atmosphere was added tetra-*n*-butylammonium fluoride in THF (1 M, 310 µL, 310 µmol) dropwise. To this solution with *in situ* formed PBI **43**, triethylamine (2 mL) was added and the resulting raspberry colored mixture was degassed twice. Additionally, to a second mixture of *N*-(3-iodophenyl)-*N*'-(12-tricosanyl)perylene-3,4:9,10-tetracarboxylic acid bisimide (**30**, 258 mg, 282 µmol), copper(I) iodide (4.4 mg, 23.1 µmol), triphenylphosphine (7.0 mg, 26.7 µmol), and bis(triphenylphosphine)palladium(II) dichloride (8.5 mg, 12.1 µmol) was added dry THF (35 mL), which was afterwards degassed by three "*freeze-pump-thaw*" cycles. The resulting red reaction mixture was heated to 75 °C and the PBI **43** containing solution was added dropwise within 45 min. The reaction mixture was stirred over night at 75 °C and after being cooled to room temperature poured into saturated aqueous ammonium chloride solution, diluted with dichloromethane and washed successively with water, aqueous 2 M HCl solution, and water. The combined organic layers were dried over magnesium sulfate and evaporated under reduced pressure. The resulting deep-red residue was prepurified by column chromatography on silica gel (dichloromethane → dichloromethane/methanol, 98/2 (v/v)) to obtain a bright red solid (crude product, 413 mg, 92%). Afterwards, a portion (54 mg) of the crude product was submitted to recycling gel permeation chromatography (GPC) to separate from side-products. After drying under 10^{-2} mbar vacuum at 100 °C, a deep-red solid was obtained (40.2 mg, 21.5 µmol, overall yield 69%).

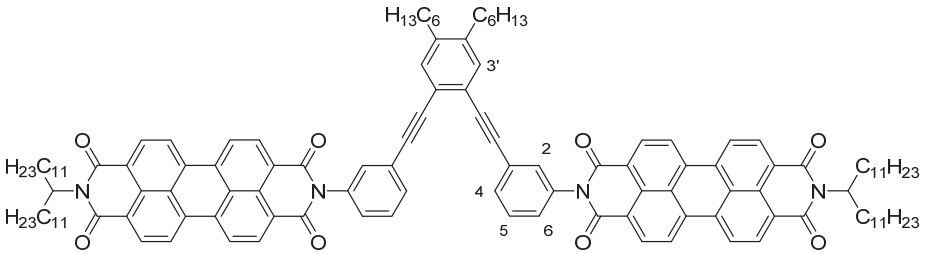

32

M.p. > 300 °C; ^{1}H NMR (600 MHz, $CDCl_3$): δ = 8.59–8.44 (m, 16H, H_{PBI}), 7.68–7.66 (dt, 1H, ^{3}J(H,H) = 7.92 Hz, ^{4}J(H,H) = 1.28 Hz, CH^{4}), 7.58 (t, ^{3}J(H,H) = 1.56 Hz, 1H, CH^{2}), 7.53 (t, ^{4}J(H,H) = 7.83 Hz, 1H, CH^{5}), 7.32 (s, 2H, 2 × CCH), 7.30–7.28 (dq, ^{3}J(H,H) = 7.80 Hz, ^{4}J(H,H) = 0.92 Hz, 1H, CH^{6}), 5.20–5.05 (m, 2H, 2 × NCH), 2.73–2.57 (m, 4H, 2 × CCH_2), 2.25–2.17 (m, 2H, 2 × CH(CH_2)$_2$), 1.90–1.86 (m, 2H, 2 × CH(CH_2)$_2$), 1.68–1.57 (m, 4H, 2 × CH_2(CH$_2$)$_3$CH$_3$), 1.39–1.19 (m, 48H, CH_2), 0.89 (t, ^{3}J(H,H) = 6.93 Hz, 6H, 2 × (CH$_2$)$_5$CH_3), 0.83 ppm (t, ^{3}J(H,H) = 7.08 Hz, 6H, 2 × (CH$_2$)$_{10}$CH_3); ^{13}C NMR (151 MHz, $CDCl_3$): δ = 163.2, 141.6, 135.0, 134.9, 134.1, 132.2, 132.1, 131.7, 129.8, 129.6, 129.3, 128.6, 125.0, 123.5, 123.4, 123.2, 123.0, 89.8, 88.7, 55.1, 32.7, 32.6, 32.1, 31.9, 31.0, 29.83, 29.80, 29.78 (2×), 29.74, 29.50, 29.48, 27.2, 22.8, 22.7, 14.2 ppm; IR (ATR): $\tilde{\nu}$ = 2154 (C≡C), 1697, 1655 cm^{-1} (C=O); UV/Vis ($CHCl_3$): λ_{max} (ε) = 529 (123600), 493 (96100), 462 (37300), 370 nm (8500 M^{-1} cm^{-1}); UV/Vis (THF): λ_{max} (ε) = 526 (73800), 492 (91400), 369 nm (7900 M^{-1} cm^{-1}); fluorescence: λ_{max} ($CHCl_3$) = 537, 580 nm (λ_{exc} = 480 nm); λ_{max} (THF) = 533, 575, 615 nm (λ_{exc} = 480 nm), Φ_{fl} ($CHCl_3$) = 0.28 ± 0.02; Φ_{fl} (THF) = 0.16 ± 0.02; MS (MALDI, positive mode, matrix: DCTB; $CHCl_3$): *m*/*z* calcd for $C_{128}H_{146}N_4O_8$: 1867.114 [M^+], found: 1867.084. HRMS (ESI, positive mode, acetonitrile/$CHCl_3$ = 1/1): *m*/*z* calcd for $C_{128}H_{147}N_4O_8$: 1868.12185 [M^++H], found: 1868.12186; elemental analysis calcd (%) for $C_{128}H_{146}N_4O_8$: C 82.28, H 7.88, N 3.00; found: C 82.33, H 7.80, N 3.15.

Folda-trimer 33

This compound was synthesized and purified according to the procedure described for folda-dimer **32** using PBI compound **42** (357.4 mg, 289 µmol), dry THF (40 mL), and tetra-*n*-butylammonium fluoride in THF (1 M, 350 µL, 350 µmol) as well as triethylamine (2.7 mL) to prepare *in situ* the PBI **43** containing solution. A mixture of copper(I) iodide (5.4 mg, 28.4 µmol), bis(triphenylphosphine)palladium(II) dichloride (11.4 mg, 16.2 µmol), triphenylphosphine (8.4 mg, 32.0 µmol), and *N*-(3,5-diiodophenyl)-*N*'-(12-tricosanyl)perylene-3,4:9,10-tetracarboxylic acid bisimide (**44**, 142 mg, 136 µmol) in dry

THF (80 mL) was prepared, which was degassed three times and afterwards heated to 75 °C before the solution containing compound **43** was added dropwise. After column chromatography on silica gel (dichloromethane → dichloromethane/methanol, 98/2 (v/v)) a bright red solid (crude product; 362 mg, 90%) was obtained. The use of GPC was necessary affording a deep-red solid (overall yield 44%).

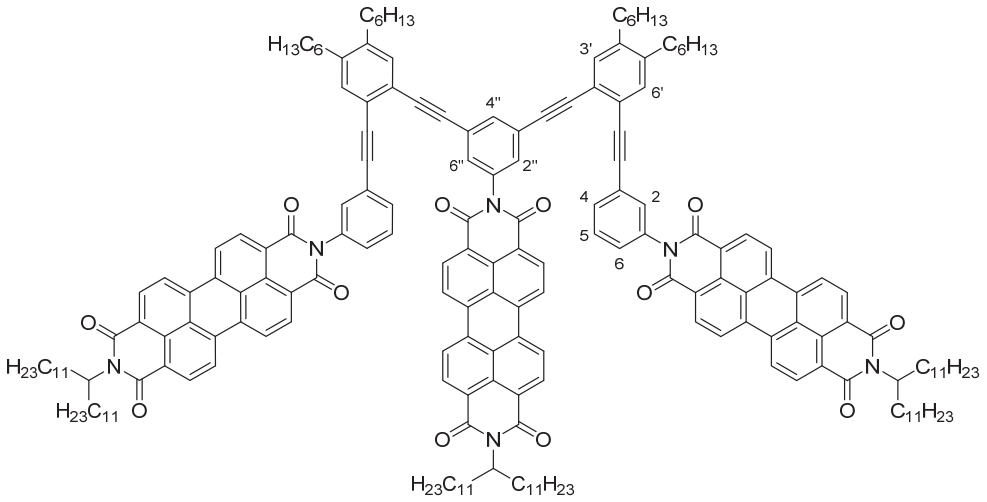

33

M.p. = 273–276 °C; ^{1}H NMR (600 MHz, [D$_8$]THF, 328 K): δ = 8.39 (d, 2H, H_{PBI}), 8.31 (d, 4H, H_{PBI}), 8.15 (d, 4H, H_{PBI}), 7.99 (d, 2H, H_{PBI}), 7.87 (s, 4H, H^2,$H^{2''}$), 7.81 (d, 4H, H_{PBI}), 7.74 (br s, 4H, H_{PBI}), 7.65 (s, 1H, $H^{4''}$), 7.56 (d, 2H, H^4), 7.44–7.41 (m, 10H, H_{PBI},H^5,$H^{3'}$,$H^{6'}$), 7.22 (d, 2H, H^6), 5.36–5.31 (m, 1H, NCH(CH$_2$)$_2$), 4.93 (quin, 2H, NCH(CH$_2$)$_2$), 2.72–2.66 (m, 8H, CCH_2(CH$_2$)$_4$CH$_3$), 2.16–2.10 (m, 4H, NCH(CH_2)$_2$), 2.00–1.94 (m, 8H, NCH(CH_2)$_2$), 1.70–1.63 (m, 8H, CCH$_2$CH_2(CH$_2$)$_3$CH$_3$), 1.58–1.27 (m, 126H, CH_2), 0.90–0.82 ppm (m, 30H, CH_3); ^{13}C NMR (151 MHz, [D$_8$]THF): δ = 163.0, 162.4, 142.1, 142.0, 137.3, 134.2, 133.7, 133.5, 132.5, 132.2, 132.1, 131.5, 131.0, 130.1, 130.0, 129.8, 129.2, 128.9, 126.1, 125.8, 125.7, 125.3, 125.2, 124.7, 124.5, 123.9, 123.6, 123.3, 122.6, 121.6, 93.4, 92.7, 89.6, 89.4, 55.4, 55.2, 33.6, 33.2, 33.1, 32.7, 32.6, 32.5, 32.4, 31.7, 31.6, 30.9, 30.7, 30.6, 30.53, 30.51, 30.47, 30.43, 30.42, 30.40, 30.37, 30.33, 30.12, 30.08, 30.06, 30.04, 30.01, 29.2, 28.7, 28.1, 27.8, 27.2, 23.3, 23.2, 14.12, 14.09 ppm; IR (ATR): $\tilde{\nu}$ = 1697, 1657 cm^{-1} (C=O); UV/Vis (CHCl$_3$): λ_{max} (ε) = 531 (118300), 495 (12100), 371 nm (11900 M^{-1} cm^{-1}); UV/Vis (THF): λ_{max} (ε) = 535 (66700), 495 (109300), 372 nm (10800 M^{-1} cm^{-1}); fluorescence: λ_{max} (CHCl$_3$) = 540, 600 nm (λ_{exc} = 480 nm); λ_{max} (THF) = 532, 617 nm (λ_{exc} = 480 nm), Φ_{fl} (CHCl$_3$) = 0.22 ± 0.02, Φ_{fl} (THF) = 0.12 ± 0.01; MS (MALDI, positive mode, matrix: DCTB; CHCl$_3$): m/z calcd for C$_{203}$H$_{232}$N$_6$O$_{12}$: 2945.773 [M^+], found: 2945.799; elemental analysis calcd (%) for C$_{203}$H$_{232}$N$_6$O$_{12}$: C 82.70, H 7.93, N 2.85; found: C 82.61, H 8.28, N 2.82.

1-Phenylethynyl-2-(2-triisopropylsilylethynyl)-4,5-di-*n*-hexylbenzene (46)

1-Ethynyl-2-(2-triisopropylsilylethynyl)-4,5-di-*n*-hexylbenzene (**39**, 171 mg, 378 µmol) and dry triethylamine (20 mL) were placed in a 100 mL two-necked-flask. A portion iodobenzene (**45**, 94.3 mg, 453 µmol), bis(triphenylphosphine)palladium(II) dichloride (9.6 mg, 13.4 µmol), and copper(I) iodide (7.0 mg, 36.8 µmol) were added and the reaction mixture was degassed by three "*freeze-pump-thaw*" cycles to remove residual oxygen. Afterwards the mixture was heated at 50 °C for 4 h under stirring and then allowed to cool down to room temperature, diluted with dichloromethane, and washed with 2 M hydrochloric acid and water. The organic phase was dried over magnesium sulfate, concentrated by rotary evaporator, and purified by column chromatography on silica gel (*n*-hexane). The product was then dried at room temperature under 10^{-2} mbar to yield a yellow, viscous oil (172 mg, 326 µmol, 86%).

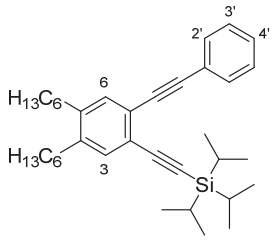

46

^{1}H NMR (400 MHz, CD_2Cl_2): δ = 7.55–7.50 (m, 2H, C$H^{2'}$), 7.38–7.27 (m, 5H, C$H^{3,6,3',4'}$), 2.62–2.57 (m, 4H, CCH_2), 1.62–1.54 (m, 4H, CCH_2CH_2), 1.43–1.31 (m, 12H, $(CH_2)_3CH_3$), 1.18–1.13 (m, 21H, SiCH(CH_3)$_2$), 0.91 (t, ^3J = 7.1 Hz, 3H, $(CH_2)_5CH_3$), 0.91 ppm (t, ^3J = 7.0 Hz, 3H, CH_3); ^{13}C NMR (101 MHz, CD_2Cl_2): δ = 142.1, 142.0, 133.8, 133.2, 132.1, 128.64, 128.59, 123.9, 123.28, 123.25, 106.2, 94.0, 92.3, 88.9, 32.9, 32.8, 32.2, 32.1, 31.44, 31.38, 29.8, 29.7, 23.07, 23.05, 18.9, 14.3, 11.8 ppm; MS (EI, 70 eV): *m/z* (%) 526.3 (100) [M^+]; MS (MALDI, positive mode, matrix: DCTB, $CHCl_3$): *m/z* calcd for $C_{37}H_{54}Si$: 526.399 [M^+], found: 526.329; elemental analysis calcd (%) for $C_{37}H_{54}Si$: C 84.34, H 10.33; found: C 84.43, H 10.50.

1-Ethynyl-2-(phenylethynyl)-4,5-di-*n*-hexylbenzene (47)

In a 50 mL Schlenk flask were placed 1-phenylethynyl-2-(2-triisopropylsilylethynyl)-4,5-di-*n*-hexylbenzene (**46**, 127 mg, 240 µmol) and dry THF (20 mL). The flask was purged with argon and a septum was added. The reaction mixture was cooled down to 0 °C and TBAF solution in THF (1 M, 1 mL, 1 mmol) was dropped to the flask. The reaction mixture was stirred for 2.75 h at 0 °C and then 2 h at room temperature. Afterwards, water (3 mL)

was poured into the flask to quench the reaction. The biphasic mixture was then extracted with *n*-hexane and washed with saturated aqueous ammonium chloride solution and water. The organic layer was then dried over sodium sulfate and concentrated under reduced pressure. The residue was submitted to column chromatography on silica (*n*-hexane) to obtain a pale yellow oil (89.1 mg, 240 µmol, quant.).

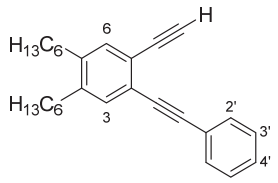

47

^{1}H NMR (400 MHz, CD_2Cl_2): δ = 7.58–7.53 (m, 2H, C$H^{2'}$), 7.40–7.35 (m, 3H, C$H^{3',4'}$), 7.34 (s, 1H, C$H_{arom.}$), 7.33 (s, 1H, C$H_{arom.}$), 3.35 (s, 1H, C≡CH), 2.63–2.58 (m, 4H, 2 × CCH_2), 1.62–1.54 (m, 4H, 2 × CCH$_2$CH_2), 1.44–1.30 (m, 12H, 2 × (CH_2)$_3$CH$_3$), 0.93–0.89 ppm (m, 6H, 2 × CH_3); ^{13}C NMR (101 MHz, CD_2Cl_2): δ = 142.6, 142.1, 133.6, 132.8, 132.0, 129.8, 128.8, 123.8, 123.6, 122.1, 92.6, 88.6, 82.9, 80.3, 32.8, 32.8, 32.1, 31.3, 29.74, 29.73, 23.0, 14.3 ppm; MS (EI, 70 eV): *m*/*z* (%) 370.3 (100); MS (MALDI, positive mode, matrix: DCTB; $CHCl_3$): *m*/*z* calcd for $C_{28}H_{34}$: 370.266 [M^+], found: 370.235; HRMS (ESI, positive mode, acetonitrile/$CHCl_3$ = 1/1): *m*/*z* calcd for $C_{28}H_{34}$: 371.27388 [M^+], found: 371.27355; elemental analysis calcd (%) for $C_{28}H_{34}$: C 90.75, H 9.25; found: C 90.73, H 9.51.

PBI reference compound 31

To a mixture of PBI **30** (174 mg, 190 µmol), copper(I) iodide (3.0 mg, 15.8 µmol), bis(triphenylphosphine)palladium(II) dichloride (8.3 mg, 11.8 µmol), and triphenylphosphine (4.8 mg, 18.3 µmol) was added dry THF (70 mL). A second solution containing 1-ethynyl-2-(phenylethynyl)-4,5-di-*n*-hexylbenzene (**47**, 66.5 mg, 180 µmol), dry THF (8 mL), and dry NEt_3 (1 mL) was prepared. Both solutions were degassed by three "*freeze-pump-thaw*" cycles. The solution containing compound **47** was then dropped into the first solution at 75 °C reaction temperature. The reaction mixture was stirred over night at 75 °C and after being cooled to room temperature, poured into a saturated, aqueous ammonium chloride solution, diluted with dichloromethane, and washed successively with water, aqueous 2 M HCl solution, and water. The combined organic layers were dried over magnesium sulfate and evaporated under reduced pressure. The resulting crude product was

purified by column chromatography on silica gel (dichloromethane), dried at 120 °C and 10^{-2} mbar to yield a red solid (44.3 mg, 38.7 µmol, 21%).

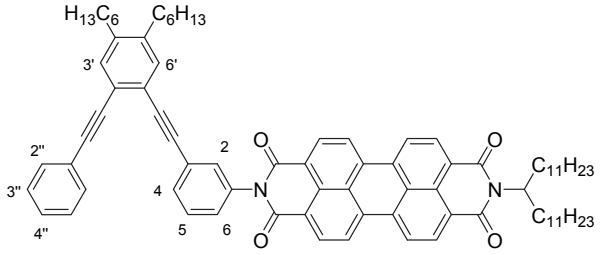

31

M.p. 116–121 °C; ^{1}H NMR (400 MHz, CD_2Cl_2): δ = 8.66–8.56 (m, 8H, H_{PBI}), 7.68–7.65 (m, 1H, H^4), 7.58–7.54 (td, ^3J = 7.86 Hz, 0.44 Hz, 1H, H^5), 7.54–7.50 (m, 3H, $H^2 + 2 \times H^{2''}$), 7.38–7.36 (dq, ^3J = 7.88 Hz, 1.09 Hz, 1H, H^6), 7.34 (s, 1H, $H^{6'}$), 7.33 (s, 1H, $H^{3'}$), 7.27–7.23 (m, 2H, 2 × $H^{3''}$), 7.17–7.13 (tt, ^3J = 7.79 Hz, 1.32 Hz, 1H, $H^{4''}$), 5.20–5.13 (m, 1H, NC*H*), 2.60 (t, ^3J = 7.90 Hz, 4H, CCH_2), 2.29–2.20 (m, 2H, CH(CH_2)$_2$), 1.91–1.83 (m, 2H, CH(CH_2)$_2$), 1.63–1.55 (m, 4H, 2 × CCH$_2$CH_2), 1.43–1.21 (m, 54H, CH_2), 0.91 (t, ^3J = 7.04 Hz, 3H, (CH$_2$)$_5$CH_3), 0.90 (t, ^3J = 7.08 Hz, 3H, (CH$_2$)$_5$CH_3), 0.84 ppm (t, ^3J = 7.90 Hz, 6H, (CH$_2$)$_{10}$CH_3); ^{13}C NMR (101 MHz, CD_2Cl_2): δ = 163.7, 142.3, 142.1, 136.2, 135.6, 134.6, 132.74, 132.70, 132.5, 131.9, 130.2, 129.9, 129.8, 129.3, 128.8, 128.6, 127.1, 126.7, 125.2, 123.81, 123.78, 123.6, 123.5, 123.4, 123.0, 92.9, 91.8, 90.2, 88.9, 55.0, 32.9, 32.84, 32.77, 32.3, 32.1, 31.29, 31.27, 30.04, 30.01, 29.98, 29.97, 29.8, 27.4, 23.1, 23.0, 14.3 ppm; UV/Vis ($CHCl_3$): λ_{max} (ε) = 527.5 (84200), 490.5 (50800), 459.5 (18800), 434.5 (5900), 369.5 (5500), 306 (25000), 282 (64200), 261.5 nm (65500 M^{-1} cm^{-1}); fluorescence ($CHCl_3$): λ_{max} = 537, 579, 627 nm (λ_{exc} = 480 nm), Φ_{fl} = 0.21 ± 0.01; MS (MALDI, positive mode, matrix: DCTB; $CHCl_3$): *m*/*z* calcd for $C_{81}H_{92}N_2O_4$: 1156.706 [M^+], found: 1156.730; HRMS (ESI, positive mode, acetonitrile/$CHCl_3$ = 1/1): *m*/*z* calcd for $C_{81}H_{93}N_2O_4$: 1157.71387 [M^++H], found: 1157.71351; elemental analysis calcd (%) for $C_{81}H_{92}N_2O_4$: C 84.04, H 8.01, N 2.42; found: C 83.12, H 7.90, N 2.24.

1,2-Bis(phenylethynyl)-4,5-di-*n*-hexylbenzene (49)

In a 50 mL flask were placed 1,2-diethynyl-4,5-di-*n*-hexylbenzene (**48**, 66.2 mg, 225 µmol), bis(triphenylphosphine)palladium(II) dichloride (5.5 mg, 7.84 µmol), and copper(I) iodide (4.8 mg, 25.2 µmol) under nitrogen atmosphere. The flask was evacuated again and degassed diisopropylamine (10 mL) were added under nitrogen atmosphere. A second solution containing iodobenzene (**45**, 103 mg, 504 µmol) in diisopropylamine (4 mL) was prepared under nitrogen. Both flasks were degassed by two "*freeze-pump-*

thaw". The solution containing iodobenzene was then dropped into the first solution with a septum at 50 °C within 30 min. The reaction mixture was stirred over night at 50 °C. After being cooled to room temperature, the reaction mixture was poured into a 2 M aqueous HCl solution, diluted with *n*-hexane, and washed with water. The combined organic layers were dried over magnesium sulfate and the solvent was removed under reduced pressure. The resulting crude product was purified by column chromatography on silica gel (*n*-hexane/dichloromethane, 3/1 (v/v)) to obtain prepurified compound. As other reaction by-products could not be separated from the product, recycling GPC was used to get pure compound in the form of yellow viscous oil (19.9 mg, 44.6 μmol, 20%).

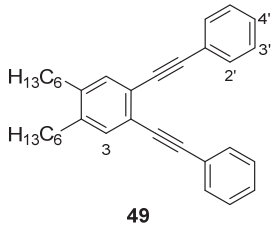

49

^{1}H NMR (400 MHz, 300 K, CD_2Cl_2): δ = 7.59–7.55 (m, 4H, $H^{2'}$), 7.40–7.34 (m, 8H, $H^{3,3',4'}$), 2.63 (t, ^{3}J = 7.90 Hz, 4H, CCH_2), 1.65–1.57 (m, 4H, CCH_2CH_2), 1.43–1.33 (m, 12H, CH_2), 0.92 ppm (t, ^{3}J = 7.13 Hz, 6H, CH_3); ^{13}C NMR (101 MHz, 300 K, CD_2Cl_2): δ = 142.1, 132.8, 131.9, 128.9, 128.7, 123.9, 123.2, 92.7, 89.0, 32.9, 32.2, 31.3, 29.8, 23.0, 14.3 ppm; UV/Vis (CH_2Cl_2): λ_{max} (ε) = 266 (39600), 281 (67000), 317 nm (21600 M^{-1} cm^{-1}); fluorescence (CH_2Cl_2): λ_{max} = 368 nm (λ_{ex} = 320 nm); Φ_{fl} = 0.30; MS (MALDI, matrix: DCTB; positive, chloroform): *m/z* calcd for $C_{34}H_{38}$ $[M]^+$ 446.297, found 446.208; HRMS (ESI, positive, acetonitrile/chloroform = 1/1): *m/z* calcd for $C_{34}H_{39}$ $[M+H]^+$ 447.30518, found 447.30432; SWV (CH_2Cl_2, 0.1 M TBAHFP, *vs*. Fc/Fc^+): E_{ox} (**49**/**49**$^+$) = +1.18 V.

6.3. UV/Vis and Fluorescence Spectra

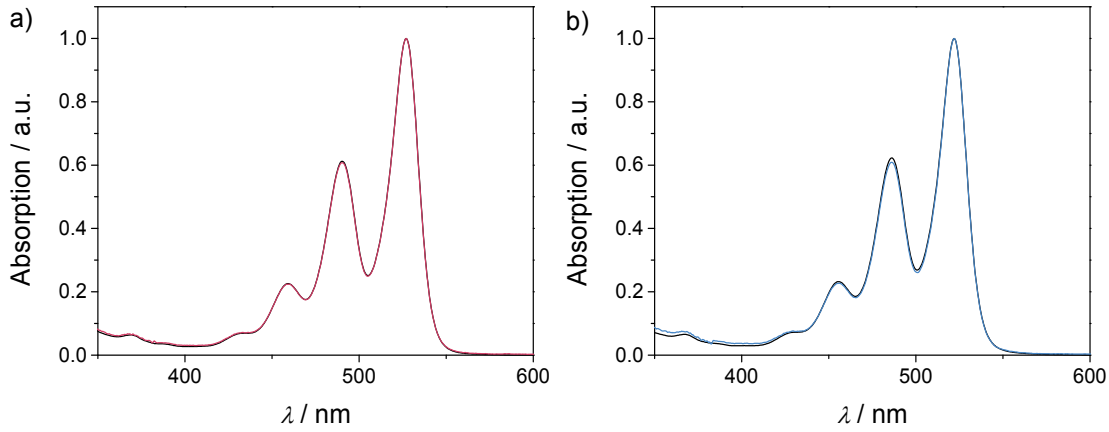

Figure S1. Concentration-dependent UV/Vis absorption spectra of **31** in a) $CHCl_3$ (cerise line, $c = 3 \times 10^{-6}$ M; black line, $c = 2 \times 10^{-4}$ M) and b) THF (blue line, $c = 2 \times 10^{-6}$ M; black line, $c = 2 \times 10^{-4}$ M). The spectra are normalized to the absorption maxima at approximately 525 nm.

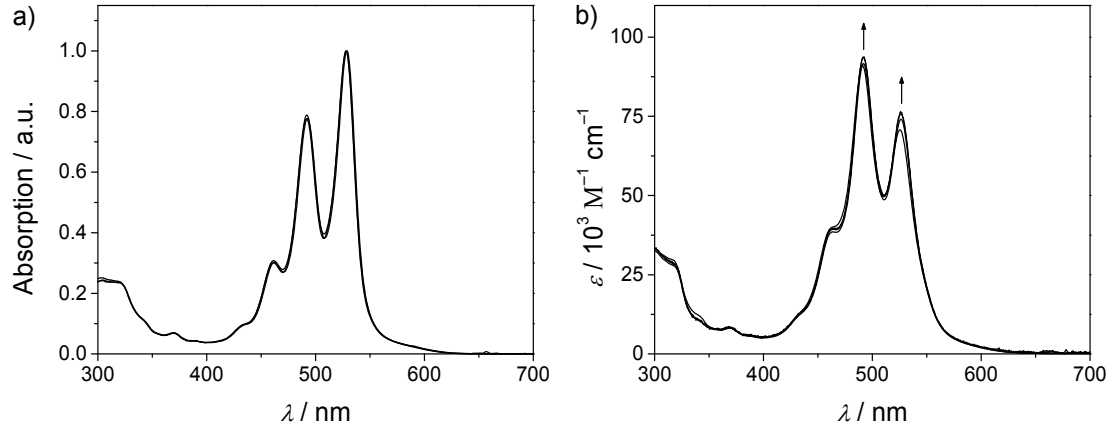

Figure S2. Concentration-dependent UV/Vis absorption spectra of folda-dimer **32** in a) $CHCl_3$ (1×10^{-6} to 8×10^{-4} M) and b) THF (5×10^{-7} to 6×10^{-5} M) at 25 °C. In a) the spectra are normalized at 529 nm and show no significant spectral changes, whereas in b) the arrows indicate the spectral changes upon decreasing concentration.

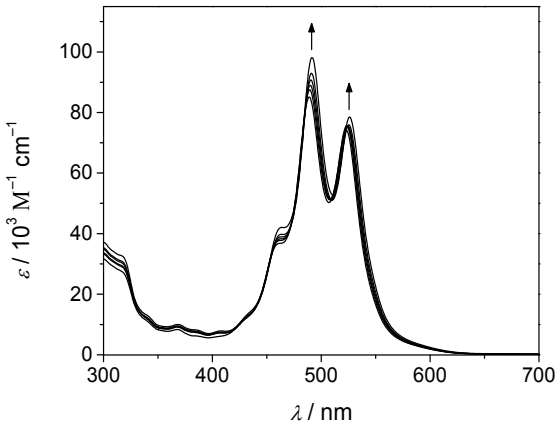

Figure S3. Temperature-dependent UV/Vis absorption spectra of **32** in [D_8]THF, $c = 2 \times 10^{-4}$ M, starting at 60 °C down to 10 °C in 10 °C intervals. The arrows indicate the spectral changes with decreasing temperature.

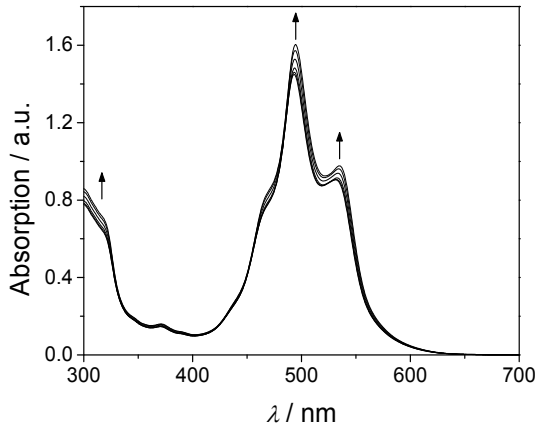

Figure S4. Temperature-dependent UV/Vis absorption spectra of **33** in [D_8]THF, $c = 2 \times 10^{-4}$ M, starting at 60 °C down to 10 °C in 10 °C intervals. The arrows indicate the spectral changes with decreasing temperature.

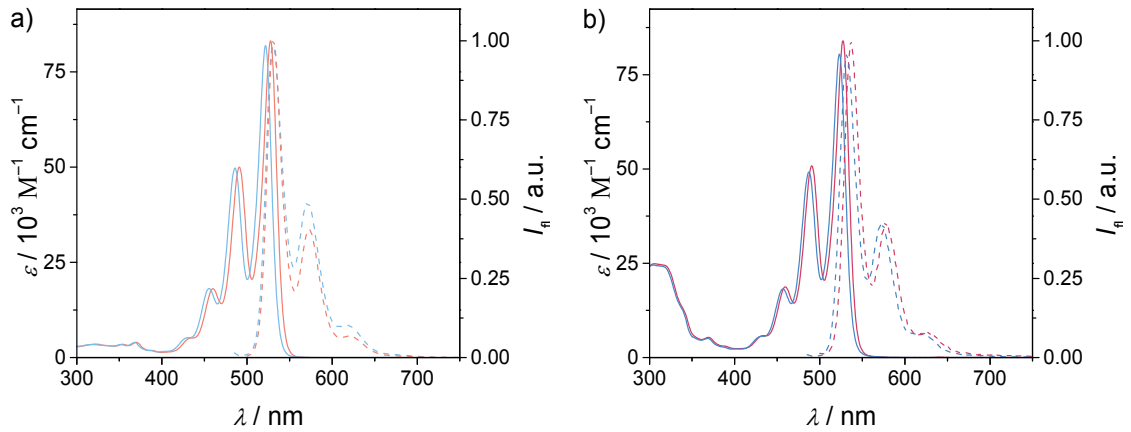

Figure S5. UV/Vis-absorption (solid lines, at 25 °C) and fluorescence spectra (dashed lines, at room temperature) of reference PBIs a) **30** and b) **31** in $CHCl_3$ (reddish colors) and THF (bluish colors).

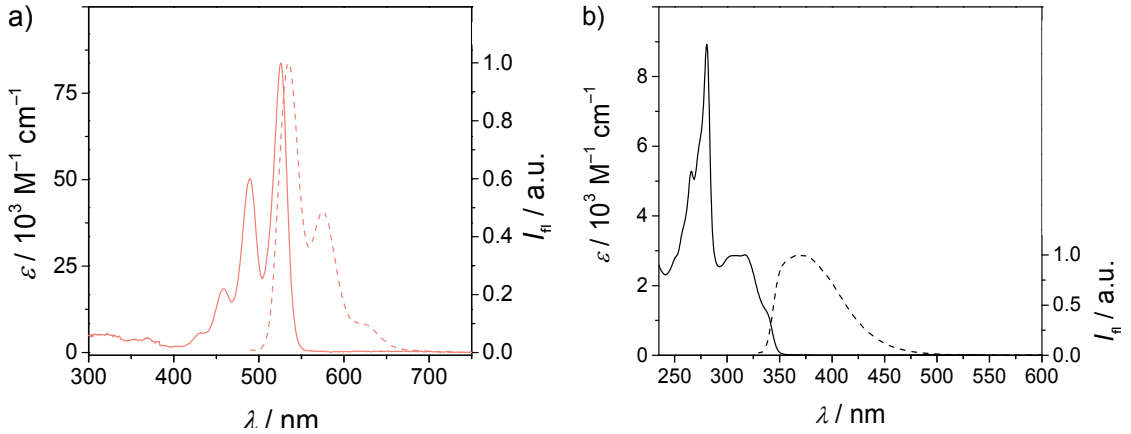

Figure S6. UV/Vis-absorption (solid lines, at 25 °C) and fluorescence spectra (dashed lines, at room temperature) of reference PBIs a) **30** (red lines; λ_{exc} = 480 nm) and b) **49** (black lines; λ_{exc} = 230 nm) in CH_2Cl_2.

6.4. NMR Spectra

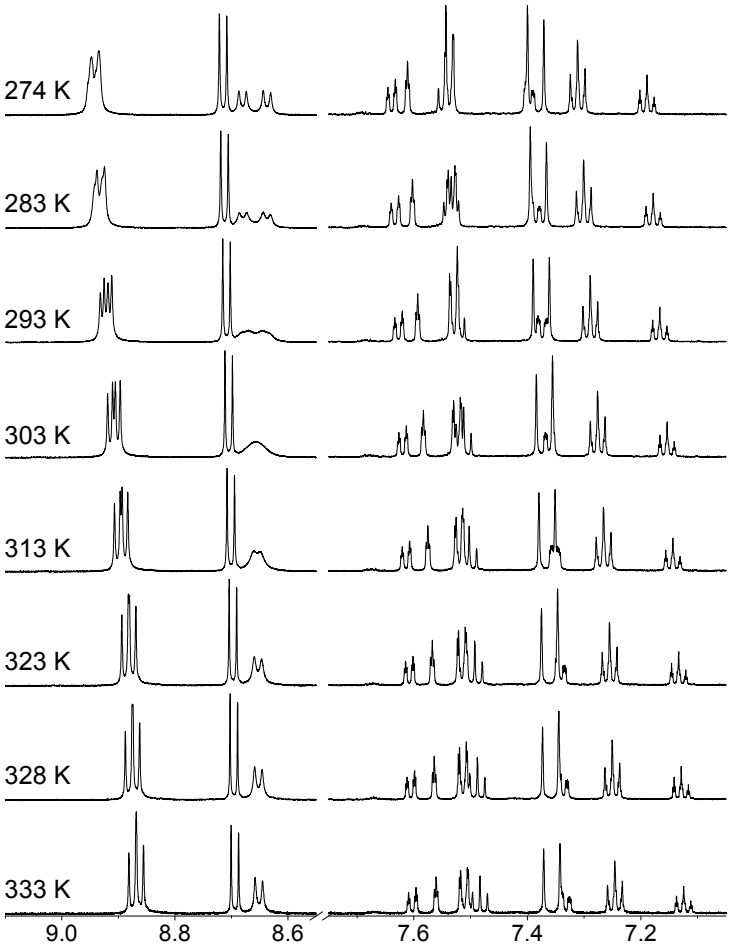

Figure S7. Aromatic regions of temperature-dependent (274 to 333 K) ^{1}H NMR spectra (600 MHz) of reference compound **31** ($c = 5 \times 10^{-4}$ M) in [D_8]THF. The temperature is indicated above the respective spectrum.

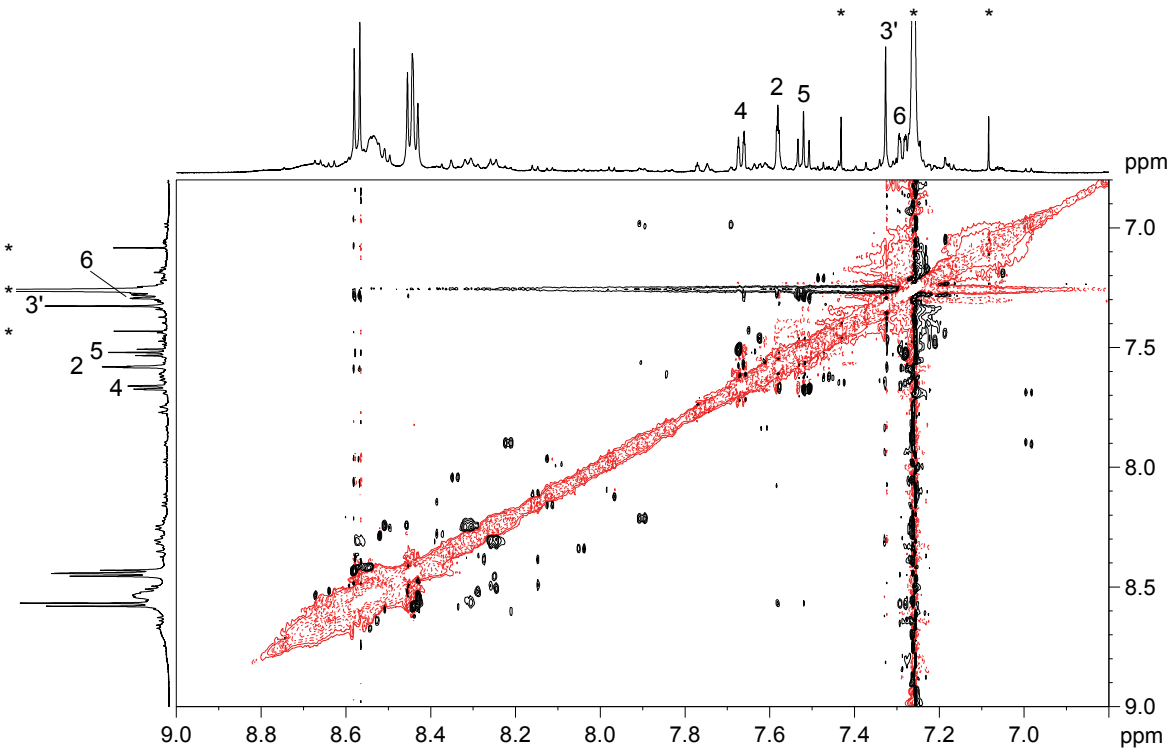

Figure S8. ^{1}H,^{1}H-2D-ROESY NMR spectrum (aromatic region, 600 MHz, black: positive, red: negative cross couplings) of folda-dimer **32** in $CDCl_3$ ($c = 8 \times 10^{-4}$ M) at 313 K. Solvent signals are marked in the spectrum with the asterisks (*).

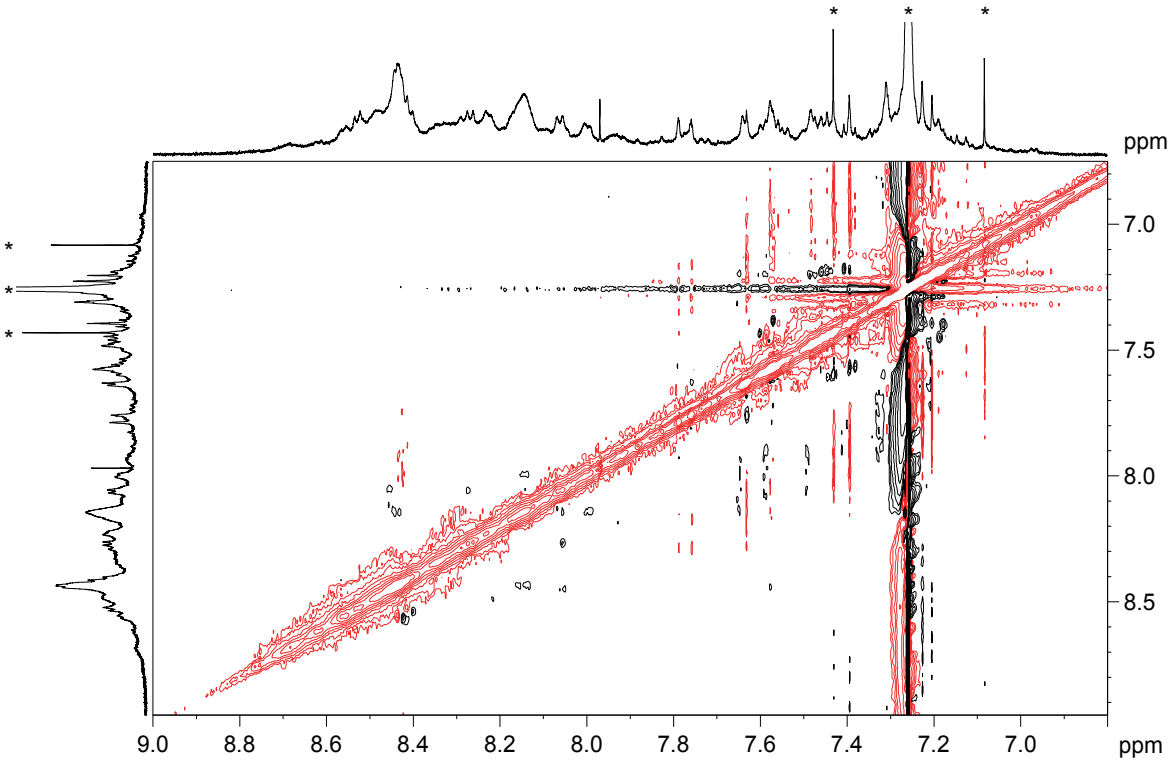

Figure S9. ^{1}H,^{1}H-2D-ROESY NMR spectrum (aromatic region, 600 MHz, black: positive, red: negative cross couplings) of folda-trimer **33** in $CDCl_3$ ($c = 10^{-4}$ M) at 323 K. Solvent signals are marked in the spectrum with asterisks (*).

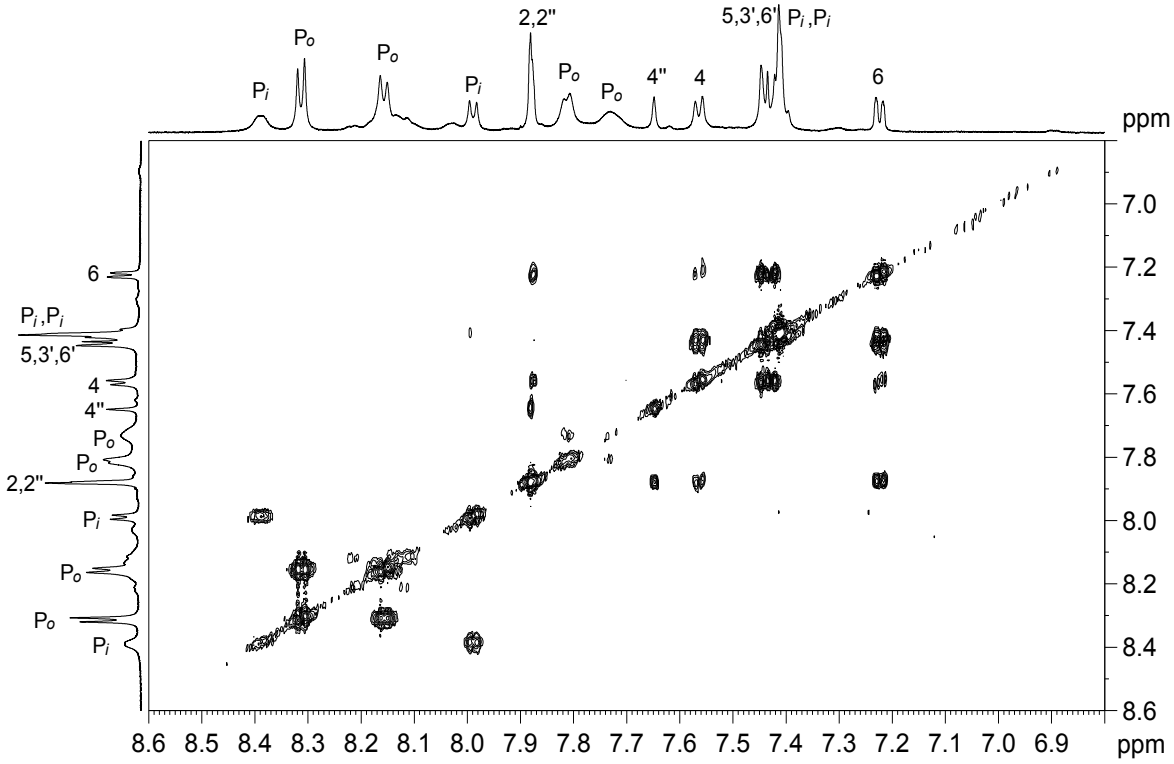

Figure S10. ^{1}H,^{1}H-2D-COSY NMR spectrum (aromatic region, 600 MHz) of folda-trimer **33** in [D_8]THF ($c = 4 \times 10^{-4}$ M) at 328 K.

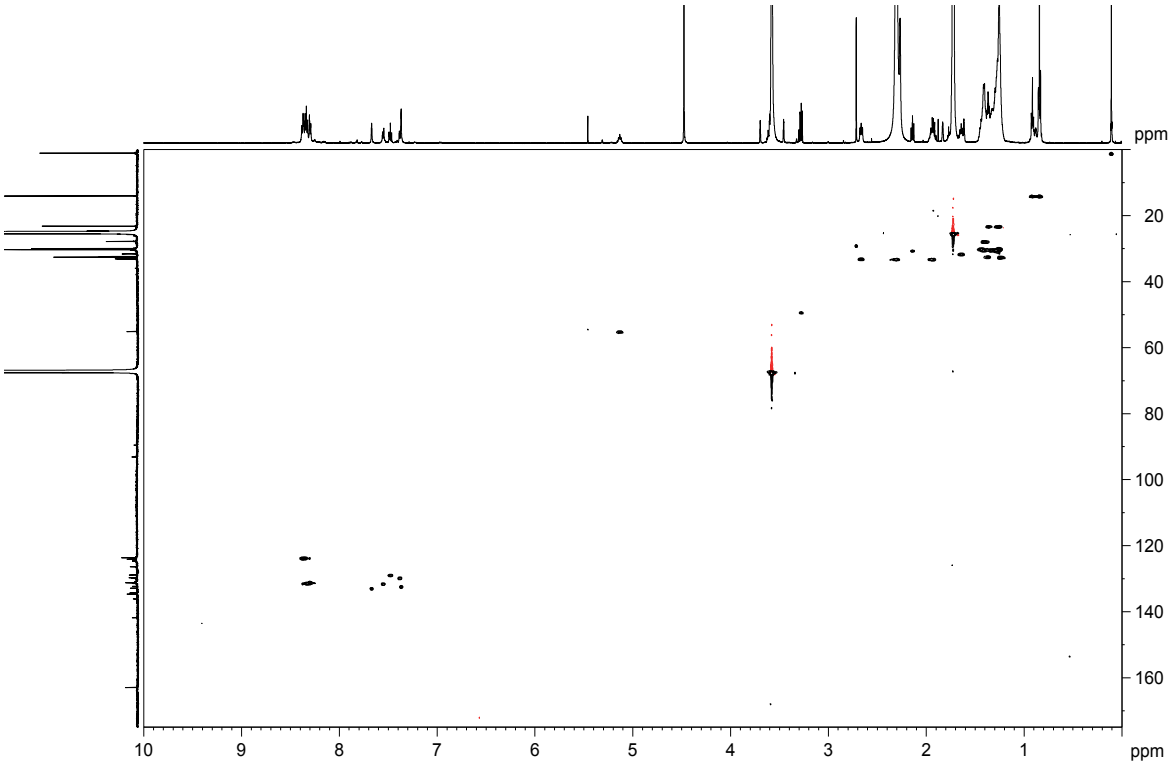

Figure S11. HSQC NMR spectrum of folda-dimer **32** (600 MHz, [D_8]THF, 328 K).

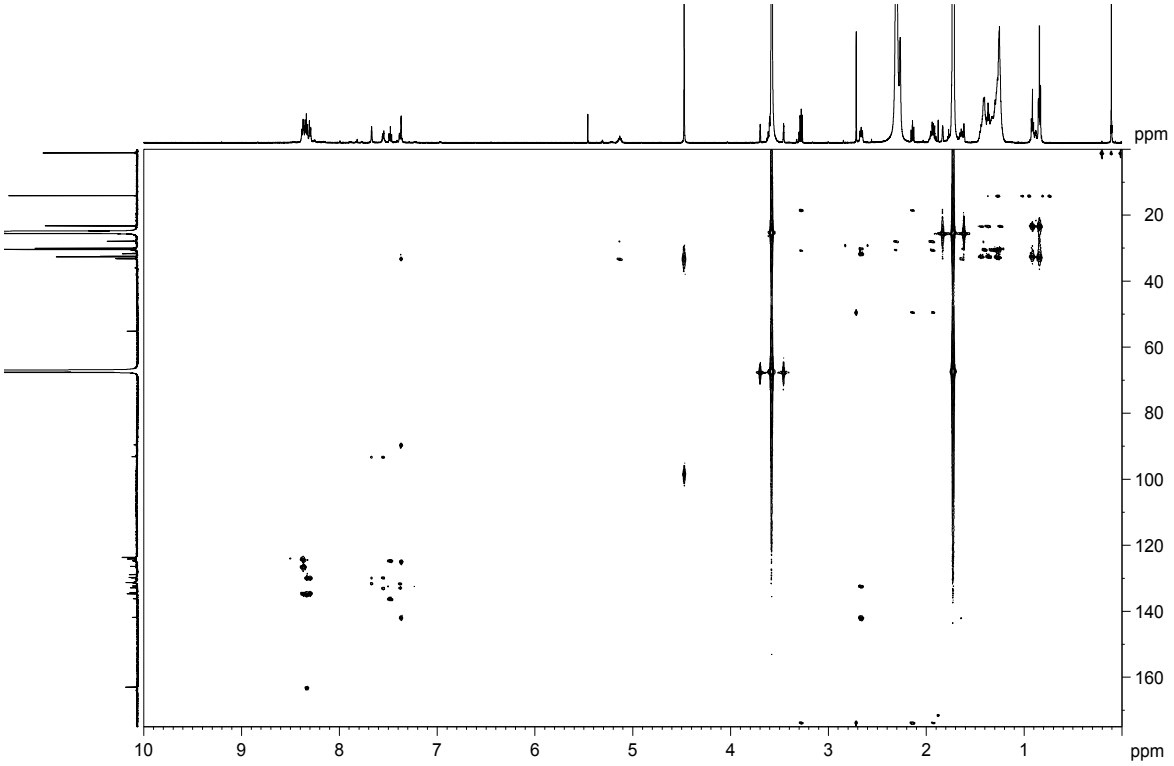

Figure S12. HMBC NMR spectrum of folda-dimer **32** (600 MHz, [D_8]THF, 328 K).

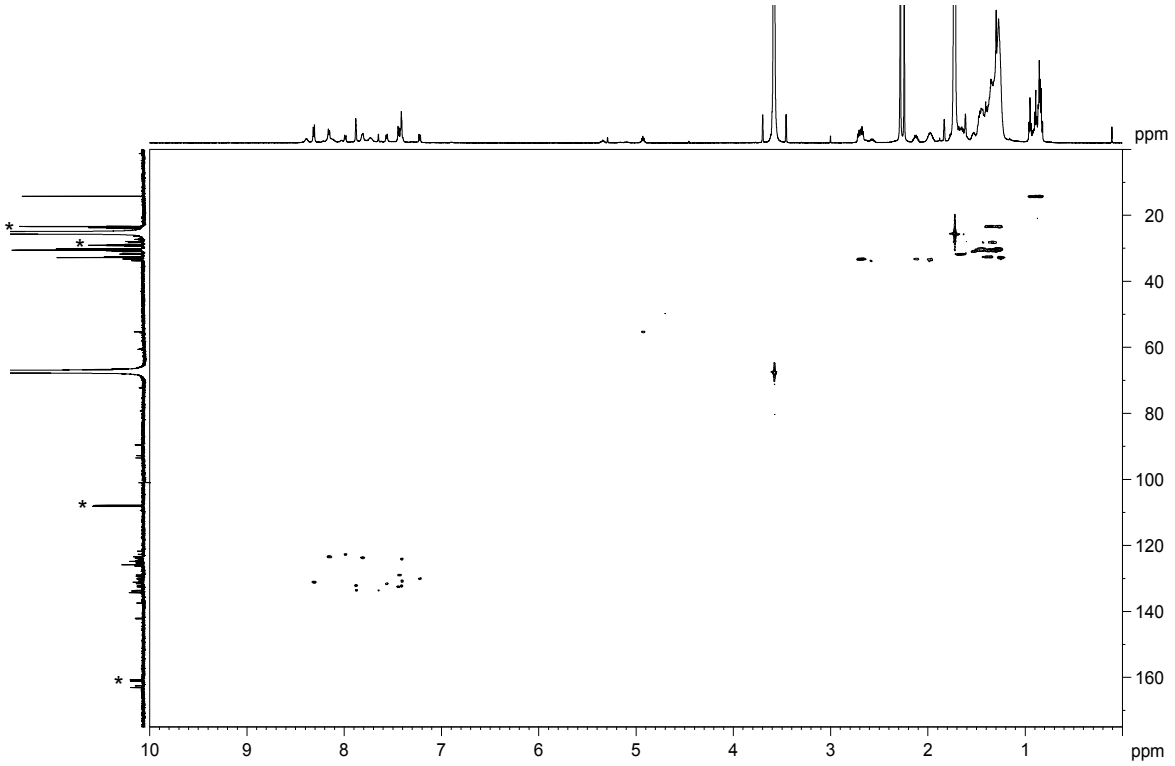

Figure S13. HSQC NMR spectrum of folda-trimer **33** (600 MHz, [D_8]THF, 328 K). Note: Deuterated solvent impurity marked with asterisks (*).

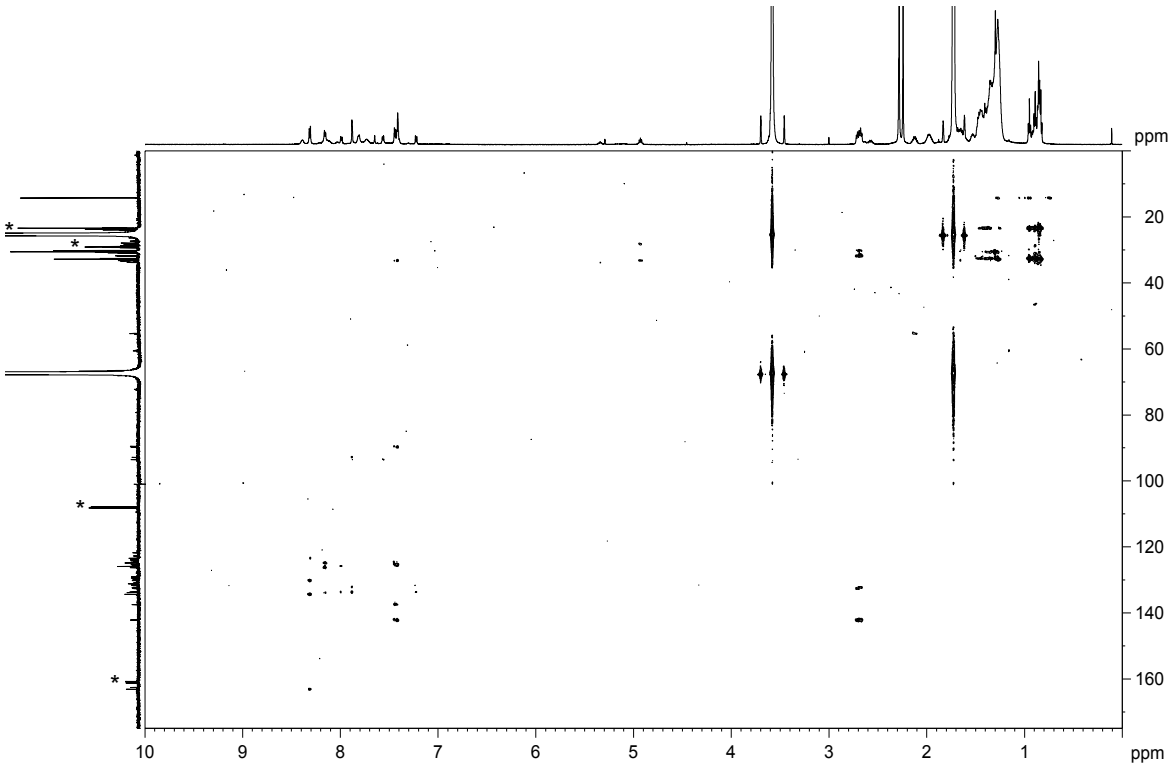

Figure S14. HMBC NMR spectrum of folda-trimer **33** (600 MHz, [D_8]THF, 328 K). Note: Deuterated solvent impurity marked with asterisks (*).

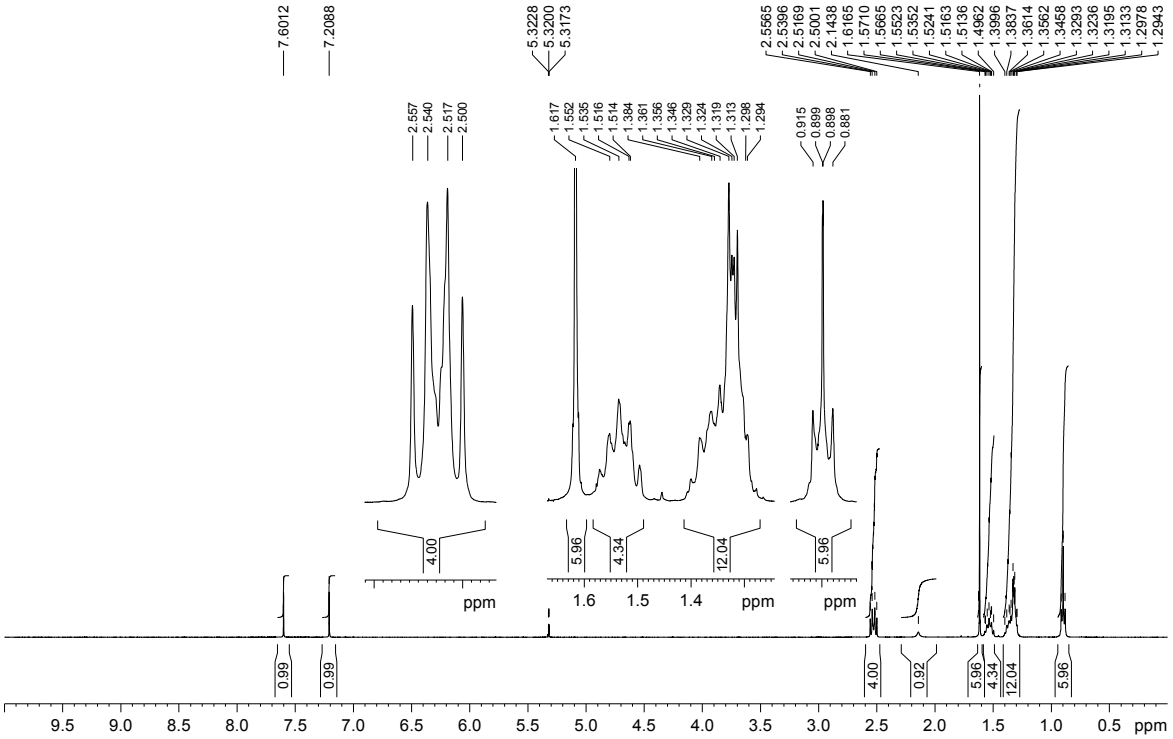

Figure S15. ^{1}H NMR spectrum of **36** (400 MHz, CD_2Cl_2, 300 K).

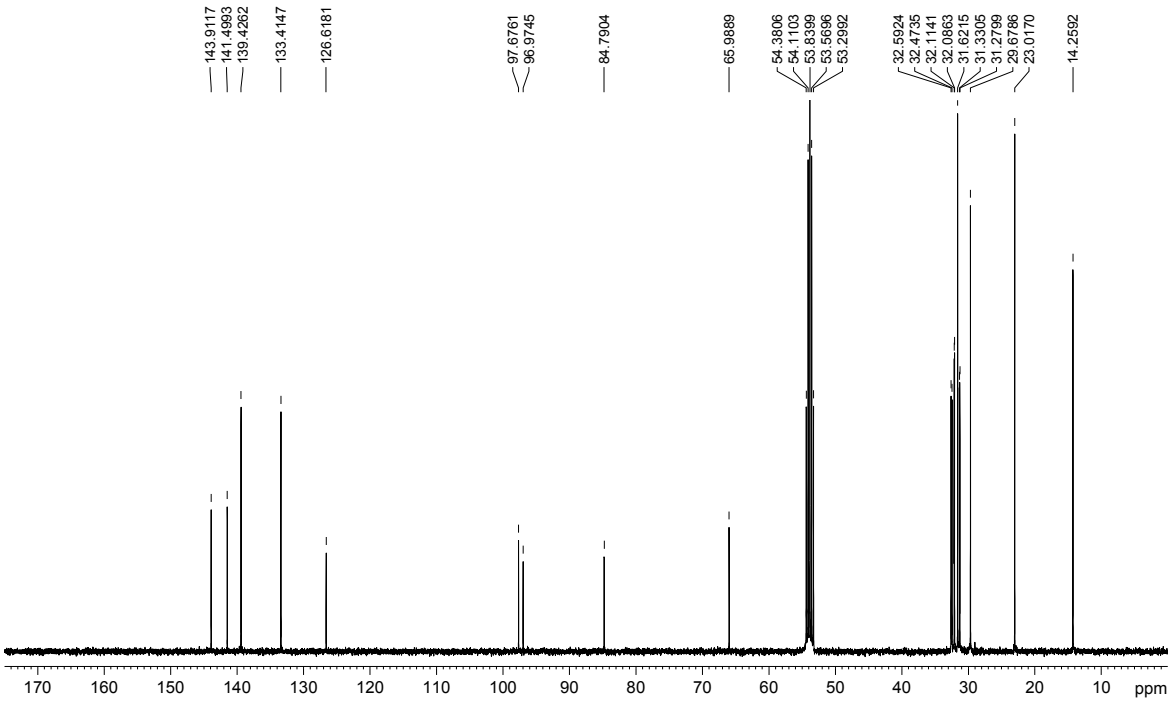

Figure S16. ^{13}C NMR spectrum of **36** (101 MHz, CD_2Cl_2, 300 K).

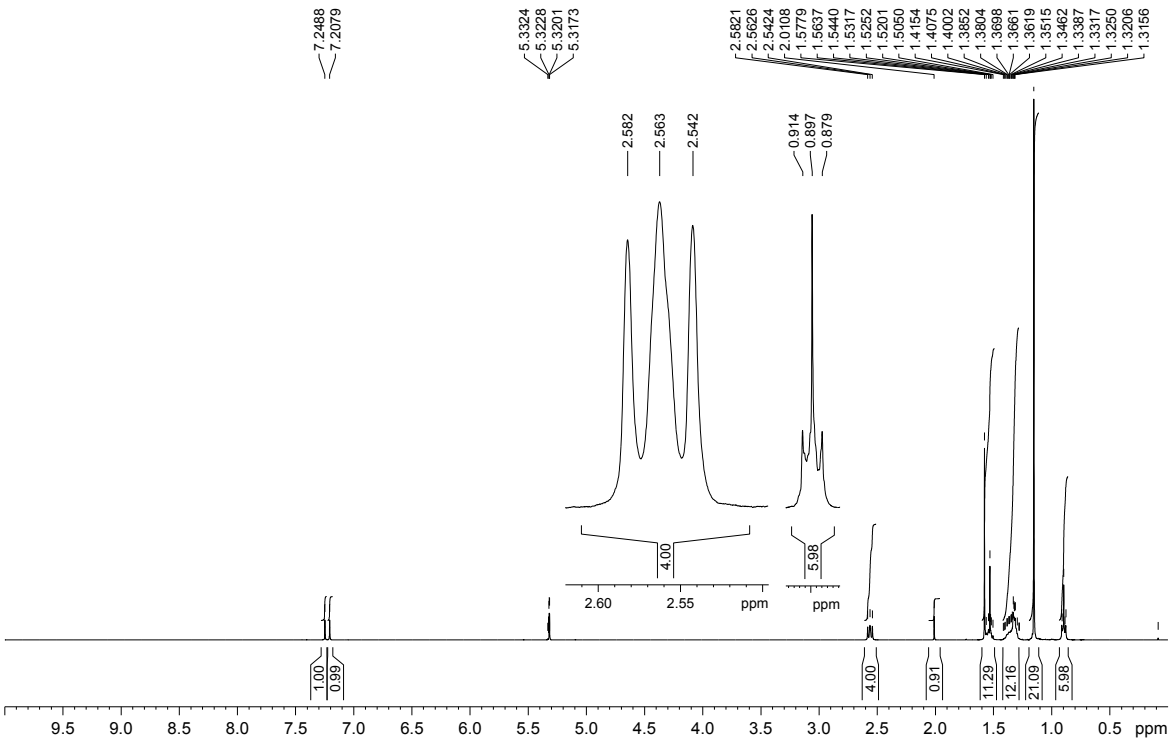

Figure S17. ^{1}H NMR spectrum of **38** (400 MHz, CD_2Cl_2, 300 K).

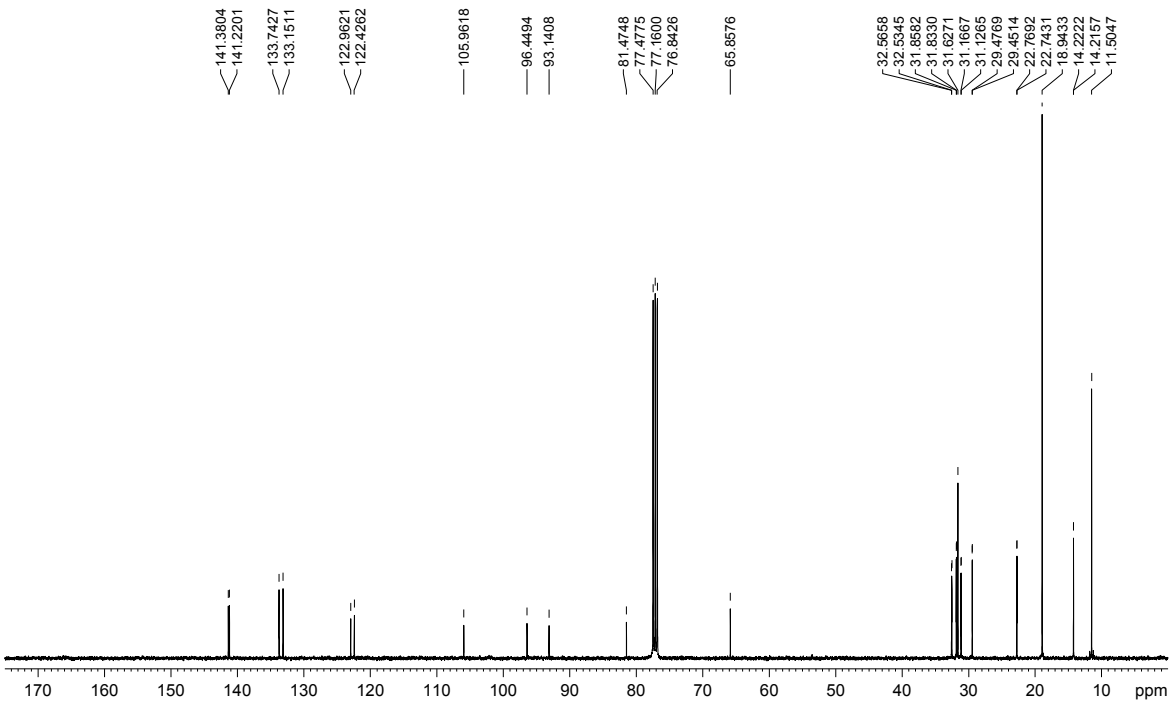

Figure S18. ^{13}C NMR spectrum of **38** (101 MHz, $CDCl_3$, 300 K).

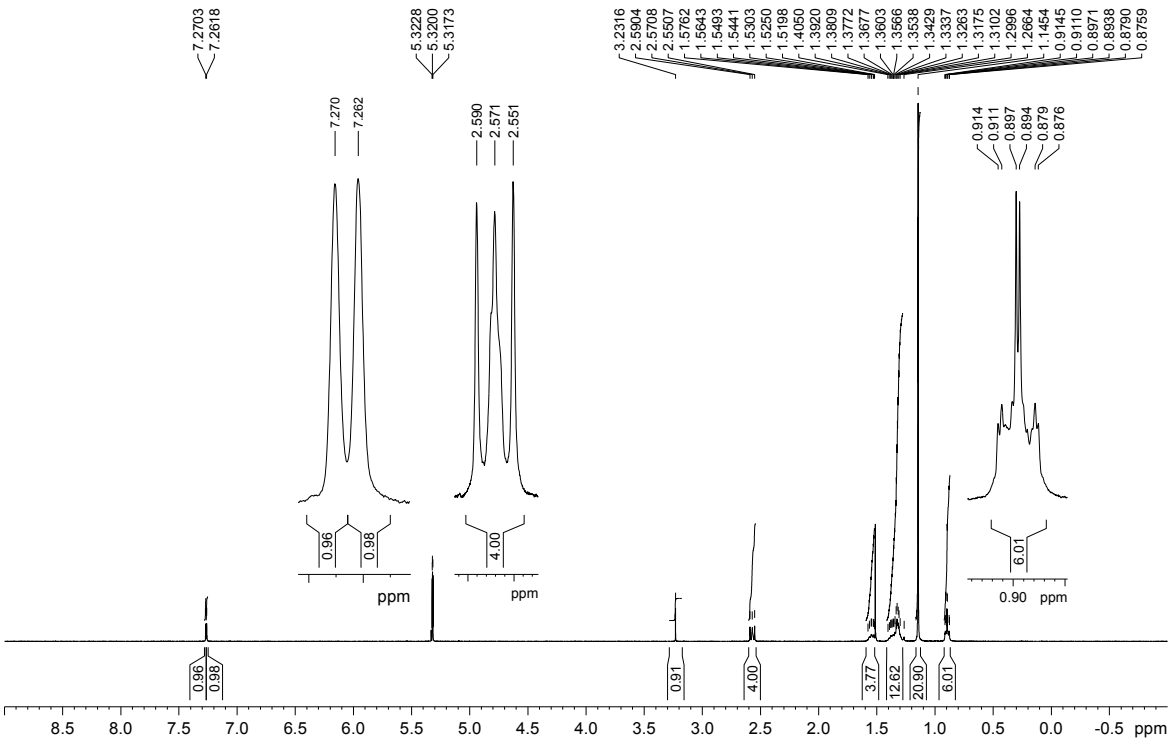

Figure S19. ^{1}H NMR spectrum of **39** (400 MHz, CD_2Cl_2, 300 K).

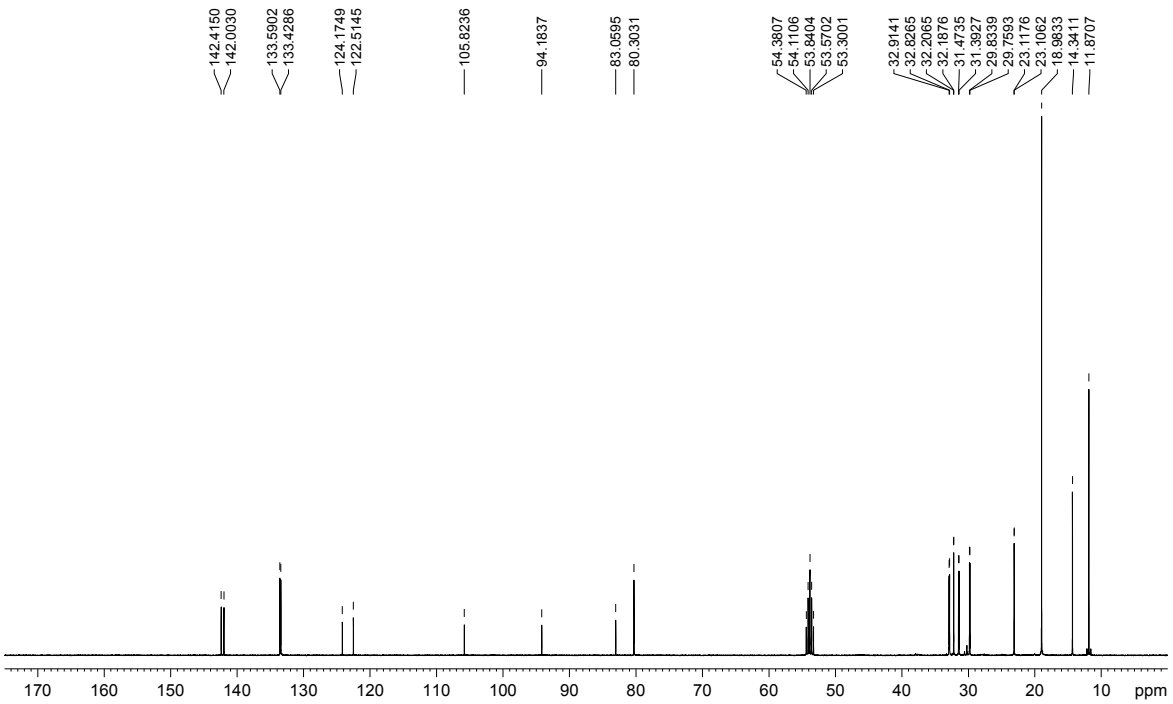

Figure S20. ^{13}C NMR spectrum of **39** (101 MHz, CD_2Cl_2, 300 K).

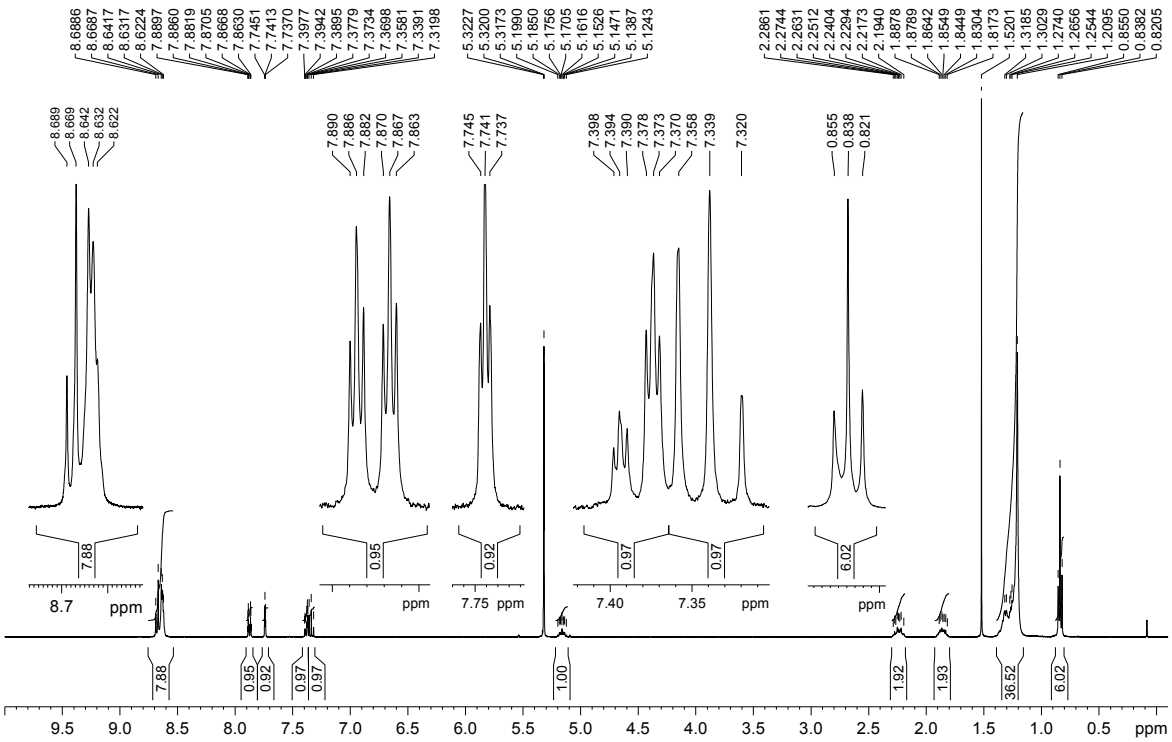

Figure S21. ^{1}H NMR spectrum of **30** (400 MHz, CD_2Cl_2, 300 K).

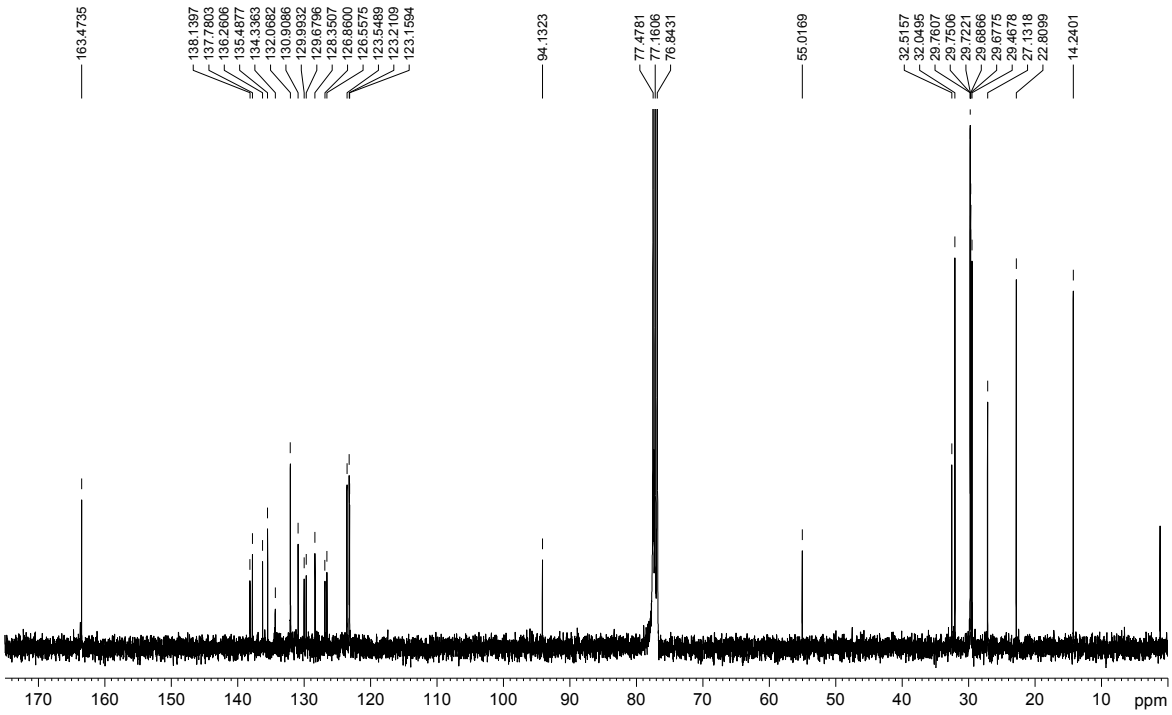

Figure S22. ^{13}C NMR spectrum of **30** (101 MHz, $CDCl_3$, 300 K).

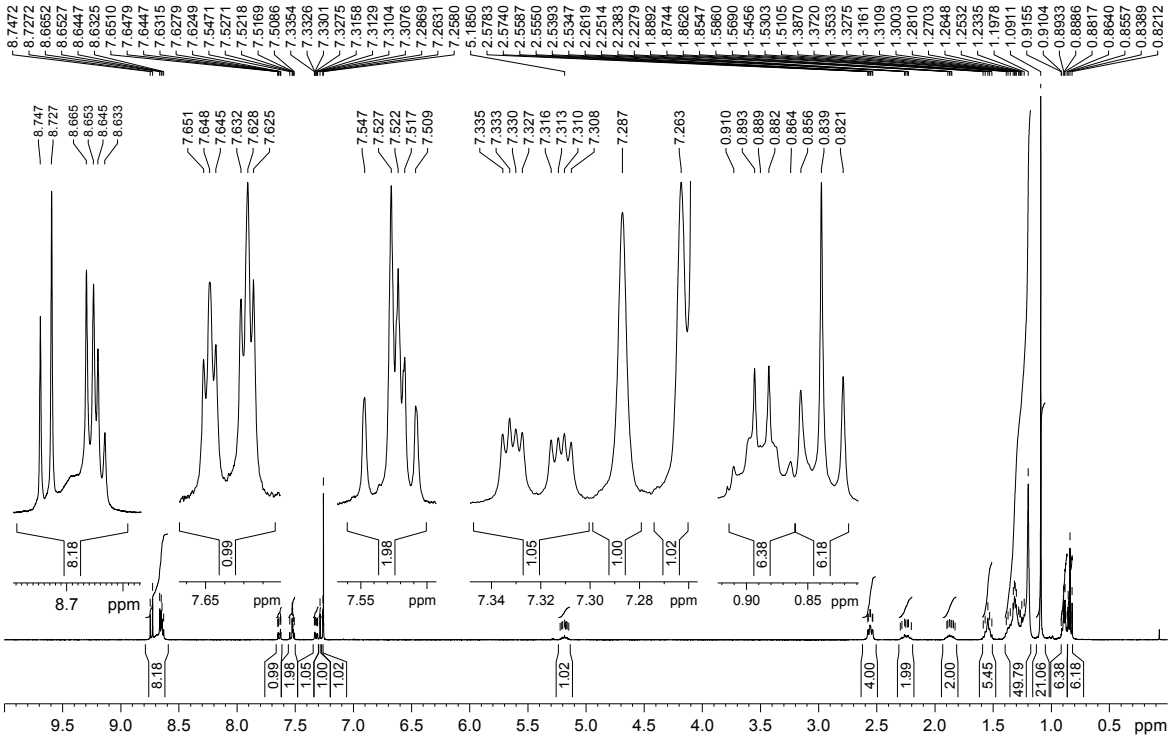

Figure S23. ^{1}H NMR spectrum of **42** (400 MHz, $CDCl_3$, 300 K).

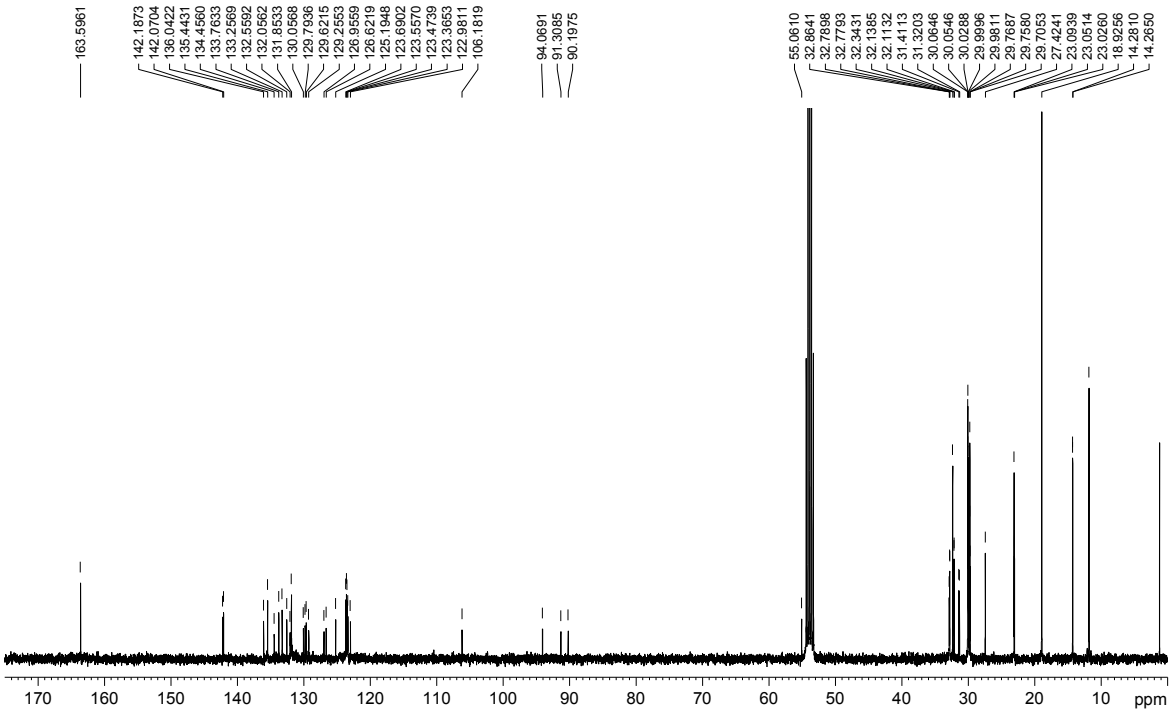

Figure 24. ^{13}C NMR spectrum of **42** (101 MHz, CD_2Cl_2, 300 K).

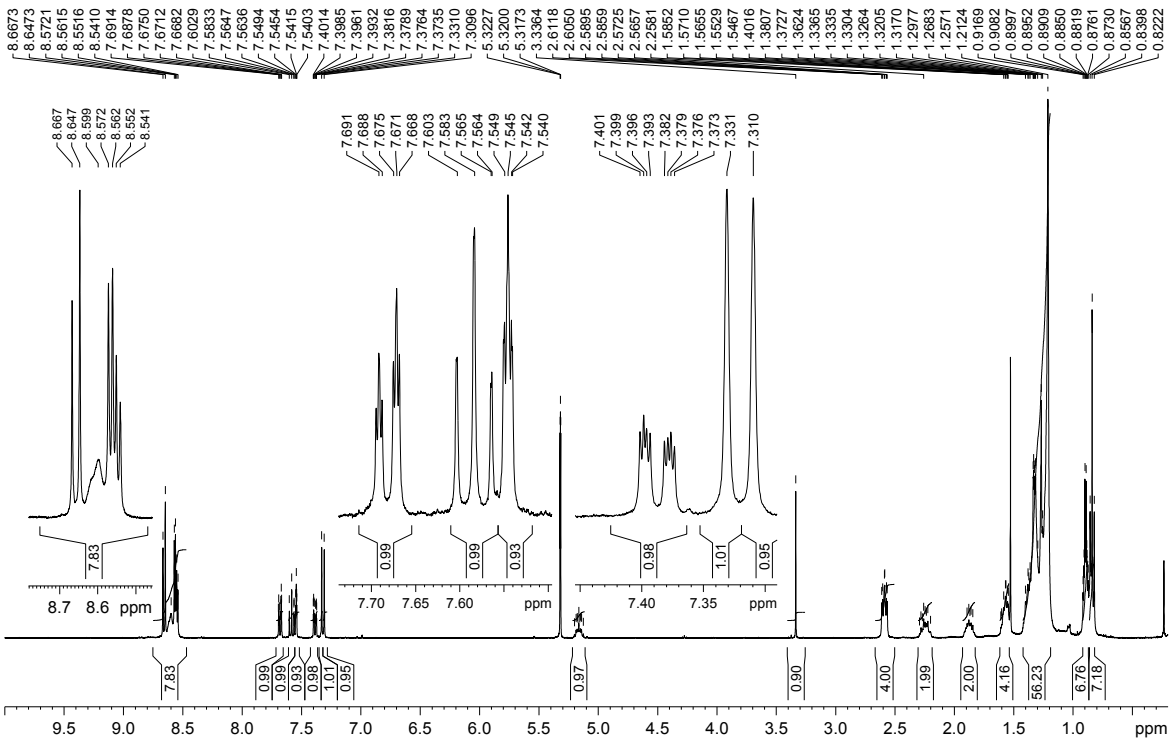

Figure S25. ^{1}H NMR spectrum of **43** (400 MHz, CD_2Cl_2, 300 K).

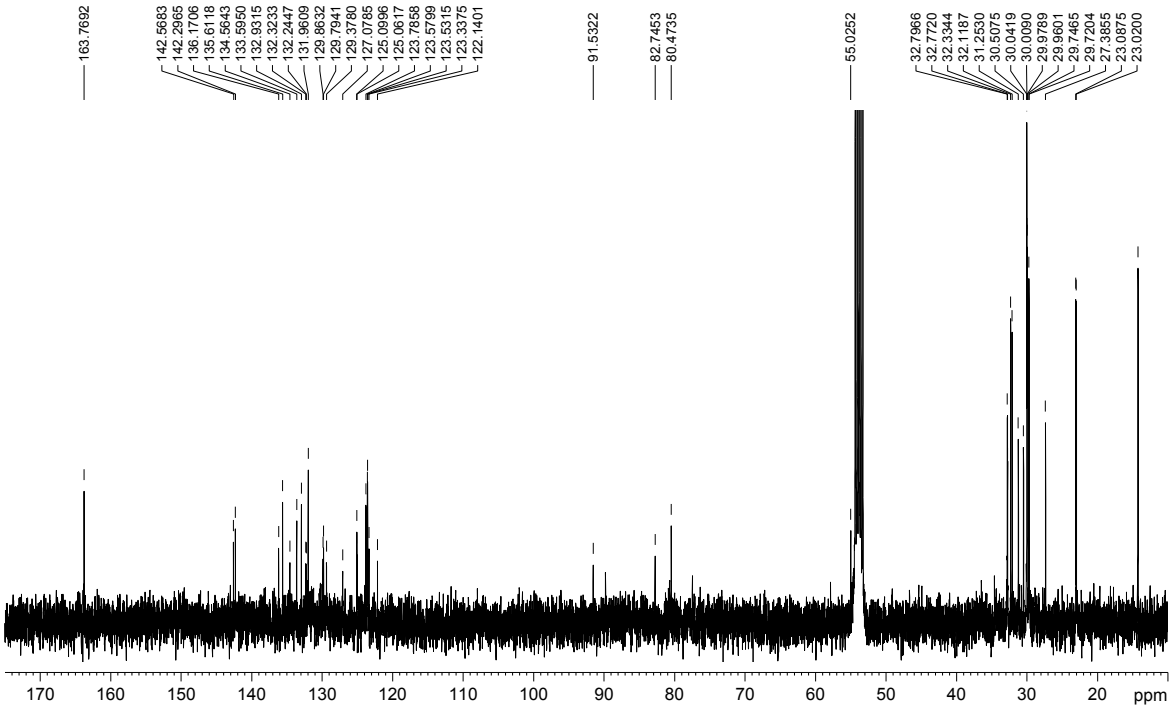

Figure S26. ^{13}C NMR spectrum of **43** (101 MHz, CD_2Cl_2, 300 K).

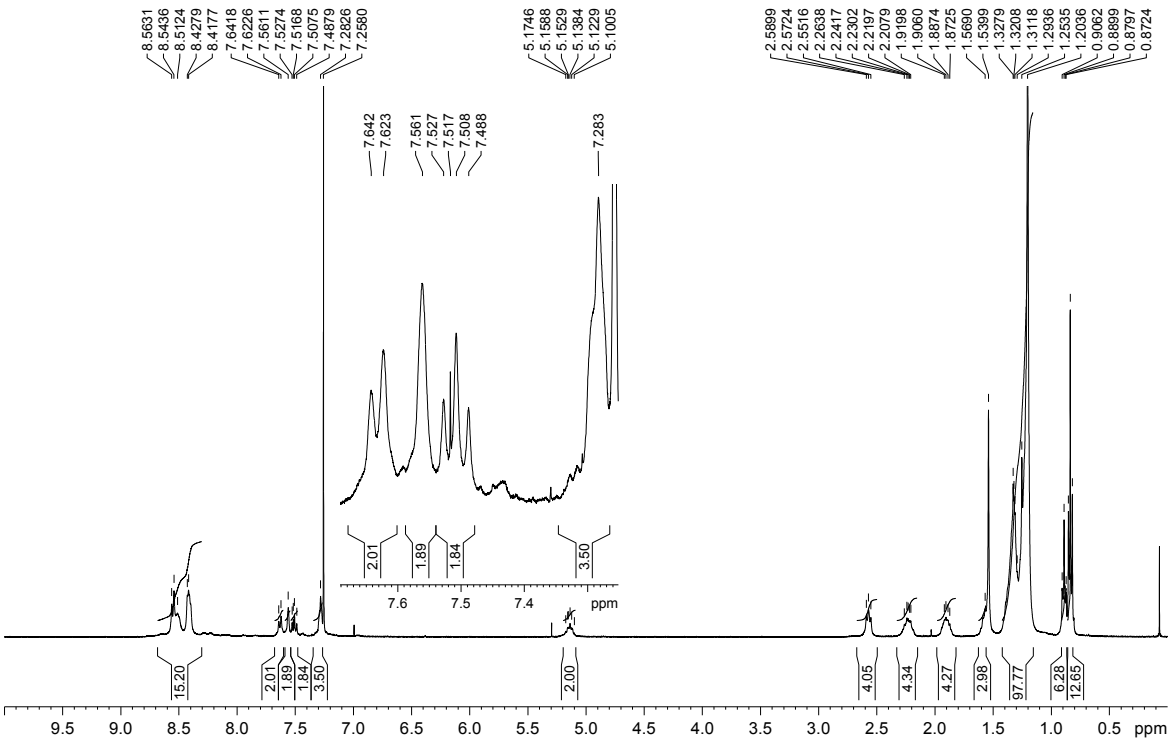

Figure S27. ^{1}H NMR spectrum of folda-dimer **32** (600 MHz, $CDCl_3$, 313 K).

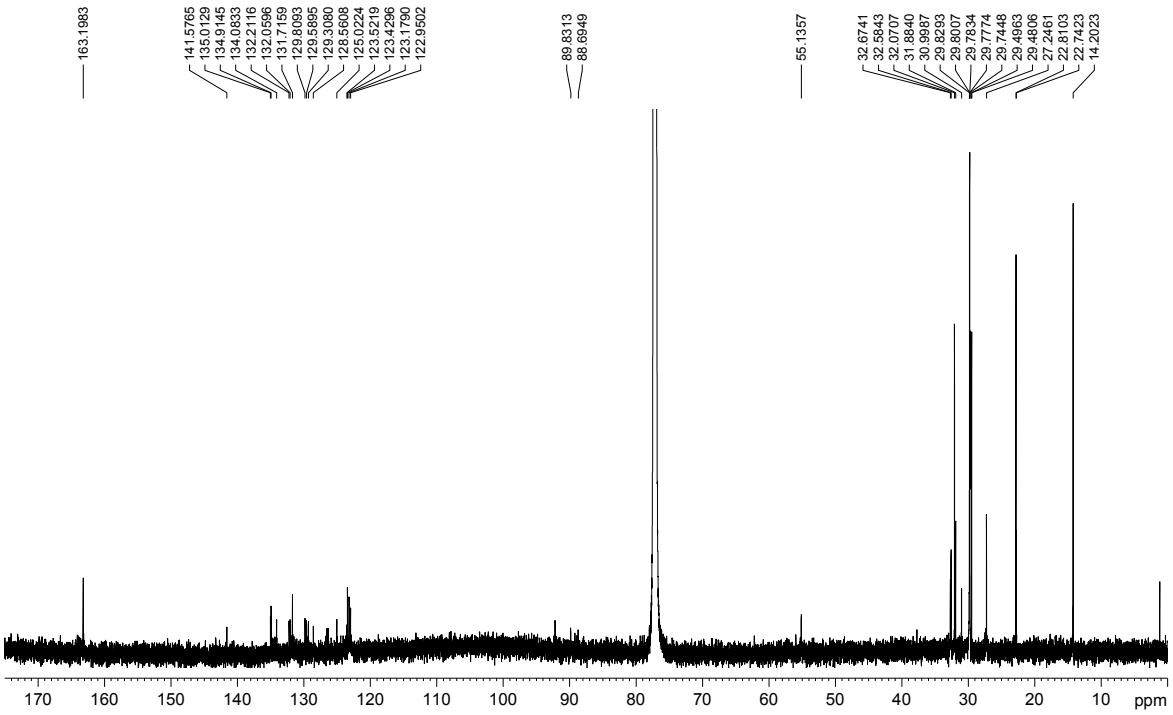

Figure S28. ^{13}C NMR spectrum of folda-dimer **32** (151 MHz, $CDCl_3$, 313 K).

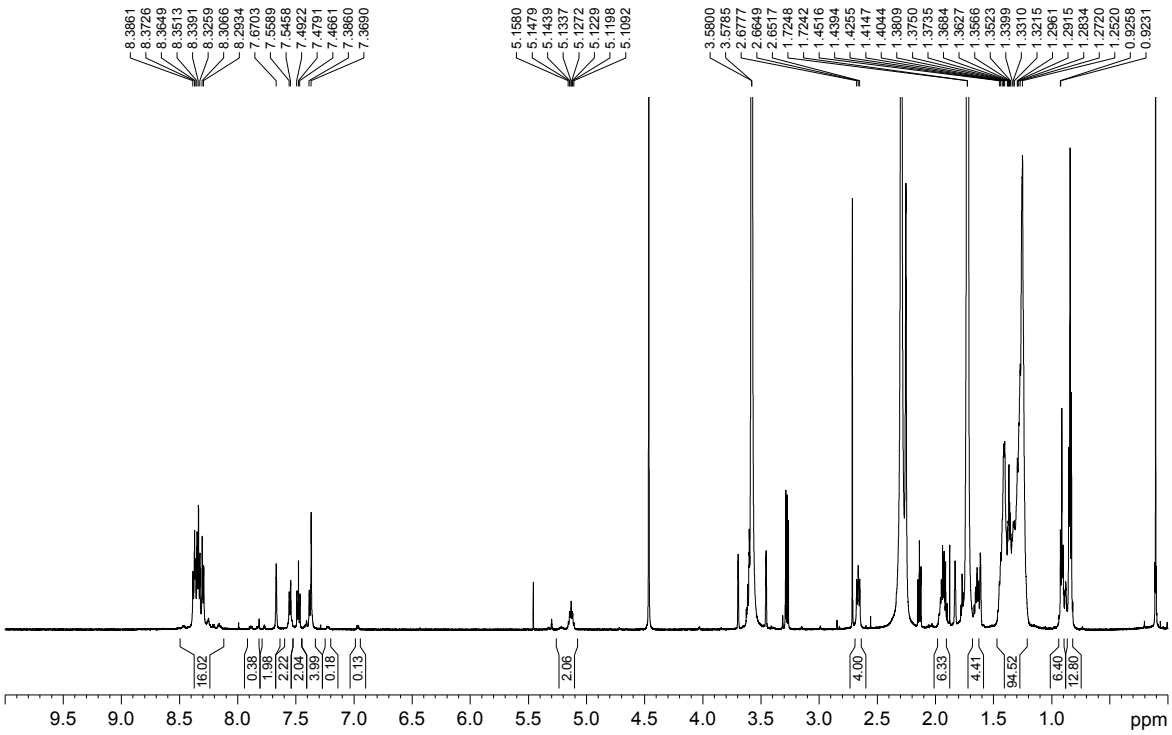

Figure S29. ^{1}H NMR spectrum of folda-dimer **32** (600 MHz, [D_8]THF, 328 K).

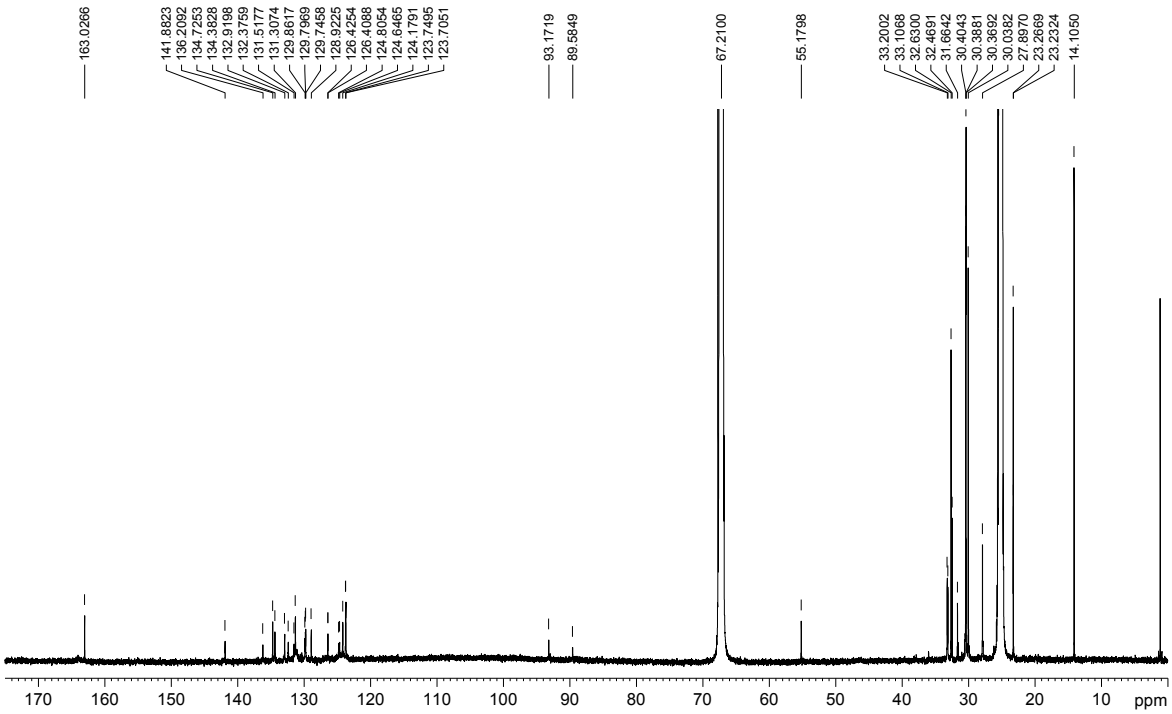

Figure S30. ^{13}C NMR spectrum of folda-dimer **32** (151 MHz, [D_8]THF, 328 K).

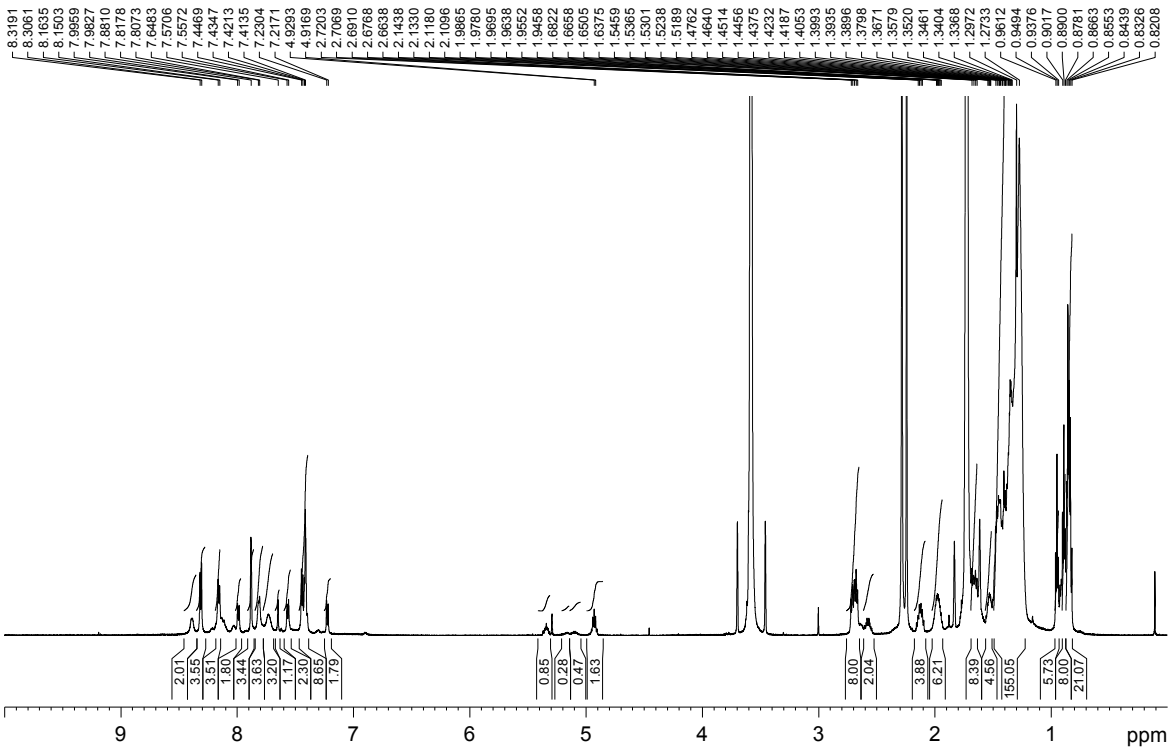

Figure S31. ^{1}H NMR spectrum of folda-trimer **33** (600 MHz, [D_8]THF, 328 K).

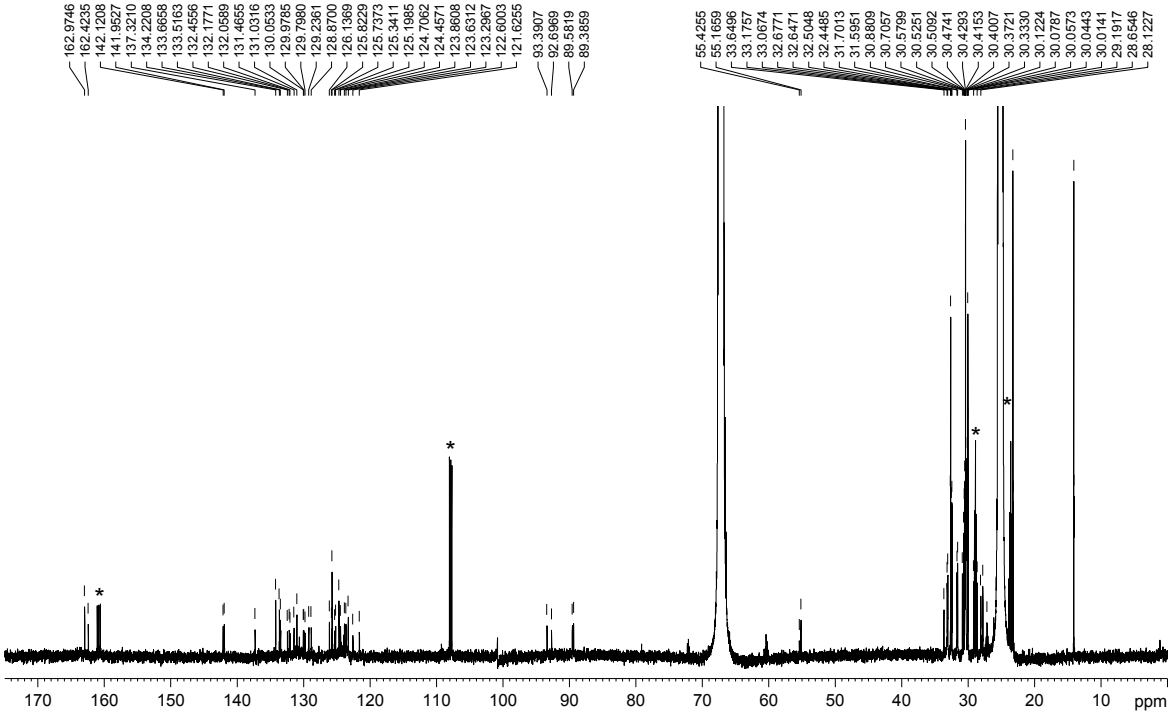

Figure S32. ^{13}C NMR spectrum of folda-trimer **33** (151 MHz, [D_8]THF, 328 K). Note: Deuterated solvent impurity (*).

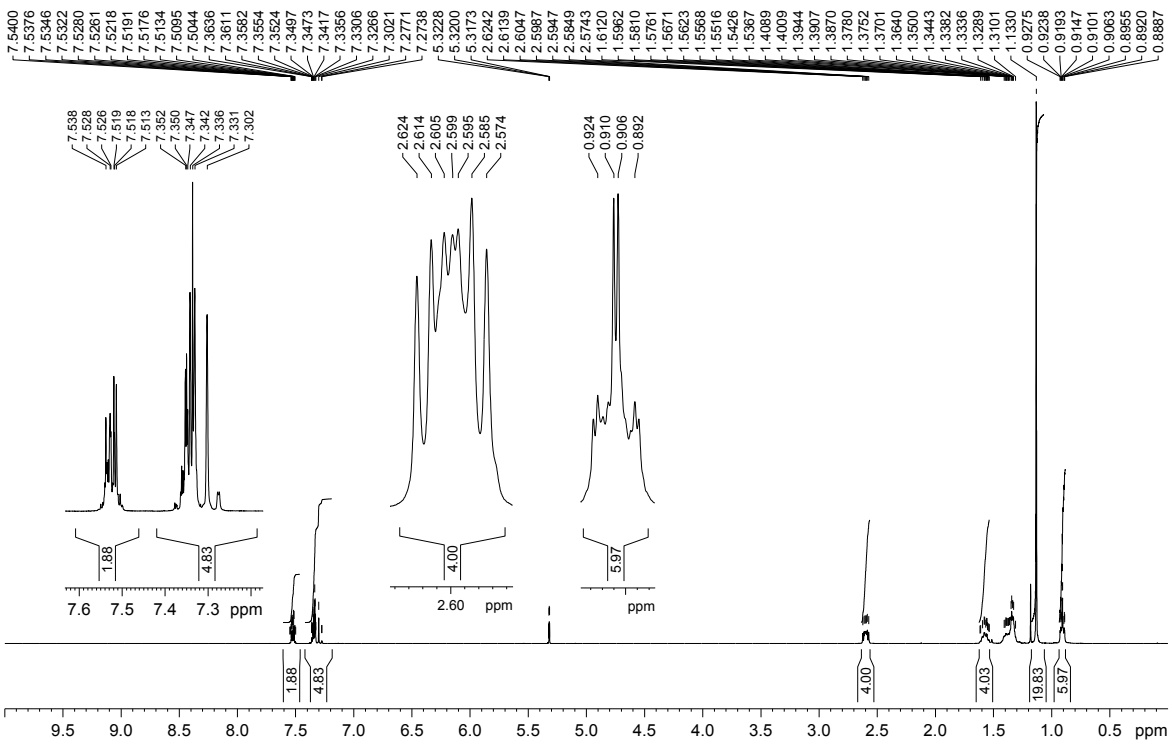

Figure S33. ^{1}H NMR spectrum of **46** (400 MHz, CD_2Cl_2, 300 K).

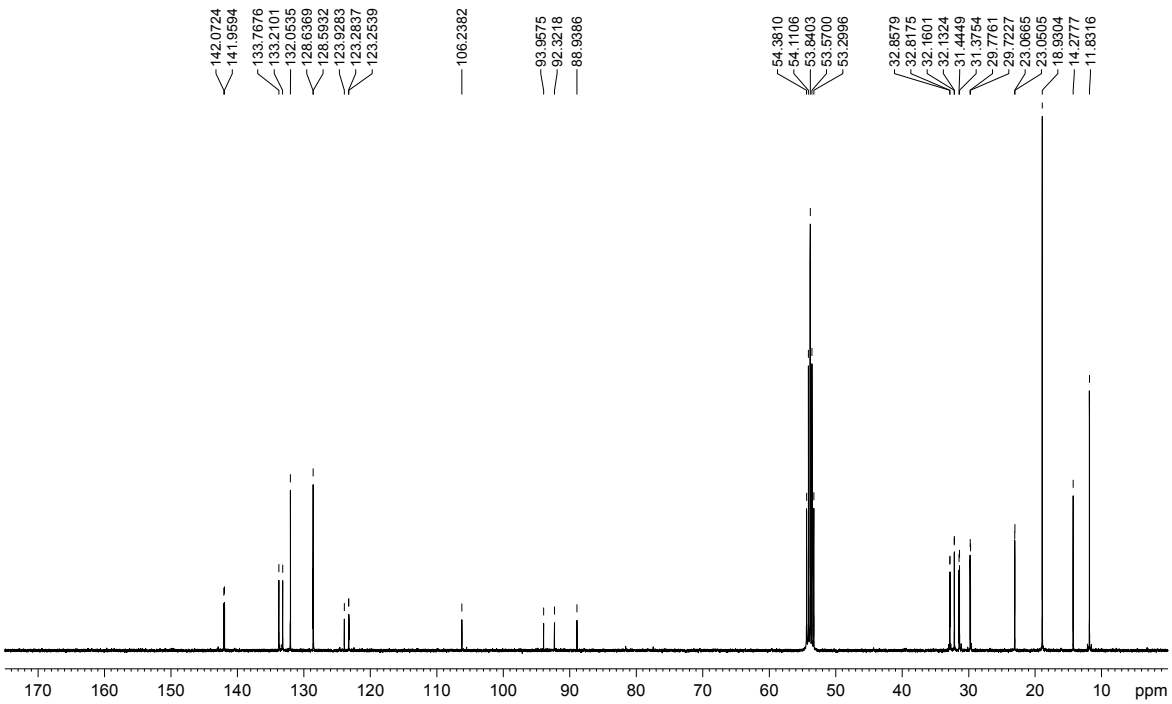

Figure S34. ^{13}C NMR spectrum of **46** (101 MHz, CD_2Cl_2, 300 K).

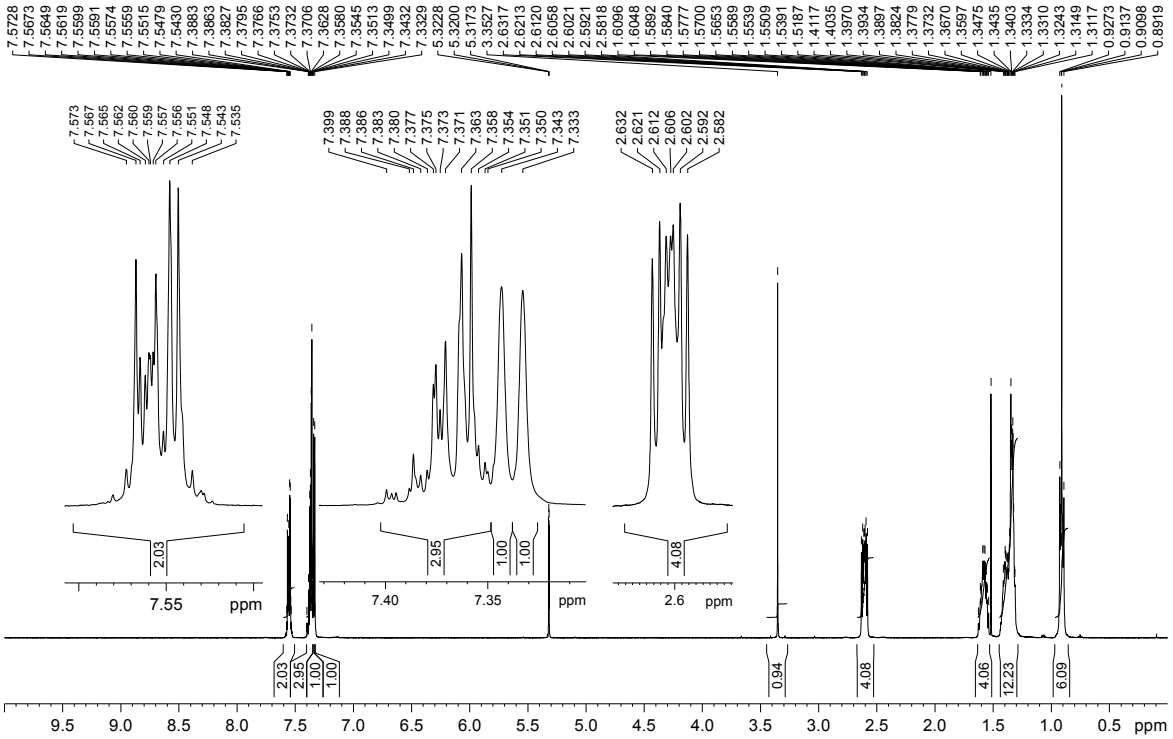

Figure S35. ^{1}H NMR spectrum of **47** (400 MHz, CD_2Cl_2, 300 K).

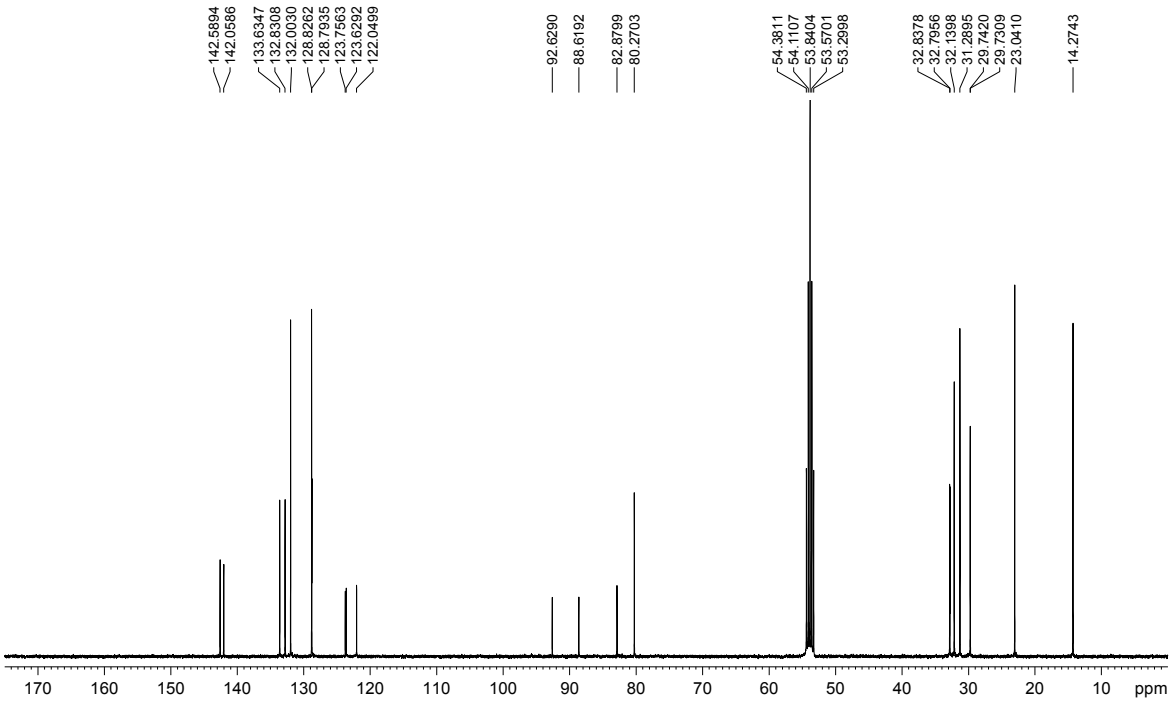

Figure S36. ^{13}C NMR spectrum of **47** (101 MHz, CD_2Cl_2, 300 K).

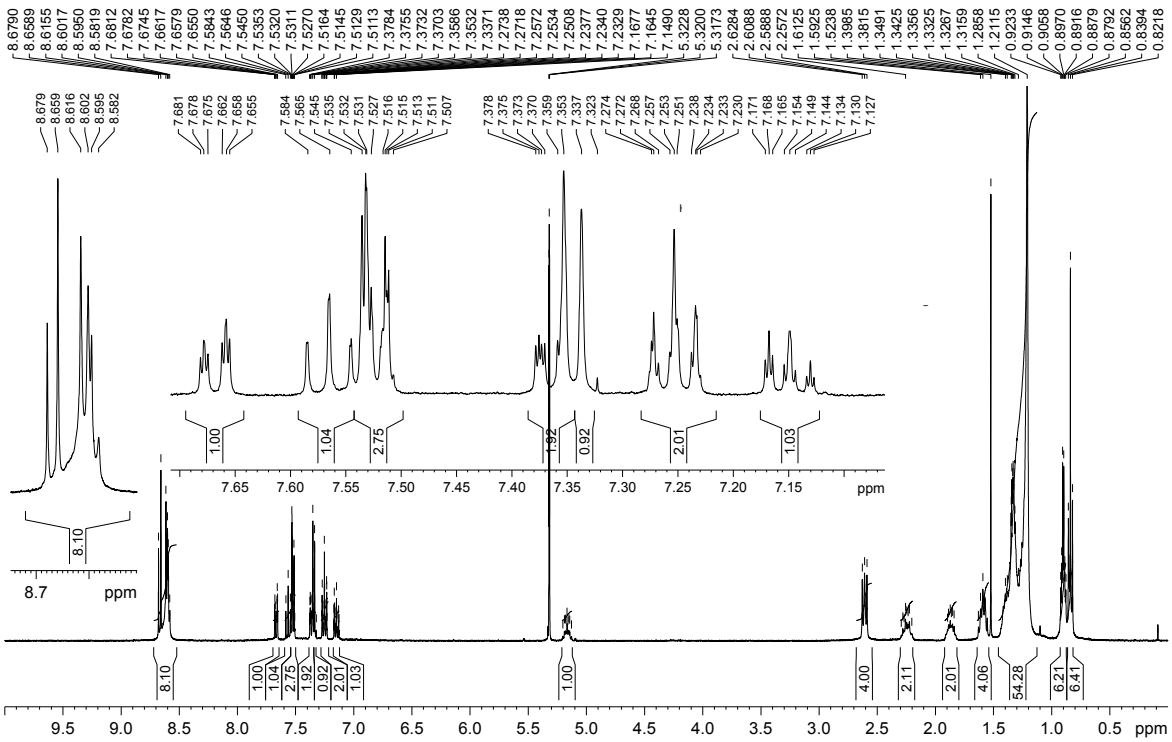

Figure S37. ^{1}H NMR spectrum of **31** (400 MHz, CD_2Cl_2, 300 K).

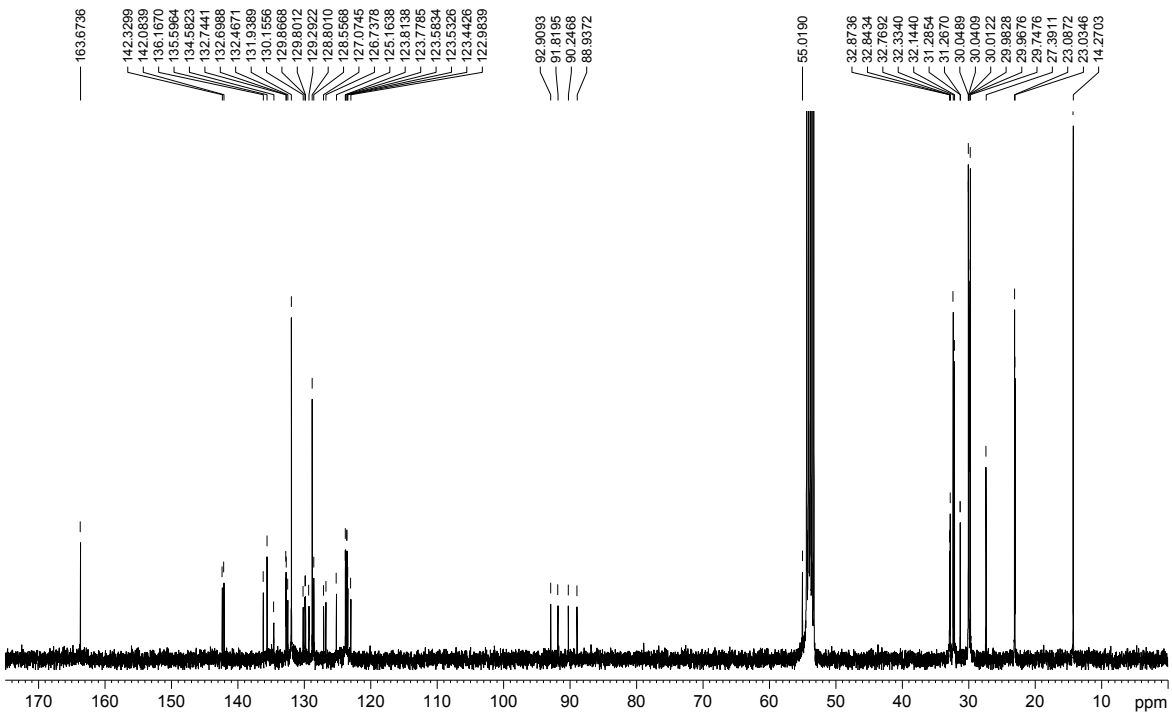

Figure S38. ^{13}C NMR spectrum of **31** (101 MHz, CD_2Cl_2, 300 K).

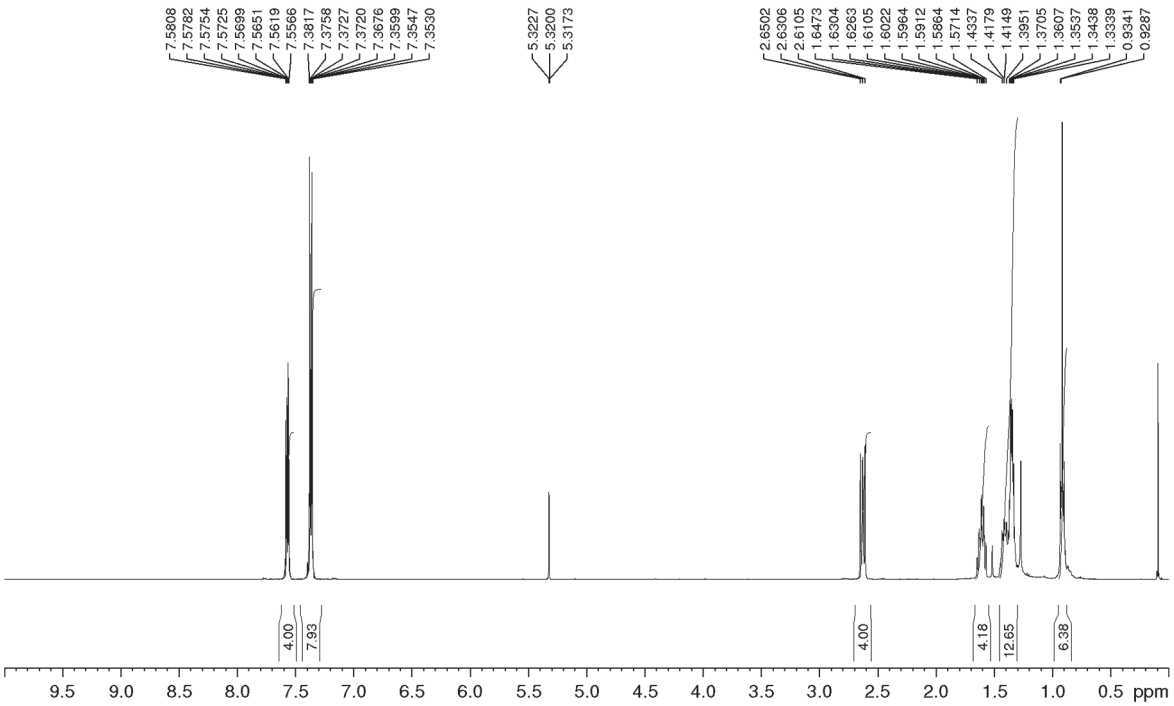

Figure S39. ^{1}H NMR spectrum of **49** (400 MHz, CD_2Cl_2, 300 K).

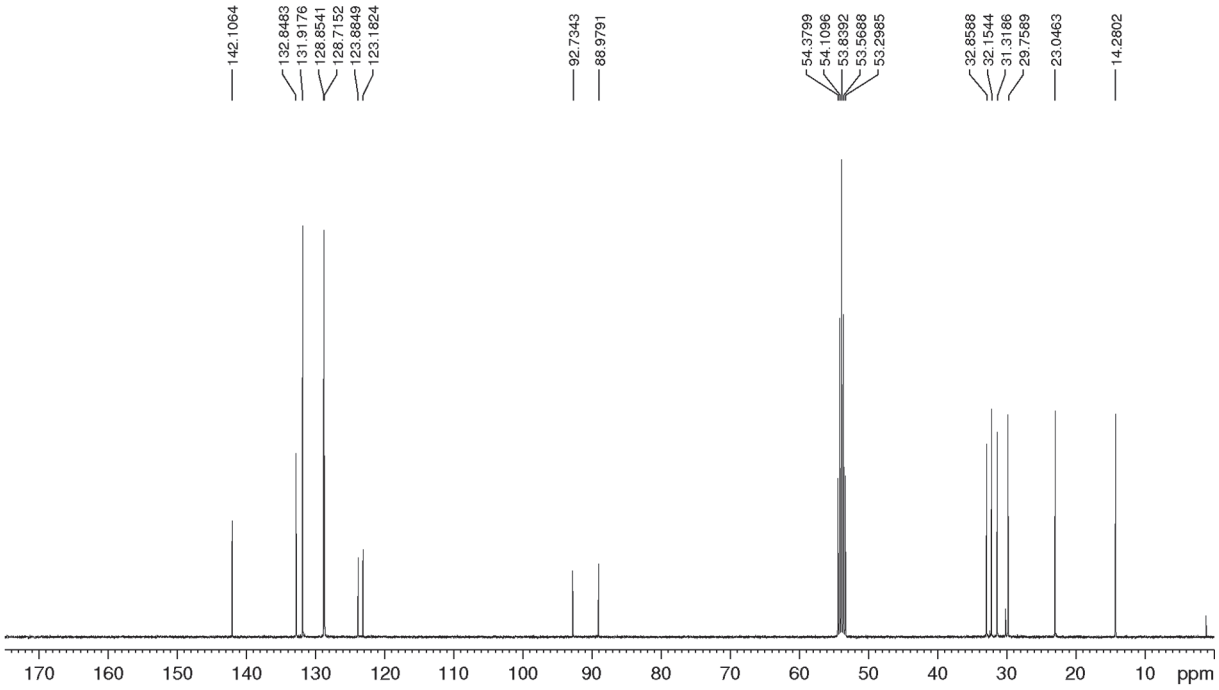

Figure S40. ^{13}C NMR spectrum of **49** (101 MHz, CD_2Cl_2, 300 K).

6.5. Computational Results

Table S1. Relative energies (E_{rel}) of geometry optimized (B3LYP/6-311G**) reference molecule *N*-(*iso*-propyl)-1,8-naphthalene imide (shown in Figure S41) with different dihedral angles around the C–N bond (ϕ_{CNCH}) of the imide substituent (*iso*-propyl) and frozen dihedral angles in the imide ring to ensure the flat naphthalene imide moiety.

ϕ_{CNCH} [°]	0	60	90
E_{rel} [kJ mol^{-1}]	0	38.5	60.5

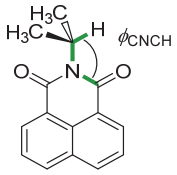

Figure S41. Reference molecule *N*-(*iso*-propyl)-1,8-naphthalene imide used for evaluation of the energy barrier ($\Delta G^{\ddagger}$) of the internal, restricted rotation around the C–N bond of the imide substituent. The investigated dihedral angle is indicated with green, bold bonds.

Table S2. B97D/STO-3G geometry optimized structure of **32-I-a** (Figure 36a). Cartesian coordinates in Å. The energy of the system is indicated.

E [Hartree]	–3771.576968		
Atom	X	Y	Z
C	-12.228636	0.741916	2.778282
C	-12.400335	-0.630119	2.391421
C	-11.424145	-1.252384	1.574259
C	-10.262863	-0.549546	1.123499
C	-10.091344	0.838421	1.515492
C	-11.084774	1.453546	2.336494
C	-13.637468	-1.421463	2.860016
C	-9.268602	-1.185955	0.282250
C	-8.395888	-1.664243	-0.437993
C	-7.394994	-2.267041	-1.299900
C	-7.752548	-3.375660	-2.139662
C	-6.786441	-3.983723	-2.972625
C	-5.452061	-3.509490	-2.987340
C	-5.081410	-2.415580	-2.149369
C	-6.042530	-1.787385	-1.310194
N	-3.667470	-1.967581	-2.134567
C	-2.647993	-3.015105	-1.846515
C	-1.208703	-2.503368	-1.819612
C	-0.873473	-1.112214	-2.017120
C	-1.911743	-0.141991	-2.279835
C	-3.394998	-0.517104	-2.354056
C	-0.183274	-3.436787	-1.559130
C	1.174880	-3.033585	-1.497872
C	1.556595	-1.676443	-1.679715
C	0.518159	-0.683622	-1.927096

C	0.840575	0.731304	-2.063955
C	2.256485	1.177098	-1.886717
C	3.296955	0.179386	-1.672295
C	2.983095	-1.241205	-1.603825
C	4.681165	0.609946	-1.518625
C	5.002643	2.017961	-1.519976
C	3.970834	2.961647	-1.704981
C	2.625606	2.549720	-1.900456
C	5.726768	-0.371527	-1.354366
C	7.195968	0.020178	-1.219876
N	7.456057	1.475608	-1.215583
C	6.431212	2.532566	-1.306309
C	5.396926	-1.742855	-1.335107
C	4.049099	-2.169421	-1.448880
C	-1.561765	1.213628	-2.453228
C	-0.213992	1.644308	-2.339939
O	6.722302	3.766741	-1.218813
O	8.144988	-0.820667	-1.123420
O	-2.973029	-4.221294	-1.626988
O	-4.327881	0.307155	-2.589994
C	8.925626	1.884590	-1.098843
C	9.204672	2.632104	0.248559
C	-8.919065	1.554411	1.047302
C	-7.897733	2.046776	0.577125
C	-6.671872	2.558733	-0.011566
C	-6.709728	3.466303	-1.119521
C	-5.504929	3.907397	-1.714698
C	-4.254240	3.453676	-1.232925
C	-4.202179	2.558572	-0.120325
C	-5.406208	2.119043	0.494550
N	-2.890095	2.080878	0.372604
C	-2.738494	0.621745	0.660203
C	-1.313723	0.191613	1.005319
C	-0.211277	1.121398	1.065033
C	-0.438800	2.533243	0.865129
C	-1.813721	3.105770	0.533843
C	-1.073565	-1.182872	1.221538
C	0.238961	-1.667903	1.454032
C	1.362726	-0.796368	1.483001
C	1.139448	0.634203	1.319430
C	2.239873	1.587027	1.394298
C	3.627481	1.085913	1.622009
C	3.859768	-0.349288	1.715380
C	2.758880	-1.302407	1.648578
C	5.223972	-0.841260	1.864227
C	6.322470	0.092989	1.959197
C	6.060665	1.477633	1.901022

C	4.740207	1.964886	1.724019
C	5.474701	-2.262848	1.905241
C	6.888135	-2.834498	1.999435
N	7.963280	-1.821444	2.114752
C	7.770519	-0.365180	2.146432
C	4.389673	-3.162170	1.831373
C	3.056020	-2.691607	1.713943
C	0.644774	3.432158	0.952963
C	1.958950	2.969399	1.219587
O	8.745027	0.436323	2.321689
O	7.155406	-4.077312	1.981337
O	-3.710085	-0.187957	0.566585
O	-2.045932	4.343886	0.390331
C	9.382047	-2.375455	2.250372
C	9.965366	-2.063559	3.671366
C	-13.279353	1.437681	3.665855
C	9.368524	2.718518	-2.349751
C	10.311474	-1.851145	1.103496
H	1.857480	3.326592	-2.046869
H	4.233674	4.036197	-1.697479
H	3.840704	-3.250889	-1.411756
H	6.212827	-2.480067	-1.216330
H	-2.369783	1.939805	-2.658133
H	0.002403	2.718235	-2.461822
H	1.939349	-3.799786	-1.290321
H	-0.464692	-4.494926	-1.400852
H	9.464299	0.905580	-1.094184
H	8.835939	3.688891	-2.366701
H	10.459242	2.904799	-2.292423
H	9.145564	2.162296	-3.281548
H	8.590089	3.550985	0.304448
H	8.975862	1.960020	1.105990
H	10.275576	2.913208	0.285407
H	-8.792959	-3.746474	-2.125519
H	-5.737030	-0.949635	-0.656381
H	-4.692828	-3.980619	-3.635483
H	-7.072350	-4.833616	-3.618265
H	4.593776	3.055385	1.662066
H	6.908459	2.181627	1.983101
H	2.243183	-3.433620	1.654120
H	4.602757	-4.247359	1.859923
H	0.448111	4.510174	0.801343
H	2.772587	3.710922	1.268933
H	0.375081	-2.752359	1.594813
H	-1.930808	-1.880561	1.177975
H	9.236522	-3.478076	2.141881
H	10.508699	-0.770869	1.241516

H	11.271127	-2.404148	1.135563
H	9.827696	-2.005112	0.119224
H	10.081819	-0.969836	3.798198
H	9.290554	-2.454631	4.458080
H	10.956903	-2.547878	3.772395
H	-7.686159	3.806742	-1.507549
H	-5.537834	4.601842	-2.573524
H	-3.317808	3.791909	-1.707435
H	-5.372493	1.432386	1.356935
H	-11.557446	-2.307864	1.275783
H	-10.953814	2.510022	2.632345
H	-13.680995	-1.456749	3.969480
H	-14.570374	-0.933236	2.505905
H	-13.606818	-2.457615	2.470774
H	-12.988671	2.487896	3.862374
H	-14.274943	1.427714	3.173108
H	-13.383424	0.907272	4.636412

Table S3. B97D/STO-3G geometry optimized structure of **32-II-b** (Figure 36b). Cartesian coordinates in Å. The energy of the system is indicated.

E [Hartree]	–3771.573827		
Atom	X	Y	Z
C	-7.738232	-0.397915	-1.681225
C	-6.264666	-0.735403	-1.441174
C	-5.204359	0.198753	-1.745099
C	-5.520898	1.531795	-2.200531
C	-6.961775	2.029655	-2.309366
N	-7.996766	1.010988	-2.010708
C	-5.940029	-2.021544	-0.964366
C	-4.587793	-2.403470	-0.759375
C	-3.510525	-1.525756	-1.058488
C	-3.812401	-0.203179	-1.590265
C	-2.752802	0.725348	-1.964862
C	-1.325694	0.299509	-1.832202
C	-1.024109	-1.001265	-1.246630
C	-2.085222	-1.912354	-0.836422
C	-0.244406	1.126937	-2.240612
C	1.107950	0.726345	-2.071861
C	1.432380	-0.513851	-1.482129
C	0.367150	-1.395586	-1.060809
C	0.673827	-2.656510	-0.429025
C	2.104715	-3.134427	-0.206415
N	3.149859	-2.263192	-0.821857
C	2.913012	-0.885813	-1.353860
C	-1.730063	-3.140402	-0.215258
C	-0.375057	-3.499403	-0.004501

C	-4.474291	2.419427	-2.529671
C	-3.116033	2.018850	-2.429812
C	4.500877	-2.854213	-0.959974
C	4.601701	-4.176811	-1.495259
C	5.870773	-4.773025	-1.675830
C	7.046415	-4.055767	-1.360368
C	6.964050	-2.720701	-0.839391
C	5.674977	-2.126837	-0.619677
C	8.194547	-2.002586	-0.568370
C	9.286918	-1.463545	-0.409110
C	10.572753	-0.820616	-0.241210
C	10.657410	0.585761	0.107825
C	11.950026	1.183355	0.252959
C	13.140980	0.440474	0.065594
C	13.057685	-0.951834	-0.279321
C	11.786148	-1.557494	-0.426923
C	9.452614	1.359406	0.313494
C	8.414838	1.989021	0.499851
C	7.221124	2.759525	0.785716
C	5.915614	2.192467	0.597762
C	4.763389	2.947363	0.949405
C	4.903389	4.275130	1.463267
C	6.188965	4.845268	1.611019
C	7.344030	4.098810	1.285110
N	3.401043	2.377523	0.844378
C	3.158680	0.998138	1.370223
C	1.676816	0.641430	1.521279
C	0.614491	1.532168	1.111159
C	0.925004	2.788263	0.471360
C	2.357433	3.256720	0.237644
C	-0.777476	1.149953	1.313793
C	-1.083525	-0.144274	1.911861
C	-0.004752	-0.981243	2.307039
C	1.349087	-0.594835	2.116735
C	-1.835338	2.064898	0.903192
C	-1.476907	3.285638	0.269653
C	-0.121199	3.635961	0.049953
C	-2.512548	-0.558160	2.060329
C	-3.567860	0.367463	1.669760
C	-3.261360	1.685885	1.130454
C	-4.961039	-0.034563	1.811212
C	-6.016219	0.890840	1.471150
C	-5.688390	2.178021	0.998922
C	-4.334598	2.564790	0.821216
C	-5.284092	-1.361191	2.278897
C	-4.241012	-2.240340	2.639743
C	-2.881797	-1.841777	2.547774

C	-6.726490	-1.870358	2.364834
N	-7.752773	-0.872121	2.003092
C	-7.490765	0.530742	1.624633
O	4.107030	0.223062	1.695742
O	2.663022	4.310585	-0.397873
O	-7.028935	-3.055144	2.711134
C	-9.226043	-1.275815	2.091058
C	-9.620425	-1.638186	3.563903
O	-8.438736	1.360097	1.440416
O	3.865453	-0.124000	-1.698173
O	2.408706	-4.189350	0.428226
O	-7.280663	3.218785	-2.625727
C	-9.445220	1.457136	-2.223926
C	-10.023020	0.826618	-3.537993
O	-8.676240	-1.255507	-1.611204
C	-9.546671	-2.430288	1.082923
C	-10.337778	1.140449	-0.976050
H	0.141892	4.587810	-0.448580
H	-2.259330	3.982665	-0.070988
H	-0.204929	-1.962566	2.767023
H	2.172297	-1.265882	2.426675
H	-4.129657	3.574191	0.429500
H	-6.510500	2.875981	0.753033
H	-4.507365	-3.253907	2.994158
H	-2.103904	-2.563664	2.845485
H	-9.768208	-0.349489	1.782965
H	-9.376501	-0.798934	4.244721
H	-9.075158	-2.544948	3.889481
H	-10.637828	-2.621173	1.091056
H	-9.015897	-3.352776	1.386467
H	-10.709967	-1.834718	3.609028
H	-9.231910	-2.133837	0.057879
H	5.810621	1.172241	0.190613
H	4.002416	4.846652	1.745011
H	-0.115024	-4.455661	0.487102
H	-2.514566	-3.835831	0.123984
H	-0.441729	2.110822	-2.696307
H	1.932995	1.389479	-2.393599
H	-4.387329	-3.413354	-0.366254
H	-6.762092	-2.728230	-0.745273
H	-4.736139	3.439094	-2.869538
H	-2.334430	2.745177	-2.706234
H	-9.355475	2.563008	-2.354031
H	-9.796630	1.403834	-0.042378
H	-10.587472	0.062788	-0.952767
H	-10.067699	-0.275122	-3.435864
H	-11.273883	1.728640	-1.045441

H	3.682750	-4.723797	-1.767565
H	5.595349	-1.111757	-0.192782
C	14.514239	1.120555	0.230967
H	12.013319	2.253920	0.518889
H	11.721802	-2.628023	-0.692812
C	14.340744	-1.780167	-0.487620
H	-9.385021	1.089901	-4.404647
H	-11.046191	1.215369	-3.711257
H	8.350535	4.533332	1.419205
H	6.288764	5.873623	2.002648
H	8.040773	-4.509782	-1.518504
H	5.941188	-5.797383	-2.083915
H	14.390083	2.188080	0.497490
H	15.104843	0.618845	1.026933
H	15.099619	1.052178	-0.710726
H	14.090090	-2.827412	-0.745515
H	14.956287	-1.347413	-1.304898
H	14.961343	-1.776759	0.433753

Table S4. B97D/STO-3G geometry optimized structure of **32-III-c** (Figure 36c). Cartesian coordinates in Å. The energy of the system is indicated.

E [Hartree]	–3771.514151		
Atom	X	Y	Z
C	9.921435	-2.687503	-1.396680
C	10.839773	-1.876049	-0.674777
C	10.312600	-0.826078	0.190065
C	8.867930	-0.640421	0.291372
C	7.977871	-1.493268	-0.463310
C	8.518563	-2.498621	-1.293140
C	6.456591	-1.349738	-0.413532
N	5.969451	-0.269613	0.496250
C	6.833144	0.639941	1.308662
C	8.333421	0.395532	1.145845
C	11.200642	0.041965	0.955718
C	10.624121	1.046077	1.781726
C	9.218390	1.218238	1.875039
C	12.319842	-2.067604	-0.777076
C	13.206957	-1.198956	-0.011724
C	12.680697	-0.147977	0.851658
C	14.650928	-1.385332	-0.111747
C	15.186357	-2.423293	-0.963059
C	14.303136	-3.248128	-1.691021
C	12.896936	-3.073975	-1.600137
C	15.543092	-0.532388	0.640303
C	15.003420	0.475889	1.466110
C	13.600081	0.665146	1.570380

C	17.067999	-0.677755	0.579440
N	17.543618	-1.755577	-0.308336
C	16.688739	-2.664520	-1.106038
C	4.503101	-0.082687	0.598964
C	3.656476	-1.205678	0.843814
C	2.254233	-1.020748	0.933056
C	1.687031	0.266866	0.798869
C	2.528064	1.405788	0.558547
C	3.944069	1.216952	0.451943
C	1.939870	2.723550	0.410610
C	1.404738	3.821973	0.285212
C	0.705848	5.082385	0.141327
C	-0.716387	5.088207	-0.158296
C	-1.391027	6.344281	-0.272496
C	-0.708225	7.574711	-0.107698
C	0.698820	7.569109	0.181589
C	1.381021	6.333187	0.301497
C	1.461120	8.896468	0.362719
C	-1.469896	8.908128	-0.240462
C	-1.416157	3.834242	-0.347953
C	-1.952583	2.741711	-0.512939
C	-2.543186	1.431194	-0.708690
C	-1.708217	0.307182	-1.027402
C	-2.277835	-0.973664	-1.208135
C	-3.676838	-1.165949	-1.088699
C	-4.517253	-0.058156	-0.765689
C	-3.955393	1.234124	-0.571645
N	-5.979876	-0.252921	-0.630051
C	-6.867251	0.695471	-1.369345
C	-8.362062	0.443099	-1.172293
C	-8.871192	-0.635116	-0.355432
C	-7.959317	-1.525215	0.326708
C	-6.440132	-1.377964	0.238519
C	-10.312280	-0.825791	-0.218606
C	-11.222459	0.081151	-0.909525
C	-10.670489	1.125845	-1.701265
C	-9.268098	1.301958	-1.830491
C	-10.813804	-1.919511	0.606373
C	-9.874617	-2.766870	1.256647
C	-8.475378	-2.572144	1.120026
C	-12.290251	-2.116707	0.744198
C	-13.199501	-1.207850	0.055332
C	-12.698840	-0.112391	-0.767033
C	-14.639941	-1.398427	0.191778
C	-15.150103	-2.481179	1.001849
C	-14.245840	-3.344980	1.654940
C	-12.842891	-3.166344	1.529119

C	-15.553826	-0.504650	-0.482803
C	-15.038658	0.546755	-1.269560
C	-13.638959	0.739647	-1.409835
C	-17.076324	-0.650761	-0.378821
N	-17.525611	-1.777175	0.461016
C	-16.647682	-2.729246	1.179409
O	-6.394787	1.612715	-2.105746
O	-5.619525	-2.123132	0.853747
O	-17.895826	0.126119	-0.962328
O	-17.134608	-3.670702	1.881950
O	6.337837	1.520139	2.074675
O	5.655387	-2.062600	-1.089612
O	17.868560	0.061386	1.233941
O	17.197479	-3.566768	-1.843700
H	-12.179878	-3.868892	2.060274
H	-14.654525	-4.168475	2.270469
H	-13.289656	1.576513	-2.036751
H	-15.753073	1.221451	-1.778092
H	-7.761993	-3.241472	1.636968
H	-10.224307	-3.600523	1.887442
H	-11.333712	1.825507	-2.235820
H	-8.859701	2.119990	-2.453559
H	-0.619126	0.458032	-1.133230
H	-4.606338	2.087074	-0.313628
H	-4.122992	-2.163460	-1.243264
H	-1.628705	-1.832894	-1.456188
H	12.251008	-3.745224	-2.189633
H	14.731018	-4.037532	-2.337394
H	13.231239	1.467641	2.230195
H	15.701391	1.119498	2.034276
H	7.821727	-3.139837	-1.865339
H	10.290745	-3.487963	-2.058534
H	11.270224	1.716249	2.372130
H	8.790665	2.004355	2.525614
H	0.595018	0.411408	0.880895
H	1.600328	-1.891609	1.120647
H	4.100525	-2.209113	0.961937
H	4.599997	2.082050	0.254001
H	-2.472308	6.348645	-0.499947
H	2.462287	6.328743	0.529012
H	-1.033858	9.527351	-1.053186
H	-2.538541	8.724962	-0.465175
H	-1.396864	9.494591	0.700205
H	2.529782	8.704762	0.580111
H	1.387912	9.516943	-0.555847
H	1.025695	9.485732	1.197737
C	-19.026066	-2.011710	0.628985

C	19.048496	-1.985616	-0.438722
H	19.116418	-2.840439	-1.155533
C	19.758914	-0.730802	-1.052331
C	19.674558	-2.404360	0.935540
H	20.828736	-0.964973	-1.221312
H	19.291094	-0.461080	-2.019530
H	19.680404	0.126140	-0.355790
H	20.744072	-2.653500	0.787309
H	19.592900	-1.569240	1.657771
H	19.149703	-3.291843	1.340484
H	-19.072838	-2.906919	1.296513
C	-19.709909	-0.793503	1.339046
C	-19.700354	-2.347681	-0.745147
H	-20.774818	-1.033984	1.528894
H	-19.209419	-0.583175	2.304631
H	-19.649790	0.103044	0.692287
H	-20.765061	-2.603346	-0.575035
H	-19.640428	-1.471573	-1.419365
H	-19.193009	-3.210634	-1.219484

Table S5. Relative energies of local optimized (with PM6-DH2 in CAST) structures of folded **32-II** after gradual distortion of one phenylene fragment close to one PBI moiety (as discussed in subchapters 3.3.3 and 3.4.2) mimicking the backbone flapping.

Entry	E_{rel} [kJ mol^{-1}][a]	ϕ_{CCCC} (initial) [°][b]	ϕ_{CCCC} (final) [°][c]
1	4	–85.3	–138.8
2	4	–61.5	–137.3
3	4	–35.9	–115.5
4	50	27.1	52.5
5	38	65.0	123.1
6	0	90.5	136.7
7	0	128.1	137.0

[a] Relative to the structure with the lowest energy (i.e. entry 6 and 7). [b] Gradual distortion by hand of one phenylene fragment similar to the experiments shown in Figure 32c. [c] After local optimazation.

Table S6. Relative energies of local optimized (with PM6-DH2 in CAST) structures of folded **32** after gradual distortion of one imide fragment (as discussed in subchapters 3.3.3 and 3.4.2) for comparison of the energies of the backbone flapping.

Entry	E_{rel} [kJ mol^{-1}][a]	ϕ_{CNCH} (initial) [°][b]	ϕ_{CNCH} (final) [°][c]
1	0	16.5	–175.1
2	0	–19.9	–174.4
3	33	–56.2	–46.4
4	0	–95.0	4.4
5	0	–131.1	5.0
6	0	–155.8	5.8
7	0	162.7	6.0

[a] Relative to the structure with the lowest energy (i.e. entry 6 and 7). [b] Gradual distortion by hand of one imide substituent similar to the experiments shown in Figure 32d. [c] After local optimazation.

Reference List

[1] Power generation in Germany, https://www.destatis.de/DE/ZahlenFakten/Wirtschaftsbereiche/Energie/Erzeugung/Erzeugung.html, Statistisches Bundesamt, accessed 8th of April, 2015.

[2] C. W. Tang, *Appl. Phys. Lett.* **1986**, *48*, 183–185.

[3] International Year of Light and Light-based Technologies (IYL2015) - Press Release, http://www.light2015.org/Home/About/Press-Office.html, United Nations Educational, Scientific and Cultural Organization (UNESCO), accessed 4th of April, 2015.

[4] International Year of Light and Light-based Technologies (IYL2015), http://www.light2015.org/Home.html, United Nations Educational, Scientific and Cultural Organization (UNESCO), accessed 4th of April, 2015.

[5] G. M. Whitesides, *Angew. Chem. Int. Ed.* **2015**, *54*, 3196–3209.

[6] I. McConnell, G. Li, G. W. Brudvig, *Chem. Biol.* **2010**, *17*, 434–447.

[7] H. Langhals, *Heterocycles* **1995**, *40*, 477–500.

[8] F. Würthner, *Chem. Commun.* **2004**, 1564–1579.

[9] C. Huang, S. Barlow, S. R. Marder, *J. Org. Chem.* **2011**, *76*, 2386–2407.

[10] J. A. A. W. Elemans, R. van Hameren, R. J. M. Nolte, A. E. Rowan, *Adv. Mater.* **2006**, *18*, 1251–1266.

[11] X. Zhan, A. Facchetti, S. Barlow, T. J. Marks, M. A. Ratner, M. R. Wasielewski, S. R. Marder, *Adv. Mater.* **2011**, *23*, 268–284.

[12] T. Seki, X. Lin, S. Yagai, *Asian J. Org. Chem.* **2013**, *2*, 708–724.

[13] F. Würthner, M. Stolte, *Chem. Commun.* **2011**, *47*, 5109–5115.

[14] T. Liu, A. Troisi, *Adv. Mater.* **2013**, *25*, 1038–1041.

[15] M. M. Safont-Sempere, P. Osswald, K. Radacki, F. Würthner, *Chem. Eur. J.* **2010**, *16*, 7380–7384.

[16] M. M. Safont-Sempere, P. Osswald, M. Stolte, M. Grüne, M. Renz, M. Kaupp, K. Radacki, H. Braunschweig, F. Würthner, *J. Am. Chem. Soc.* **2011**, *133*, 9580–9591.

[17] M. M. Safont Sempere, PhD thesis, University of Würzburg (Germany), **2011**.

[18] C. Shao, M. Grüne, M. Stolte, F. Würthner, *Chem. Eur. J.* **2012**, *18*, 13665–13677.

[19] C. Shao, PhD thesis, University of Würzburg (Germany), **2012**.

[20] M. Son, K. H. Park, C. Shao, F. Würthner, D. Kim, *J. Phys. Chem. Lett.* **2014**, *5*, 3601–3607.

[21] H. Langhals, R. Ismael, *Eur. J. Org. Chem.* **1998**, 1915–1917.

[22] J. Feng, Y. Zhang, C. Zhao, R. Li, W. Xu, X. Li, J. Jiang, *Chem. Eur. J.* **2008**, *14*, 7000–7010.

[23] F. Schlosser, M. Moos, C. Lambert, F. Würthner, *Adv. Mater.* **2013**, *25*, 410–414.

[24] K. E. Brown, W. A. Salamant, L. E. Shoer, R. M. Young, M. R. Wasielewski, *J. Phys. Chem. Lett.* **2014**, 2588–2593.

[25] V. Dehm, M. Büchner, J. Seibt, V. Engel, F. Würthner, *Chem. Sci.* **2011**, *2*, 2094–2100.

[26] V. Dehm, PhD thesis, University of Würzburg (Germany), **2010**.

[27] M. R. Wasielewski, *Acc. Chem. Res.* **2009**, *42*, 1910–1921.

[28] Y. Zhao, M. R. Wasielewski, *Tetrahedron Lett.* **1999**, *40*, 7047–7050.

[29] A. S. Lukas, Y. Zhao, S. E. Miller, M. R. Wasielewski, *J. Phys. Chem. B* **2002**, *106*, 1299–1306.

[30] J. M. Giaimo, A. V. Gusev, M. R. Wasielewski, *J. Am. Chem. Soc.* **2002**, *124*, 8530–8531.

[31] J. E. Bullock, M. T. Vagnini, C. Ramanan, D. T. Co, T. M. Wilson, J. W. Dicke, T. J. Marks, M. R. Wasielewski, *J. Phys. Chem. B* **2010**, *114*, 1794–1802.
[32] S. Nakazono, S. Easwaramoorthi, D. Kim, H. Shinokubo, A. Osuka, *Org. Lett.* **2009**, *11*, 5426–5429.
[33] S. Nakazono, Y. Imazaki, H. Yoo, J. Yang, T. Sasamori, N. Tokitoh, T. Cédric, H. Kageyama, D. Kim, H. Shinokubo, A. Osuka, *Chem. Eur. J.* **2009**, *15*, 7530–7533.
[34] G. Battagliarin, M. Davies, S. Mackowiak, C. Li, K. Müllen, *ChemPhysChem* **2012**, *13*, 923–926.
[35] N. Mizoshita, T. Tani, H. Shinokubo, S. Inagaki, *Angew. Chem. Int. Ed.* **2012**, *51*, 1156–1160.
[36] N. Mizoshita, T. Tani, S. Inagaki, *Adv. Mater.* **2012**, *24*, 3350–3355.
[37] N. Mizoshita, K.-i. Yamanaka, S. Hiroto, H. Shinokubo, T. Tani, S. Inagaki, *Langmuir* **2012**, *28*, 3987–3994.
[38] Z. Chen, V. Stepanenko, V. Dehm, P. Prins, L. D. A. Siebbeles, J. Seibt, P. Marquetand, V. Engel, F. Würthner, *Chem. Eur. J.* **2007**, *13*, 436–449.
[39] T. E. Kaiser, H. Wang, V. Stepanenko, F. Würthner, *Angew. Chem. Int. Ed.* **2007**, *46*, 5541–5544.
[40] E. E. Jelley, *Nature* **1936**, *138*, 1009–1010.
[41] E. E. Jelley, *Nature* **1937**, *139*, 631–631.
[42] A. Eisfeld, J. S. Briggs, *Chem. Phys.* **2006**, *324*, 376–384.
[43] F. Würthner, T. E. Kaiser, C. R. Saha-Möller, *Angew. Chem. Int. Ed.* **2011**, *50*, 3376–3410.
[44] Y. Tian, V. Stepanenko, T. E. Kaiser, F. Würthner, I. G. Scheblykin, *Nanoscale* **2012**, *4*, 218–223.
[45] A. Merdasa, Á. J. Jiménez, R. Camacho, M. Meyer, F. Würthner, I. G. Scheblykin, *Nano Lett.* **2014**, *14*, 6774–6781.
[46] S. W. Eaton, L. E. Shoer, S. D. Karlen, S. M. Dyar, E. A. Margulies, B. S. Veldkamp, C. Ramanan, D. A. Hartzler, S. Savikhin, T. J. Marks, M. R. Wasielewski, *J. Am. Chem. Soc.* **2013**, *135*, 14701–14712.
[47] E. G. McRae, M. Kasha, *J. Phys. Chem. A* **1958**, *28*, 721–722.
[48] M. Kasha, *Radiation Res.* **1963**, *20*, 55–70.
[49] M. Kasha, H. R. Rawls, M. A. El-Bayoumi, *Pure Appl. Chem.* **1965**, *11*, 371–392.
[50] P. E. Hartnett, A. Timalsina, H. S. S. R. Matte, N. Zhou, X. Guo, W. Zhao, A. Facchetti, R. P. H. Chang, M. C. Hersam, M. R. Wasielewski, T. J. Marks, *J. Am. Chem. Soc.* **2014**, *136*, 16345–16356.
[51] J. Seibt, P. Marquetand, V. Engel, Z. Chen, V. Dehm, F. Würthner, *Chem. Phys.* **2006**, *328*, 354–362.
[52] J. Seibt, V. Dehm, F. Würthner, V. Engel, *J. Phys. Chem. A* **2007**, *126*, 164308.
[53] J. Seibt, T. Winkler, K. Renziehausen, V. Dehm, F. Würthner, H. D. Meyer, V. Engel, *J. Phys. Chem. A* **2009**, *113*, 13475–13482.
[54] A. Loudet, K. Burgess, *Chem. Rev.* **2007**, *107*, 4891–4932.
[55] M. Kaur, D. H. Choi, *Chem. Soc. Rev.* **2015**, *44*, 58–77.
[56] R. Klajn, *Chem. Soc. Rev.* **2014**, *43*, 148–184.
[57] M. Kasha, *Discuss. Faraday Soc.* **1950**, *9*, 14–19.
[58] H. Langhals, J. Karolin, L. B-Å. Johansson, *J. Chem. Soc., Faraday Trans.* **1998**, *94*, 2919–2922.
[59] M. W. Holman, R. Liu, L. Zang, P. Yan, S. A. DiBenedetto, R. D. Bowers, D. M. Adams, *J. Am. Chem. Soc.* **2004**, *126*, 16126–16133.
[60] C.-C. You, R. Dobrawa, C. R. Saha-Möller, F. Würthner, in *Supermolecular Dye Chemistry, Vol. 258* (Ed.: F. Würthner), Springer Berlin Heidelberg, **2005**, pp. 39–82.

[61] J. M. Giaimo, J. V. Lockard, L. E. Sinks, A. M. Scott, T. M. Wilson, M. R. Wasielewski, *J. Phys. Chem. A* **2008**, *112*, 2322–2330.
[62] W. E. Ford, P. V. Kamat, *J. Phys. Chem.* **1987**, *91*, 6373–6380.
[63] D. Veldman, S. M. A. Chopin, S. C. J. Meskers, M. M. Groeneveld, R. M. Williams, R. A. J. Janssen, *J. Phys. Chem. A* **2008**, *112*, 5846–5857.
[64] H. Langhals, W. Jona, *Angew. Chem. Int. Ed.* **1998**, *37*, 952–955.
[65] S. Demmig, H. Langhals, *Chem. Ber.* **1988**, *121*, 225–230.
[66] H. Langhals, J. Gold, *J. Prakt. Chem.* **1996**, *338*, 654–659.
[67] R. Liu, M. W. Holman, L. Zang, D. M. Adams, *J. Phys. Chem. A* **2003**, *107*, 6522–6526.
[68] M. W. Holman, P. Yan, D. M. Adams, S. Westenhoff, C. Silva, *J. Phys. Chem. A* **2005**, *109*, 8548–8552.
[69] F. P. Diehl, C. Roos, A. Duymaz, B. Lunkenheimer, A. Köhn, T. Basché, *J. Phys. Chem. Lett.* **2014**, *5*, 262–269.
[70] A. Perez-Velasco, V. Gorteau, S. Matile, *Angew. Chem. Int. Ed.* **2008**, *47*, 921–923.
[71] J. Hernando, J. P. Hoogenboom, E. M. H. P. Van Dijk, J. J. García-López, M. Crego-Calama, D. N. Reinhoudt, N. F. Van Hulst, M. F. García-Parajó, *Phys. Rev. Lett.* **2004**, *93*, 236404.
[72] J. Hernando, E. M. H. P. van Dijk, J. P. Hoogenboom, J.-J. García-López, D. N. Reinhoudt, M. Crego-Calama, M. F. García-Parajó, N. F. van Hulst, *Phys. Rev. Lett.* **2006**, *97*, 216403.
[73] J. P. Hoogenboom, J. Hernando, E. M. H. P. van Dijk, N. F. van Hulst, M. F. García-Parajó, *ChemPhysChem* **2007**, *8*, 823–833.
[74] J. Hernando, J. Hoogenboom, E. van Dijk, M. Garcia-Parajo, N. F. van Hulst, *J. Lumin.* **2008**, *128*, 1050–1052.
[75] T. Vosch, E. Fron, J.-i. Hotta, A. Deres, H. Uji-i, A. Idrissi, J. Yang, D. Kim, L. Puhl, A. Haeuseler, K. Müllen, F. C. De Schryver, M. Sliwa, J. Hofkens, *J. Phys. Chem. C* **2009**, *113*, 11773–11782.
[76] J. t. Schiphorst, A. M. Kendhale, M. G. Debije, C. Menelaou, L. M. Herz, A. P. H. J. Schenning, *Chem. Mat.* **2014**, *26*, 3876–3878.
[77] A. M. Kendhale, A. P. H. J. Schenning, M. G. Debije, *J. Mater. Chem. A* **2013**, *1*, 229–232.
[78] C. Menelaou, J. t. Schiphorst, A. M. Kendhale, P. Parkinson, M. G. Debije, A. P. H. J. Schenning, L. M. Herz, *J. Phys. Chem. Lett.* **2015**, *6*, 1170–1176.
[79] H. W. Bahng, M.-C. Yoon, J.-E. Lee, Y. Murase, T. Yoneda, H. Shinokubo, A. Osuka, D. Kim, *J. Phys. Chem. B* **2012**, *116*, 1244–1255.
[80] C. C. Jumper, J. M. Anna, A. Stradomska, J. Schins, M. Myahkostupov, V. Prusakova, D. G. Oblinsky, F. N. Castellano, J. Knoester, G. D. Scholes, *Chem. Phys. Lett.* **2014**, *599*, 23–33.
[81] Y. Shi, H. Wu, L. Xue, X. Li, *J. Colloid Interface Sci.* **2012**, *365*, 172–177.
[82] H. Langhals, A. Hofer, S. Bernhard, J. S. Siegel, P. Mayer, *J. Org. Chem.* **2011**, *76*, 990–992.
[83] H. Langhals, J. Gold, *Liebigs Ann.* **1997**, 1151–1153.
[84] T. Kawai, K. Kawamura, H. Tsumatori, M. Ishikawa, M. Naito, M. Fujiki, T. Nakashima, *ChemPhysChem* **2007**, *8*, 1465–1468.
[85] H. Tsumatori, T. Nakashima, J. Yuasa, T. Kawai, *Synt. Met.* **2009**, *159*, 952–954.
[86] H. Tsumatori, T. Nakashima, T. Kawai, *Org. Lett.* **2010**, *12*, 2362–2365.
[87] J. Kumar, T. Nakashima, H. Tsumatori, T. Kawai, *J. Phys. Chem. Lett.* **2014**, *5*, 316–321.
[88] Y. Tang, A. E. Cohen, *Science* **2011**, *332*, 333–336.

[89] K. M. Lefler, K. E. Brown, W. A. Salamant, S. M. Dyar, K. E. Knowles, M. R. Wasielewski, *J. Phys. Chem. A* **2013**, *117*, 10333–10345.
[90] H. Liu, L. Shen, Z. Cao, X. Li, *Phys. Chem. Chem. Phys.* **2014**, *16*, 16399–16406.
[91] E. A. Margulies, L. E. Shoer, S. W. Eaton, M. R. Wasielewski, *Phys. Chem. Chem. Phys.* **2014**, *16*, 23735–23742.
[92] C. Hippius, I. H. M. van Stokkum, E. Zangrando, R. M. Williams, M. Wykes, D. Beljonne, F. Würthner, *J. Phys. Chem. C* **2008**, *112*, 14626–14638.
[93] D. Ernst, R. Hildner, C. Hippius, F. Würthner, J. Köhler, *Chem. Phys. Lett.* **2009**, *482*, 93–98.
[94] A. Issac, R. Hildner, D. Ernst, C. Hippius, F. Würthner, J. Köhler, *Phys. Chem. Chem. Phys.* **2012**, *14*, 10789–10798.
[95] C. Hippius, F. Schlosser, M. O. Vysotsky, V. Böhmer, F. Würthner, *J. Am. Chem. Soc.* **2006**, *128*, 3870–3871.
[96] C. Hippius, I. H. M. van Stokkum, M. Gsänger, M. M. Groeneveld, R. M. Williams, F. Würthner, *J. Phys. Chem. C* **2008**, *112*, 2476–2486.
[97] W. Wang, L.-S. Li, G. Helms, H.-H. Zhou, A. D. Q. Li, *J. Am. Chem. Soc.* **2003**, *125*, 1120–1121.
[98] A. D. Q. Li, W. Wang, L.-Q. Wang, *Chem. Eur. J.* **2003**, *9*, 4594–4601.
[99] J. J. Han, A. D. Shaller, W. Wang, A. D. Q. Li, *J. Am. Chem. Soc.* **2008**, *130*, 6974–6982.
[100] A. D. Shaller, W. Wang, A.-X. Li, G. Moyna, J. J. Han, G. L. Helms, A. D. Q. Li, *Chem. Eur. J.* **2011**, *17*, 8350–8362.
[101] A. D. Q. Li, in *Molecular Self-Assembly: Advances and Applications* (Ed.: A. D. Q. Li), Pan Stanford Publishing Pte Ltd., Singapore, **2013**, pp. 123–206.
[102] K. A. Kistler, C. M. Pochas, H. Yamagata, S. Matsika, F. C. Spano, *J. Phys. Chem. B* **2012**, *116*, 77–86.
[103] R. F. Fink, J. Seibt, V. Engel, M. Renz, M. Kaupp, S. Lochbrunner, H.-M. Zhao, J. Pfister, F. Würthner, B. Engels, *J. Am. Chem. Soc.* **2008**, *130*, 12858–12859.
[104] W. Wang, W. Wan, H.-H. Zhou, S. Niu, A. D. Q. Li, *J. Am. Chem. Soc.* **2003**, *125*, 5248–5249.
[105] P. A. J. De Witte, J. Hernando, E. E. Neuteboom, E. M. H. P. van Dijk, S. C. J. Meskers, R. A. J. Janssen, N. F. van Hulst, R. J. M. Nolte, M. F. García-Parajó, A. E. Rowan, *J. Phys. Chem. B* **2006**, *110*, 7803–7812.
[106] C. E. Finlayson, R. H. Friend, M. B. J. Otten, E. Schwartz, J. J. L. M. Cornelissen, R. J. M. Nolte, A. E. Rowan, P. Samorì, V. Palermo, A. Liscio, K. Peneva, K. Müllen, S. Trapani, D. Beljonne, *Adv. Funct. Mater.* **2008**, *18*, 3947–3955.
[107] E. Schwartz, V. Palermo, C. E. Finlayson, Y.-S. Huang, M. B. J. Otten, A. Liscio, S. Trapani, I. González-Valls, P. Brocorens, J. J. L. M. Cornelissen, K. Peneva, K. Müllen, F. C. Spano, A. Yartsev, S. Westenhoff, R. H. Friend, D. Beljonne, R. J. M. Nolte, P. Samorì, A. E. Rowan, *Chem. Eur. J.* **2009**, *15*, 2536–2547.
[108] S. Foster, C. E. Finlayson, P. E. Keivanidis, Y.-S. Huang, I. Hwang, R. H. Friend, M. B. J. Otten, L.-P. Lu, E. Schwartz, R. J. M. Nolte, A. E. Rowan, *Macromolecules* **2009**, *42*, 2023–2030.
[109] F. Spreitler, M. Sommer, M. Thelakkat, J. Köhler, *Phys. Chem. Chem. Phys.* **2012**, *14*, 7971–7980.
[110] F. Spreitler, M. Sommer, M. Hollfelder, M. Thelakkat, S. Gekle, J. Köhler, *Phys. Chem. Chem. Phys.* **2014**, *16*, 25959–25968.
[111] J. Wang, A. Kulago, W. R. Browne, B. L. Feringa, *J. Am. Chem. Soc.* **2010**, *132*, 4191–4196.
[112] M. Son, B. Fimmel, V. Dehm, F. Würthner, D. Kim, *ChemPhysChem* **2015**, *16*, 1757–1767.

[113] D. J. Cram, *Angew. Chem. Int. Ed. Engl.* **1988**, *27*, 1009–1020.
[114] J.-M. Lehn, *Angew. Chem. Int. Ed. Engl.* **1988**, *27*, 89–112.
[115] C. J. Pedersen, *Angew. Chem. Int. Ed. Engl.* **1988**, *27*, 1021–1027.
[116] F. Gao, Y. Zhao, W. Liang, *J. Phys. Chem. B* **2011**, *115*, 2699–2708.
[117] P. Spenst, F. Würthner, *Angew. Chem. Int. Ed.* **2015**, (10.1002/anie.201503542).
[118] W. Wang, L. Wang, B. J. Palmer, G. J. Exarhos, A. D. Q. Li, *J. Am. Chem. Soc.* **2006**, *128*, 11150–11159.
[119] W. Wang, A. D. Shaller, A. D. Q. Li, *J. Am. Chem. Soc.* **2008**, *130*, 8271–8279.
[120] A. D. Shaller, W. Wang, H. Gan, A. D. Q. Li, *Angew. Chem. Int. Ed.* **2008**, *47*, 7705–7709.
[121] F. Schlosser, V. Stepanenko, F. Würthner, *Chem. Commun.* **2010**, *46*, 8350–8352.
[122] F. Schlosser, J. Sung, P. Kim, D. Kim, F. Würthner, *Chem. Sci.* **2012**, *3*, 2778–2785.
[123] J.-E. Lee, V. Stepanenko, J. Yang, H. Yoo, F. Schlosser, D. Bellinger, B. Engels, I. G. Scheblykin, F. Würthner, D. Kim, *ACS Nano* **2013**, *7*, 5064–5076.
[124] S. Ham, J. Yang, F. Schlosser, F. Würthner, D. Kim, *J. Phys. Chem. Lett.* **2014**, *5*, 2830–2835.
[125] Q. Zhou, P. J. Carroll, T. M. Swager, *J. Org. Chem.* **1994**, *59*, 1294–1301.
[126] D. Sahoo, S. Thiele, M. Schulte, N. Ramezanian, A. Godt, *Beilstein J. Org. Chem.* **2010**, *6*.
[127] H. Kaiser, J. Lindner, H. Langhals, *Chem. Ber.* **1991**, *124*, 529–535.
[128] D. F. Louw, J. Strating, H. J. Backer, *Recl. Trav. Chim. Pay.-B.* **1954**, *73*, 649–654.
[129] M. J. Tauber, R. F. Kelley, J. M. Giaimo, B. Rybtchinski, M. R. Wasielewski, *J. Am. Chem. Soc.* **2006**, *128*, 1782–1783.
[130] H. Langhals, C. Wagner, R. Ismael, *New J. Chem.* **2001**, *25*, 1047–1049.
[131] D. Shanks, S. Preus, K. Qvortrup, T. Hassenkam, M. B. Nielsen, K. Kilså, *New J. Chem.* **2009**, *33*, 507–516.
[132] H. Langhals, A. Hofer, S. Bernhard, J. S. Siegel, P. Mayer, *J. Org. Chem.* **2011**, *76*, 990–992.
[133] R. van der Weegen, P. A. Korevaar, P. Voudouris, I. K. Voets, T. F. A. de Greef, J. A. J. M. Vekemans, E. W. Meijer, *Chem. Commun.* **2013**, *49*, 5532–5534.
[134] M. Myahkostupov, V. Prusakova, D. G. Oblinsky, G. D. Scholes, F. N. Castellano, *J. Org. Chem.* **2013**, *78*, 8634–8644.
[135] B. Rybtchinski, L. E. Sinks, M. R. Wasielewski, *J. Phys. Chem. A* **2004**, *108*, 7497–7505.
[136] Z. Chen, B. Fimmel, F. Würthner, *Org. Biomol. Chem.* **2012**, *10*, 5845–5855.
[137] H. Langhals, S. Demmig, H. Huber, *Spectrochim. Acta A* **1988**, *44*, 1189–1193.
[138] K. D. Shimizu, T. M. Dewey, J. Rebek, *J. Am. Chem. Soc.* **1994**, *116*, 5145–5149.
[139] S. Kohmoto, K. Sakayori, K. Kishikawa, M. Yamamoto, *J. Chem. Soc., Perk. Trans. 2* **1999**, 833–836.
[140] L. D. Wescott, D. L. Mattern, *J. Org. Chem.* **2003**, *68*, 10058–10066.
[141] C. F. Degenhardt, J. M. Lavin, M. D. Smith, K. D. Shimizu, *Org. Lett.* **2005**, *7*, 4079–4081.
[142] Y. Zhong, B. Kumar, S. Oh, M. T. Trinh, Y. Wu, K. Elbert, P. Li, X. Zhu, S. Xiao, F. Ng, M. L. Steigerwald, C. Nuckolls, *J. Am. Chem. Soc.* **2014**, *136*, 8122–8130.
[143] M. Hesse, H. Meier, B. Zeeh, *Spectroscopic Methods in Organic Chemistry*, 2nd ed., Thieme, Stuttgart, **2007**.
[144] W. J. Hehre, R. Ditchfield, J. A. Pople, *J. Phys. Chem. A* **1972**, *56*, 2257–2261.
[145] M. S. Gordon, *Chem. Phys. Lett.* **1980**, *76*, 163–168.
[146] M. M. Francl, W. J. Pietro, W. J. Hehre, J. S. Binkley, M. S. Gordon, D. J. DeFrees, J. A. Pople, *J. Phys. Chem. A* **1982**, *77*, 3654–3665.
[147] M. J. Frisch, J. A. Pople, J. S. Binkley, *J. Phys. Chem. A* **1984**, *80*, 3265–3269.

[148] A. D. Becke, *J. Phys. Chem. A* **1993**, *98*, 5648–5652.
[149] Y. Cohen, L. Avram, L. Frish, *Angew. Chem. Int. Ed.* **2005**, *44*, 520–554.
[150] J. Řezáč, J. Fanfrlík, D. Salahub, P. Hobza, *J. Chem. Theory Comput.* **2009**, *5*, 1749–1760.
[151] M. Korth, M. Pitoňák, J. Řezáč, P. Hobza, *J. Chem. Theory Comput.* **2010**, *6*, 344–352.
[152] W. J. Hehre, R. F. Stewart, J. A. Pople, *J. Phys. Chem. A* **1969**, *51*, 2657–2664.
[153] J. B. Collins, P. von R. Schleyer, J. S. Binkley, J. A. Pople, *J. Phys. Chem. A* **1976**, *64*, 5142–5151.
[154] S. Grimme, *J. Comput. Chem.* **2006**, *27*, 1787–1799.
[155] A. Schäfer, H. Horn, R. Ahlrichs, *J. Phys. Chem. A* **1992**, *97*, 2571–2577.
[156] S. Grimme, J. Antony, S. Ehrlich, H. Krieg, *J. Phys. Chem. A* **2010**, *132*, 154104.
[157] J. B. Birks, *Rep. Prog. Phys.* **1975**, *38*, 903–974.
[158] M. J. Ahrens, L. E. Sinks, B. Rybtchinski, W. Liu, B. A. Jones, J. M. Giaimo, A. V. Gusev, A. J. Goshe, D. M. Tiede, M. R. Wasielewski, *J. Am. Chem. Soc.* **2004**, *126*, 8284–8294.
[159] C. Hippius, I. H. M. van Stokkum, E. Zangrando, R. M. Williams, F. Würthner, *J. Phys. Chem. C* **2007**, *111*, 13988–13996.
[160] J. R. Lakowicz, *Principles of Fluorescence Spectroscopy*, 2nd ed., Kluwer Academic/Plenum Publishers, New York, **1999**.
[161] E. H. A. Beckers, S. C. J. Meskers, A. P. H. J. Schenning, Z. Chen, F. Würthner, R. A. J. Janssen, *J. Phys. Chem. A* **2004**, *108*, 6933–6937.
[162] C. C. Hofmann, S. M. Lindner, M. Ruppert, A. Hirsch, S. A. Haque, M. Thelakkat, J. Köhler, *Phys. Chem. Chem. Phys.* **2010**, *12*, 14485–14491.
[163] T. Förster, K. Kasper, *Z. Elektrochem.* **1955**, *59*, 976–980.
[164] J. B. Birks, D. J. Dyson, I. H. Munro, *P. Roy. Soc. Lond. A Mat.* **1963**, *275*, 575–588.
[165] A. T. Haedler, H. Misslitz, C. Buehlmeyer, R. Q. Albuquerque, A. Köhler, H.-W. Schmidt, *ChemPhysChem* **2013**, *14*, 1818–1829.
[166] J. Salbeck, *J. Electroanal. Chem.* **1992**, *340*, 169–195.
[167] R. O. Marcon, S. Brochsztain, *J. Phys. Chem. A* **2009**, *113*, 1747–1752.
[168] N. Vân Anh, F. Schlosser, M. M. Groeneveld, I. H. M. van Stokkum, F. Würthner, R. M. Williams, *J. Phys. Chem. C* **2009**, *113*, 18358–18368.
[169] M. Wolffs, N. Delsuc, D. Veldman, N. Vân Anh, R. M. Williams, S. C. J. Meskers, R. A. J. Janssen, I. Huc, A. P. H. J. Schenning, *J. Am. Chem. Soc.* **2009**, *131*, 4819–4829.
[170] D. Rehm, A. Weller, *Ber. Bunsenges. Phys. Chem.* **1969**, *73*, 834–839.
[171] D. Rehm, A. Weller, *Isr. J. Chem.* **1970**, *8*, 259–271.
[172] A. Weller, *Z. Phys. Chem.* **1982**, *133*, 93–98.
[173] M. C. R. Delgado, E.-G. Kim, D. A. d. S. Filho, J.-L. Bredas, *J. Am. Chem. Soc.* **2010**, *132*, 3375–3387.
[174] S. Samori, S. Tojo, M. Fujitsuka, T. Ryhding, A. G. Fix, B. M. Armstrong, M. M. Haley, T. Majima, *J. Org. Chem.* **2009**, *74*, 3776–3782.
[175] S. Asir, A. S. Demir, H. Icil, *Dyes Pigm.* **2010**, *84*, 1–13.
[176] L. Perrin, P. Hudhomme, *Eur. J. Org. Chem.* **2011**, *2011*, 5427–5440.
[177] R. Shivanna, S. Shoaee, S. Dimitrov, S. K. Kandappa, S. Rajaram, J. R. Durrant, K. S. Narayan, *Energy Environ. Sci.* **2014**, *7*, 435–441.
[178] T. Ye, R. Singh, H.-J. Butt, G. Floudas, P. E. Keivanidis, *ACS Appl. Mater. Interfaces* **2013**, *5*, 11844–11857.
[179] Y. Lin, Y. Wang, J. Wang, J. Hou, Y. Li, D. Zhu, X. Zhan, *Adv. Mater.* **2014**, *26*, 5137–5142.

[180] Y. Zang, C.-Z. Li, C.-C. Chueh, S. T. Williams, W. Jiang, Z.-H. Wang, J.-S. Yu, A. K. Y. Jen, *Adv. Mater.* **2014**, *26*, 5708–5714.
[181] Y. Zhong, M. T. Trinh, R. Chen, W. Wang, P. P. Khlyabich, B. Kumar, Q. Xu, C.-Y. Nam, M. Y. Sfeir, C. Black, M. L. Steigerwald, Y.-L. Loo, S. Xiao, F. Ng, X. Y. Zhu, C. Nuckolls, *J. Am. Chem. Soc.* **2014**, *136*, 15215–15221.
[182] G. Dennler, M. C. Scharber, C. J. Brabec, *Adv. Mater.* **2009**, *21*, 1323–1338.
[183] H. Bürckstümmer, E. V. Tulyakova, M. Deppisch, M. R. Lenze, N. M. Kronenberg, M. Gsänger, M. Stolte, K. Meerholz, F. Würthner, *Angew. Chem.* **2011**, *123*, 11832–11836.
[184] J.-L. Brédas, D. Beljonne, V. Coropceanu, J. Cornil, *Chem. Rev.* **2004**, *104*, 4971–5004.
[185] M. C. Scharber, D. Mühlbacher, M. Koppe, P. Denk, C. Waldauf, A. J. Heeger, C. J. Brabec, *Adv. Mater.* **2006**, *18*, 789–794.
[186] J. E. Anthony, *Chem. Mat.* **2011**, *23*, 583–590.
[187] X. Liu, P. Cai, D. C. Chen, J. W. Chen, S. J. Su, Y. Cao, *Sci. China: Chem.* **2014**, *57*, 973–981.
[188] Y. Liu, C. Mu, K. Jiang, J. Zhao, Y. Li, L. Zhang, Z. Li, J. Y. L. Lai, H. Hu, T. Ma, R. Hu, D. Yu, X. Huang, B. Z. Tang, H. Yan, *Adv. Mater.* **2015**, *27*, 1015–1020.
[189] X. Zhang, C. Zhan, J. Yao, *Chem. Mat.* **2015**, *27*, 166–173.
[190] L. Ye, K. Sun, W. Jiang, S. Zhang, W. Zhao, H. Yao, Z. Wang, J. Hou, *ACS Appl. Mater. Interfaces* **2015**, *7*, 9274–9280.
[191] D. D. Perrin, W. L. Armarego, D. R. Perrin, *Purification of Laboratory Chemicals – Second Edition*, Pergamon Press Ltd., Oxford, **1980**.
[192] B. Fimmel, diploma thesis, University of Würzburg (Germany), **2010**.
[193] A. J. Fry, in *Laboratory Techniques in Electroanalytical Chemistry*, 2nd ed. (Eds.: P. Kissinger, W. R. Heineman), Marcel Dekker Ltd., New York, **1996**, p. 481.
[194] G. Seybold, G. Wagenblast, *Dyes Pigm.* **1989**, *11*, 303–317.
[195] HyperChem, Release 7.1 for Windows, Hypercube, Inc., Gainesville (FL, USA), **2002**.
[196] MacroModel 9.8 User Manual, Schrödinger Press, **2010**.
[197] N. L. Allinger, Y. H. Yuh, J. H. Lii, *J. Am. Chem. Soc.* **1989**, *111*, 8551–8566.
[198] Maestro, version 9.3, Schrödinger, LLC, New York (NY, USA), **2011**.
[199] MacroModel, version 9.8, Schrödinger, LLC, New York (NY, USA), **2011**.
[200] Jay W. Ponder, Tinker, version 6.2, Jay W. Ponder Lab, Saint Louis (MO, USA), **2013**.
[201] J. J. P. Stewart, *J Mol Model* **2007**, *13*, 1173–1213.
[202] G. W. T. M. J. Frisch, H. B. Schlegel, G. E. Scuseria, M. A. Robb, J. R. Cheeseman, G. Scalmani, V. Barone, B. Mennucci, G. A. Petersson, H. Nakatsuji, M. Caricato, X. Li, H. P. Hratchian, A. F. Izmaylov, J. Bloino, G. Zheng, J. L. Sonnenberg, M. Hada, M. Ehara, K. Toyota, R. Fukuda, J. Hasegawa, M. Ishida, T. Nakajima, Y. Honda, O. Kitao, H. Nakai, T. Vreven, J. A. Montgomery, J. E. Peralta, F. Ogliaro, M. Bearpark, J. J. Heyd, E. Brothers, K. N. Kudin, V. N. Staroverov, T. Keith, R. Kobayashi, J. Normand, K. Raghavachari, A. Rendell, J. C. Burant, S. S. Iyengar, J. Tomasi, M. Cossi, N. Rega, J. M. Millam, M. Klene, J. E. Knox, J. B. Cross, V. Bakken, C. Adamo, J. Jaramillo, R. Gomperts, R. E. Stratmann, O. Yazyev, A. J. Austin, R. Cammi, C. Pomelli, J. W. Ochterski, R. L. Martin, K. Morokuma, V. G. Zakrzewski, G. A. Voth, P. Salvador, J. J. Dannenberg, S. Dapprich, A. D. Daniels, O. Farkas, J. B. Foresman, J. V. Ortiz, J. Cioslowski, D. J. Fox, Gaussian 09, Revision B.01, Gaussian, Inc., Wallingford (CT, USA), **2010**.
[203] TurboMole, version 6.5, TurboMole GmbH, Karlsruhe (Germany), **2013**.

[204] J. J. P. Stewart, MOPAC2012, Stewart Computational Chemistry, Colorado Springs (CO, USA), **2012**.
[205] J. D. C. Maia, G. A. Urquiza Carvalho, C. P. Mangueira, S. R. Santana, L. A. F. Cabral, G. B. Rocha, *J. Chem. Theory Comput.* **2012**, *8*, 3072–3081.
[206] C. Grebner, J. Becker, D. Weber, D. Bellinger, M. Tafipolski, C. Brückner, B. Engels, *J. Comput. Chem.* **2014**, *35*, 1801–1807.

Danksagung

Vor allem möchte ich mich bei Herrn Prof. Dr. Frank Würthner für seine zahlreichen Hilfestellungen jeglicher Art, seine Geduld, seine vielen Ratschläge an mich, das Anvertrauen und Überlassen des Forschungsthemas und insgesamt für die ausgezeichnete Betreuung besonders bedanken.

Herrn Prof. Dr. Bernd Engels danke ich für die zeitweise Aufnahme in seine Arbeitsgruppe sowie die Einblicke in die Theoretische Chemie und die zahlreichen Besprechungen, die letztlich in einer gemeinsamen Publikation mündeten. An dieser Stelle sei auch schon Herrn M. Sc. Daniel Bellinger aus der Arbeitsgruppe um Herrn Prof. Dr. Bernd Engels für das geduldige Erklären von Programmen und Sachverhalten gedankt.

Herrn Prof. Dr. Dongho Kim von der Yonsei University, Seoul, Südkorea, möchte ich meinen Dank für die Ermöglichung eines Besuchs seiner Arbeitsgruppe aussprechen, bei welchem ich zusammen mit seiner Studentin Frau M. Sc. Minjung Son spektroskopische Messungen durchführen durfte, woraus bisher zwei Publikationen entstanden sind.

Herrn Prof. Dr. Tobias Brixner danke ich sehr für die Ermöglichung der Teilnahme am Workshop zur Ultrakurzzeitspektroskopie und Quantenkontrolle in Zell am See sowie Herrn Dipl.-Chem. Florian Kanal aus seiner Arbeitsgruppe.

Für die finanzielle Unterstützung bei Konferenzen, Workshops und letztlich der Reise nach Korea bin ich dem Graduiertenkolleg GRK 1221 „Steuerung elektronischer Eigenschaften von Aggregaten π-konjugierter Moleküle“ sowie der Forschergruppe FOR1809 „Lichtinduzierte Dynamik in molekularen Aggregaten“ zu Dank verpflichtet.

Den beiden Mitgliedern aus der Arbeitsgruppe um Herrn Prof. Dr. Dongho Kim, Frau M. Sc. Minjung Son und Herrn Dr. Young Mo Sung, möchte ich sehr für die herzliche Aufnahme in die Gruppe sowie die notwendigen Hilfen im alltäglichen Leben vor Ort als auch für die Hilfe bei Messungen für unser gemeinsames Projekt danken. Vor allem aber möchte ich Frau M. Sc. Minjung Son für die außergewöhnliche Unterstützung während des gesamten Aufenthalts in Seoul "감사합니다" sagen. Weiterhin möchte ich den anderen Arbeitskreismitgliedern für ihre aufmerksame Art danken. Besonders sei hier die fürsorgliche Hilfe von Herrn M. Sc. Sangsu Lee sowie die freundliche Einbindung durch Herrn Dr. Jong Min Lim wie auch Frau M. Sc. Jooyoung Sung, Frau Dr. Ji-Eun Lee und Frau Min-Kyung Jeong genannt.

Herrn Dr. Matthias Grüne sowie Frau Elfriede Ruckdeschel gebührt mein Dank für die Aufnahme der NMR-Spektren am 600 MHz-NMR-Gerät, die immer freundliche und hilfreiche Unterstützung bei Fragen sowie die Mitarbeit bei einem gemeinsamen Projekt.

Herrn Dr. Chantu R. Saha-Möller möchte ich für die professionelle Korrekturhilfe bei zwei Manuskripten als auch für die Organisation zahlreicher Angelegenheiten Danke sagen.

Für das Korrekturlesen dieser Arbeit bzw. Teile derer danke ich sehr herzlich Herrn Dr. Martin Berberich, Herrn M. Sc. Ayan Dhara sowie Frau Dipl.-Chem. Stefanie Klotzbach.

Die zuverlässige Aufnahme von MS-Spektren durch Herrn Dr. Michael Büchner, Herrn Fritz Dadrich sowie Frau Antje Hautzinger möchte ich voller Dank hier aufführen. Frau Liselotte Michels und Frau Sabine Timmroth vielen Dank für die Durchführung der CHN-Elementaranalysen am Institut für Anorganische Chemie, Würzburg.

Herrn Dipl.-Ing. Bernd Brunner möchte ich für die stets freundlichen Hilfen in Bezug auf Computer und Drucker danken.

Den Chemielaboranten Herrn Joachim Bialas, Herrn Johannes Thein, Herrn Christian Simon sowie Frau Petra Seufert-Baumbach ein großes Dankeschön für alle Hilfen und Handgriffe beim alltäglichen Laborleben wie auch für alle Unterhaltungen.

Frau Christiana Toussaint, Frau Anette Häfner danke ich sehr herzlich für die große Hilfsbereitschaft bei allen organisatorischen Angelegenheiten sowie für das offene Ohr zu jeder Zeit. Weiterhin ein Dankeschön an Frau Petra Leckert und Frau Anette Krug. Für schnelle und unkomplizierte Hilfe bei der Organisation der Reise nach Korea lieben Dank an Frau Ursula Rüppel sowie zusätzlich Danke für die Organisation weiterer Fahrten und Besuche von Workshops, Klausurtagungen oder Konferenzen als GRK-Stipendiat. Frau Andrea Gehring danke ich für die Planung des FOR-Workshops in Niederstetten.

Danke allen Personen, die am Gelingen dieser Arbeit geholfen haben bzw. sich am Erfolg dieser beteiligt haben, die mir kleine und große Sachverhalte erklärt haben oder die mich an Geräten oder Programmen eingewiesen haben. Das sind Herr Prof. Dr. Frank Würthner, Herr Prof. Dr. Bernd Engels, Herr Prof. Dr. Dongho Kim, Prof. Dr. Adelheid Godt, Herr Dr. Volker C. Dehm, Herr Dr. Martin Berberich, Herr Dr. Thomas H. Rehm, Herr Dr. Matthias Stolte, Herr Dr. Matthias Grüne, Frau M. Sc. Minjung Son, Herr Dr. Young Mo Sung, Herr Dr. Gustavo Fernández, Frau Dr. María José Mayoral Muñoz, Herr Dr. Ángel Jiménez, Herr Dr. Pete Frischmann, Herr Dr. Karl Thorley, Herr Dr. Felix Schlosser, Herr Dr. Vladimir Stepanenko, Elfriede Ruckdeschel, Herr Dr. Marcel Gsänger, Herr Dr. Sabin-Lucian Suraru, Herr Dr. Xin Zhang, Frau Dr. Charlotte Grzeszkewicz, Frau Ana-Maria Krause, Herr Dr. André Zitzler-Kunkel, Frau Christina Rest und Frau Jennifer Begall, Frau Dipl.-Chem. Jana Gershberg, Herr M. Sc. Valentin Kunz, Herr M. Sc. Martin Pfeffermann, Herr M. Sc. Daniel Bellinger, Herr Dr. Torsten Bruhn, Frau Dr. Anu Schaumlöffel, Frau Dipl.-Chem. Yasmin Hemberger und Frau Dipl.-Chem. Anca Boariu.

Herrn Markus Braun danke ich für organisatorische Angelegenheiten. Weiterhin den Glasbläsern am Institut, Herrn Ludwig sowie Herrn Jonathan Landeck, vielen Dank.

Herzlichen Dank besonders den Arbeitskreismitgliedern des Labors 412 für die lustige Zeit und Hilfsbereitschaft.

Meinen stets hochmotivierten und voller Ideen sprudelnden Studenten Herr M. Sc. Julian Böhnke (Bachelorarbeit 2011) sowie den Master-F-Praktikantinnen Frau M. Sc. Anja Belz

(2011) und Frau M. Sc. Stefanie Griesbeck (2013) sowie den „AK-Präplern“ danke ich für weitere Unterstützung bei synthetischen Anstrengungen. Dem Auszubildenden Herrn Michael Fitzner danke ich für die kurzzeitige Mithilfe im Labor.

Meinen Studienkollegen Dr. Ginka Kubelka, Dipl.-Chem. Christoph Fischer, M. Sc. Sergej Fisenko und Sebastian Dräger möchte ich sehr herzlich für die gemeinsam verbrachte Zeit, u.a. auch Lernnachmittage, danken.

Allen aktuellen sowie ehemaligen Arbeitskreismitgliedern danke ich.

Meiner gesamten Familie bin ich für ihre Unterstützung und ihre Verständnis zu größtem Dank verpflichtet. Insbesondere möchte ich hier den Dank an meine Großeltern und meine lieben Eltern herausstellen. Zu guter Letzt möchte ich aber vor allem Dir, meine liebe Stefanie, für einfach alles danken!

List of Publications

Halochromic Phenolate Perylene Bisimides with Unprecedented NIR Spectroscopic Properties.
M.-J. Lin, B. Fimmel, K. Radacki, F. Würthner, *Angew. Chem.* **2011**, *123*, 11039–11042; *Angew. Chem. Int. Ed.* **2011**, *50*, 10847–10850.

Bright Near-Infrared Fluorophores Based on Squaraines by Unexpected Halogen Effects.
U. Mayerhöffer, B. Fimmel, F. Würthner, *Angew. Chem.* **2012**, *124*, 168–171; *Angew. Chem. Int. Ed.* **2012**, *51*, 164–167.

Solvent and substituent effects on aggregation constants of perylene bisimide π-stacks – a linear free energy relationship analysis.
Z. Chen, B. Fimmel, F. Würthner, *Org. Biomol. Chem.* **2012**, *10*, 5845–5855.

Synthesis and Molecular Properties of Acceptor-Substituted Squaraine Dyes.
U. Mayerhöffer, M. Gsänger, M. Stolte, B. Fimmel, F. Würthner, *Chem. Eur. J.* **2013**, *19*, 218–232.

An Organogelator Design without Solubilizing Side Chains by Backbone Contortion of Perylene Bisimide Pigment.
Z. Xie, V. Stepanenko, B. Fimmel, F. Würthner, *Mater. Horiz.* **2014**, *1*, 355–359.

Phenylene Ethynylene Tethered Perylene Bisimide Folda-Dimer and Folda-Trimer: Investigations on Folding Features in Ground and Excited States. (Ranked as Hot Paper)
B. Fimmel, M. Son, Y. M. Sung, M. Grüne, B. Engels, D. Kim, F. Würthner, *Chem. Eur. J.* **2015**, *21*, 615–630.

Folding-Induced Modulation of Excited-State Dynamics in an Oligophenylene-Ethynylene-Tethered Spiral Perylene Bisimide Aggregate.
M. Son, B. Fimmel, V. Dehm, F. Würthner, D. Kim, *ChemPhysChem* **2015**, *16*, 1757–1767.

Photoinduced electron transfer (PET) versus excimer formation in supramolecular p/n-heterojunctions of perylene bisimide dyes and implications for organic photovoltaics.
A. Nowak-Król, B. Fimmel, M. Son, D. Kim, F. Würthner, *Faraday Discuss.* **2015**, *accepted*.

Perylene Bisimide Dye Assemblies as Archetype Functional Supramolecular Materials.
F. Würthner, C. R. Saha-Möller, B. Fimmel, O. Soichiro, P. Leowanawat, D. Schmidt, *Chem. Rev.*, *accepted* (DOI: 10.1002/acs.chemrev.5b00188).

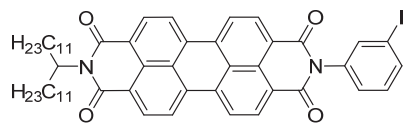

30

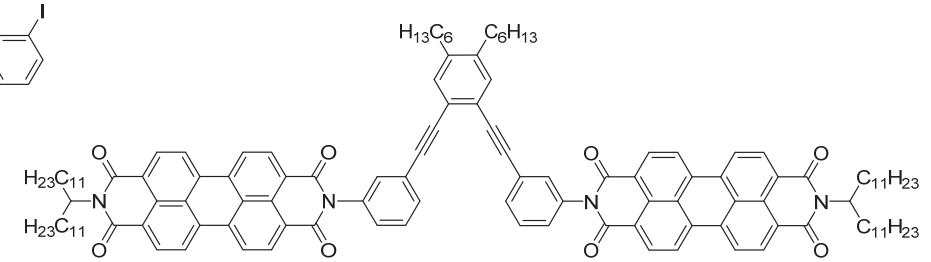

32

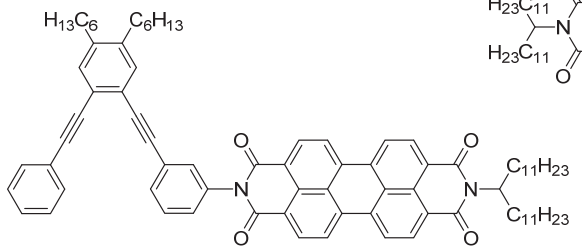

31

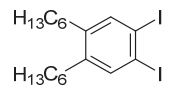

34

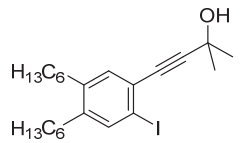

36

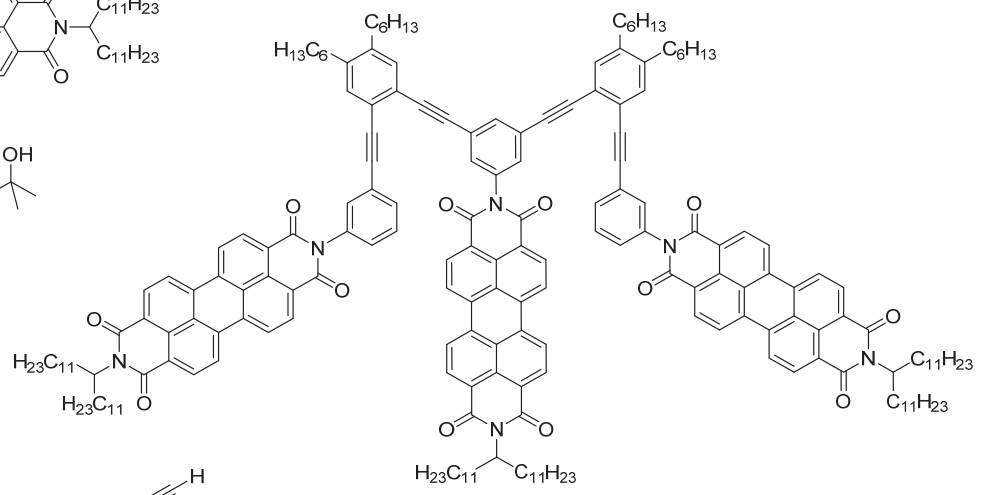

33

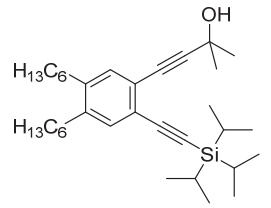

38

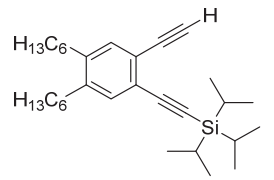

39

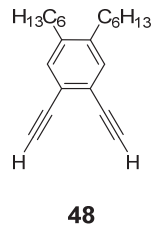

48

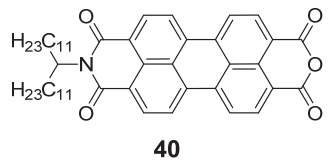

40

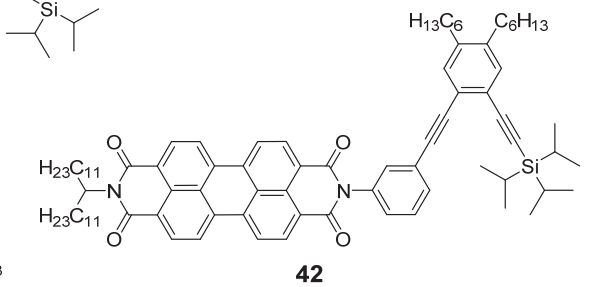

42

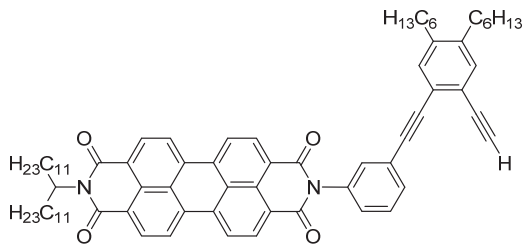

43

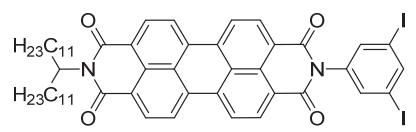

44

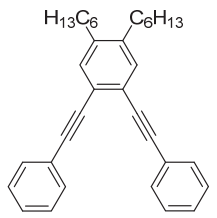

49